
HARD X-RAY SCANNING MICROSCOPE USING NANOFOCUSING PARABOLIC REFRACTIVE LENSES

Dissertation

zur Erlangung des akademischen Grades

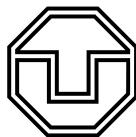
Doctor rerum naturalium

(Dr. rer. nat.)

vorgelegt

der Fakultät Mathematik und Naturwissenschaften

der Technischen Universität Dresden



**TECHNISCHE
UNIVERSITÄT
DRESDEN**

von

Diplom-Physiker Jens Patommel

geboren am 7. Juni 1977

in Wilhelm-Pieck-Stadt Guben

Eingereicht am 13. Juli 2010

Die Dissertation wurde in der Zeit von April 2006 bis Juni 2010
am Institut für Strukturphysik angefertigt.

Gutachter: Prof. Dr. C. G. Schroer
Prof. Dr. U. Klemradt

Datum des Rigorosum: 12. November 2010
Prüfer: Prof. Dr. C. G. Schroer
Prof. Dr. K. Leo

Datum der Disputation: 12. November 2010
Promotionskommission: Prof. Dr. F. Jülicher (Vorsitz)
Prof. Dr. C. G. Schroer
Prof. Dr. U. Klemradt
Prof. Dr. M. Kobel
Prof. Dr. K. Leo
PD Dr. F. Grossmann

Abstract

Hard x rays come along with a variety of extraordinary properties which make them an excellent probe for investigation in science, technology and medicine. Their large attenuation length in matter opens up the possibility to use hard x-rays for non-destructive investigation of the inner structure of specimens. Medical radiography is one important example of exploiting this feature. Since their discovery by W. C. Röntgen in 1895, a large variety of x-ray analytical techniques have been developed and successfully applied, such as x-ray crystallography, reflectometry, fluorescence spectroscopy, x-ray absorption spectroscopy, small angle x-ray scattering, and many more. Each of those methods reveals information about certain physical properties, but usually, these properties are an average over the complete sample region illuminated by the x rays. In order to obtain the spatial distribution of those properties in inhomogeneous samples, scanning microscopy techniques have to be applied, screening the sample with a small x-ray beam. The spatial resolution is limited by the finite size of the beam. The availability of highly brilliant x-ray sources at third generation synchrotron radiation facilities together with the development of enhanced focusing x-ray optics made it possible to generate increasingly small high intense x-ray beams, pushing the spatial resolution down to the sub-100 nm range.

During this thesis the prototype of a hard x-ray scanning microscope utilizing microstructured nanofocusing lenses was designed, built, and successfully tested. The nanofocusing x-ray lenses were developed by our research group of the Institute of Structural Physics at the Technische Universität Dresden. The prototype instrument was installed at the ESRF beamline ID 13. A wide range of experiments like fluorescence element mapping, fluorescence tomography, x-ray nano-diffraction, coherent x-ray diffraction imaging, and x-ray ptychography were performed as part of this thesis. The hard x-ray scanning microscope provides a stable x-ray beam with a full width at half maximum size of 50–100 nm near the focal plane. The nanoprobe was also used for characterization of nanofocusing lenses, crucial to further improve them. Based on the experiences with the prototype, an advanced version of a hard x-ray scanning microscope is under development and will be installed at the PETRA III beamline P06 dedicated as a user instrument for scanning microscopy.

This document is organized as follows. A short introduction motivating the necessity for building a hard x-ray scanning microscope is followed by a brief review of the fundamentals of hard x-ray physics with an emphasis on free-space propagation and interaction with matter. After a discussion of the requirements on the x-ray source for the nanoprobe, the main features of synchrotron radiation from an undulator source are shown. The properties of the nanobeam generated by refractive x-ray lenses are treated as well as a two-stage focusing scheme for tailoring size, flux and the lateral coherence properties of the x-ray focus. The design and realization of the microscope setup is addressed, and a selection of experiments performed with the prototype version is presented, before this thesis is finished with a conclusion and an outlook on prospective plans for an improved microscope setup to be installed at PETRA III.

Kurzfassung

Aufgrund ihrer hervorragenden Eigenschaften kommt harte Röntgenstrahlung in vielfältiger Weise in der Wissenschaft, Industrie und Medizin zum Einsatz. Vor allem die Fähigkeit, makroskopische Gegenstände zu durchdringen, eröffnet die Möglichkeit, im Innern ausgehnter Objekte verborgene Strukturen zum Vorschein zu bringen, ohne den Gegenstand zerstören zu müssen. Eine Vielzahl röntgenanalytischer Verfahren wie zum Beispiel Kristallographie, Reflektometrie, Fluoreszenzspektroskopie, Absorptionsspektroskopie oder Kleinwinkelstreuung sind entwickelt und erfolgreich angewendet worden. Jede dieser Methoden liefert gewisse strukturelle, chemische oder physikalische Eigenschaften der Probe zutage, allerdings gemittelt über den von der Röntgenstrahlung beleuchteten Bereich. Um eine orts aufgelöste Verteilung der durch die Röntgenanalyse gewonnenen Information zu erhalten, bedarf es eines sogenannten Mikrostrahls, durch den die Probe lokal abgetastet werden kann. Die dadurch erreichbare räumliche Auflösung ist durch die Größe des Mikrostrahls begrenzt. Aufgrund der Verfügbarkeit hinreichend brillanter Röntgenquellen in Form von Undulatoren an Synchrotronstrahlungseinrichtungen und des Vorhandenseins verbesserter Röntgenoptiken ist es in den vergangenen Jahren gelungen, immer kleinere intensive Röntgenfokusse zu erzeugen und somit das räumliche Auflösungsvermögen der Röntgenrastermikroskope auf unter 100 nm zu verbessern.

Gegenstand dieser Arbeit ist der Prototyp eines Rastersondenmikroskops für harte Röntgenstrahlung unter Verwendung refraktiver nanofokussierender Röntgenlinsen, die von unserer Arbeitsgruppe am Institut für Strukturphysik entwickelt und hergestellt werden. Das Rastersondenmikroskop wurde im Rahmen dieser Promotion in Dresden konzipiert und gebaut sowie am Strahlrohr ID 13 des ESRF installiert und erfolgreich getestet. Das Gerät stellt einen hochintensiven Röntgenfokus der Größe 50–100 nm zur Verfügung, mit dem im Verlaufe dieser Doktorarbeit zahlreiche Experimente wie Fluoreszenztomographie, Röntgenanobeugung, Abbildung mittels kohärenter Röntgenbeugung sowie Röntgenptychographie erfolgreich durchgeführt wurden. Das Rastermikroskop dient unter anderem auch dem Charakterisieren der nanofokussierenden Linsen, wobei die dadurch gewonnenen Erkenntnisse in die Herstellung verbesserten Linsen einfließen.

Diese Arbeit ist wie folgt strukturiert. Ein kurzes einleitendes Kapitel dient als Motivation für den Bau eines Rastersondenmikroskops für harte Röntgenstrahlung. Es folgt eine Einführung in die Grundlagen der Röntgenphysik mit Hauptaugenmerk auf die Ausbreitung von Röntgenstrahlung im Raum und die Wechselwirkungsmechanismen von Röntgenstrahlung mit Materie. Anschließend werden die Anforderungen an die Röntgenquelle besprochen und die Vorzüge eines Undulators herausgestellt. Wichtige Eigenschaften eines mittels refraktiver Röntgenlinsen erzeugten Röntgenfokus werden behandelt, und das Konzept einer Vorfokussierung zur gezielten Anpassung der transversalen Kohärenzeigenschaften an die Erfordernisse des Experiments wird besprochen. Das Design und die technische Realisierung des Rastermikroskops werden ebenso dargestellt wie eine Auswahl erfolgreicher Experimente, die am Gerät vollzogen wurden. Die Arbeit endet mit einem Ausblick, der mögliche Weiterentwicklungen in Aussicht stellt, unter anderem den Aufbau eines verbesserten Rastermikroskops am PETRA III-Strahlrohr P06.

Contents

1	Introduction	1
2	Basic Properties of Hard X Rays	3
2.1	Free Propagation of X Rays	3
2.1.1	The Helmholtz Equation	4
2.1.2	Integral Theorem of Helmholtz and Kirchhoff	6
2.1.3	Fresnel-Kirchhoff's Diffraction Formula	8
2.1.4	Fresnel-Kirchhoff Propagation	11
2.2	Interaction of X Rays with Matter	13
2.2.1	Complex Index of Refraction	13
2.2.2	Attenuation	15
2.2.3	Refraction	18
3	The X-Ray Source	21
3.1	Requirements	21
3.1.1	Energy and Energy Bandwidth	21
3.1.2	Source Size and Divergence	23
3.1.3	Brilliance	23
3.2	Synchrotron Radiation	24
3.3	Layout of a Synchrotron Radiation Facility	27
3.4	Liénard-Wiechert Fields	29
3.5	Dipole Magnets	31
3.6	Insertion Devices	36
3.6.1	Multipole Wigglers	36
3.6.2	Undulators	37
4	X-Ray Optics	39
4.1	Refractive X-Ray Lenses	40
4.2	Compound Parabolic Refractive Lenses (CRLs)	41
4.3	Nanofocusing Lenses (NFLs)	43
4.4	Adiabatically Focusing Lenses (AFLs)	45
4.5	Focal Distance	46
4.6	Transverse Focus Size	50

4.7	Beam Caustic	52
4.8	Depth of Focus	53
4.9	Beam Divergence	53
4.10	Chromaticity	54
4.11	Transmission and Cross Section	55
4.12	Transverse Coherence	56
	4.12.1 Mutual Intensity Function	57
	4.12.2 Free Propagation of Mutual Intensity	57
	4.12.3 Mutual Intensity In The Focal Plane	58
	4.12.4 Diffraction Limited Focus	59
4.13	Coherent Flux	60
4.14	Two-Stage Focusing	64
	4.14.1 The Prefocusing Parameter η	65
	4.14.2 Required Refractive Power	67
	4.14.3 Flux Considerations	70
	4.14.4 Astigmatic Prefocusing	75
5	Nanoprobe Setup	77
5.1	X-Ray Optics	78
	5.1.1 Nanofocusing Lenses	79
	5.1.2 Entry Slits	82
	5.1.3 Pinhole	82
	5.1.4 Additional Shielding	83
	5.1.5 Vacuum and Helium Tubes	83
5.2	Sample Stages	84
	5.2.1 High Resolution Scanner	84
	5.2.2 High Precision Rotational Stage	85
	5.2.3 Coarse Linear Stages	85
	5.2.4 Goniometer Head	85
5.3	Detectors	86
	5.3.1 High Resolution X-Ray Camera	86
	5.3.2 Diffraction Cameras	89
	5.3.3 Energy Dispersive Detectors	91
	5.3.4 Photodiodes	93
5.4	Control Software	94
6	Experiments	97
6.1	Lens Alignment	97
6.2	Focus Characterization	99
	6.2.1 Knife-Edge Scans	100
	6.2.2 Far-Field Measurements	102
	6.2.3 X-Ray Ptychography	103
6.3	Fluorescence Spectroscopy	105

6.3.1	Fluorescence Element Mapping	107
6.3.2	Fluorescence Tomography	110
6.4	Diffraction Experiments	111
6.4.1	Microdiffraction on Phase Change Media	112
6.4.2	Microdiffraction on Stranski-Krastanow Islands	113
6.4.3	Coherent X-Ray Diffraction Imaging of Gold Particles	115
6.4.4	X-Ray Ptychography of a Nano-Structured Microchip	117
7	Conclusion and Outlook	121
	Bibliography	125
	List of Figures	139
	List of Publications	141
	Danksagung	145
	Curriculum Vitae	149
	Erklärung	151

Chapter 1

Introduction

This PhD thesis treats of the prototype of a hard x-ray high resolution scanning microscope using nanofocusing refractive lenses. The scanning microscope (synonymously called “nanoprobe”) was developed, built and operated by our study group in Dresden in the course of a project supported by the German Department of Education and Research (Bundesministerium für Bildung und Forschung, BMBF). The main goal of the project was to demonstrate the possibility to generate a small intense x-ray focus with a full width at half maximum size below 100 nm, which can be employed for spatially resolved x-ray analysis. In a follow-up venture, we are currently assembling an upgraded version of a hard x-ray scanning microscope to be installed at the PETRA III beamline P06, bringing in the experiences we made with the prototype version.

Hard x rays are capable of pervading matter and, therefore, x rays — in contrast to visible light, soft x rays, or electron beams — are capable of revealing the interior properties of specimens without destructive sample preparation. Since their discovery by W. C. Röntgen in 1895 [Rön95, Rön98], a large variety of x-ray analytical techniques have been developed and successfully applied. Among others, there are x-ray crystallography, x-ray reflectometry, x-ray fluorescence spectroscopy, x-ray absorption spectroscopy, small angle x-ray scattering, and grazing incidence small angle x-ray scattering. For years, these methods were performed with large (unfocused) x-ray beams, illuminating the complete sample or at least large areas of the specimen, and for this reason, these methods were insensitive to the spatial Distribution of the investigated properties. In order to retrieve the local distribution of the observed property rather than just an average over the complete object, the sample has to be scanned by a small x-ray beam. Generating small and intense x-ray beams requires highly brilliant x-ray sources and high quality focusing optics. Compared with visible light available x-ray sources are comparably weak and focusing optics quite inefficient. Thus, the generation of highly intense and small sized x-ray beams is difficult, and it was not until the advent of third generation synchrotron radiation facilities, that hard x-ray scanning microscopy has begun to emerge as a beneficial tool for sample investigations.

The hard x-ray scanning microscope makes use of nanofocusing refractive x-ray lenses made of silicon (NFLs) [SKH⁺03, SKP⁺05a] and of compound parabolic refractive lenses made of beryllium (CRLs) [LST⁺99]. The NFLs provide a sub-100nm focal spot by in-

ducing a demagnified image of the x-ray source, while the CRLs are employed as part of a prefocusing device, which adapts the transverse coherence length to the aperture of the NFL. The nanofocusing lenses are developed by our study group in Dresden, and the compound parabolic refractive lenses are manufactured in cooperation with Prof. Lengeler at the RWTH Aachen. In fact, the evolution of the hard x-ray scanning microscope and the development of the nanofocusing lenses are interdependent. The NFLs provide the focal spot which is used by the scanning microscope for sample investigation, while, as a side effect, the NFLs are additionally characterized. The characterization delivers valuable information about aberrations from the ideal lens shape, and this information is incorporated in the design and manufacturing process of improved NFLs, pushing forward the performance of the nanoprobe.

The prototype was built in Dresden, but since it requires the highly brilliance of an undulator x-ray source, it was installed at the ESRF beamline ID 13. A long-term collaboration with the beamline ID 13 offered the possibility to regularly test the instrument and to carry out a lot of experiments, verifying the performance of the nanoprobe and offer its possibilities to other research groups. Based on the experiences with that prototype, the beamline ID 13 has implemented its own nanoprobe setup, for which we provided an interface module in order to mount NFLs developed by our research group in Dresden.

The remainder of this document is organized as follows. Chapter 2 gives a general introduction to the properties of hard x rays, dealing with the subject of free-space propagation and the interaction of x rays with matter. The properties of x-ray sources are discussed in chapter 3. After identifying the demands on the source, the most important characteristics of synchrotron radiation produced by undulators are highlighted. Focusing x-ray optics are treated in chapter 4. Besides NFLs and CRLs, which are the core of the scanning microscope, I also touch on adiabatically focusing lenses (AFLs). The basic properties of the nano beam, which is generated by NFLs, are discussed, and a two-stage focusing scheme is presented. The conceptual design and the realization of the hard x-ray scanning microscope are given in chapter 5. The layout of the ESRF beamline ID 13 is shown as well as the hardware components of the instrument, including optics, stages, and detectors. Finally, in chapter 6 a selection of experiments will give evidence of the performance of the hard x-ray scanning microscope. This work is completed by a conclusion and an outlook on prospective plans in implementing an improved version of the prototype instrument.

Chapter 2

Basic Properties of Hard X Rays

Like visible light, x-ray radiation is part of the electromagnetic spectrum but with a wavelength much shorter than that of visible light. Whereas the wavelength of visible light is in the range between 380 nm and 780 nm, the wavelength of x rays is shorter than 1 nm. The corresponding photon energies $E_{ph} = hc_0/\lambda$ (h the Planck number, c_0 the speed of light in vacuum) are in the order of 1 eV for visible light, but higher than 200 eV for x rays. As a common convention, there is the distinction between soft x rays with photon energies of several 100 eV up to about several keV on the one hand, and hard x rays with photon energies larger than a few keV on the other hand. In contrast to hard x rays, soft x rays do not penetrate very deeply into matter, they are even absorbed significantly in the air for short propagation distances. The phenomenological difference between the properties of soft and hard x rays is quite significant, the experimental handling of soft x rays as well as their potential applications are much different from that of hard x rays and, therefore, different scientific communities for soft x-ray physics and hard x-ray physics have emerged. The scanning microscope treated in this thesis is intended to be employed for hard x rays, allowing to investigate the inner structure of objects. For this reason, the emphasis is laid on hard x rays, even though some of the properties discussed in this chapter are also valid for soft x rays.

2.1 Free Propagation of X Rays

In the scanning microscope x rays propagate from the source to several optical elements, then they propagate to the sample (which hopefully is located in the focal plane of the focusing lens), and finally — after interacting with the sample — x rays propagate from the sample to the detector. Obviously, knowledge about free propagation of x rays is critical in order to understand the scanning microscope. In this section, I provide the theoretical basis that is needed to quantitatively treat the propagation of light, and consequently of hard x rays.

The question to be treated in this section will be the following. Given the electromagnetic field amplitudes of the x rays within a certain plane perpendicular to the optical axis, what are the field amplitudes within a plane at some distance further in the direction of

propagation, if there is only free space between the two planes? This question will be answered by classic electrodynamics, using Maxwell's equations. In a first step I will introduce the Helmholtz equation, a scalar wave function for monochromatic waves. The Helmholtz equation will be used to deduce the integral theorem of Helmholtz and Kirchhoff, which will be adapted to a physical situation which conforms with the needs of simulating free propagation of x rays in the scanning microscope, leading to the Fresnel-Kirchhoff diffraction formula. In a last step I will discuss some approximations being of special relevance in practical situations.

2.1.1 The Helmholtz Equation

We start with Maxwell's equations

$$\frac{\partial}{\partial \mathbf{r}} \times \mathbf{E}(\mathbf{r}, t) = -\frac{\partial}{\partial t} \mathbf{B}(\mathbf{r}, t), \quad (2.1)$$

$$\frac{\partial}{\partial \mathbf{r}} \mathbf{E}(\mathbf{r}, t) = \frac{1}{\epsilon_0} \rho(\mathbf{r}, t), \quad (2.2)$$

$$\frac{\partial}{\partial \mathbf{r}} \times \mathbf{B}(\mathbf{r}, t) = \mu_0 \mathbf{j}(\mathbf{r}, t) + \epsilon_0 \mu_0 \frac{\partial}{\partial t} \mathbf{E}(\mathbf{r}, t), \quad (2.3)$$

$$\frac{\partial}{\partial \mathbf{r}} \mathbf{B}(\mathbf{r}, t) = 0. \quad (2.4)$$

This set of partial differential equations describes the fields $\mathbf{E}(\mathbf{r}, t)$ and $\mathbf{B}(\mathbf{r}, t)$ and forms the fundament of classic electrodynamics. Applying some mathematical manipulations on these equations leads to wave equations for the electromagnetic fields. With $1/c^2 = \mu_0 \epsilon_0$ the wave equations read

$$\begin{aligned} \frac{\partial^2}{\partial \mathbf{r}^2} \mathbf{E} - \frac{1}{c^2} \frac{\partial^2}{\partial t^2} \mathbf{E} &= \frac{1}{\epsilon_0} \frac{\partial}{\partial \mathbf{r}} \rho + \mu_0 \frac{\partial}{\partial t} \mathbf{j}, \\ \frac{\partial^2}{\partial \mathbf{r}^2} \mathbf{B} - \frac{1}{c^2} \frac{\partial^2}{\partial t^2} \mathbf{B} &= -\mu_0 \frac{\partial}{\partial \mathbf{r}} \times \mathbf{j}. \end{aligned} \quad (2.5)$$

If we consider a region far away from any charged particles, the charge density ρ and the current density \mathbf{j} are zero and the inhomogeneous wave equations become homogeneous

$$\begin{aligned} \frac{\partial^2}{\partial \mathbf{r}^2} \mathbf{E} - \frac{1}{c^2} \frac{\partial^2}{\partial t^2} \mathbf{E} &= 0, \\ \frac{\partial^2}{\partial \mathbf{r}^2} \mathbf{B} - \frac{1}{c^2} \frac{\partial^2}{\partial t^2} \mathbf{B} &= 0. \end{aligned} \quad (2.6)$$

It can be shown that *plane waves*

$$\begin{aligned} \mathbf{E}(\mathbf{r}, t) &= \mathbf{E}_0 f(\mathbf{n}\mathbf{r} - ct), \\ \mathbf{B}(\mathbf{r}, t) &= \mathbf{B}_0 f(\mathbf{n}\mathbf{r} - ct) \end{aligned} \quad (2.7)$$

with $|\mathbf{n}| = 1$ are valid solutions of the wave equations. For each given point in time the field values are constant over planes orthogonal to \mathbf{n} . These planes of constant field values propagate in time along the direction given by \mathbf{n} . Since we consider regions free of electric charges ($\rho = 0$), it follows from equations (2.2) and (2.4) that

$$\begin{aligned}\mathbf{n}\mathbf{E} &= 0, \\ \mathbf{n}\mathbf{B} &= 0\end{aligned}$$

and, therefore, the field vectors \mathbf{E} and \mathbf{B} are both orthogonal to the direction of propagation. Furthermore, on applying equation (2.1), the expression

$$\mathbf{n} \frac{\partial}{\partial \mathbf{r}} \times \mathbf{E}_0 = c\mathbf{B}_0 \quad (2.8)$$

can be deduced, showing that the three vectors \mathbf{n} , \mathbf{E} and \mathbf{B} are all perpendicular to each other and form in this order an orthogonal right-handed tripod. If one neglects polarization effects, the electric and the magnetic field amplitudes maybe written in a scalar form. Following the convention in [BW99], I use $V(\mathbf{r}, t)$ to represent the scalar electric field amplitude. This is possible without loss of information, since equation (2.8) allows to determine the magnetic field, once the electric field is known, or vice versa.

A special class of solutions of the homogeneous wave equation (2.6) is that for which the space-dependence separates from the time-dependence, i. e., which can be written in the form

$$V(\mathbf{r}, t) = U(\mathbf{r})T(t). \quad (2.9)$$

Inserting this ansatz into (2.6) one retrieves

$$\left(\frac{\partial^2}{\partial \mathbf{r}^2} + k^2 \right) U(\mathbf{r}) = 0, \quad (2.10)$$

$$\left(\frac{\partial^2}{\partial t^2} + k^2/c^2 \right) T(t) = 0. \quad (2.11)$$

Equation (2.11) has time harmonic solutions

$$T(t) = T_0 e^{i\omega t} \quad (2.12)$$

with $\omega = k/c$. The time-independent wave equation (2.10) is called *Helmholtz equation* and delivers solutions $U_\omega(\mathbf{r})$, which, together with (2.12), solve equation (2.9)

$$V_\omega(\mathbf{r}, t) = T_0 e^{i\omega t} U_\omega(\mathbf{r}). \quad (2.13)$$

If $U_\omega(\mathbf{r})$ solves the Helmholtz equation (2.10), then $T_0 U_\omega(\mathbf{r})$ is also a solution and, therefore, instead of (2.13), one can also write

$$V_\omega(\mathbf{r}, t) = U_\omega(\mathbf{r}) e^{i\omega t}. \quad (2.14)$$

These solutions are called monochromatic waves, and each general solution of the general homogeneous wave equation (2.6) can be written as a linear superposition of such monochromatic waves

$$\begin{aligned} V(\mathbf{r}, t) &= \int d\omega V_\omega(\mathbf{r}, t) \\ &= \int d\omega U_\omega(\mathbf{r}) e^{i\omega t}. \end{aligned} \quad (2.15)$$

To go a step forward, we display $U_\omega(\mathbf{r})$ as a linear combination of plane waves

$$V(\mathbf{r}, t) = \int d\omega \int d^3\mathbf{k} \tilde{U}_{\mathbf{k},\omega} e^{i\mathbf{k}\mathbf{r}} e^{i\omega t}. \quad (2.16)$$

In order to be a solution of (2.6), the relation $k = |\mathbf{k}| = \omega/c$ is required, and after integration over $d\omega$ one obtains

$$V(\mathbf{r}, t) = \int d^3\mathbf{k} \left(\tilde{U}_1(\mathbf{k}) e^{i(\mathbf{k}\mathbf{r} - ckt)} + \tilde{U}_2(\mathbf{k}) e^{i(\mathbf{k}\mathbf{r} + ckt)} \right) \quad (2.17)$$

with $k = |\mathbf{k}|$. From these considerations it becomes obvious, that the Helmholtz equation (2.10), together with appropriate boundary conditions, completely describes the propagation of x rays in vacuum.

2.1.2 Integral Theorem of Helmholtz and Kirchhoff

Now, we will apply the Helmholtz equation to calculate the amplitude $U(P_0)$ of the x-ray field in a point $P_0 = \mathbf{r}_0$ with the assumption that the amplitude and its derivative are known on an arbitrary surface S which surrounds the point P_0 (Figure 2.1). We start with a small sphere S_ϵ with radius ϵ centered around P_0 and examine the following integral

$$I_{S_\epsilon} = \iint_{S_\epsilon} d\mathbf{s} \left(U(\mathbf{s}) \frac{\partial G(\mathbf{s})}{\partial n} - G(\mathbf{s}) \frac{\partial U(\mathbf{s})}{\partial n} \right) \quad (2.18)$$

with

$$G(\mathbf{s}) = \frac{e^{ik_0 r(\mathbf{s})}}{r(\mathbf{s})}. \quad (2.19)$$

$r(\mathbf{s}) = |\mathbf{s} - \mathbf{r}_0|$ is the distance from the observation point P_0 , and $\partial/\partial n = \mathbf{n}\boldsymbol{\partial}$ denotes the directional derivative along the inward facing surface normal \mathbf{n} . We evaluate the integral for the limit $\epsilon \rightarrow 0$

$$\begin{aligned} I_{S_\epsilon} &= \iint_{S_\epsilon} d\mathbf{s} \left(-U(\mathbf{s}) \left[\frac{1}{\epsilon} - ik_0 \right] \frac{e^{ik_0\epsilon}}{\epsilon} - \frac{e^{ik_0\epsilon}}{\epsilon} \frac{\partial U(\mathbf{s})}{\partial n} \right) \\ &= e^{ik_0\epsilon} \left[\int_{\phi=0}^{2\pi} d\phi \int_{\theta=0}^{\pi} d\theta \sin\theta (-U + \epsilon i k_0 U - \epsilon \mathbf{n} \boldsymbol{\partial} U) \right] \\ &= -4\pi U(P_0) \text{ as } \epsilon \rightarrow 0 \end{aligned}$$

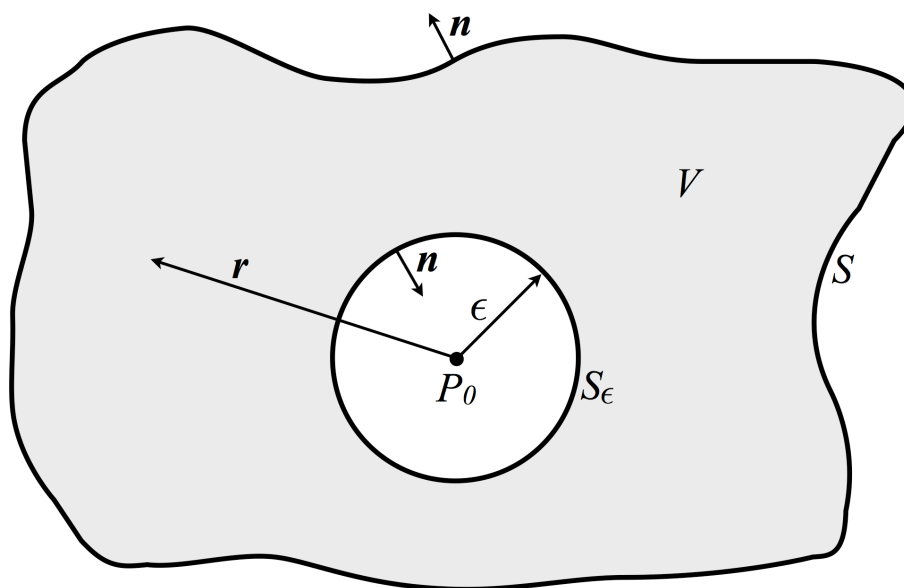


Figure 2.1: Derivation of the Integral Theorem of Helmholtz and Kirchhoff. The field U is known on the surface S . Since U is a solution of the Helmholtz equation, the field on the surface S_ϵ is completely determined by the field on S . Computing the limit for $\epsilon \rightarrow 0$, the field amplitude in the observation point P_0 can be deduced.

and thus

$$U(P_0) = \frac{1}{4\pi} \iint_{S_\epsilon} ds \left(G \frac{\partial U}{\partial n} - U \frac{\partial G}{\partial n} \right). \quad (2.20)$$

This expression relates the field amplitude $U(P_0)$ observed at location P_0 with the integral over the infinitesimal spherical surface S_ϵ around P_0 . Now we use Green's theorem together with the Helmholtz equation to connect the field amplitude at the observation point P_0 with the field on the surface S . In contrast to S_ϵ the surface S needs neither to be spherical nor to be infinitesimal small. Shall V denote the volume which is surrounded from outside by the surface S and from inside by the surface S_ϵ . If the partial derivatives of the functions U and G exist and are continuous everywhere on S , on S_ϵ , and within the volume V , then Green's theorem states

$$\iint_{S \cup S_\epsilon} ds \left(G \frac{\partial U}{\partial n} - U \frac{\partial G}{\partial n} \right) = \iiint_V dv \left(G \frac{\partial^2 U}{\partial r^2} - U \frac{\partial^2 G}{\partial r^2} \right) \quad (2.21)$$

Here, the surface normal \mathbf{n} is chosen to face away from the volume V , which conforms with the convention used in the derivation of (2.20). The function $G = \exp(ik_0 r)/r$ has been chosen such that it is a solution of the Helmholtz equation (2.10) with the wave number

$k = k_0$. If U satisfies the Helmholtz equation with the same wave number k_0 , i. e.,

$$\begin{aligned}\frac{\partial^2}{\partial \mathbf{r}^2} U &= -k_0^2 U, \\ \frac{\partial^2}{\partial \mathbf{r}^2} G &= -k_0^2 G,\end{aligned}$$

then the integrand of the volume integral vanishes and Green's theorem (2.21) simplifies to

$$\iint_{S \cup S_\epsilon} d\mathbf{s} \left(G \frac{\partial U}{\partial n} - U \frac{\partial G}{\partial n} \right) = 0$$

or

$$\iint_{S_\epsilon} d\mathbf{s} \left(G \frac{\partial U}{\partial n} - U \frac{\partial G}{\partial n} \right) = \iint_S d\mathbf{s} \left(U \frac{\partial G}{\partial n} - G \frac{\partial U}{\partial n} \right).$$

This expression can be inserted into equation (2.20), and finally one gets the relation between the wave field on the surface S and the amplitude at the observed point P_0

$$U(P_0) = \frac{1}{4\pi} \iint_S d\mathbf{s} \left(U \frac{\partial}{\partial n} G - G \frac{\partial U}{\partial n} \right) \quad (2.22)$$

with

$$G = \frac{e^{i k_0 r}}{r}. \quad (2.23)$$

This formula is a special version of the integral theorem of Helmholtz and Kirchhoff and will be used in the next subsection to derive Fresnel-Kirchhoff's diffraction formula.

2.1.3 Fresnel-Kirchhoff's Diffraction Formula

In the preceding subsection the integral theorem of Helmholtz and Kirchhoff was presented. This theorem admits the calculation of the scalar field amplitude in an observation point from the knowledge of the field and its derivatives on a surface which encloses this point. Now, we will apply this theorem to manage the following situation, which is illustrated in Figure 2.2. X rays, which have been emitted from a source, are propagating from the left to the right along the optical axis and arrive at an open aperture within an opaque screen. The source distance shall be large compared to the transverse dimensions of the open aperture. Knowing the wave field in the aperture plane, one would like to estimate the field amplitude $U(P_0)$ in a point P_0 behind the aperture plane. In order to apply the integral theorem from the previous subsection, we introduce an imaginary surface S , which encloses P_0 as shown in Figure 2.2. The enclosing surface shall be composed of three disjoint parts S_1 , S_2 and S_3 with S_1 matching the opening aperture, S_2 conforming a part of the opaque screen and S_3 being the surface of a large sphere with radius R centered around P_0 and cutting the opaque

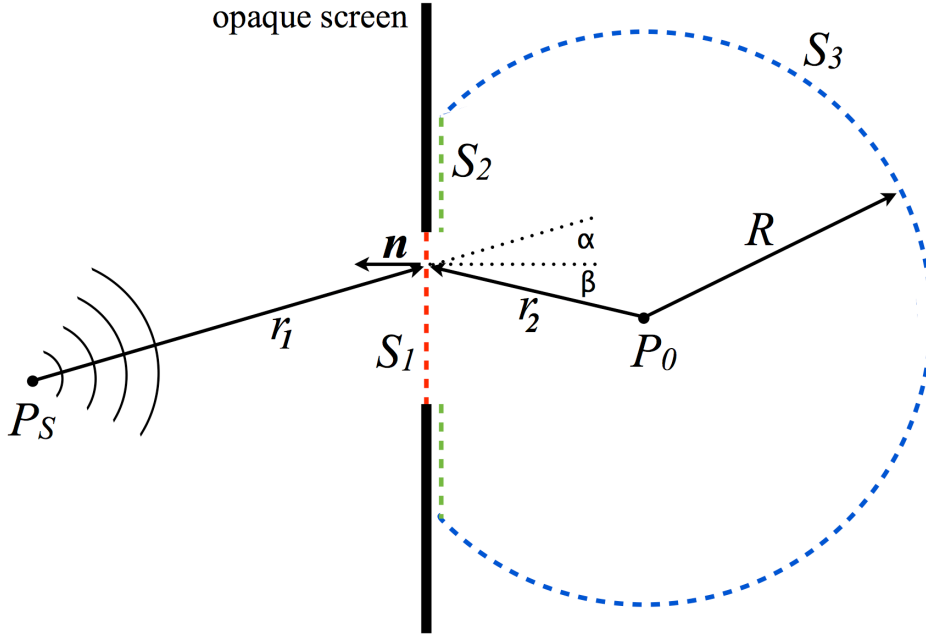


Figure 2.2: Illustrating the derivation of Fresnel-Kirchhoff's Diffraction Formula. A source radiates a wavefield which propagates to an opaque screen with an open aperture S_1 . Knowing the wavefield on S_1 is sufficient to compute the amplitude in the observation point P_0 , because the contributions from S_2 and S_3 can be neglected.

screen in a way that the opening aperture lies within the cutting circle. Due to (2.22) it follows for the field amplitude in P_0

$$\begin{aligned} U(P_0) &= \frac{1}{4\pi} \iint_{S_1 \cup S_2 \cup S_3} d\mathbf{s} \left(U \frac{\partial}{\partial n} G - G \frac{\partial U}{\partial n} \right) \\ &= \sum_{i \in \{1,2,3\}} U_i \end{aligned} \quad (2.24)$$

with

$$U_i = \frac{1}{4\pi} \iint_{S_i} d\mathbf{s} \left(U \frac{\partial}{\partial n} G - G \frac{\partial U}{\partial n} \right), \quad i \in \{1, 2, 3\}. \quad (2.25)$$

The contributions from the three surfaces S_i can be evaluated separately, but it will be necessary to establish some boundary conditions for the field and its derivative on these surfaces. For the open aperture S_1 it is reasonable to assume that U and its derivative should be the same as without the opaque screen around, even though there may be some deviations near the edge of the aperture. The influence of the field, that is generated by the illuminated opaque screen, on the field in the aperture S_1 , is very low and can be neglected, which is especially true for the hard x-ray regime of the electromagnetic spectrum. In the shadow just behind the opaque screen the field and its derivative can be expected to be zero,

since the opaque screen absorbs all illuminating radiation, and again, the influence of the field, which is generated by the presence of the screen, can be neglected in comparison with the incident wavefront. It remains to show that the field and its derivatives on the spheric surface S_3 vanish for a radius R which is sufficiently large. The argumentat is not as obvious as it seems, because, even if the field U falls with increasing radius, the area of S_3 increases beyond all limits and the contribution of U_3 would not vanish. Instead, as suggested in [BW99], one can presume that the source of the incident wavefront has been switched on at a certain point in time t_0 and that there was no electromagnetic field before. Thus, at the time t_1 for which we evaluate the amplitude in P_0 , no photon has reached S_3 if only the radius R is sufficiently large ($R > c(t_1 - t_0)$). Of course this argumentation contradicts with the use of the Helmholtz equation which assumes a stationary situation with strictly monochromatic waves. A more rigorous argumentation avoiding this difficulty can be found in [Bor06] or [BC03]. As a summary, the following boundary conditions are encountered:

- on S_1 : $U = U^{(i)}$, $\frac{\partial U}{\partial n} = \frac{\partial U^{(i)}}{\partial n}$,
- on S_2 : $U = 0$, $\frac{\partial U}{\partial n} = 0$,
- on S_3 : $U = 0$, $\frac{\partial U}{\partial n} = 0$,

from which it follows that U_2 and U_3 do not contribute to the amplitude $U(P_0)$ and, therefore,

$$U(P_0) = U_1 = \frac{1}{4\pi} \iint_{S_1} d\mathbf{s} \left(U \frac{\partial}{\partial n} G - G \frac{\partial U}{\partial n} \right).$$

The Green function G is given by (2.23) and the wavefront U must obey the Helmholtz equation with the wavenumber k_0 . I start with a special solution given by a spherical wave emitted from a point source at P_S and deduce the general case by a linear superposition of many spherical wavelets. With

$$\begin{aligned} U &= U_0 \frac{e^{ik_0 r_1}}{r_1}, \\ G &= \frac{e^{ik_0 r_2}}{r_2} \end{aligned} \tag{2.26}$$

one gets

$$\begin{aligned} U(P_0) &= \frac{1}{4\pi} \iint_{S_1} d\mathbf{s} \left(U_0 \frac{e^{ik_0 r_1}}{r_1} \frac{\partial}{\partial n} \frac{e^{ik_0 r_2}}{r_2} - \frac{e^{ik_0 r_2}}{r_2} \frac{\partial U_0 \frac{e^{ik_0 r_1}}{r_1}}{\partial n} \right) \\ &= \frac{1}{4\pi} \iint_{S_1} d\mathbf{s} U_0 \frac{e^{ik_0(r_1+r_2)}}{r_1 r_2} \left(\left[ik_0 \cos \beta + \frac{1}{r_2} \right] + \left[ik_0 \cos \alpha + \frac{1}{r_1} \right] \right) \\ &= \frac{1}{4\pi} \iint_{S_1} d\mathbf{s} U(r_1) G(r_2) \left(ik_0 [\cos \alpha + \cos \beta] + \frac{1}{r_1} + \frac{1}{r_2} \right). \end{aligned}$$

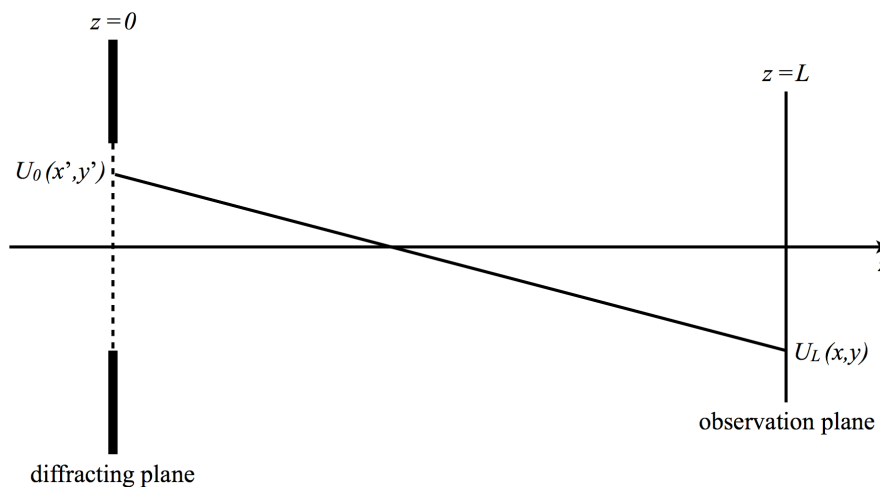


Figure 2.3: Illustrating the Diffraction formula. The observation plane is given by $z = 0$ and the observation plane is at $z = L$.

In most practical situations the distance between the source and the diffracting screen and the distance between the screen and the observation point P_0 will be much larger than the wavelength (which is less than 0.1 nm for hard x rays), i. e., $k \gg 1/r_1$ and $k \gg 1/r_2$. For this reason the expression for $U(P_0)$ can be written in the simplified form

$$U(P_0) = \frac{ik_0}{4\pi} \iint_{S_1} d\mathbf{s} U(r_1) G(r_2) (\cos \alpha + \cos \beta). \quad (2.27)$$

Equation (2.27) is the famous Fresnel-Kirchhoff diffraction formula known from optical text books and is often used in microscopy and other fields of visible light optics. Owing to the short wavelength, for hard x rays the assumptions made during the derivation of the diffraction formula are even more strictly fulfilled than for visible light and, therefore, it is appropriate to use it for the theoretical treatment of the optical properties of the hard x-ray scanning microscope. In the following subsection I discuss some approximations which can be performed on the Fresnel-Kirchhoff diffraction formula in order to simplify analytic treatment or fasten up numerical simulations applied to retrieve the optical properties of the microscope.

2.1.4 Fresnel-Kirchhoff Propagation

Let us consider some useful approximations of the Fresnel-Kirchhoff diffraction formula. In the deduction of the formula, it was assumed that the diffracting plane is far away from the source and from the observation point as compared with the wavelength. If these distances are not only large compared to the wavelength, but also large compared to the aperture of the diffracting plane, the cosine of the angles α and β in the diffraction formula can be approximated by 1 with an error which is in the order of $\alpha^2/6$ or $\beta^2/6$, respectively. In

hard x-ray optics, the numeric apertures of the optical devices are always very small and, therefore, the cosine approximation is well justified. The diffraction formula then becomes

$$U(P_0) = \frac{ik_0}{2\pi} \iint_{S_1} d\mathbf{s} U(\mathbf{s}) \frac{e^{ik_0 r(\mathbf{s})}}{r(\mathbf{s})}. \quad (2.28)$$

For further approximations a system of coordinates is introduced such that the optical axis is given by the z axis ($x = 0$, $y = 0$), and that the diffracting plane and the observation plane are both parallel to the x - y plane of the coordinate system, as depicted in Figure 2.3. The diffracting plane and the observation plane are located at $z = 0$ and $z = L$, respectively. Then the diffraction formula can be written as

$$U_L(x, y) = \frac{ik_0}{2\pi} \iint_{S_1} dx' dy' U_0(x', y') \frac{e^{ik_0 r(x-x', y-y', L)}}{r(x-x', y-y', L)} \quad (2.29)$$

with the definitions

$$\begin{aligned} U_z(x, y) &= U(x, y, z), \text{ and} \\ r(x, y, z) &= \sqrt{x^2 + y^2 + z^2}. \end{aligned} \quad (2.30)$$

If the lateral dimensions of the aperture are small compared to the distance L of the observation plane from the diffracting aperture, the diffraction formula may be approximated in the following way:

$$\begin{aligned} U_L(x, y) &= \frac{ik_0}{2\pi} \iint_{S_1} dx' dy' U_0(x', y') \frac{e^{ik_0 L \sqrt{\frac{(x-x')^2 + (y-y')^2}{L^2} + 1}}}{L \sqrt{\frac{(x-x')^2 + (y-y')^2}{L^2} + 1}} \\ &= \frac{ik_0}{2\pi} \iint_{S_1} dx' dy' U_0(x', y') \frac{e^{ik_0 L \left[1 + \frac{(x-x')^2 + (y-y')^2}{2L^2} + \mathcal{O}\left(\left(\frac{\sqrt{(x-x')^2 + (y-y')^2}}{L}\right)^4\right)\right]}}{L \left[1 + \mathcal{O}\left(\left(\frac{\sqrt{(x-x')^2 + (y-y')^2}}{L}\right)^2\right)\right]} \\ &\approx \frac{ik_0}{2\pi} \iint_{S_1} dx' dy' U_0(x', y') \frac{e^{ik_0 \left[L + \frac{(x-x')^2 + (y-y')^2}{2L} \right]}}{L} \\ &= \frac{ik_0 e^{ik_0 L}}{2\pi L} \iint_{S_1} dx' dy' U_0(x', y') e^{ik_0 \frac{(x-x')^2 + (y-y')^2}{2L}}. \end{aligned}$$

The Taylor series of the square root is terminated differently in the argument of the exponential function and in the denominator, because $k_0 L \gg 2\pi$ and, therefore a small deviation

of the square root value in the exponential function has dramatic effect on the integrand. Compared to this, a small deviation of the square root in the denominator has a negligible effect on the integrand, and thus, the series can be aborted after the first term. With this approximation it is possible to define a propagator kernel

$$K_L(x, y) = \frac{ik_0 e^{ik_0 L}}{2\pi L} e^{ik_0 \frac{(x)^2 + (y)^2}{2L}} \quad (2.31)$$

which can be used to express the propagated field amplitude in the observation plane as a convolution of the field in the diffraction plane with the propagator kernel

$$U_L(x, y) = \iint_{S_1} dx' dy' U_0(x', y') K_L(x - x', y - y'). \quad (2.32)$$

This permits to calculate the propagated field by a multiplication in Fourier space

$$\tilde{U}_L(\eta, \xi) = \tilde{U}_0(\zeta, \xi) \tilde{K}_L(\zeta, \xi), \quad (2.33)$$

where the tilde denotes the 2-dimensional fourier transformation of the function with respect to the variables x and y . Expression (2.33) is widely used in computer simulations, because it is possible to implement the discrete fourier transformation very efficiently with the *fast fourier transformation* algorithm [CT65].

2.2 Interaction of X Rays with Matter

In the x-ray microscope the x rays pass several optical elements, they penetrate the sample, and finally they arrive at a detector. In all these cases the x rays interact with matter. This section gives a summary of the most important aspects regarding interaction of x ray photons with matter.

2.2.1 Complex Index of Refraction

The major quantity to describe the behavior of x rays in matter is the *complex index of refraction*

$$\begin{aligned} \hat{n}_\omega(\mathbf{r}) &= n_\omega(\mathbf{r}) + i\beta_\omega(\mathbf{r}) \\ &= 1 - \delta_\omega(\mathbf{r}) + i\beta_\omega(\mathbf{r}). \end{aligned}$$

The real part of the refractive index describes the refraction of the x rays, whereas the imaginary part is a measure of their attenuation in the medium. If the sample is thin in a sense that will be explained later, the effect of the medium on the transmitted x rays can be described by a complex transmission function $T_{\Delta z}(x, y)$, which yields the field amplitude $U_{\Delta z}(x, y)$ immediately behind the sample if multiplied with the field amplitude $U_0(x, y)$ before the sample:

$$U_{\Delta z}(x, y) = T_{\Delta z}(x, y) U_0(x, y) \quad (2.34)$$

Without loss of generality the direction of propagation has been chosen along the z axis. The transmission function can be calculated by means of a line integral through the sample, with the complex index of refraction as the integrand

$$\begin{aligned} T_{\Delta z}(x, y) &= e^{ik \int_{z=0}^{\Delta z} dz \hat{n}(x, y, z)} \\ &= e^{ik\Delta z} \cdot e^{-ik \int_{z=0}^{\Delta z} dz \delta(x, y, z)} \cdot e^{-k \int_{z=0}^{\Delta z} dz \beta(x, y, z)} \end{aligned} \quad (2.35)$$

and gives the transmitted wave field behind the object

$$U_{\Delta z}(x, y) = U_0(x, y) e^{ik\Delta z} \cdot e^{-ik \int_{z=0}^{\Delta z} dz \delta(x, y, z)} \cdot e^{-k \int_{z=0}^{\Delta z} dz \beta(x, y, z)}. \quad (2.36)$$

We realize that δ causes an additional phase shift compared to the case without the object, whereas β leads to a reduction of the magnitude of the field amplitude. In an experiment, the field amplitudes are not measured directly. Instead, a detector measures the *photon flux*, the *flux density*, or the *intensity*, which are all proportional to the square of the field amplitude. The photon flux is the number of photons that pass a certain cross section during a time interval, divided by the time interval, whereas the flux density is the photon flux divided by the area of the cross section. The term *intensity* is defined similar to flux density, but intensity refers to the energy rather than to the number of photons. In case of monochromatic light, photon flux and intensity are proportional and, therefore, I use these terms interchangeably. We are interested in the flux density I_0 immediately before the sample and the flux density $I_{\Delta z}$ right behind it

$$\begin{aligned} I_0(x, y) &= C |U_0(x, y)|^2 \\ I_{\Delta z}(x, y) &= C |U_{\Delta z}(x, y)|^2 \\ &= C |T_{\Delta z}(x, y) U_0(x, y)|^2 \\ &= C |U_0(x, y)|^2 e^{-2k \int_{z=0}^{\Delta z} dz \beta(x, y, z)}, \end{aligned}$$

wherein C represents a constant factor. Defining the *linear attenuation coefficient*

$$\mu(x, y, z) = \frac{4\pi}{\lambda} \beta(x, y, z) \quad (2.37)$$

this yields

$$I_{\Delta z}(x, y) = I_0(x, y) \cdot e^{-\int_{z=0}^{\Delta z} dz \mu(x, y, z)} \quad (2.38)$$

for the intensity measured by a detector located immediately behind the object. Formula (2.38) is a generalized form of the Lambert-Beer law with an attenuation coefficient depending on the position z along the direction of propagation. It describes the decrease of the flux density of the transmitted x rays by the sample. This phenomenon is called attenuation

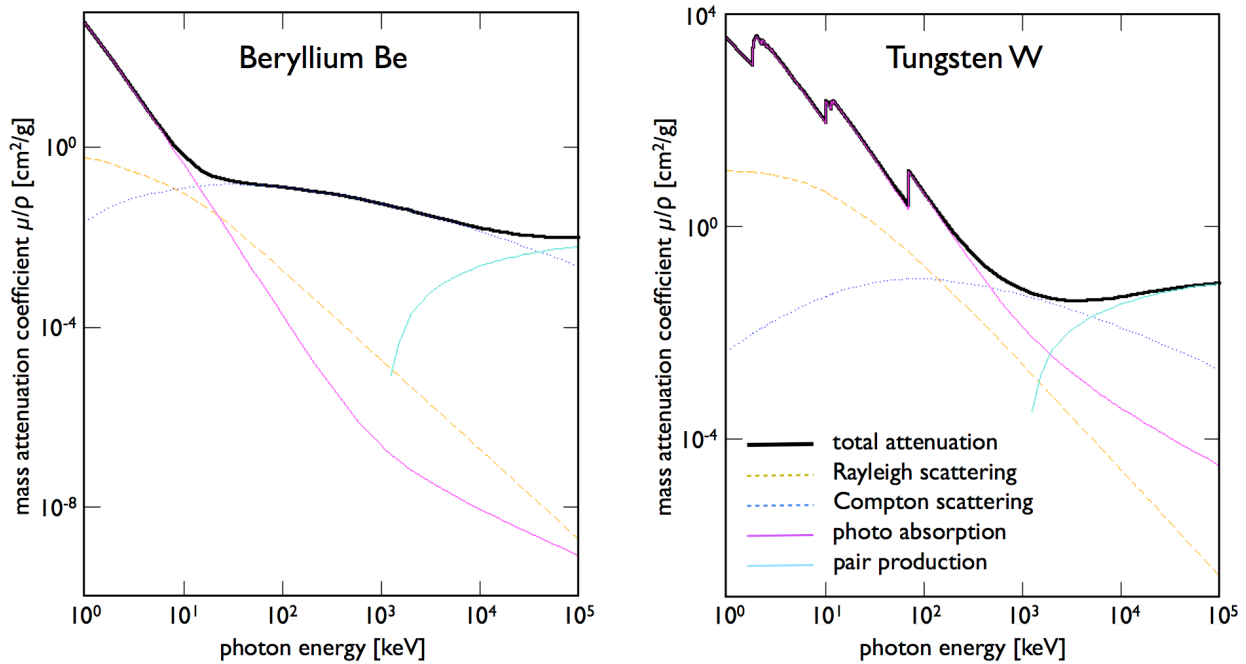


Figure 2.4: Contributions to the mass attenuation coefficient. At low photon energies, photo absorption is the main contributor, while for increasing energy the relevance of photo absorption is reduced in favor of Compton scattering. For low atomic number elements, this occurs at lower energies than for elements with a large atomic number. (Data calculated with the XCOM database [BHS⁺07].)

and is explained in subsection (2.2.2). Obviously, the attenuation of x rays is described by the imaginary part β of the complex index of refraction. But the measured transmission signal contains no information about the refractive decrement δ , since the detector measures only the x ray intensity and is not sensitive with regard to the phase of the amplitude.¹ Nevertheless the refractive decrement has many observable effects on the transmitted x rays as shown in subsection (2.2.3).

2.2.2 Attenuation

The term *attenuation* is defined as reduction of the x-ray flux density as a result of the x rays passing through an object. Physical processes responsible for the attenuation are absorption as well as scattering. Absorption may be induced by photoelectron absorption (photo absorption) or by electron-positron pair production. Scattering processes may be Rayleigh scattering or Compton scattering. Attenuation is quantitatively described by the linear attenuation coefficient μ and the Lambert Beer law (2.38). In addition to the linear attenuation coefficient, the mass attenuation coefficient μ/ρ is defined and often used in public databases like the SAO/NASA ADS[PCH81], the XAAMD database[HS07], the XCOM

¹The unobservability of the phase is not a fundamental law, it is just a consequence of the performance of the detectors, which are available today.

database[BHS⁺07], or the FFAST database[COD⁺07]. The cross sections σ_i of the individual underlying physical processes $i \in \{\text{rayleigh}, \text{photo}, \text{compton}, \text{pair}\}$, which are responsible for the attenuation, are related to the corresponding attenuation coefficient μ_i over the particle density dN/dV :

$$\mu_i = \frac{dN}{dV} \sigma_i. \quad (2.39)$$

With the assumption that the individual processes i contribute to the overall attenuation independently from each other, the attenuation coefficient μ can be written as a sum of the attenuation coefficients of the individual contributors:

$$\mu = \sum_i \mu_i = \mu_{\text{rayleigh}} + \mu_{\text{photo}} + \mu_{\text{compton}} + \mu_{\text{pair}}. \quad (2.40)$$

Figure 2.4 shows the overall mass attenuation coefficients of beryllium and tungsten for a wide photon energy range together with the mass attenuation coefficients of the individual contributors. Beryllium has been chosen as a representative of a low atomic number element, because it is widely used in x-ray physics as a material with comparably weak attenuation. In the scanning microscope, for example, the compound parabolic refractive x-ray lenses used for pre-focusing are made of beryllium. In contrast to beryllium, tungsten is a typical high atomic number element with rather strong attenuation and is used in x-ray optics for optical diaphragm and shielding purposes. The blades of the aperture defining double slits of the nanofocusing lenses used in the scanning microscope are made of tungsten. The individual contributing processes will be treated in the following paragraphs.

Rayleigh scattering

An x-ray photon passing through an object has the chance to interact with the electrons, which are bound to the atomic nucleus. If the result of such an interaction is the change of the direction of propagation of the photon without changing the photon energy, this process is called *Rayleigh scattering* or *elastic scattering*. The change of direction is observed as an attenuation of the x-ray beam behind the sample, because the scattered photon does not contribute to the transmission signal (assuming that the change in direction is larger than the acceptance angle of the detector behind the object). Rayleigh scattering occurs if the scattering electron is strongly bound in the inner shell of the atom. In contrast to that, weakly bound electrons rather contribute to Compton scattering. In opposition to the other contributions (photo absorption, Compton scattering and pair production), the elastic scattering process is almost never more than a minor contributor to the attenuation coefficient. An exception are crystalline materials (single crystals or polycrystalline objects). At certain orientations between crystal and incident x-ray beam, strong scattered peaks, called *Bragg-Laue reflections*, are excited, giving rise to intensity transfer away from the primary beam direction into the direction of the Bragg peak, leading to significant attenuation. This effect can be observed, for example, if tomography is performed with a single crystal. Particularly polycrystalline samples give rise to attenuation by elastic Bragg scattering, since the large

number of differently oriented single crystals increase the chance of conforming the Bragg condition.

The Rayleigh scattering cross section is strongest at low photon energies and decreases with increasing energies. In the range of low energies, Rayleigh scattering is stronger than Compton scattering, but photo absorption is even much stronger. At higher photon energies Rayleigh scattering overtakes photo absorption, but this occurs at energies for which Compton scattering gets so strong that it dominates the overall attenuation coefficient. Even though Rayleigh scattering is negligible for attenuation, it is still important in many experiments with x rays either as volitional signal or as disturbing background. Beyond that, elastic scattering contributes to the refractive part of the complex index of refraction, since the scattering process generates a phase shift in the corresponding complex wave amplitude.

Photo absorption

If the energy E_{ph} of the incident x-ray photon is larger than the ionization energy E_{ion} of an electron bound to the nucleus of an atom, the photon is able to raise the electron from its bound state into a free state. As a result, the photon has vanished and the freed electron has a kinetic energy E_{kin} necessary to satisfy the conservation of energy $E_{ph} = E_{ion} + E_{kin}$. This process is known as *photoelectric absorption* or short *photo absorption* and is the major contributor to attenuation in the low x-ray energy range, especially for elements with high atomic numbers. The photo absorption cross section is proportional to Z^m/E^n with atomic number Z and $m, n \approx 3$. For high Z elements like tungsten, gold, or lead, photo absorption is the dominant process at energies up to several hundred keV, whereas for low Z elements like lithium, beryllium or boron, photo absorption loses its dominance for the benefit of Compton scattering at photon energies of several tens of keV.

Compton scattering

Photons with energies not too small compared to the energy equivalent of the rest mass of an electron will potentially be scattered at a free electron transferring part of its energy to the electron and, at the same time, changing its direction of propagation. After the occurrence of a Compton scattering process, the incident photon has lost part of its energy such that the wavelength has been increased by

$$\Delta\lambda = \frac{h}{mc} (1 - \cos \theta), \quad (2.41)$$

or

$$E'_{ph} = \frac{E_{ph}}{1 + \frac{E_{ph}}{m_e c^2} (1 - \cos \theta)}. \quad (2.42)$$

As a contributor to the attenuation coefficient, Compton scattering is especially important for high energies. The energy, where Compton scattering starts to exceed photo absorption depends on the atomic number of the material.

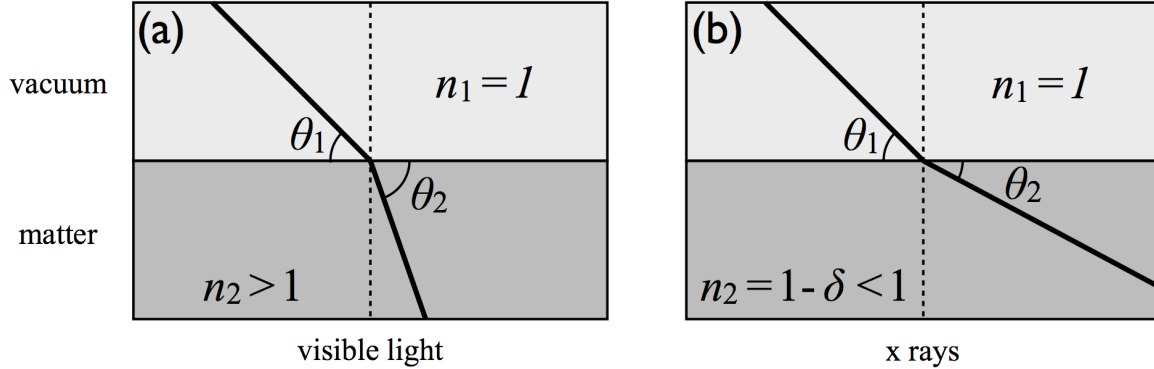


Figure 2.5: Refraction of visible light and x rays at an interface. (a) By its passage from vacuum or air into matter, visible light is refracted towards the interface normal. (b) In the case of x rays, the real part of the complex index of refraction is smaller than 1. As a consequence, x rays are refracted away from the interface normal, if they pass the interface from vacuum or air into matter.

Pair production

As soon as the energy of the incident x-ray photon exceeds the energy equivalent of the rest mass $2m_e$ of two electrons, i. e., as soon the energy is larger than about 1022 keV, the photon is able to disappear and to generate an electron-positron pair. By reason of conservation of momentum such an event must happen in the electric field of another charged particle. In the atom this might be either the electric field of the nucleus or the electric field of the bound electrons. For energies larger than some tens of MeV pair production the main contributor to the attenuation coefficient, but the x-ray energies as used for the hard x-ray scanning microscope (10 keV up to 30 keV) are much lower than 1022 keV needed to initiate pair production.

2.2.3 Refraction

While the imaginary part β of the complex index of refraction is responsible for attenuation, the refractive decrement δ manifests in an additional phase shift

$$e^{-ik \int_{z=0}^{\Delta z} dz \delta(x,y,z)} \quad (2.43)$$

of the wave amplitude and shows up in refraction and in phase contrast effects. Refraction is the change of the incidence angle θ when light passes the interface between two media of different refractive indices n_1 and n_2 (Figure 2.5). The refraction angles θ_1 and θ_2 are related with Snell's law

$$n_1 \cos \theta_1 = n_2 \cos \theta_2. \quad (2.44)$$

The incident rays are refracted towards the axis of incidence if $n_1 < n_2$, and away from it if $n_1 > n_2$. Media with high refractive indices are called *optically denser* than media with lower refractive indices. For visible light we are familiar with the fact that transparent media

are optically denser than vacuum and also than air². If, for example, visible light enters the interface from air into a glass panel, the light beam is bent towards the interface normal, and bent away from it if the beam leaves the glass pane again. For this reason focusing refractive lenses must have a convex shape and dispersing refractive lenses must be concave. But this conversant property of visible light is not true for x rays, because the real part of the complex index of refraction is less than 1 ($\delta > 0$) for almost all materials, i. e., vacuum is optically denser than the material. One consequence of this property is that focusing refractive lenses for x rays must exhibit a concave shape which is different from visible light optics. Furthermore the value of δ is very low compared to 1. Dependent on the density of the material and the x-ray energy, the value of the refractive decrement is of the order of 10^{-5} to 10^{-7} and thus refraction is very weak for x rays. As an example consider x rays of 15 keV coming from vacuum and passing the surface of a beryllium pane. If the angle of incidence is 45° , the beam will be deviated by an angle of only 0.000087° ($1.5 \mu\text{rad}$), i. e., the direction of propagation is almost not effected by the interface. In comparison to this, visible light passing the interface between air and silica glass at an angle of 45° would be deviated to an angle of 62.7° , the difference of $62.5^\circ - 45^\circ = 17.5^\circ$ being of quite significance.

Another important phenomenon in connection with refraction is *total reflection*. Total reflection occurs when an electromagnetic wave hits the interface between two media of different refractive indices $n_1 > n_2$ and tries to get out of the optically denser medium at an angle smaller than the critical angle

$$\theta_c = \arccos \frac{n_2}{n_1}. \quad (2.45)$$

Instead of leaving the optically denser medium, the wave is totally reflected at the interface. For visible light total reflection happens, if the beam tries to get out of a transparent object into vacuum (*internal* total reflection), but for x rays total reflection takes place if the x ray beam hits the interface coming from vacuum and trying to enter the material (*external* total reflection). The critical angle for visible light in opaque media is in the order of several tens of degrees, for instance 40° for water or even 65° for diamond, whereas for x rays the critical angle is always smaller than about 1° , namely about 0.1° for beryllium or 0.3° for tungsten in case of 15 keV photon energy. External total refraction is of great importance for many applications in x-ray physics and is made use of, for example, in x-ray mirrors and polycapillaries. Moreover, total reflection must be considered in the design of the blades in slit systems and will be discussed in chapter 5.

The real part of the complex index of refraction is also responsible for the appearance of phase contrast. After passing the sample, the field amplitude behind the object is given by (2.36), and as shown in (2.38), the measured flux density contains no information about the real part of the complex index of refraction. But if we calculate the intensity some distance behind the object, i. e., if we propagate the complex wave field some distance further and then calculate the intensity, the additional phase shift caused by δ will become apparent in

²The difference between the refractive index of vacuum and air is negligible compared to the difference between vacuum and most transparent solid state materials.

the intensity distribution. In some experimental situations this may be disturbing, because phase contrast would complicate the interpretation of the projected absorption image, as for example in the case of the alignment of the nanofocusing lenses with the high resolution x-ray camera (treated in section 6.1). But, dependent on the distance from the object, this so-called phase contrast can be exploited in several ways. For small distances compared to the fresnel length d^2/λ (d lateral dimension of the object, λ the wavelength) the phase contrast is quite weak and just increases the contrast between regions of different refractive indices, which is called *edge enhancement*. Objects that contain only elements with low atomic numbers (e. g. biological samples) or which are very small compared to the attenuation coefficient often show very weak absorption contrast, whereas the additional phase shift $ik \int dz \delta(x, y, z)$ often becomes comparable with 2π . Measuring the phase contrast in an appropriate distance from the sample allows the reconstruction of the real part of the complex index of refraction and gives insight to the inner of the specimen [SSK⁺95]. Other methods which utilize the δ -induced phase shift are interferometry with separate interfering beams [BH15], resolving phase variations using diffraction from analyzer crystals [DGG⁺nt, DGG⁺17, IB95, Mom05, WGG⁺96, CTJ⁺97], Talbot interferometry [MYT⁺06, PWBDnt], coherent x-ray diffraction imaging (CXDI) [Fie82, MCKS99, Els03], and ptychography [RF04, FR04, RHC⁺07]. CXDI and x-ray ptychography are two main applications carried out with the hard x-ray scanning microscope and are described in chapter 6.

Chapter 3

The X-Ray Source

The choice of an appropriate x-ray source is one of the most essential considerations for the hard x-ray scanning microscope. To meet the requirements of highest spatial resolution, the potential specimen must be scanned by an x-ray spot as small as possible. On the other hand, the photon flux in the focal spot has to be maximized in order to keep exposure times as small as possible. Both properties, the size of the focus and its photon flux, depend on the properties of the x-ray source and on the optical components used to generate the focal spot. In this chapter the influence of the source properties on the features of the x-ray focus are discussed. First, a set of requirements on the x-ray source, which is used for the scanning microscope, is formulated. From this, it will become apparent that x-ray tubes are inappropriate and that synchrotron light has to be used. Therefore, in the subsequent sections, third generation synchrotron radiation facilities are introduced, and the key properties of dipole magnets, multipole wigglers and undulators are described.

3.1 Requirements

3.1.1 Energy and Energy Bandwidth

Almost all experiments which make use of hard x rays require a narrow energy bandwidth $\Delta E/E$ around a nominal energy value E_0 for the x-ray photons. The choice of energy and its bandwidth depend on the kind of experiment. X-ray absorption spectroscopy, for example, needs energy values E_0 which can be tuned around certain absorption edges with very narrow energy bandwidths. On the other hand, the method of fluorescence spectroscopy just needs x rays with energies high enough to excite fluorescence lines of the elements of interest with an energy band which might be quite broad.

The hard x-ray scanning microscope provides a large variety of possible experimental methods and of course one would wish the hard x-ray scanning microscope to operate at arbitrarily adjustable photon energies with arbitrarily adjustable energy bandwidths. Unfortunately, there are constraints limiting the available energy range, such as the problem of strong absorption at low energies and weak absorption at high energies. Soft x rays, for

example, show extremely strong absorption in air and thus they must be guided through vacuum tubes. Because any window would also significantly absorb the soft x-ray photons, not only the propagation distance from the source to the sample has to be inside vacuum, but the whole sample environment with all the detectors has to be kept within the vacuum tank. For this reason, there are completely different experimental setups for soft and hard x ray experiments. On the other hand, all materials (including high atomic number elements) are quite transparent for x rays of very high energy and it becomes very difficult to find appropriate slits, pinholes and shielding materials for high energy x-ray photons. These are the most dominant conditions limiting the x-ray energy from below and above. There are many more factors that may limit the available energy range of experimental x-ray setups. Since silicon is used as material for the nanofocusing lens, the hard x-ray scanning microscope has to be operated at photon energies of about 10 keV or above, because silicon lenses become too absorbent at lower energies.

As already mentioned, the required energy bandwidth depends on the specific experiment that is being performed with the scanning microscope. But there is another aspect to be considered in case of the hard x-ray scanning microscope, namely the chromatic aberration of the refractive x-ray lenses used for focusing. In chapter 4, equation (4.28) is deduced

$$\Delta z_F = \left(\cos \omega L + \frac{\omega L}{\sin \omega L} \right) f \frac{\Delta E}{E},$$

from which it follows, that the displacement Δz_F of the focal position caused by a small deviation of the x-ray energy is proportional to the relative energy bandwidth. Chromatic aberrations become eminent as soon as the displacement of the focal position becomes comparable with the depth of focus. As shown in chapter 4, the relative energy bandwidth must be in the range of 10^{-3} – 10^{-2} or smaller, in order to avoid chromatic aberrations, if using nanofocusing lenses.

Usually an x-ray source emits a broad energy range and a monochromator has to be installed allowing only those photons to pass which are within a certain energy band required for the experiment in question. Dependent on the energy bandwidth this reduces the available flux on the sample drastically. Given a source which radiates a certain total photon flux F_{rad} (defined as photons per time interval), it would be appreciable to have this flux radiated within a narrow energy band rather than distributed over a broad energy range. For this reason it is common to define spectral quantities SQ which are normalized with respect to a certain spectral standard bandwidth BW_{std} , i. e. the radiated flux F_{rad} that enters the spectral quantity refers to photons within BW_{std} and is divided by that bandwidth:

$$SQ = \frac{F_{rad}}{BW_{std}}$$

The standard bandwidth might be an absolute quantity ΔE (or $\Delta \lambda$, or $\Delta \nu$) or a relative quantity like $\Delta E/E$. Given a source with a spectral radiation strength SQ in combination with a monochromator providing the required spectral bandwidth of $BW_{req} \lesssim BW_{std}$, the available flux F_{exp} in that experiment can be estimated as

$$F_{exp} = SQ \cdot BW_{req}.$$

Of course, the standard spectral bandwidth should be chosen such that the spectral distribution is more or less constant within BW_{std} , otherwise the estimated available flux F_{exp} may become quite inexact. In the field of x-ray physics it has become natural to use a relative energy bandwidth of $BW = 10^{-3} = 0.1\%$ and to let this value be part of the unit of measurement even though it is of dimension 1.

3.1.2 Source Size and Divergence

In the scanning microscope the focal x-ray spot is generated by a focusing lens system which creates a demagnified image of the x-ray source. Given a light source of size S and a focusing lens with a focal length f which is located a distance L away from the source, the geometric image size B_{geo} can be calculated by means of geometric optics as

$$B_{geo} = \frac{f}{L - f} S \quad (3.1)$$

Expression (3.1) shows that a small geometric image size B_{geo} can be achieved by a small focal length f , a large distance L from the source, and by a small source size S .

As result of refraction, the finite size of the aperture of the focusing lens affects the image of the source. Each point of the object plane (containing the source) is imaged as a certain diffraction pattern rather than a point (as would be expected from geometric optics). The shape of that diffraction pattern depends on the shape of the lens aperture and is called *Airy disk* in case of a circular lens apertures. The resulting focal spot of a chaotic light source (each point of the source radiates independently from all the other points of the source) is given by the geometric image of the source convolved by the Airy disk of the finite lens aperture. As a consequence, a small geometric image size is needed, in order to get a small focus. This means that we need a small source in combination with a large source-to-lens distance.

In principle, the source could be made smaller by means of a circular (or rectangular) pupil, which is transparent only near the center of the source. But this leads directly to a loss of photon flux in the focus, because a large fraction of the radiated photons of the source is absorbed by the pupil and does not contribute to the focal spot.

The same problem appears if the distance of the focusing lens from the source is enlarged while the aperture of the lens is kept constant. The solid angle spanned by the source and the lens aperture decreases quadratically with increasing distance, and thus the divergence of the radiated x rays leads to a loss of photon flux collected by the lens. So, what one needs is a small source which still radiates a high flux of photons into a small solid angle in the direction of the optical axis.

3.1.3 Brilliance

An appropriate quantity which incorporates the source size as well as the directionality and the spectral distribution is given by the quantity *brilliance* \mathcal{B} . Brilliance specifies the

radiated spectral flux within a relative energy bandwidth of $BW = 10^{-3}$ emitted by the source normalized by that bandwidth and by the four dimensional phase space spanned by the size $\Sigma_{x,y}$ and by the divergence $\Sigma'_{x,y}$ of the source:

$$\mathcal{B} = \frac{F_{rad}}{BW \cdot \Sigma_x \Sigma_y \Sigma'_x \Sigma'_y}. \quad (3.2)$$

High brilliance means a large available photon flux despite a small energy band, small source size, and small solid angle due to a large distance of the experiment from the source. In accordance with SYSTÈME INTERNATIONAL D'UNITÉS (SI), the coherent derived unit of the quantity brilliance would be

$$[\mathcal{B}] = \frac{1}{\text{s} \cdot \text{m}^2 \cdot \text{sr}},$$

but the practically used unit in nearly all scientific literature is [MHK⁺05]

$$[\mathcal{B}] = \frac{\text{photons}}{\text{s} \cdot \text{mm}^2 \cdot \text{mrad}^2 \cdot 0.1\%}$$

The authors of [HS08] suggest to introduce the name *Schwinger*¹ for the practically used unit, and I will make use of this abbreviation in the course of this document,

$$1 \text{ Sch} = 1 \frac{\text{photons}}{\text{s} \cdot \text{mm}^2 \cdot \text{mrad}^2 \cdot 0.1\%} = 10^{15} \frac{1}{\text{s} \cdot \text{m}^2 \cdot \text{sr}}.$$

The quantity brilliance has been defined as a property of the source, referring to the size and divergence of the light beam at the location of the source. Nevertheless, the same quantity can be used to describe the density properties of the beam at an arbitrary distance z behind the source. The spectral flux at position z is normalized by the size $\Sigma_{x,y}(z)$ and divergence $\Sigma'_{x,y}(z)$ of the beam at that position,

$$\mathcal{B}(z) = \frac{F_{rad}(z)}{BW \cdot \Sigma_x(z) \Sigma_y(z) \Sigma'_x(z) \Sigma'_y(z)}. \quad (3.3)$$

With this generalized definition, the brilliance \mathcal{B} of the source is just the brilliance of the beam at position $z = 0$, i. e., $\mathcal{B} = \mathcal{B}(0)$. The usefulness of this generalized definition of brilliance shows in its invariance with respect to optical propagation in an ideal optical system². This invariance can be shown by *Liouville's theorem* [Lio37, Wol87] that is known from thermodynamics.

3.2 Synchrotron Radiation

As a summary of the previous section we can state that for the hard x-ray scanning microscope one needs a highly brilliant x-ray source, the energy of which is tunable in the range of

¹J. S. Schwinger was one of the first who developed the fundamental theory of synchrotron radiation [Sch45, Sch46, Sch49].

²*Ideal* optical system means that no photons are lost by attenuation.

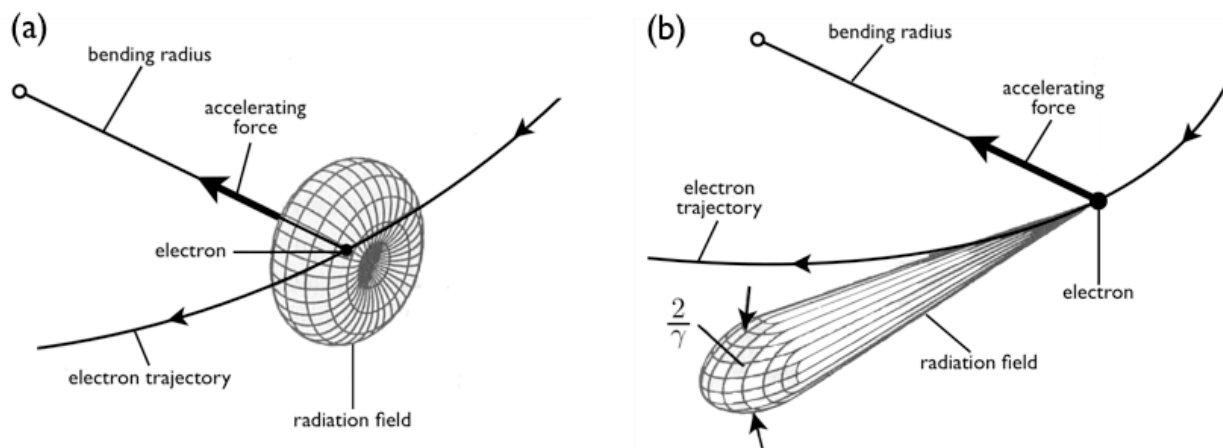


Figure 3.1: Radiation field of an accelerated electron. (a) In the center of mass frame the electron radiates an electromagnetic field conforming that of a classic electric dipole. (b) In the laboratory frame the Lorentz-transformation of the directional characteristic is observed. In case of highly relativistic electrons the transformation converts the axial symmetric radiation distribution into a sharply forward peaked cone with opening angle of $\pm 1/\gamma$. (Page 42, Fig. 2.3 from [Wil92], copyright 1992 by VIEWEG+TEUBNER, by courtesy of VIEWEG+TEUBNER.)

several tens of keV. X rays can be generated with x-ray tubes making use of bremsstrahlung and characteristic radiation, which are emitted when electrons hit a metallic anode. While x-ray tubes are frequently used in medical, industrial and scientific fields, their brilliance is quite limited and does not meet the requirements for many scientific applications. Unfortunately, this is also true for the hard x-ray scanning microscope.

Another kind of x-ray source has emerged with the development of particle accelerators which are used to accelerate charged particles to energies much higher than their rest energy ($\beta = v/c \approx 1$, $\gamma = \mathcal{E}/(mc^2) \gg 1$). Highly relativistic accelerated charged particles emit electromagnetic radiation which is concentrated in the forward direction of the moving particle (confer Figure 3.1). This kind of radiation was first observed and used in synchrotrons [EGLP47], therefore it is called *synchrotron radiation*. Nowadays, nearly all synchrotron radiation is generated at storage rings. In contrast to x-ray tubes, for which the angular distribution of the radiated photon flux is nearly constant, the photons of synchrotron radiation are emitted within a very small cone directed in forward direction, which is the main reason for the very high brilliance of synchrotron light sources being many orders of magnitudes larger than the brilliance of x-ray tubes. To illustrate the enormous superiority of synchrotron light sources over x-ray tubes, imagine an experiment which requires a specimen to be illuminated with a certain photon dose. At the undulator source of a synchrotron radiation facility (brilliance $\mathcal{B} = 10^{21}$ Sch) this photon dose maybe attained after an exposure time of 1 second. If this experiment has to be performed with an x-ray tube ($\mathcal{B} = 10^9$ Sch), the same photon dose would be achieved after an illumination time of 10^{12} seconds, i. e., the experiment would last more than 31 000 years! Even though the hard x-ray scanning microscope has been installed at a third generation synchrotron radiation facility, lots of

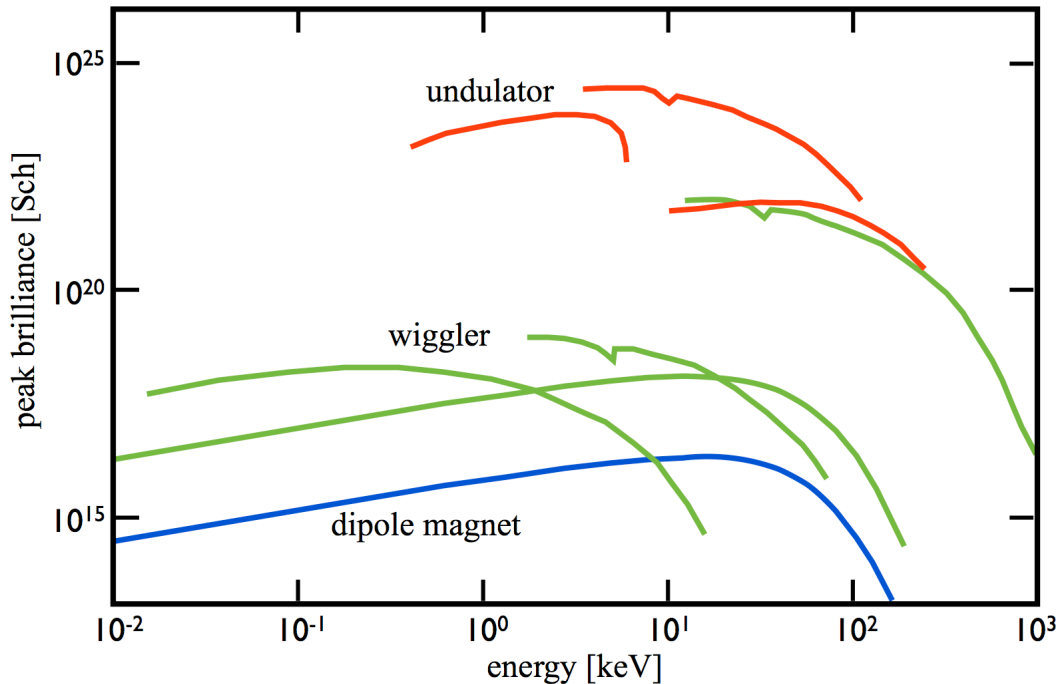


Figure 3.2: Peak brilliance of dipole magnets, wigglers and undulators as function of photon energy. The values refer to the synchrotron light sources DORIS III, PETRA II, and PETRA III at HASYLAB. The unit Schwinger for the brilliance [$1 \text{ Sch} = 1 \text{ ph}/(\text{s} \cdot \text{mrad}^2 \cdot \text{mm}^2 \cdot 0.1\%)$] is introduced in section 3.1.3. (Drawing adapted from [TDR07].)

experiments performed with that microscope require total exposure times in the order of several hours for a single sample. Experiments of this kind would be impossible without synchrotron radiation.

As a coarse classification one can distinguish between three main types of synchrotron light sources, as there are *dipole magnets* (also called *bending magnets*), *multipole wigglers* and *undulators*. While dipole magnets and multipole wigglers deliver a broad energy spectrum, undulators provide a quasi-monochromatic spectrum consisting of a fundamental harmonic and a number of higher harmonics. Because of this, together with the fact that undulators have much smaller divergence angles for the radiated photon flux, the brilliance of undulator sources is about 3 orders of magnitudes higher than that of multipole wigglers and even 6 orders of magnitudes higher than that of dipole magnets (while the brilliance of a dipole magnet is still 6 orders of magnitudes higher than that of an x-ray tube). The peak brilliance of dipole magnets, wigglers, and undulators as function of x-ray energy is drawn in Figure 3.2.

In the next paragraph I will describe the layout of a modern third generation synchrotron radiation facility. Thereafter I will summarize the main properties of dipole magnets, multipole wigglers and undulators, the latter of which serves as highly brilliant x-ray source for the scanning microscope. Detailed information and elaborated treatment of synchrotron light sources can be found in text books [Wil00, Hof04, Tal07, Wie07, FM10].

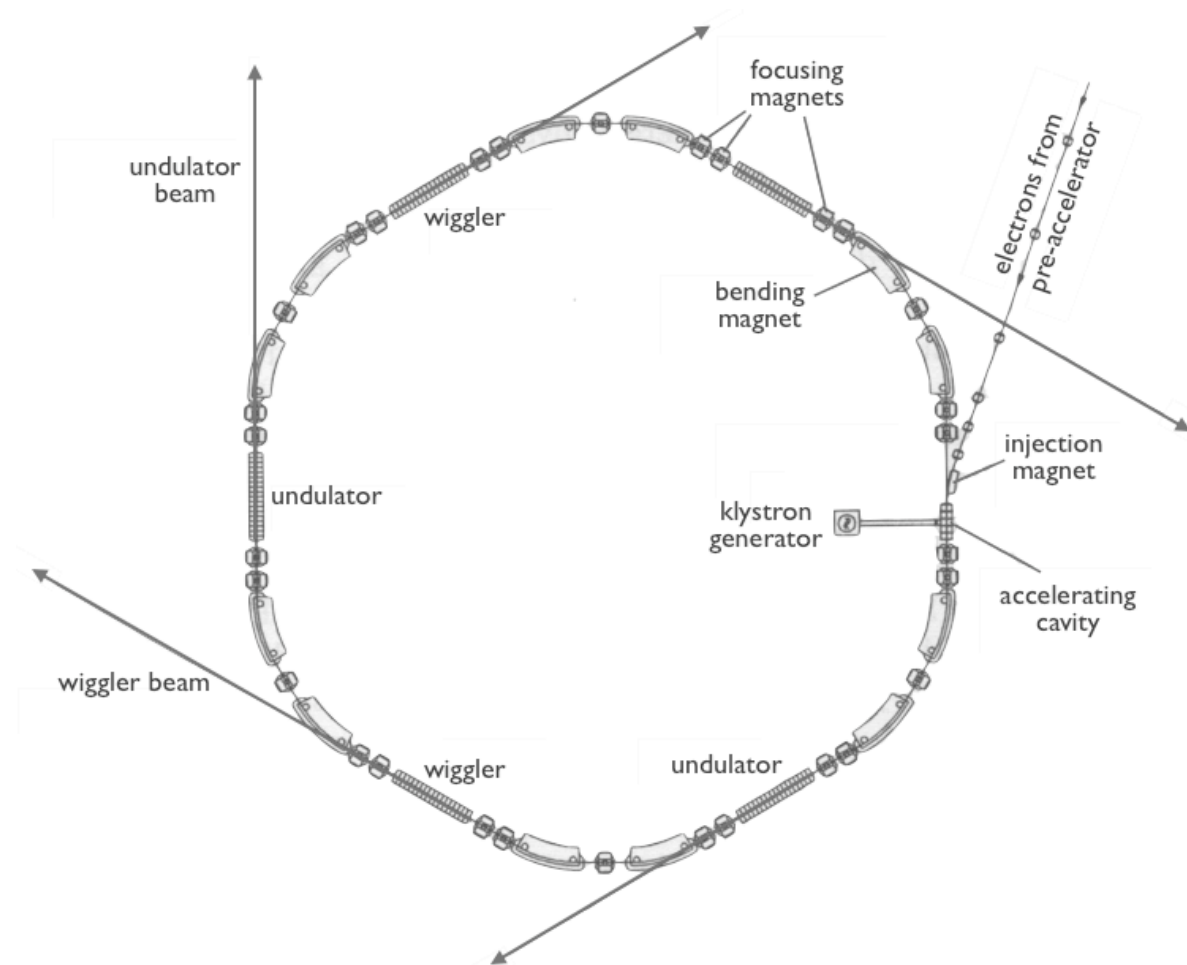


Figure 3.3: Top view on the storage ring of a 3rd generation synchrotron radiation facility. For simplicity only six straight sections have been drawn, whereas real storage rings are made of many more straight sections. (Page 49, Fig. 2.8 from [Wil92], copyright 1992 by VIEWEG+TEUBNER, by courtesy of VIEWEG+TEUBNER.)

3.3 Layout of a Synchrotron Radiation Facility

The layout of a modern third generation synchrotron radiation facility is shown in Figure 3.3. The main parts of such a facility are the pre-accelerator, the storage ring and the beamlines.

Pre-accelerator

The pre-accelerator generates charged particles, accelerates them to the required energy and injects the pre-accelerated particles into the storage ring.

The radiated power of a highly relativistic single particle of charge q and rest mass m

accelerated in a magnetic field of constant strength B to an energy of \mathcal{E} is given by [Jac98]

$$P = \frac{q^4 B^2 \mathcal{E}^2}{6\pi\epsilon_0 c^5 m^4},$$

and will be deduced in section 3.5. Since the mass of a proton is about three orders of magnitude larger than the electron mass ($m_{prot} \approx 1836 m_e$), synchrotron radiation emitted by electrons (or positrons) is about 13 orders of magnitudes more intensive than that of protons, and for this reason all synchrotron radiation facilities operate either with electrons or with positrons. In the matter of radiating synchrotron radiation, electrons and positrons behave exactly equivalently and the difference is rather of technical nature³. For this reason, without loss of generality, I will speak of electrons even though there might be positrons used, as for example at PETRA III, Hamburg.

The pre-acceleration is done in several steps. In most cases the electrons pass through a combination of a linear accelerator and a small synchrotron (called booster). The acceleration is induced by a series of cavity resonators applying high-frequency alternating electric fields on the electrons resulting in a bunching of the electron beam. The shape, size and distance between these bunches determine the brilliance as well as the time structure of the synchrotron radiation. The energy \mathcal{E} of the accelerated electrons determine the energy spectrum of the synchrotron radiation. Applying equation (3.15) with typical values for the magnetic field (≈ 1 T), the characteristic photon energy of the radiation emitted by a dipole magnet can be estimated. It turns out that the energy of the accelerated electrons must be in the range of several GeV, in order to obtain photon energies of several tens of keV. The largest third generation synchrotron radiation facilities operate at particle energies between 6 GeV and 8 GeV and, therefore, deliver radiation in the hard x-ray regime.

Storage ring

After the process of pre-acceleration, the electrons are injected into the storage ring, in which they are stored for several hours. The storage ring consists of straight sections that are connected by bending sections, forming a polygon with a circumference of several hundred meters. The bending is achieved by means of dipole magnets which can also be used as a source for synchrotron radiation. The straight sections contain the multipole wigglers and the undulators. As those devices are inserted between the bending parts of the storage ring, they are also called *insertion devices* (IDs).

In addition to the dipole magnets and the insertion devices, the storage ring contains several other components that are needed to post-accelerate the circulating electrons and to form the shape of the electron beam. Post-acceleration is necessary, because the electrons loose energy, which they transfer to the emitted synchrotron radiation. Appropriate quadrupole and sextupole magnets are used to make the size $\sigma_{x,y}$ and divergence $\sigma'_{x,y}$ of the

³Positrons are positively charged particles and, therefore, they reject the positively charged ions which are still present in the ultra high vacuum tubes of the particle accelerator. In contrast to that, the negatively charged electrons attract the ions and thus beam stability is derogated.

electron beam as small as possible, that is to decrease its emittance $\epsilon = \sigma_x \sigma_y \sigma'_x \sigma'_y$. The overall size and divergence of the x-ray source is given by the size and divergence of the radiation field of a single electron convolved with the size and divergence of the electron beam. Thus, in order to ensure highest brilliance of the synchrotron radiation source, the emittance must be minimized.

While the electrons are circulating on their orbit in the storage ring, they not only radiate synchrotron light, but they also interact with molecules, which are still present even inside ultra high vacuum tubes. This leads to a decrease of the electron beam current. Synchrotron radiation facilities come up against this loss of beam current by injecting new electrons from the pre-accelerator into the storage ring. This so-called refill has to be repeated periodically within a certain time interval which is typically several hours, corresponding to the live time of the electron beam. Some storage rings keep the beam current nearly constant (called *top-up mode*), injecting new electrons within time intervals which are short compared to the live time of the electron beam.

Beamlines

In order to make use of the synchrotron radiation emitted by a dipole magnet or by an insertion device, the storage ring is surrounded by a number of beamlines which guide the radiation from the source to the experimental station. The beamlines are located just at the end of the dipole magnet or of the insertion device and are directed tangentially with respect to the electron orbit. In order to avoid air scattering and absorption of the x-ray beam in air, the synchrotron beam is guided from the source to the experiment inside vacuum tubes. Concerning radiation protection, the experiments must be installed within x-ray shielded hutches furnished with an interlock system, which prevents people from being inside the hutch together with synchrotron radiation.

The hard x-ray scanning microscope has been installed at the beamline ID 13 of the ESRF, Grenoble. All experiments reported in this thesis took place at that beamline and, therefore, a more detailed description of beamline ID 13 is given in chapter 5.

3.4 Liénard-Wiechert Fields

A complete rigorous mathematical treatment of the radiated electromagnetic field of accelerated relativistic charged particles has first been published by J. Schwinger [Sch45, Sch46, Sch49], even though the fundamental mathematical basis had already been developed by Liénard at the end of the nineteenth century [Lié98]. Starting point of a quantitative description are the Liénard-Wiechert fields

$$\mathbf{E}(t) = \frac{e}{4\pi\epsilon_0} \left[\frac{(1 - \beta^2)(\mathbf{n} - \boldsymbol{\beta})}{R^2(1 - \mathbf{n} \cdot \boldsymbol{\beta})^3} + \frac{\mathbf{n} \times ((\mathbf{n} - \boldsymbol{\beta}) \times \dot{\boldsymbol{\beta}})}{cR(1 - \mathbf{n} \cdot \boldsymbol{\beta})^3} \right]_{t'}, \quad (3.4)$$

$$\mathbf{B}(t) = \frac{1}{c} \mathbf{n}(t') \times \mathbf{E}(t). \quad (3.5)$$

These equations allow one to calculate the electric and the magnetic fields $\mathbf{E}(t)$ and $\mathbf{B}(t)$ generated by an arbitrarily moving electron with charge e and mass m as seen by an observer. R is the distance between the electron and the observer, \mathbf{n} is the unit vector directed from the electron to the observer, and $\boldsymbol{\beta} = \mathbf{v}/c$ is the normalized velocity of the electron. The squared brackets $[\dots]_{t'}$ imply that all time dependencies within those brackets have to be evaluated with respect to the *emission time* t' in order to retrieve the fields at *observation time* t . The effect $E(t)$ which is registered by the observer at time t had been caused by the moving electron at an emitted (or retarded) time t'

$$\begin{aligned} t' &= t - \frac{R(t')}{c}, \\ dt &= (1 - \mathbf{n}(t') \cdot \boldsymbol{\beta}(t')) dt' \end{aligned}$$

and, therefore, the time dependent variables R , \mathbf{n} , $\boldsymbol{\beta}$, and $\dot{\boldsymbol{\beta}}$ in equation (3.4) have to be substituted by $R(t')$, $\mathbf{n}(t')$, $\boldsymbol{\beta}(t')$, and $d\boldsymbol{\beta}(t')/dt'$. The fields $\mathbf{E}(t)$ and $\mathbf{B}(t)$ allow one to compute the poynting vector

$$\mathbf{S}(t) = \frac{1}{\mu_0} \mathbf{E}(t) \times \mathbf{B}(t), \quad (3.6)$$

which can be used to obtain the angular power distribution and the total radiated power

$$\frac{dP}{d\Omega} = \mathbf{n} \cdot \mathbf{S} R^2, \quad (3.7)$$

$$P = \int d\Omega \mathbf{n} \cdot \mathbf{S} R^2. \quad (3.8)$$

As indicated by equation (3.4) the observed electric field \mathbf{E} is a superposition of a near-field and a far-field term, the first of which is proportional to $1/R^2$ and the latter is proportional to $1/R$. The near-field contribution depends only on the velocity $\boldsymbol{\beta}(t')$ of the electron, whereas the far-field contribution depends on the electron's acceleration $d\boldsymbol{\beta}(t')/dt'$. Inserting the near-field contribution into (3.6) reveals that there is no net energy flux from the electron to the outer space regions. We are interested in synchrotron radiation as a highly brilliant light source and thus, the near field can be neglected. As a matter of fact, in all practical situations, the distance R of the observer from the synchrotron source is large enough to justify the assumption that we are always in the far-field region, where the $1/R$ term wins over the $1/R^2$ term. Hence, the Liénard-Wiechert fields (3.4) and (3.5) reduce to

$$\mathbf{E}(t) = \frac{e}{4\pi\epsilon_0} \left(\frac{\mathbf{n} \times ((\mathbf{n} - \boldsymbol{\beta}) \times \dot{\boldsymbol{\beta}})}{cR(1 - \mathbf{n} \cdot \boldsymbol{\beta})^3} \right)_{t'} \quad (3.9)$$

$$\mathbf{B}(t) = \frac{1}{c} \mathbf{n}(t') \times \mathbf{E}(t). \quad (3.10)$$

As a consequence, far away from the moving electron, the fields \mathbf{E} and \mathbf{B} are not only orthogonal on each other, but they are also both perpendicular to \mathbf{n} .

The straight forward way to proceed would be to calculate the radiated angular power distribution and total power using equations (3.6)-(3.10). The variables $R(t')$, $\mathbf{n}(t')$, and $\dot{\boldsymbol{\beta}}(t')$ have to be evaluated from the geometry of the magnetic field given by the dipole magnet, multipole wiggler or undulator. This procedure is typically quite difficult and encounters a lot of mathematical manipulation. Even the simplest case of a circular trajectory, which is present in a dipole magnet, results in Airy integrals or (alternatively) modified Bessel functions. Even though they are very useful for exact quantitative calculations, they are not very intuitive, and for this reason, I will proceed with hand waving arguments, which have to be treated with care, but which allow a better physical insight to the physics of synchrotron radiation. An exact treatment can for example be found in [Sch45, Cla04, Tal07].

3.5 Dipole Magnets

A schematic sketch of a dipole magnet is shown in Figure 3.4(a). Originally, dipole magnets were used in synchrotrons or storage rings in order to bend the path of the charged particles and to force them onto a closed trajectory. In the early days of particle accelerators, the synchrotron light emitted in a dipole magnet by the accelerated relativistic electrons was a nuisance because energy is transferred from the electrons to the synchrotron radiation and this effectively limits the achievable electron energy for high energy particle collision experiments. On the other hand, dipole magnets as a source of synchrotron radiation exceed the brilliance of x-ray tubes by a factor of 10^6 , and thus they are used for both, keeping the electrons on a closed orbit and as a highly brilliant x-ray source.

Radiated power

The constant magnetic field \mathbf{B} of the bending magnet forces the electron on a circular trajectory with bending radius

$$\rho = \frac{m\beta c}{eB}. \quad (3.11)$$

Knowing the orbit of the electron, the Liénard-Wiechert fields (3.9) and (3.10) can be used to calculate the Poynting vector, the angular power distribution, and so on. But as mentioned in the previous section I will follow another approach. For this we change into an inertial system K' in which the electron is moving with non-relativistic speed, perform the calculation in K' and transform the result back into the inertial system K in which the observer is in rest.

In K' the electron is moving slowly ($\beta \ll 1$) and equations (3.9) and (3.10) become

$$\begin{aligned} \mathbf{E}(t) &= \left(\frac{e}{4\pi\epsilon_0 c R} \mathbf{n} \times (\mathbf{n} \times \dot{\boldsymbol{\beta}}) \right)_{t'} \\ \mathbf{B}(t) &= \frac{1}{c} \mathbf{n}(t') \times \mathbf{E}(t) \end{aligned}$$

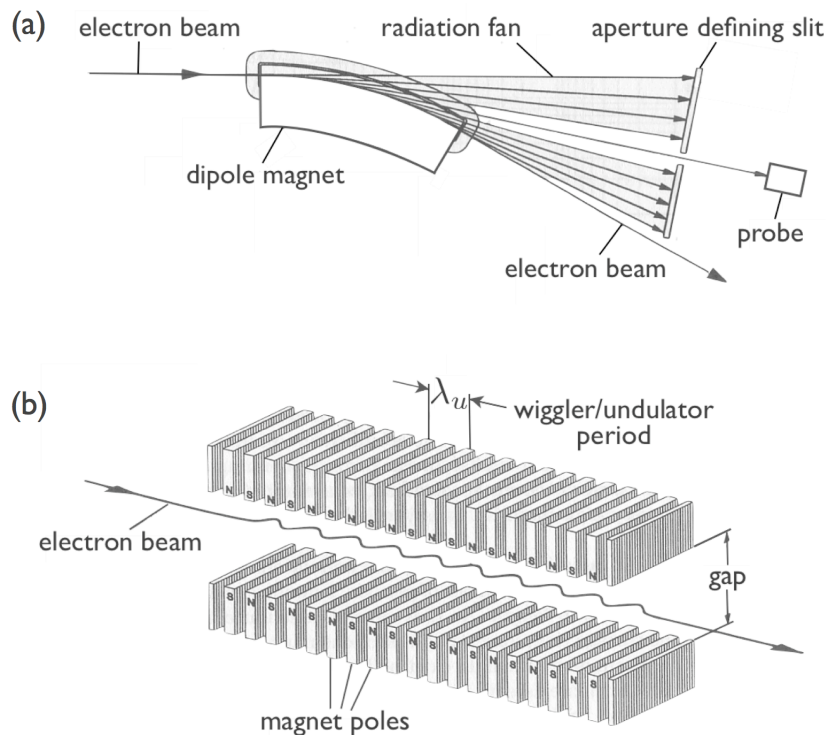


Figure 3.4: Overview of the three main types of synchrotron radiation sources. (a) Schematic drawing of a dipole magnet. The electron beam is forced to follow a circular arc. (b) Sketch of an insertion device. Depending on the strength of the amplitude of the wiggling electron beam the ID might either work as a wiggler or as an undulator (Page 47, Fig. 2.6 and page 48, Fig. 2.7 from [Wil92], copyright 1992 by VIEWEG+TEUBNER, by courtesy of VIEWEG+TEUBNER.)

Together with equations (3.6), (3.7), and (3.8) the angular power distribution and the total power are obtained as

$$\frac{dP}{d\Omega} = \frac{e^2}{16\pi^2\epsilon_0 c} \dot{\beta}^2 \sin^2 \theta, \quad (3.12)$$

$$P = \frac{e^2}{6\pi\epsilon_0 c} \dot{\beta}^2, \quad (3.13)$$

which was already found by J. Lamor in 1897 [Lar97]. The total radiated power must be invariant against a change of the inertial system. Therefore, equation (3.13) can be expressed as a scalar product of four-vectors. With the definition of the four-momentum $p_\mu = (\mathcal{E}/c, \mathbf{p})$ and $p^\mu = (\mathcal{E}/c, -\mathbf{p})$ equation (3.13) becomes

$$P = \frac{e^2}{6\pi\epsilon_0 m^2 c^3} \left(\frac{dp_\mu}{dt'} \cdot \frac{dp^\mu}{dt'} \right).$$

In this expression, d/dt' refers to the inherent time of the inertial frame K' . Transformation

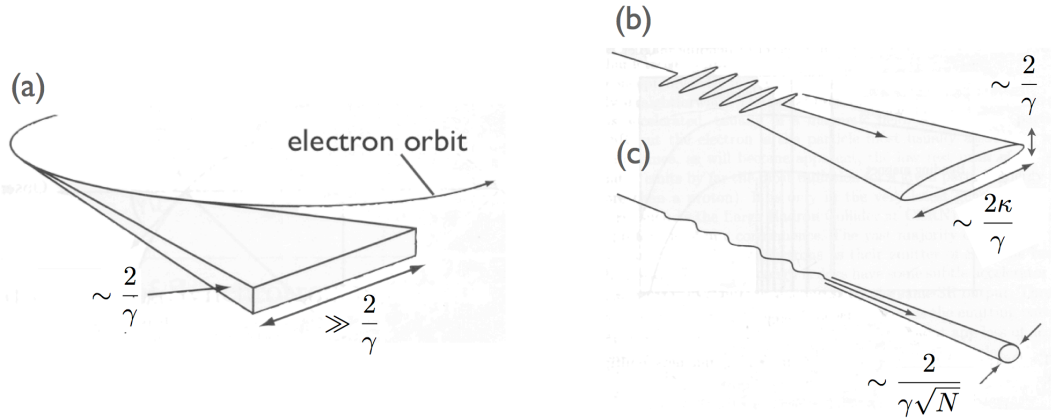


Figure 3.5: Angular distribution of synchrotron light radiated by the three main types of synchrotron radiation sources. (a) Dipole magnet. The vertical opening angle is about $2/\gamma$, while the horizontal opening angle is much larger. (b) Multipole wiggler. The angular distribution is similar to that of a dipole magnet with the same vertical opening angle. The horizontal opening angle is proportional to the deflection parameter κ . (c) The undulator features a very sharp collimation of the radiated synchrotron light in the vertical direction as well as in the horizontal direction scaling with $1/\sqrt{N}$ (N number of periods). This property in connection with its narrow shaped energy harmonics is the reason for the enormous gain in brilliance of three orders of magnitudes as compared to the brilliance of multipole wigglers. (Page 5, Figure 1.2 from [Cla04], by permission of Oxford University Press.)

into K and using $dt' = dt/\gamma$ yields

$$\begin{aligned} P &= \frac{e^2 \gamma^2}{6\pi \epsilon_0 m^2 c^3} \left(\frac{dp_\mu}{dt} \cdot \frac{dp^\mu}{dt} \right) \\ &= \frac{e^2 \gamma^2}{6\pi \epsilon_0 m^2 c^3} \left[\left(\frac{d\mathbf{p}}{dt} \right)^2 - \left(\frac{1}{c} \frac{d\mathcal{E}}{dt} \right)^2 \right]. \end{aligned}$$

In a dipole magnet the electron is forced on a trajectory with bending radius as given in (3.11) and, therefore, the total power radiated by a single electron is given by the expression

$$P = \frac{e^2 \mathcal{E}^4}{6\pi \epsilon_0 m^4 c^7 \rho^2} = \frac{e^4 B^2 \mathcal{E}^2}{6\pi \epsilon_0 c^5 m^4}. \quad (3.14)$$

Angular distribution

Synchrotron light shows a very sharply forward peaked power distribution and, therefore, it is quite well represented by the half opening angle Θ that defines a cone into which half of the radiated energy is emitted. For this reason, rather than calculating the exact angular power distribution, only the half opening angle Θ is derived.⁴

⁴Like the total radiated power P , also the angular power distribution $dP/d\Omega$ of synchrotron radiation can be retrieved by calculating the electric and magnetic fields with equations (3.9) and (3.10) and using them to obtain the Poynting vector.

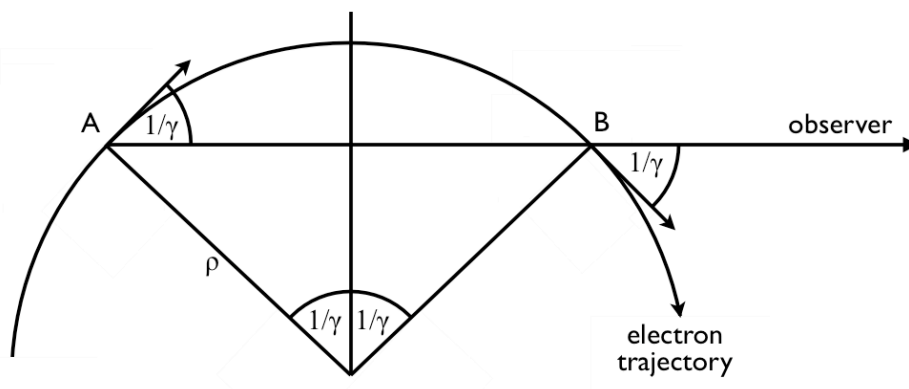


Figure 3.6: Schematic drawing of the geometry for an observer of dipole magnet radiation. (Page 6, Figure 1.3 from [Cla04], by permission of Oxford University Press.)

Again we change into the inertial frame K' in which the electron is moving non-relativistically. Then the Larmor equation (3.12) is valid and the angular power distribution is circularly symmetric around the direction of acceleration as seen in Figure 3.1(a), and in K' the half opening angle is $\pi/2$. The half opening angle in the laboratory frame K (in which the electron is moving with relativistic speed) can be retrieved if the momentum of a photon which leaves the electron at an angle of $\pi/2$ with respect to the moving direction is Lorentz-transformed from K' into K . As a result of this Lorentz transformation the opening angle changes from $\pi/2$ to $1/\gamma$ which is illustrated in Figure 3.1. The radiation cone depicted in Figure 3.1(b) shows the situation of an infinitesimal small movement of the electron on its bent trajectory. While the electron continues its circular movement, its moving direction changes and the cone smears in the horizontal plane forming the shape of a fan as seen in Figure 3.5(a). For this reason, radiation from a bending magnet is only collimated in the vertical direction.

Spectral distribution

The spectral distribution of synchrotron light from a dipole magnet has first been calculated by J. Schwinger [Sch45, Sch46, Sch49] and can be expressed in terms of Airy integrals or by integrals over modified Bessel functions. It turns out that the spectrum has a broad distribution and that it is completely determined by the *critical energy*⁵ \mathcal{E}_c which divides the spectrum into two regions of equally radiated power. The critical photon energy of a dipole magnet is given by [Cla04]

$$\mathcal{E}_c = \frac{3\hbar c\gamma^3}{2\rho} = \frac{3\hbar\mathcal{E}^3}{2\rho m^3 c^5} = \frac{3\hbar e}{2m^3 c^4} B\mathcal{E}^2 \quad (3.15)$$

with bending radius ρ as given in equation (3.11).

⁵The critical energy is also known as *characteristic energy*.

The critical energy can be approximated by considering the time dependence of the radiation field as seen by the observer. As the electron travels on its circular arc, the collimated radiation cone with half opening angle $1/\gamma$ is seen by the observer only during a short period of time Δt . In order to estimate this time period consider Figure 3.6. The beginning of the pulse and its end correspond to the points A and B, respectively, defining an angle $2/\gamma$ and a circular arc $s_e = 2\rho/\gamma$. The time t_e for the electron to travel from A to B along the circular arc is

$$t_e = \frac{s_e}{v_e} = \frac{2\rho}{c\beta\gamma}.$$

During that time, the emission amplitude at A propagates a distance $s_\gamma = ct_e$, gaining an advance against the electron of

$$\Delta s = s_\gamma - s_{\overline{AB}}$$

with $s_{\overline{AB}} = 2\rho \sin(1/\gamma)$ denoting the length of the chord between A and B. The time period Δt is now given by $\Delta s/c$. The electrons in a storage ring are highly relativistic with γ values in the order of 10^4 , and thus $\sin(1/\gamma) \approx 1/\gamma + 1/(6\gamma^3)$ and $\beta = \sqrt{1 - 1/\gamma^2} \approx 1 - 1/\gamma^2$ are good approximations. The time period experienced by the observer becomes

$$\begin{aligned} \Delta t &= \frac{1}{c} \Delta s = \frac{2\rho}{c} \left(\frac{1}{\beta\gamma} - \sin \frac{1}{\gamma} \right) \approx \frac{2\rho}{c} \left(\frac{1}{\beta\gamma} - \frac{1}{\gamma} + \frac{1}{6\gamma^3} \right) \\ &= \frac{2\rho}{c} \left(\frac{1-\beta}{\beta\gamma} + \frac{1}{6\gamma^3} \right) \approx \frac{2\rho}{c} \left(\frac{1 - \left(1 - \frac{1}{2\gamma^2}\right)}{\gamma \left(1 - \frac{1}{2\gamma^2}\right)} + \frac{1}{6\gamma^3} \right) \\ &\approx \frac{2\rho}{c} \left(\frac{1}{2\gamma^3} + \frac{1}{6\gamma^3} \right) = \frac{4\rho}{3c\gamma^3}. \end{aligned} \quad (3.16)$$

A photon detected by the observer could have been emitted by the electron at any of the locations on the arc between A and B with a time uncertainty of Δt as given by expression (3.16). All these alternatives are quantum mechanically undistinguished [Len03] and hence, the energy uncertainty of the photon is given by the time-energy uncertainty relation $\Delta \mathcal{E} \Delta t \geq 2\pi\hbar$. Thus, the high cut-off energy in the observed spectrum becomes

$$\mathcal{E}_{\text{typical}} = \frac{3\pi\hbar c\gamma^3}{2\rho}.$$

Obviously, we cannot expect this typical energy to represent the characteristic energy exactly. Compared with equation (3.15) the typical energy is by a factor π larger than the critical energy.

Polarization

A bending magnet accelerates the electrons in the horizontal plane and, therefore, the radiation emitted by the electrons is horizontally polarized in the plane of the electron orbit. Below and beneath the plane of the electron orbit vertically polarized contributions with a

phase shift of $\pi/2$ occur with increasing inclination angle and lead to elliptical polarization. A quantitative treatment reveals that 7/8 of the radiated power is horizontally and 1/8 is vertically polarized [Cla04].

3.6 Insertion Devices

A more efficient way to produce synchrotron radiation is to use insertion devices (IDs) instead of dipole magnets. Insertion devices are integrated in the straight sections between the bending segments of a storage ring. An ID forces the electrons to move on a wiggling trajectory by means of an array of magnets with alternating fields directed up to down and vice versa. A schematic drawing of such an ID is shown in Figure 3.4(b).

The electron trajectory in an insertion device with period length $\lambda_u = 2\pi/k_u$ and magnetic peak value B_0 can be approximated by a sine with same periodic length λ_u as the ID

$$x(s) = x_0 \sin(k_u s)$$

with amplitude

$$x_0 = \frac{\lambda_u^2 e B_0}{2\pi m \gamma c}.$$

The maximal deflection angle Θ_D experienced by the electron is therefore given by

$$\Theta_D = \frac{\kappa}{\gamma}$$

with the *deflection parameter*

$$\kappa = \frac{\lambda_u e B_0}{2\pi m c}.$$

The trajectory can be considered as a series of circular arcs changing the direction of curvature successively from the left to the right. Depending on the maximal deflection angle Θ_D the synchrotron light emission amplitudes of different parts of the trajectory add up coherently or incoherently. Small deflection angles make it impossible to distinguish between different emission alternatives and, therefore, the emission amplitudes have to be added coherently and interference effects become present. In this case the insertion device acts as an undulator. On the other hand, large deflection angles make the emission alternatives from different parts of the trajectory distinguished, and the amplitudes must be added incoherently [Len03]. Interference is not observed, and the ID operates as a multipole wiggler. By definition, an insertion device is called a multipole wiggler, if the deflection angle Θ_D is much larger than the half opening angle $1/\gamma$ of the radiated cone, otherwise one speaks of an undulator.

3.6.1 Multipole Wigglers

The magnetic field of a multipole wiggler is strong enough to make the maximal deflection angle of the wiggling electron larger than the half opening angle $1/\gamma$ of the emitted synchrotron

radiation, i. e., the deflection parameter κ is much larger than 1. Emission amplitudes from different parts of the electron trajectory add up incoherently, i. e., the intensities are added instead of the amplitudes. Hence, the radiated intensity of a multipole wiggler with N periods is increased by a factor of $2N$ compared to a dipole magnet with the same magnetic field strength. The angular distribution and the power spectrum of a multipole wiggler are similar to that of a dipole magnet. The radiation is sharply collimated in the vertical direction with half opening angle $1/\gamma$ and it is less collimated in the horizontal direction with half opening angle of κ/γ as shown in Figure 3.5(b). The energy spectrum shows a broad distribution and is characterized by the critical Energy \mathcal{E}_c as known from equation (3.15). Similar as dipole magnets, multipole wigglers generate x rays that are horizontally polarized in the plane of the electron orbit.

3.6.2 Undulators

Even though undulators were proposed already in the middle of the 20th century [Mot51, MTW53], their routine operation has emerged not until the construction of third generation synchrotron radiation facilities in the mid-1990s. Due to the coherent superposition of the emission amplitudes from different undulator wigglers, the performance of undulators is superior as compared to wigglers. A necessary condition to show up such interference effects is the overlap of the radiation cones emitted from different parts of the electron trajectory. Since the opening angle of the emission cone is in the order of $1/\gamma$, the maximal deflection angle Θ_D must not be much larger than about $1/\gamma$, and the deflection parameter κ must not be much larger than 1. The consequence of the interference is a quasi-monochromatic energy spectrum with a fundamental energy mode \mathcal{E}_1 and higher energy harmonics \mathcal{E}_n and an additional collimation of the emitted radiation cone in the vertical and the horizontal direction. Another implication is that the radiated spectral power density does not scale with the number N of undulator periods but with its square N^2 , even though the radiated total power of an undulator is similar to that of a wiggler. This makes the undulator an extreme highly brilliant x-ray source with a brilliance exceeding the values of bending magnets and wigglers by some orders of magnitudes.

Energy harmonics

The energy harmonics of an undulator can be estimated by the interference condition, which states that the phase difference of amplitudes of photons emitted from neighboring wiggler periods must be 2π in order to gain constructive interference. For an undulator with period λ_u and deflection parameter κ , the n th harmonic observed at an angle θ off the undulator axis is given by [ANM01]

$$\mathcal{E}_1(\theta) = \frac{2n\gamma^2}{\lambda_u} \left(1 + \frac{1}{2}\kappa^2 + (\gamma\theta)^2 \right)^{-1}. \quad (3.17)$$

Typical undulator periods are of order 10 mm and γ is about 10^4 (electron energy of several GeV) and, therefore, the photon energy of the fundamental energy mode observed in the

undulator axis is in the order of some keV. This energy value can be tuned by varying the undulator gap, which changes the magnetic field and the deflection parameter κ . To increase the photon energy, the undulator gap has to be made larger to reduce the magnetic field strength and thus the deflection parameter. On account of the finite length of the undulator, the energy harmonics have a non-zero width which can be approximated by

$$\frac{\Delta\mathcal{E}}{\mathcal{E}} \approx \frac{1}{nN}, \quad (3.18)$$

where n denotes the number of the harmonic and N is the number of undulator periods. In a typical undulator N is in the range of 100, so the relative energy bandwidth of the fundamental harmonic is of order percent.

Angular distribution

The interference condition defines the energy harmonics for a given observation angle θ with respect to the undulator axis. On the other hand, for a certain energy harmonic E_n , the interference condition limits the angular spread of the radiation to a half opening angle of

$$\Theta = \frac{1}{\gamma} \sqrt{\frac{1 + \kappa^2/2}{nN}} \approx \frac{1}{\gamma} \sqrt{\frac{1}{nN}} \quad (3.19)$$

both in horizontal and vertical direction, respectively. This angle is smaller than the opening angle of a dipole magnet or a multipole wiggler and the collimation is not only in the vertical direction.

Polarization

Synchrotron radiation from an undulator is always linearly polarized. In the plane of the electron trajectory the vertical polarization component is zero and the polarization is horizontally directed. Outside this plane, the vertical component is non-zero and increases with increasing observation angle θ . While in a dipole magnet the horizontal and the vertical polarization components are shifted by a phase of $\pi/2$, there is no phase shift in an undulator and, therefore, instead of elliptic polarization, there is still linear polarization with an axis of polarization which is slightly tilted against the horizontal direction. The relevance of the horizontal polarization shows in the fact that the intensity of elastically and in-elastically scattered x-rays is reduced in the horizontal direction perpendicular to the incident x-ray beam. In the hard x-ray scanning microscope, we make use of this effect by aligning the energy dispersive fluorescence detector orthogonal to the optical axis, which leads to a significant reduction of the background signal.

As a summary of this paragraph the undulator features highly collimated, quasi-monochromatic and horizontally polarized light with tunable energy in the range of several keV. The extraordinary high brilliance of undulators is the reason to choose them as a source for the hard x-ray scanning microscope.

Chapter 4

X-Ray Optics

Since the discovery of x rays at the end of the nineteenth century, scientists have been trying hard to develop efficient x-ray optics. Similar to visible light optics, there are a lot of applications which would benefit from appropriate focusing optical devices for x rays, such as full field imaging, generation of small focused x-ray beams with high photon flux, or collimation of diverging beams. The hard x-ray scanning microscope, for example, makes use of a highly intense focal spot generated by a so-called nanofocusing lens. In addition, the scanning microscope can be operated in a two-stage focusing mode, activating a prefocusing lens system, which generates a secondary source and matches the available coherent photon flux provided by the source to the aperture of the nanofocusing lens.

Compared to visible light, developing optics for the x-ray regime is quite difficult. In visible light optics there are two major kinds of focusing optics, namely refractive lenses and mirror optics. Simply transferring the concept of refractive lenses from visible light optics to hard x rays is not possible just like that, because of the very small refraction index decrement δ , which is in the order of 10^{-5} to 10^{-7} (see chapter 2), and because of the comparably strong absorption of x rays in the lens material. Focusing mirror optics, too, cannot be taken over without significant modifications, because reflection of x rays on surfaces is efficient only in case of external total reflection, and the critical angle for total reflection is very small ($\theta_c = \sqrt{2\delta} < 1^\circ$). Despite these difficulties, refractive lenses (compound parabolic refractive lenses and nanofocusing lenses) and mirror optics (Kirkpatrick-Baez mirrors) [KB48, SU92, HIS⁺01, HRC⁺01] have been built and successfully used, but their designs differ from those of visible light optics. Other optics appropriate for hard x rays are available today, for example capillary optics [BHT94, HTB94], bent crystals [LSH⁺98, SLH⁺98, HWF98, MUF⁺99], multilayers [UBF86, Und86, UTWG88, SG95, SGB⁺99, MPPZ99], waveguides [SS74, FSF⁺95, LCC⁺97, FSD⁺98, ZBP⁺00, JCD⁺01], Fresnel zone plates [LYL⁺92, DKM⁺95, YLC⁺99, SSA95, SJT97, MBP97, AOH⁺00, TYK⁺02, KSA⁺02], multilevel zone plates [DRG⁺99], multilayer laue lenses [LCQ⁺07, KYW⁺08], Bragg-Fresnel optics [ABK⁺89, CDL⁺95, HFS⁺97], and photon sieves [KSJ⁺01].

In this chapter compound parabolic refractive x-ray lenses (CRLs) [LST⁺99] and nanofocusing lenses (NFLs) [SKH⁺03, SKP⁺05b, BFP⁺09, Boy10] are introduced, since they have applications in the hard x-ray scanning microscope. Moreover, I will present adiabatically

focusing lenses (AFLs) [SL05], a new kind of focusing x-ray optics with a maximal numerical aperture exceeding the value $\sqrt{2\delta}$, which was believed to hold as a limit for all focusing x-ray optics [BHT94, ZBP⁺00, BKv03, Suz04]. Even though not yet realized, our study group is going to fabricate such AFLs and integrate them as focusing optics in the scanning microscope at PETRA III beamline P06. After discussing the most important properties of a micro-beam that is generated by refractive x-ray lenses the concept of a two-stage focusing scheme is presented. Two-stage focusing is applied in the hard x-ray scanning microscope in order to adjust the transverse coherence length of the incident x-ray beam to the size of the effective aperture of the horizontal and vertical nanofocusing lens, and thereby increasing the coherent photon flux in the focal spot.

4.1 Refractive X-Ray Lenses

The most common optics for visible light are refractive lenses made of transparent materials like glass or plastics. In Wilhelm Conrad Röntgen's original publication about his discovery of x rays in 1895 [Rön95, Rön98] he already reports about his unsuccessful attempts to focus x rays with refractive lenses made of different materials. In fact, he could not observe refraction of x rays at all. This is because the real part n of the complex index of refraction $\hat{n} = n + i\beta = 1 - \delta + i\beta$ of any material does not differ very much from 1 in the x-ray regime. The refractive index decrement δ is in the order of 10^{-5} to 10^{-7} , while for visible light the value of $|\delta|$ is significantly larger than 0 for most materials. Common crown glasses, for example, have refractive indices around 1.5 - 1.6, and the denser flint glasses have values up to 1.75. The refractive index of gemstones are as high as 2.4 (diamond) or even 2.6 (rutile). As the focal distance of a spherical thin lens is proportional to δ^{-1} , small values of the refractive index decrement result in large focal distances and, therefore, the focal distance of refractive lenses are many orders of magnitudes larger for hard x rays than for visible light, if their geometric profile would be the same.

To illustrate the difference in refraction between x rays and visible light, let us consider an ordinary spherical thin lens with a radius of curvature of 0.1 m. For visible light the material maybe crown glass with an index of refraction of about 1.5. To make the lens focus the light rather than defocusing it, the lens shape should be convex. Following the lens maker's equation for thin lenses [Hecht, §5.2.3], the focal distance of such a lens is given by $f = R/(2\delta) = 0.1$ m. In analogy, for hard x rays a lens must have a concave shape in order to focus the beam, but apart from that, the refractive index decrement is 6 orders of magnitudes smaller than for visible light. Therefore, the focal distance would be larger in the same manner, i. e., while for visible light the focal distance is about 0.1 m, it would be about 100 km for hard x rays. In view of such a weak refraction it is not surprising, that refractive lenses were considered impossible for hard x rays. This conventional wisdom lingered until the mid-1990s. With the availability of third generation synchrotron radiation facilities, scientists began again to think about refractive x-ray lenses. In 1995, A. Snigirev et al. proved experimentally that focusing hard x rays with refractive lenses is feasible, if lots of single lenses are put in series, thus increasing the refractive power linearly with the number of

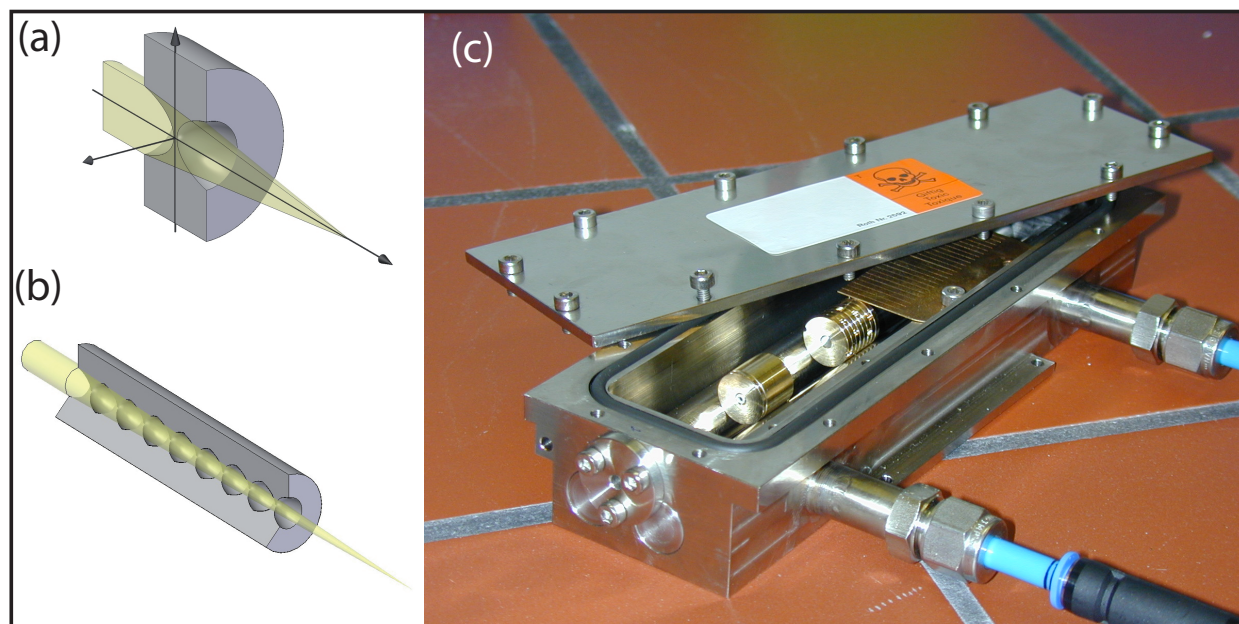


Figure 4.1: Compound parabolic refractive x-ray lenses (CRLs). (a) Drawing of a single lens. The concave profile has the shape of a paraboloid of rotation and is pressed into both sides of a coin-like blank of beryllium, aluminum, or nickel. (b) An array of single lenses stacked one behind the other forms a compound parabolic refractive lens. (c) Photograph of a lens holder, which contains compound parabolic refractive lenses made of beryllium.

single lenses, and if the radius of curvature is made sufficiently small [SKSL96]. Since then, refractive x-ray lenses have been developed further. Today, refractive lenses belong to the most important and successful x-ray optics for synchrotron applications, and they will also be of importance for experiments at Free Electron Laser facilities (FEL). The following sections deal with three different kinds of refractive x-ray lenses, all of them invented, developed, or manufactured by our research group originating in Aachen and continued in Dresden, namely compound parabolic refractive lenses (CRLs), nanofocusing lenses (NFLs), and adiabatically focusing lenses (AFLs).

4.2 Compound Parabolic Refractive Lenses (CRLs)

Compound parabolic refractive lenses (CRLs) are a special kind of refractive x-ray lenses. A CRL consists of a number of single lenses each of which has the shape of a paraboloid of rotation (Figure 4.1). The shape of a single lens has to be concave rather than convex, because in the x-ray regime the real part of the complex index of refraction is smaller than 1 as already seen in chapter 2.

Due to the very small refractive index decrement $\delta \approx 10^{-6}$, refractive lenses for hard x rays must have much stronger curvatures than lenses for visible light. Spherical lenses are only useful if their aperture is small compared to the radius of the sphere, otherwise strong

spherical aberration would deteriorate the optical properties of the lens. Hence spherical lenses with strong curvatures come with small useful apertures, which make them unfeasible in the field of x rays. In order to avoid spherical aberrations and still have relatively large apertures, refractive lenses must have a parabolic profile.

Besides a very small refractive index decrement, attenuation is another critical issue for refractive x-ray lenses. Attenuation directly leads to a loss of flux in the focus and limits the effective aperture of the lens and, therefore, increases the Airy disk and thus the lateral resolution of the lens. In order to have low absorption, the lens material must consist of low atomic number elements like lithium, beryllium, boron, et cetera. Besides a low absorption, the lens material must be resistant in the intense beam of a synchrotron radiation facility, and it must have a low small angle x-ray scattering cross section. It turns out that compound parabolic refractive lenses made of beryllium are most appropriate for hard x rays with energies up to about 30 keV. For higher energies, Compton scattering begins to dominate absorption in beryllium and, therefore, lenses made of materials with a larger mass density like aluminum or nickel are the better choice, because of their larger refractive index decrement.

In addition to rotationally symmetric parabolic refractive lenses there are also parabolic refractive lenses with the shape of parabolic cylinders (*cylindrically symmetric lenses*), focusing the incident x-ray beam only in one direction. Cylindrically symmetric lenses are used in experiments, which need an x-ray beam, which is large in one direction but small in the other one, as for example in reflectometry. In the hard x-ray scanning microscope, cylindrically symmetric parabolic refractive lenses are used as part of the prefocusing device. Prefocusing aims for adapting the lateral coherence length of the incident beam to the effective aperture of the nanofocusing lens, this way exploiting the full available coherent flux provided by the undulator source (treated in detail in the sections 4.12–4.14). Since the horizontal and the vertical sizes of the undulator source are different, the same is true for the horizontal and the vertical lateral coherence lengths in the plane of the lens aperture. A combination of axially symmetric and cylindrically symmetric lenses makes it possible to astigmatically prefocus the beam, and hence the horizontal and the vertical coherence lengths can be adjusted independently from each other.

Both kinds of compound parabolic refractive lenses, the rotationally symmetric as well as the cylindrically symmetric lenses, are manufactured by stamping the concave lens shape into both sides of a coin-like blank of beryllium, aluminum, or nickel. In order to minimize aberrations from the ideal lens shape, the heading tool has to be fabricated with sufficient precision.¹ But even an ideal heading tool does not guarantee an aberration free lens, since the process of pressing is quite crucial, especially in the case of beryllium. As beryllium is not very ductile but very brittle, flaws like cracks or warpage at the surface may appear. The CRLs used in the hard x-ray scanning microscope have all been fabricated by Prof. Lengeler at the RWTH Aachen.

¹The maximal rms deviation from the ideal paraboloid of rotation must be less than 1 μm on an aperture of 1 mm.

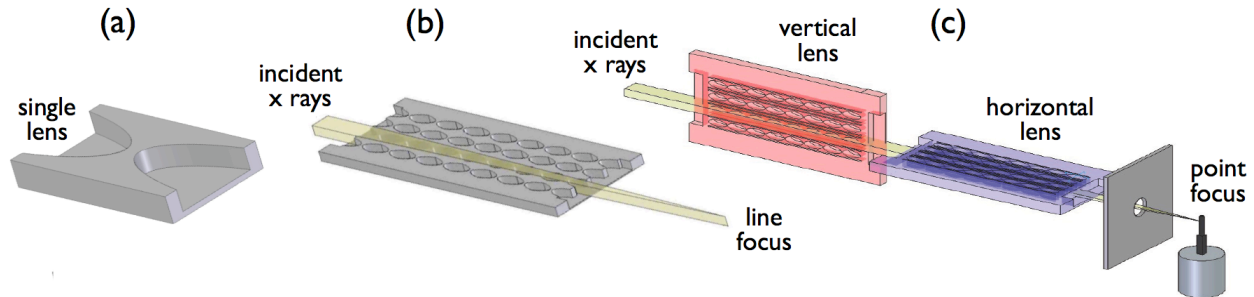


Figure 4.2: Schematic drawing of nanofocusing lenses (NFLs). (a) The concave parabolic lens profile is etched into the surface of a wafer by means of micro-structuring techniques. (b) An array of many single lenses makes up a whole NFL. Due to its cylindrical symmetric shape, a nanofocusing lens focuses only in one direction, forming a line focus. (c) In order to get a point focus, two lenses must be aligned in crossed geometry.

4.3 Nanofocusing Lenses (NFLs)

Compound parabolic refractive x-ray lenses are widely used in the synchrotron community for magnified imaging, for collimation of diverging beams and for generating micro-beams, but there are some restrictions with regard to the lateral resolution that can be achieved with these optics. Lateral resolution can be improved with a shorter focal distance leading to a larger demagnification of the source. As shown in section 4.5, the minimal focal distance of a compound refractive lens is given by $f_{min} = \sqrt{Rl/(2\delta)}$ and can be decreased with stronger curvatures and shorter single lenses. Unfortunately, the radius of curvature of compound parabolic refractive lenses is limited to about $50\ \mu\text{m}$, since the pressing technique of these lenses does not allow stronger curvatures. One possibility to make lenses with stronger curvatures is utilizing lithography techniques. Following this approach leads to micro-structured nanofocusing x-ray lenses (NFLs) [SKH⁺03, SKP⁺05b, Kur05, BFP⁺09, Boy10] as shown in Figure 4.2 and 4.3. Nanofocusing lenses were invented and first manufactured by our research group at the University of Aachen, before moving to the University of Dresden and were addressed in a PhD theses [Kur05]. At TU Dresden, the nanofocusing lenses were developed further in the context of a PhD theses [Boy10], making use of the results that were retrieved with the hard x-ray scanning microscope. Today, high quality aberration-free nanofocusing refractive x-ray lenses made of silicon are available [BFP⁺09, Boy10].

An NFL is a series of many identical single lenses arranged in a straight line, etched into a plane single crystal silicon wafer (Figure 4.2 and 4.3). The single lenses have a cylindrically symmetric parabolic shape with geometric apertures between $20\ \mu\text{m}$ and $40\ \mu\text{m}$ and with radii of curvatures in the range between $2\ \mu\text{m}$ and $15\ \mu\text{m}$. Due to its cylindrical symmetry, a nanofocusing lens focuses the incident x-ray beam in only one direction, leaving the beam size unchanged in the orthogonal direction. There are experiments (such as reflectometry), which make use of such line foci, but in most cases a focal spot that is small in the two transverse directions is required. With NFLs a point focus can be achieved connecting two NFLs in series, one NFL focusing in horizontal and the other NFL focusing in vertical

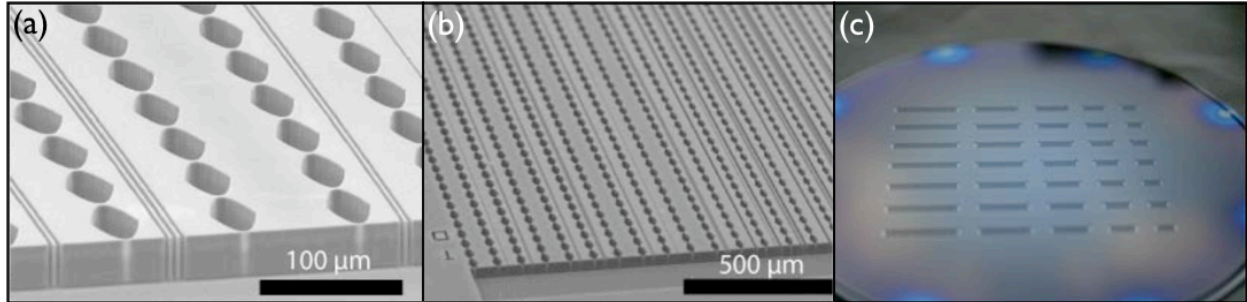


Figure 4.3: Nanofocusing lenses made of silicon. (a) and (b) show SEM images of nanofocusing lenses. Each nanofocusing lens is made of a chain of single lenses. The optical axis is given by the connecting line of the apices of the parabola. (c) shows a photograph of a 4 inch wafer with microstructured nanofocusing lenses. The lens structures are located within the array of blocks. The different lengths of the blocks are caused by nanofocusing lenses composed of different numbers of single lenses.

direction (confer Figure 4.2). Of course, the focal distances of both NFLs must be different, because they are displaced along the optical axis.

Although silicon is not the optimal lens material with respect to generating the smallest and brightest focus, most nanofocusing lenses are made of silicon, because well-optimized micro-structuring processes (e. g. Deep Reactive Ion Etching [LSFO99]) are available for this material. Other materials like boron or diamond potentially allow smaller focus sizes and higher flux, but their fabrication is not well established, yet. Much effort is invested developing nano-fabrication techniques for those materials. Recently, we successfully tested a nanofocusing x-ray lens made of diamond at the ESRF, giving rise to hope that high quality diamond lenses will be available in the near future [Boy10].

With the currently available nanofocusing lenses made of silicon, spot sizes around 50 nm vertically as well as horizontally have been generated with the hard x-ray scanning microscope [SKP⁺05b]. When published in 2005, this focus size set a kind of unofficial world record for hard x rays. But still, scientists would like to have even smaller x-ray spots in order to obtain better spatial resolutions in their experiments. The theoretical limit for the focus size of nanofocusing lenses is given by the Airy disk size d_t due to diffraction at the lens aperture. The numerical aperture of the available focusing x-ray optics is limited to the critical angle $\theta_c = \sqrt{2\delta}$, and this limit is also valid for compound parabolic refractive lenses and for nanofocusing lenses [BHT94, ZBP⁺00, BKv03, Suz04]. For this reason, the minimal focus size achievable with conventional x-ray optics is given by

$$B_t \geq d_t = 0.75 \frac{\lambda}{2NA} \geq 0.375 \frac{\lambda}{\sqrt{2\delta}}.$$

In the following section adiabatically focusing lenses (AFLs) are presented, which overcome this limit.

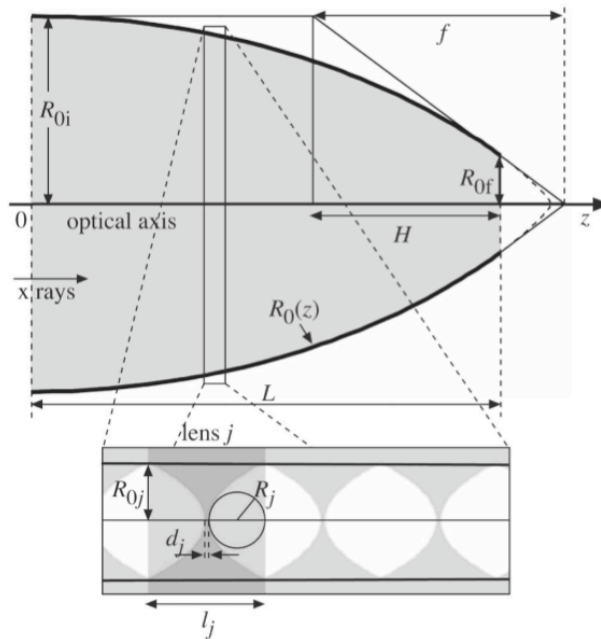


Figure 4.4: Schematic drawing of an adiabatically focusing x-ray lens. Similar with a nanofocusing lens the AFL is a stack of many single parabolic lenses etched into the surface of a flat substrate. But the aperture of the single lenses decreases along the optical path matching the diameter of the converging beam. (Published in [SL05], copyright 2005 by the American Physical Society.)

4.4 Adiabatically Focusing Lenses (AFLs)

As has been mentioned in the previous section, the theoretical limit for the spatial resolution of nanofocusing lenses is given by the limited numerical aperture $NA \leq \theta_c = \sqrt{2\delta}$. One way to enlarge the numerical aperture is to locally vary the radius of curvature along the optical axis in such a way, that the aperture of the single lenses gradually match the size of the converging beam. By this means the power of refraction is increased without compromising the effective aperture of the lens and thus the numerical aperture increases with the shorter focal distance. Because of the gradually adapted aperture and curvature of the single lenses, respectively, this kind of compound refractive x-ray lens is called adiabatically focusing lens (AFL). Figure 4.4 shows the schematic drawing of such an adiabatically focusing lens. Like an NFL the AFL is composed of many single parabolic lenses stacked behind each other. But while the NFL consists of a stack of identical single lenses, the shape of the single lenses inside an AFL changes as a function of position along the beam path. The single lens at the entry of the AFL has got the largest aperture and the largest radius of curvature. As the beam converges passing one lens after the other, the aperture of the single lenses and their radius of curvature decrease in the same manner as the diameter of the converging beam gets smaller. The refractive power per unit length grows and ends up in a theoretical singularity. The atomic structure of matter finally restricts the size of the smallest possible single lens, thereby limiting the refractive power per unit length. In [SL05] it is shown

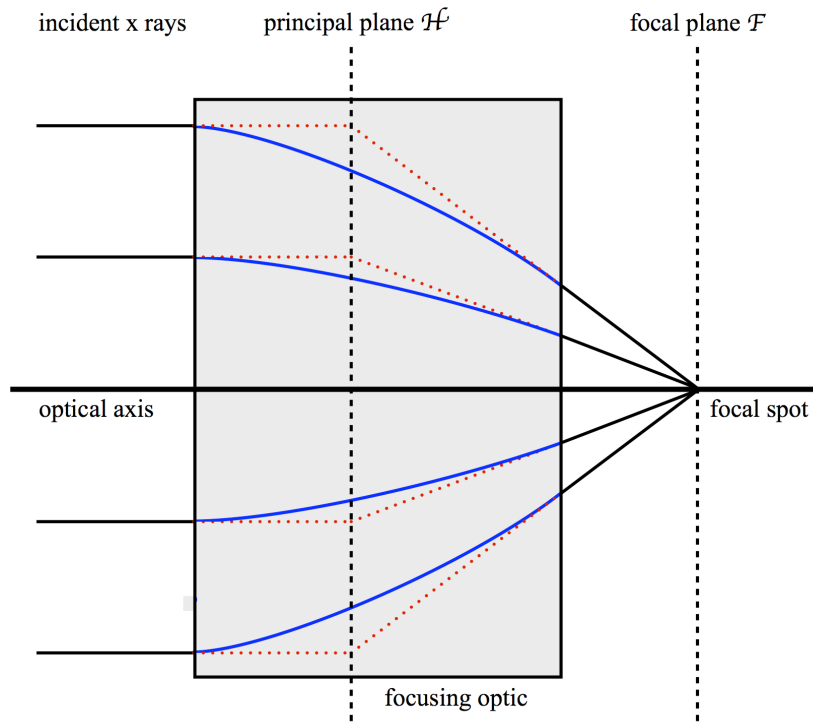


Figure 4.5: Principal and focal plane of a focusing optic. Parallel incident x rays are deviated from their straight path by the optical system. Behind the optic, the leaving rays intersect in a common point within the focal plane. The straight extensions of the incident and the leaving rays (red dotted lines) intersect within the principal plane. The actual paths are indicated by the blue curves.

that the numerical aperture of an AFL can be made larger than $\sqrt{2\delta}$ and that hard x rays can be focused down to about 2 nm using adiabatically focusing lenses made of diamond. The single lenses of an AFL must become very tiny in order to achieve such a small focus, and, therefore, AFLs have not been fabricated until today. There are plans to manufacture this kind of optics in the near future and to implement them in the hard x-ray scanning microscope.

4.5 Focal Distance

In an ideal focusing optical system, incident rays that are parallel to each other are deviated by the optical system, such that they have a common intersection point behind the optic. The distance of the intersection point from the optical axis depends on the angle θ of the incident rays with respect to the optical axis. The set of intersecting points defines the *focal plane* \mathcal{F} , which is perpendicular to the optical axis. The intersecting points of the extensions of the incident rays and of the deviated rays define the *principal plane* \mathcal{H} , which is at right angle to the optical axis and, therefore, parallel to the focal plane. The distance between the principal plane and the focal plane is called *focal distance*. The focal distance is an important

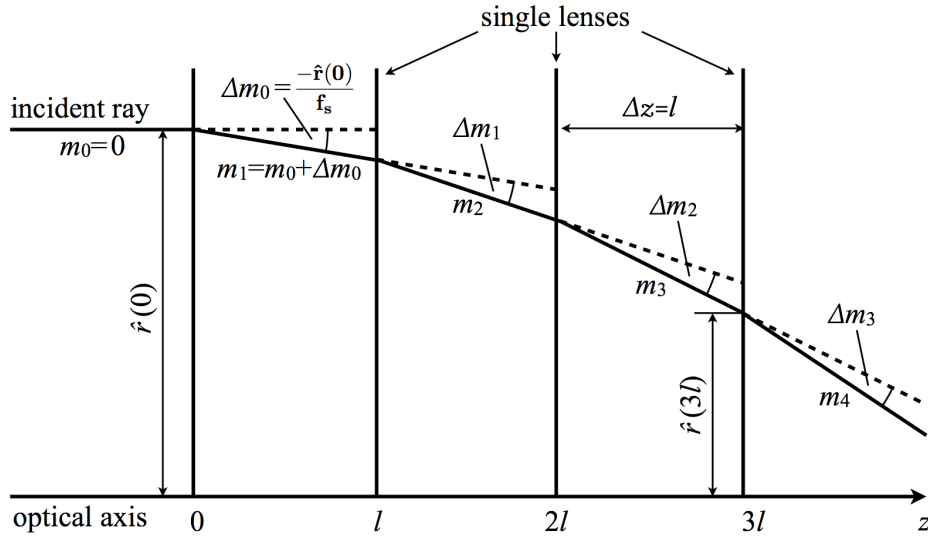


Figure 4.6: Path of a single ray as it passes through a compound parabolic refractive x-ray lens. At each single lens the slope of the ray is changed by $\Delta m(z) = -\hat{r}(z)/f_s$. The curvature of the approximated smooth path is given by $\Delta m/\Delta z$ with a constant $\Delta z = l$,

figure of merit of a lens, since it determines the position and the geometric magnification of an object when imaged by the lens. Beyond that, together with the effective aperture, the focal distance defines the numerical aperture, and thereby the maximal achievable spatial resolution. In the following paragraphs, the focal distance of a compound parabolic refractive x-ray lens (CRL or NFL) is derived.

Single thin lens

A focusing lens is called a *thin lens*, if its length l along the optical axis is short compared with its focal distance f . Since refraction is very weak for hard x rays, each single lens of a compound parabolic refractive x-ray lens or of a nanofocusing x-ray lens as used in the hard x-ray scanning microscope is thin in this sense. For a single thin lens with radius of curvature R and refractive index decrement δ the lens maker's equation allows to calculate the focal distance

$$f_s = \frac{R}{2\delta}. \quad (4.1)$$

The factor 2 in the denominator is due to the two refractive surfaces at both sides of the lens, each contributing to the refractive power of the single lens.

Compound lens

A compound lens consists of a number of single thin lenses. As long as the length L of the compound lens is small enough compared with the focal distance ($L \ll f$), the refractive power of the compound lens can be approximated by the sum of the refractive power values

of the individual lenses

$$\frac{1}{f_0} = \sum_{i=1}^N \frac{1}{f_{s,i}}.$$

CRLs and NFLs are composed of N identical single lenses with length l and focal distance f_s . If the CRL or NFL is short enough ($L = Nl \ll f$), the focal distance of such a CRL or NFL is given by

$$f_0 = \left[\sum_{i=1}^N \frac{1}{f_{s,i}} \right]^{-1} = \left[N \frac{1}{f_s} \right]^{-1} = \frac{f_s}{N} \stackrel{(4.1)}{=} \frac{R}{2N\delta}. \quad (4.2)$$

The thin lens approximation makes use of the simplifying assumption that — due to the shortness of the lens — the deviation of the rays inside the lens is negligible. But CRLs and NFLs are mostly applied to situations, which require short focal distances, and then the number N of individual single lenses is large, hence the thin lens approximation becomes too vague. For this reason, we derive an expression that allows to calculate the focal distance of a long compound parabolic refractive x-ray lens (CRL or NFL).

Consider the path $\hat{r}(z)$ of a single ray, as it passes through a compound parabolic refractive x-ray lens. The situation is illustrated in Figure 4.6. With $\hat{r}(z)$ we denote the distance of the ray from the optical axis at a position z behind the entrance aperture of the compound lens. The incident ray is a straight line with slope $m_0 = 0$. When it passes the first single lens, the slope of the line is changed by the refractive power of the single lens by a value

$$\Delta m(z) = \frac{-\hat{r}(z)}{f_s}. \quad (4.3)$$

The negative sign indicates, that the ray is deviated towards the direction of the optical axis. The deviated ray propagates to the next single lens, is bent by that lens, and so on. This procedure can be described with the transfer matrix formalism and leads to the calculation of the N th power of a 2×2 matrix. The lengthy calculus has been carried out in [PV98] and involves Tchebishev polynomials of the second kind. A more intuitive and easy way to treat the compound lens can be applied, if the distance l between two single lenses is small compared with the length L of the compound lens, i. e., if N is large enough. In that case, the path $\hat{r}(z)$ of straight lines within the compound lens can be approximated by a two times differentiable function $r(z)$, the curvature C of which is given by the slope change $\Delta m(z)$ of the straight lines, induced by the refractive power of each of the single lenses. The bending is done within the distance $\Delta z(z) = l$ between two single lenses and, therefore, the curvature of the bending is given by

$$C(z) = \frac{\Delta m(z)}{\Delta z(z)} = \frac{\Delta m(z)}{l} \stackrel{(4.3)}{=} \frac{-\hat{r}(z)}{f_s l},$$

which we identify with the second order derivative of the curve in demand

$$\frac{d^2}{dz^2} r(z) = C(z) = \frac{-r(z)}{f_s l}, \quad 0 \leq z \leq L.$$

With the definition

$$\omega = \sqrt{\frac{1}{f_s l}} \quad (4.4)$$

the approximated path through the compound lens is described by the harmonic differential equation

$$\frac{d^2}{dz^2} r(z) = -\omega^2 r(z). \quad (4.5)$$

With the boundary conditions $r(0) = r_0$ and $r'(0) = 0$ (parallel incident beam with distance r_0 away from the optical axis), the solution within the lens is a cosine with frequency ω , and the complete path of the ray is given as

$$r(z) = r_0 \cdot \begin{cases} 1 & : z \leq 0 \\ \cos(\omega z) & : 0 \leq z \leq L \\ b + mz & : L \leq z \end{cases} \quad (4.6)$$

with

$$\begin{aligned} b &= \cos(\omega L) + \omega L \sin(\omega L), \\ m &= -\omega \sin(\omega L). \end{aligned}$$

The product ωL characterizes the compound refractive lens and is called *lens parameter*. The positions z_H and z_F of the principal and the focal planes \mathcal{H} and \mathcal{F} are given by $b + m z_H = 1$ and $b + m z_F = 0$, respectively, and thus

$$z_H = L + \frac{\cot(\omega L)}{\omega} - \frac{1}{\omega \sin(\omega L)}, \quad (4.7)$$

$$z_F = L + \frac{\cot(\omega L)}{\omega}. \quad (4.8)$$

The focal distance is defined as the gap between \mathcal{H} and \mathcal{F} , $f = z_F - z_H$ and, therefore, it follows

$$f = \frac{1}{\omega \sin(\omega L)}. \quad (4.9)$$

The displacement H of the principal plane is defined as the shift of \mathcal{H} with respect to the center of the lens, $H = z_H - L/2$, and thus it reads

$$H = \frac{1}{2}L + \frac{\cot(\omega L)}{\omega} - \frac{1}{\omega \sin(\omega L)}. \quad (4.10)$$

The *working distance* WD is the distance of the focal plane from the output aperture of the lens, $WD = z_F - L$, and hence

$$WD = \frac{\cot(\omega L)}{\omega}. \quad (4.11)$$

Equation (4.6) indicates that the converging rays intersect the optical axis within the compound lens, if $\omega L \geq \pi/2$, i. e., if the lens becomes longer than the critical length

$$L_c = \frac{\pi}{2\omega}. \quad (4.12)$$

This, at the the same time, defines the minimal possible focal distance of a compound refractive lens

$$f_{min} \stackrel{(4.9)}{=} \frac{1}{\omega \sin(\omega L_c)} \stackrel{(4.12)}{=} \frac{1}{\omega \sin(\frac{1}{2}\pi)} = \frac{1}{\omega} \stackrel{(4.4)}{=} \sqrt{f_s l} \stackrel{(4.1)}{=} \sqrt{\frac{Rl}{2\delta}}. \quad (4.13)$$

Expression (4.13) demonstrates the necessity to decrease the product Rl in order to get a short focal distance and hence a small focal spot. This concept is followed when introducing nanofocusing lenses with strong curvatures.

4.6 Transverse Focus Size

In the hard x-ray scanning microscope, nanofocusing lenses generate a demagnified image of the x-ray source, in this way creating a small focal spot. There are three major contributions, which determine the lateral focus size, namely the geometric image of the source, the diffraction pattern due to the finite lens aperture, and aberrations.

Neglecting diffraction and aberrations, the geometric image size b_g of an extended source with full width at half maximum size S imaged by a lens with focal distance f placed a distance L_1 away from the source reads

$$b_g = \frac{L_2}{L_1} S = \frac{f}{L_1 - f} S. \quad (4.14)$$

The image distance L_2 is defined by $1/f = 1/L_1 + 1/L_2$. A small geometric image requires a small source and a large demagnification, i. e., a long distance from the source and a short focal distance.

The finite effective aperture D_{eff} of the focusing lens gives rise to diffraction. The image of an ideal point source generated by an aberration-free lens would be a diffraction pattern with a full width at half maximum

$$d_t = \zeta \frac{\lambda}{2NA} = \zeta \frac{\lambda L_2}{D_{eff}}. \quad (4.15)$$

The constant ζ is of order 1, and its exact value depends on the transmission function of the lens. The effective aperture of a refractive lens with short focal distance is dominated by attenuation and, therefore, its diffraction pattern is a Gaussian Airy disk with $\zeta = 2\sqrt{2\ln 2}/\pi \approx 0.75$. The diffraction limit d_t defines the resolution of the focusing lens and can be reduced by means of a large numerical aperture NA .

The nanofocusing lens may have some aberrations from the ideal shape, and there might occur chromatic aberration. Neglecting diffraction, but still considering aberrations, a point source is imaged into an aberration pattern with a lateral full width at half maximum size d_a .

The overall intensity distribution in the focal plane is the geometric image of the source convolved with the diffraction pattern and the aberration pattern. The undulator source of a third generation synchrotron radiation facility can be approximated with a Gaussian intensity distribution, and the diffraction pattern of a nanofocusing lens is a Gaussian Airy disk with size d_t .² If the aberration pattern is caused by a number of stochastically independent contributions, the aberration pattern shows a Gaussian intensity distribution. In the end, we have a convolution of three Gauss functions, the result of which is again a Gauss. The width of the resulting Gauss function is given by the quadratic sum of the widths of the original Gauss functions, and the overall lateral focal size is computed by

$$B_t = \sqrt{b_g^2 + d_t^2 + d_a^2}.$$

For further discussion in this chapter aberrations are neglected, i. e., $d_a = 0$ and then

$$B_t = \sqrt{b_g^2 + d_t^2}. \quad (4.16)$$

This expression refers to the width of the intensity distribution in the focal plane. In the next section the transverse coherence properties of the focus are discussed, and for this, one needs the width of the amplitude field rather than the width of the intensity distribution. Since the intensity is proportional to the square of the field amplitude, the transverse width of the amplitude field is obtained by

$$B_{amp} = \sqrt{2b_g^2 + 2d_t^2}. \quad (4.17)$$

The ratio of the Airy disk size and the geometric image size is an important quantity to characterize the lateral coherence in the focus. Thus we define the *focus parameter*

$$\Gamma = \frac{d_t}{b_g}. \quad (4.18)$$

With this definition equations (4.16) and (4.17) become

$$B_t = b_g \sqrt{1 + \Gamma^2} = d_t \sqrt{1 + \Gamma^{-2}} \quad (4.19)$$

$$B_{amp} = b_g \sqrt{2 + 2\Gamma^2} = d_t \sqrt{2 + 2\Gamma^{-2}} \quad (4.20)$$

A focal spot with $\Gamma \geq 1$ is called *diffraction limited*. In section 4.12 it is shown, that the lateral coherence length of a diffraction limited focus always exceeds the lateral beam size.

²This is valid, if the effective aperture of the lens is dominated by attenuation rather than by the geometric lens aperture.

4.7 Beam Caustic

The x-ray intensity distribution around the focal spot is called *caustic* and is of great importance for hard x-ray scanning microscopy, because it defines the illuminated volume of the specimen. The lateral focus size, as treated in the previous section, is only one but essential parameter of the x-ray beam. While the x rays propagate from the lens to the image plane, the lateral size of the intensity distribution decreases continuously, i. e., the beam converges on its way from the lens to the image plane. Beyond the image plane, the diverging beam widens again. The caustic has been calculated for compound parabolic refractive x-ray lenses [LST⁺99]. The result is a Gauss function

$$I(x, y, z) = I_0(z) \exp\left(\frac{-x^2}{2\sigma_h(z)^2} + \frac{-y^2}{2\sigma_v(z)^2}\right), \quad (4.21)$$

and the horizontal and vertical full width at half maximum sizes read

$$B_t(z) = 2\sqrt{2 \ln 2} \sigma_{h,v}(z) = \sqrt{(b_g^2 + d_t^2) \left(1 + \frac{z}{L_2}\right)^2 + 0.5 \ln 2 D_{eff}^2 \left(\frac{z}{L_2}\right)^2}. \quad (4.22)$$

L_1 and L_2 denote the source-to-lens and the lens-to-image-plane distances, and b_g and d_t are the geometric image size and the diffraction limit, respectively. z measures the position along the optical axis with the image plane as the origin. As expected, $B_t(0)$ recovers B_t from equation (4.16), which describes the situation in the image plane. The caustic is mirror symmetric with respect to the plane $z = z_0$ with

$$z_0 = \frac{-B_t^2}{B_t^2 + 0.5 \ln 2 D_{eff}^2} L_2.$$

It is interesting to note, that the caustic has its minimum at $z = z_0$, which is not within the image plane $z = 0$, but is slightly shifted by z_0 towards the lens, and the minimum of the beam is

$$B_t(z_0) = \sqrt{\frac{0.5 \ln 2 B_t^2 D_{eff}^2}{B_t^2 + 0.5 \ln 2 D_{eff}^2}}$$

In most practical situations, the effective aperture of the lens is much larger than B_t and, therefore, with very good approximation, the caustic is described by

$$B_t(z) = \sqrt{B_t^2 + 0.5 \ln 2 D_{eff}^2 \left(\frac{z}{L_2}\right)^2}, \quad (4.23)$$

which is mirror symmetric with respect to the plane $z = 0$.

4.8 Depth of Focus

Along both sides of the image plane, the transverse size of the x-ray beam widens continuously. The area around the focus within which the beam size does not increase significantly defines the longitudinal focus size B_l , which is called *depth of focus*

$$B_t(0 - B_l/2) = B_t(0 + B_l/2) = \sqrt{2} B_t(0). \quad (4.24)$$

Various experimental methods have certain requirements on the depth of focus. In scanning fluorescence microscopy, for example, the depth of focus determines the maximal sample thickness that can be scanned with the microbeam, and in fluorescence micro-tomography, the investigated sample must be smaller than the depth of focus. In this section the longitudinal focus size of compound parabolic refractive x-ray lenses is discussed. We insert equation (4.23) into (4.24) and obtain

$$B_l = \sqrt{\frac{2}{\ln 2}} \frac{B_t}{NA} = \frac{2}{\pi} \sqrt{1 + \Gamma^{-2}} \frac{\lambda}{(NA)^2}, \quad (4.25)$$

where $NA = 0.5D_{eff}/L_2$ denotes the numerical aperture and Γ is the ratio of the geometrical image size and the diffraction limit as given in equation (4.18). For refractive x-rays lenses the numerical aperture is of order $10^{-3} - 10^{-4}$ and, therefore, the depth of focus is a factor $10^3 - 10^4$ larger than the lateral focus size. In the hard x-ray scanning microscope, the lateral focus size is typically in the range 50 nm – 100 nm, whereas the longitudinal focus size is in the range 50 μ m – 100 μ m.

4.9 Beam Divergence

In addition to the minimal transverse size of the beam and its depth of focus, the behavior of the beam far away from the image plane is of special importance. In scattering experiments, for instance, the divergence of the primary (unscattered) beam defines the minimal observable scattering angle. Especially in small angle x-ray scattering, a small diverging angle of the primary beam is required. The divergence of the beam, generated by a compound parabolic refractive lens or a nanofocusing lens can be obtained by evaluation of equation (4.22) for a large distance z behind the image plane:

$$B_t(z) = \sqrt{B_t^2 \left(1 + \frac{z}{L_2}\right)^2 + 0.5 \ln 2 D_{eff}^2 \left(\frac{z}{L_2}\right)^2} \xrightarrow{z \gg L_2} \frac{z}{L_2} \sqrt{B_t^2 + 0.5 \ln 2 D_{eff}^2} = \theta_d z.$$

Obviously, far away from the image plane the caustic becomes a cone with a diverging angle

$$\theta_d = \frac{\sqrt{B_t^2 + 0.5 \ln 2 D_{eff}^2}}{L_2}.$$

The hard x-ray scanning microscope generates focal spots that are small compared to the lens aperture ($B_t \ll D_{eff}$), and for this reason, the diverging angle is dominated by the aperture of the lens and can be approximated with

$$\theta_d \approx \frac{\sqrt{0.5 \ln 2} D_{eff}}{L_2} = \sqrt{2 \ln 2} NA \approx NA. \quad (4.26)$$

The nanofocusing lenses that are installed in the hard x-ray scanning microscope achieve numerical apertures of order 10^{-4} , generating microbeams with a divergence angle in the range of several hundreds of microradians.

4.10 Chromaticity

The refractive index decrement δ and hence the refractive power of CRLs and NFLs depends on the photon energy. A small deviation ΔE of the energy changes the position z_F of the focal plane by a small value Δz_F . At the same time, the principal plane is also displaced by a finite amount Δz_H , and thus the change of the focal distance is different from the change of the focus position. In this paragraph we calculate Δz_F , Δf , and Δz_H in dependence of the energy change ΔE .

$$\begin{aligned} \frac{dz_F}{dE} &\stackrel{(4.8)}{=} \frac{d}{dE} \left(L + \frac{\cot \omega L}{\omega} \right) \\ &= \frac{d}{d\omega} \left(\frac{\cot \omega L}{\omega} \right) \frac{d\omega}{df_s} \frac{df_s}{dE} \\ &\stackrel{(4.4)}{=} \left(\frac{-\cot \omega L}{\omega^2} + \frac{-L}{\omega \sin^2 \omega L} \right) \left(\frac{-\omega}{2f_s} \right) \frac{df_s}{dE} \\ &= \left(\frac{\cot \omega L}{\omega} + \frac{L}{\sin^2 \omega L} \right) \left(\frac{1}{2f_s} \frac{df_s}{dE} \right) \\ &\stackrel{(4.9)}{=} \left(\cos \omega L + \frac{\omega L}{\sin(\omega L)} \right) \left(\frac{1}{2f_s} \frac{df_s}{dE} \right) f. \end{aligned} \quad (4.27)$$

In general, refractive x-ray lenses are applied at photon energies far away from any absorption edges of the refracting lens material, and for this reason, to a good approximation, we can assume $\delta \propto E^{-2}$ and $f_s \propto E^2$. With this, one obtains for the derivative

$$\frac{df_s}{dE} = 2 \frac{f_s}{E},$$

and equation (4.27) becomes

$$\frac{dz_F}{dE} = \left(\cos \omega L + \frac{\omega L}{\sin(\omega L)} \right) f \frac{1}{E},$$

or

$$\Delta z_F = \alpha_F f \frac{\Delta E}{E}$$

with the *chromaticity parameter*

$$\alpha_F = \cos \omega L + \frac{\omega L}{\sin \omega L} \quad \text{and} \quad 2 \geq \alpha_F \geq \frac{1}{2}\pi.$$

The same calculation can be applied to f and z_H with the result

$$\Delta z_F = \alpha_F f \Delta E/E, \quad (4.28)$$

$$\Delta f = \alpha_f f \Delta E/E, \quad (4.29)$$

$$\Delta z_H = \alpha_H f \Delta E/E \quad (4.30)$$

and the chromaticity parameters

$$\alpha_F = \cos \omega L + \frac{\omega L}{\sin \omega L}, \quad (4.31)$$

$$\alpha_f = 1 + \omega L \cot \omega L, \quad (4.32)$$

$$\alpha_H = \alpha_F - \alpha_f. \quad (4.33)$$

Figure 4.7 illustrates the chromaticity parameters $\alpha_{F,f,H}$ as functions of the lens parameter ωL . For a large number of single lenses (large lens parameter), the shift of the focal plane is significantly larger than the change of the focal distance. If the effect of chromaticity on the resulting focus size has to be calculated, the relevant quantity is the shift of focal plane, rather than the change of the focal distance.

4.11 Transmission and Cross Section

Different from visible light optics, attenuation is significant for refractive x-ray lenses and has to be considered, especially for lenses with short focal distances. The transmission T_p of a lens describes the fraction of incident photons, which pass through the lens and contribute to the image formed by the lens, if the lens is illuminated homogeneously by an x-ray beam. For compound parabolic refractive x-ray lenses, the transmission depends on the geometry of the single lenses (geometric half aperture R_0 , radius of curvature R), the number N of single lenses, the gap d between the single lenses, the attenuation coefficient μ , the refractive decrement δ , the surface roughness σ (given as rms value), and on the wave number k of the x rays, and is described by

$$T_p = \exp(-\mu N d) \frac{1 - \exp(-2a_p)}{2a_p}, \quad a_p = \frac{\mu N R_0^2}{2R} + \frac{N \delta^2 k^2 \sigma^2 R_0^2}{R^2}. \quad (4.34)$$

The first term $\mu N R_0^2 / (2R)$ describes attenuation in the material, and the second term $N \delta^2 k^2 \sigma^2 R_0^2 / R^2$ accounts for surface roughness. In contrast to mirror optics, the influence

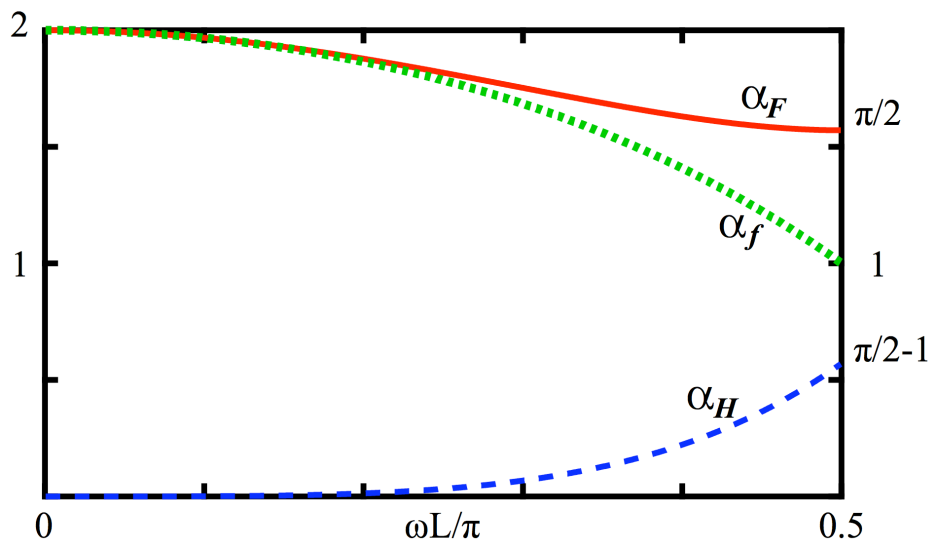


Figure 4.7: Chromaticity parameter as a function of the lens parameter for a compound parabolic refractive x-ray lens (CRL or NFL).

of surface roughness is much less significant for refractive lenses, because the momentum transfer is much lower for refraction than for reflection. In case of compound parabolic refractive x-ray lenses and also for nanofocusing x-rays lenses, transmission is dominated by attenuation within the lens, and surface roughness can be neglected.

For refractive lenses with short focal distances, a_p becomes large, and the term $\exp(-2a_p)$ can be neglected. Then the transmission becomes

$$T_p = \frac{R}{\mu N R_0^2}. \quad (4.35)$$

It is convenient to define the cross section σ_p of a lens as the quantity, which relates the homogeneous flux density I of an incident x-ray beam with the transmitted photon flux F behind the lens

$$F = \sigma_p I. \quad (4.36)$$

For a lens with transmission T_p and with an aperture area A , the cross section can be evaluated as

$$\sigma_p = T_p A. \quad (4.37)$$

4.12 Transverse Coherence

Experiments like coherent x-ray diffraction imaging or ptychography need coherent illumination. In this section, the transverse coherence length in the focal plane is related to the transverse coherence length in the aperture plane of the nanofocusing lens. For this, the mutual intensity function and the degree of spatial coherence are defined and propagated

through the microscope, starting at the source and ending in the focal plane. The results from this section are required to explain the basic concepts of the two-stage focusing scheme employed in the hard x-ray scanning microscope.

4.12.1 Mutual Intensity Function

Coherence is a measure of how much the field amplitudes $V(\mathbf{r}_1, t)$ and $V(\mathbf{r}_2, t + \tau)$ at two positions \mathbf{r}_1 and \mathbf{r}_2 are correlated, and hence a measure of the visibility of interference or speckle patterns. If the connecting line $\Delta\mathbf{r} = \mathbf{r}_2 - \mathbf{r}_1$ of the two positions is orthogonal to the direction of propagation, and if $\tau = 0$, one speaks of *transverse coherence*. For a quantitative treatment the complex *mutual intensity function*

$$J(\mathbf{r}_1, \mathbf{r}_2) = \langle V(\mathbf{r}_1, t) V^*(\mathbf{r}_2, t) \rangle_t \quad (4.38)$$

and the complex *degree of spatial coherence*

$$j(\mathbf{r}_1, \mathbf{r}_2) = \frac{J(\mathbf{r}_1, \mathbf{r}_2)}{\sqrt{J(\mathbf{r}_1, \mathbf{r}_1)J(\mathbf{r}_2, \mathbf{r}_2)}} \quad (4.39)$$

are defined, wherein $\langle \dots \rangle_t$ denotes the detector time average.

4.12.2 Free Propagation of Mutual Intensity

In chapter 2.1.4 the Fresnel-Kirchhoff propagation of a complex amplitude field that describes a stationary x-ray beam is derived. In analogy to that, the propagation of the mutual intensity function can be treated, applying the Fresnel-Kirchhoff diffraction formula. If the complex mutual intensity function $J_0(\mathbf{r}'_1, \mathbf{r}'_2)$ is known within a plane S_0 transverse to the beam direction, the mutual intensity function $J_L(\mathbf{r}_1, \mathbf{r}_2)$ in a plane S_L at a distance L behind the first plane can be calculated via [BW99]

$$J_L(x_1, y_1, x_2, y_2) = \iint_{S_0} dx'_1 dy'_1 \iint_{S_0} dx'_2 dy'_2 J_0(x'_1, y'_1, x'_2, y'_2) K_L(x_1 - x'_1, y_1 - y'_1) \cdot K_L^*(x_2 - x'_2, y_2 - y'_2). \quad (4.40)$$

K_L is the propagator kernel as defined by (2.31) and the asterisk denotes the complex conjugate. Expression (4.40) is known as *van Cittert-Zernike theorem*. In the literature, it is often applied in a specialized manner, assuming that the originating plane S_0 contains the chaotic (uncorrelated) source and that the second plane is far away from the source in the Fraunhofer regime. Then, expression (4.40) simplifies to a Fourier transform of the intensity distribution in the source plane. In contrast to that, the general form (4.40) describes the propagation of *any* mutual intensity function, i. e., J_0 might refer to a partially or fully coherent field. This is useful, for example, to calculate the spatial coherence in the focal plane of a focusing lens, for which the (partially coherent) mutual intensity function has to be propagated from behind the lens into the focal plane.

We are going to use the van Cittert-Zernike theorem to calculate the degree of spatial coherence at a certain distance behind a chaotic Gaussian source. The mutual intensity function of a chaotic Gaussian source with rms size $\sigma_{S,x} \times \sigma_{S,y}$ is described by

$$J_0(x_1, y_1, x_2, y_2) = J_0 \exp\left(-\frac{x_1^2 + x_2^2}{4(\sigma_{S,x})^2} - \frac{y_1^2 + y_2^2}{4(\sigma_{S,y})^2}\right) \delta(x_1 - x_2)\delta(y_1 - y_2). \quad (4.41)$$

If one inserts (4.41) into (4.40), the mutual intensity function, and — considering (4.39) — the degree of spatial coherence function at distance L behind the source can be calculated, with the result

$$j_L(x_1, y_1, x_2, y_2) = \exp\left(-\frac{(x_1 - x_2)^2}{2(\sigma_{lt,x})^2} - \frac{(y_1 - y_2)^2}{2(\sigma_{lt,y})^2}\right) \quad (4.42)$$

and

$$\sigma_{lt,\{x,y\}} = \frac{1}{2\pi} \frac{\lambda L}{\sigma_{S,\{x,y\}}}, \quad (4.43)$$

from which the full width at half maximum transverse coherence lengths are derived as

$$l_{t,\{h,v\}} = \frac{4 \ln 2}{\pi} \frac{\lambda L}{S_{\{h,v\}}} \quad (4.44)$$

with $S_{\{h,v\}}$ denoting the full width at half maximum source size along the horizontal and the vertical axes.

4.12.3 Mutual Intensity In The Focal Plane

In the last section, the mutual intensity function was propagated from a chaotic Gaussian source into a distant plane with the resulting transverse coherence length given with equation (4.44). In order to retrieve the transverse coherence in the focal plane, the mutual intensity function has to be propagated from the source to the nanofocusing lens, then it has to be transmitted through the nanofocusing lens and, finally, it must be propagated from behind the lens into the focal plane. Transmission is treated in section 2.2.1. According (2.34), the complex wavefield behind an object is described by the multiplication of the wavefield before the object with the object's complex transmission function (2.35). In analogy to that, the mutual intensity function is propagated through an object in the following way

$$J_0(x_1, y_1, x_2, y_2) = J_0(x_1, y_1, x_2, y_2) T(x_1, y_1) T^*(x_2, y_2) \quad (4.45)$$

Starting with a chaotic Gaussian source, the mutual intensity function J_L in the lens aperture plane is given by (4.40). Transmitting J_L through the lens and then propagating to the focal plane [distance $b = Lf/(L-f)$] yields the mutual intensity function in the focus

$$J_f(x_1, y_1, x_2, y_2) = \int\int_{\text{lens}} dx'_1 dy'_1 \int\int_{\text{lens}} dx'_2 dy'_2 J_L(x'_1, y'_1, x'_2, y'_2) T(x'_1, y'_1) T^*(x'_2, y'_2) \cdot K_b(x_1 - x'_1, y_1 - y'_1) K_b^*(x_2 - x'_2, y_2 - y'_2). \quad (4.46)$$

Evaluating the integral, the mutual intensity function in the focal plane becomes

$$J_f(x_1, y_1, x_2, y_2) = J_0 \exp\left(-\frac{x_1^2 + x_2^2}{2(\sigma_{B_{\text{ampl},x}})^2} - \frac{y_1^2 + y_2^2}{2(\sigma_{B_{\text{ampl},y}})^2}\right) \cdot \exp\left(-\frac{(x_1 - x_2)^2}{2(\sigma_{lt,x})^2} - \frac{(y_1 - y_2)^2}{2(\sigma_{lt,y})^2}\right) \quad (4.47)$$

with $\sigma_{B_{\text{ampl}}}$ and σ_{lt} describing the rms beam size and the rms transverse coherence length in the focal plane, respectively. The beam size turns out to be consistent with equation (4.17) from section 4.6. From the mutual intensity function, the degree of spatial coherence can be computed

$$j_f(x_1, y_1, x_2, y_2) \stackrel{(4.39)}{=} \exp\left(-\frac{(x_1 - x_2)^2}{2(\sigma_{lt,x})^2} - \frac{(y_1 - y_2)^2}{2(\sigma_{lt,y})^2}\right). \quad (4.48)$$

Finally, the full width at half maximum lateral coherence length in the focal plane becomes

$$l_{t,f} = 2\sqrt{2 \ln 2} \sigma_{lt} = 2\frac{d_t}{b_g} \sqrt{b_g^2 + d_t^2} = 2d_t \sqrt{1 + \Gamma^2}, \quad (4.49)$$

with b_g and d_t denoting the geometric image size and the Airy disk size as introduced by (4.14) and (4.15) in section 4.6.

4.12.4 Diffraction Limited Focus

Many experiments need coherent illumination, i. e., they require a transverse coherence length that exceeds the transverse dimension of the beam. From (4.20) and (4.49) we derive

$$\frac{l_{t,f}}{B_{\text{ampl}}} = \sqrt{2} \frac{d_t}{b_g} = \sqrt{2} \Gamma. \quad (4.50)$$

This expression relates the transverse coherence length in the focal plane with the ratio of the Airy disk size and the geometric image size, and shows, that the transverse coherence length of a diffraction limited focus is always larger than the lateral focus size.

Due to equation (4.44) the lateral coherence length $l_{t,i}$ of the incident x-rays in the aperture plane of the nanofocusing lens is determined by the source size, the wavelength and the source-to-lens distance via

$$l_{t,i} = \chi \frac{\lambda L_1}{S}, \quad (4.51)$$

with a constant factor χ in the order of 1. Its exact value depends on the intensity distribution of the source, and turn out to be $4 \ln 2 / \pi$, if the source is chaotic and has a Gaussian intensity distribution. Now we are going to connect the transverse coherence length $l_{t,i}$ of the incident x-rays in the aperture plane with the diffraction limit of the lens.

$$\begin{aligned} \Gamma &= \frac{d_t}{b_g} = \frac{\zeta \frac{\lambda L_2}{D_{\text{eff}}}}{\frac{L_2}{L_1} S} = \zeta \frac{\lambda L_1}{D_{\text{eff}} S} \\ &= \frac{\zeta}{\chi} \frac{l_{t,i}}{D_{\text{eff}}} = \frac{1}{\sqrt{2 \ln 2}} \frac{l_{t,i}}{D_{\text{eff}}} \approx 0.85 \frac{l_{t,i}}{D_{\text{eff}}}. \end{aligned} \quad (4.52)$$

Inserting this equation into (4.50) connects the lateral coherence length in the focal plane with the lateral coherence length in the aperture plane:

$$\frac{l_{t,f}}{B_{ampl}} = \frac{\zeta}{\chi} \sqrt{2} \frac{l_{t,i}}{D_{eff}} = \frac{1}{\sqrt{\ln 2}} \frac{l_{t,i}}{D_{eff}} \approx 1.20 \frac{l_{t,i}}{D_{eff}}. \quad (4.53)$$

As an important result of this section it can be summarized, that a diffraction limited focus guaranties a transverse coherence length in the focal spot, which is larger than the focus size, and that a diffraction limited focus is achieved with a lateral coherence length in the lens aperture plane, which is as large as the effective lens aperture or larger. The reversion is also valid. As long as the lateral coherence length in the lens aperture plane is smaller than the effective lens aperture, the focus is not diffraction limited, and thus the lateral coherence length in the focal spot is smaller than the spot size (width of the field amplitude distribution in the focal plane). A consequence of this is that the available coherent photon flux in a beam cannot be increased by a focusing lens.

4.13 Coherent Flux

Aside from the focus size, the photon flux is also a very important property of a focal spot. The flux F in a beam is defined as the number of photons n_{ph} passing a given cross section area A during a small time interval Δt divided by this time interval

$$F_A = \frac{n_{ph}}{\Delta t}.$$

In contrast to the flux density $I = F_A/A$, the photon flux can be increased by a larger cross section area.³ A larger sample, for example, is exposed by larger photon flux. But there are experimental techniques, which require the specimen to be coherently illuminated, such as coherent x-ray diffraction imaging or x-ray ptychography. For those methods, the lateral dimensions of the cross section area of the illuminated specimen must not exceed the lateral coherence length l_t of the beam and, therefore, the available flux is limited by the transverse coherence length. For this purpose one defines the *coherent flux* F_c as the photon flux collected by a cross section with lateral dimensions smaller than the lateral coherence length.

Let us calculate the largest possible coherent flux, which can be collected by an aperture located at a distance z behind the x-ray source with brilliance \mathcal{B} . The horizontal and vertical rms source size shall be σ_h and σ_v , respectively. The aperture has lateral dimensions D_h and D_v and spans a solid angle of D_h/z D_v/z . If $\Delta E/E$ denotes the energy bandwidth of the

³As long as the cross section does not exceed the lateral beam dimensions.

quasi monochromatic source, the coherent photon flux is calculated as

$$\begin{aligned}
 F_c &= \mathcal{B} \sigma_h \sigma_v \frac{D_h D_v}{z^2 (2\sqrt{2 \ln 2})^2} \frac{\Delta E}{E} \\
 &= \mathcal{B} \frac{S_h S_v}{(2\sqrt{2 \ln 2})^4} \frac{D_h D_v}{z^2} \frac{\Delta E}{E} \\
 &\stackrel{(4.51)}{=} \mathcal{B} \frac{\chi^2}{(2\sqrt{2 \ln 2})^4} \lambda^2 \frac{D_h}{l_{t,h}} \frac{D_v}{l_{t,v}} \frac{\Delta E}{E}
 \end{aligned}$$

To gain the coherent flux, the lateral dimensions of the aperture must not exceed the lateral coherence length, i. e., we demand $D_h \leq l_{t,h}$ and $D_v \leq l_{t,v}$ and, therefore, the coherent flux is limited by

$$F_c \leq F_{c,max}$$

with

$$F_{c,max} = \frac{\chi^2}{(2\sqrt{2 \ln 2})^4} \mathcal{B} \lambda^2 \frac{\Delta E}{E}. \quad (4.54)$$

Obviously, the maximal available coherent flux of a free propagated beam does not depend on the distance z from the source. Increasing the distance, increases the lateral coherence length and thus the maximal admissible cross section, but the lateral coherence length increases proportional with the distance and, therefore, the solid angle, spanned by that cross section, remains constant. The question may arise, whether it is possible to increase the coherent flux by means of focusing x-ray optics. Perhaps, the aperture of the focusing lens can be made larger than the lateral coherence length in the aperture plane collecting a larger photon flux, while — by means of focusing — the lateral coherence length in the focal plane becomes larger than the focus. Again, we refer to equation (4.54), but now, the quantities D_h and D_v denote the lens apertures and, therefore, equation (4.52) can be applied:

$$\begin{aligned}
 F_{c,lens} &= \mathcal{B} \frac{\chi^2}{(2\sqrt{2 \ln 2})^4} \lambda^2 \frac{D_h}{l_{t,h}} \frac{D_v}{l_{t,v}} \frac{\Delta E}{E} \\
 &\stackrel{(4.52)}{=} \mathcal{B} \frac{\zeta^2}{(2\sqrt{2 \ln 2})^4} \frac{\lambda^2}{\Gamma_h \Gamma_v} \frac{\Delta E}{E} \\
 &\stackrel{(\Gamma_{h,v} \geq 1)}{\leq} \frac{\chi^2}{(2\sqrt{2 \ln 2})^4} \mathcal{B} \lambda^2 \frac{\Delta E}{E} \\
 &\stackrel{(4.54)}{=} F_{c,max}
 \end{aligned}$$

Obviously, the coherent flux cannot be increased by means of a focusing lens. This is no surprise, since we already know from equation (4.53) that the coherent flux must be gathered

by a lens aperture, which is not larger than the lateral coherence length in the aperture plane. On the other hand, if the aperture equals the lateral coherence length (aperture matching), the focus is diffraction limited and thus highly coherent. Therefore, in the best case, the coherent portion of the photon beam is conserved, but never increased by a focusing optic. In a more general sense, the maximal available coherent flux is an invariant quantity with respect to beam propagation through any optical system [Kim87] and is therefore a property of the source. It depends on the brilliance of the source, the photon energy and the energy bandwidth.

A large energy band leads to a large maximal available coherent flux, but the energy band is restricted for some reasons. Most experiments that require lateral coherence also need longitudinal coherence. The longitudinal coherence length l_l depends on the wavelength and the degree of monochromaticity and is given by

$$l_l = \lambda \frac{\lambda}{\Delta\lambda},$$

and hence

$$\frac{\Delta E}{E} = \frac{\lambda}{l_l}. \quad (4.55)$$

The required longitudinal coherence length $l_{l,req}$ determines the admissible energy bandwidth, and so with (4.54), (4.55), and $l_l \geq l_{req}$ the available coherent flux becomes

$$\begin{aligned} F_{c,max} &= \frac{\chi^2}{(2\sqrt{2\ln 2})^4} \mathcal{B} \lambda^2 \frac{\Delta E}{E} \\ &\stackrel{(4.55)}{=} \frac{\chi^2}{(2\sqrt{2\ln 2})^4} \mathcal{B} \frac{\lambda^3}{l_l} \\ &\leq \frac{\chi^2}{(2\sqrt{2\ln 2})^4} \mathcal{B} \frac{\lambda^3}{l_{l,req}}. \end{aligned} \quad (4.56)$$

So, a large required longitudinal coherence length reduces the available coherent flux due to a narrow energy bandwidth.

But the energy bandwidth is not only limited by the longitudinal coherence length required by the experiment. In order to prevent chromatic aberrations of the focusing lens, the energy bandwidth must not be too large. Chromatic aberrations become relevant, if the corresponding aberration pattern becomes comparable with the geometric image size or with the diffraction limit. As we consider diffraction limited foci, the aberration pattern must be smaller than the Airy disk. The focus position of a refractive lens depends on the photon energy. A deviation of the energy shifts the focal plane along the optical axis. A shift of the focal plane becomes relevant, if it becomes as large as half the depth of focus. In section 4.8 the depth of focus was introduced, and with equation (4.25) the focus length can be restricted to

$$B_l = \frac{2}{\pi} \sqrt{1 + \Gamma^{-1}} \frac{\lambda}{(NA)^2} \stackrel{(\Gamma \geq 1)}{\leq} \frac{2\sqrt{2}}{\pi} \frac{\lambda}{(NA)^2}.$$

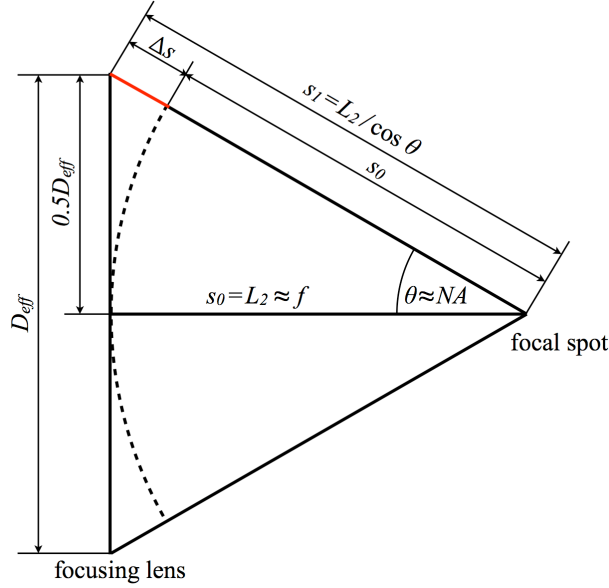


Figure 4.8: Illustration of the path difference in a focusing lens. A large numerical aperture comes with a large path difference increasing the required longitudinal coherence length and, therefore, the tolerable energy bandwidth becomes smaller.

Making use of equation (4.28) from section 4.10, the shift of the focal plane is given as

$$\Delta z_F = \alpha_F f \frac{\Delta E}{E}$$

with α_F in the range between $\pi/2$ and 2, depending on the parameters of the CRL or the NFL, respectively. We need the shift Δz_F of the focal plane along the optical axis to be smaller than half the longitudinal focus size B_l , hence, with $\Delta z_F \leq B_l/2$, one obtains

$$\frac{\Delta E}{E} \leq \frac{\sqrt{2}}{\alpha_F \pi} \frac{\lambda}{f (NA)^2}. \quad (4.57)$$

Apart from a constant factor of order 1, this result can also be obtained by the argument, that in case of generating a diffraction limited focus, the longitudinal coherence length l_l must not exceed the maximal path length difference Δs in the optical system. The maximal path length difference of a focusing lens is the difference of the paths $s_0 = L_2$ along the optical axis and the path $s_1 = L_2 / \cos \theta$ from the outermost lateral position of the effective lens aperture (see Figure 4.8). In the paraxial approximation, and for large demagnification ($L_2 \approx f$) the path length difference is

$$\begin{aligned} \Delta s &= s_1 - s_0 = \frac{L_2}{\cos \theta} - L_2 = L_2 \left(\frac{1}{\cos \theta} - 1 \right) \\ &\approx L_2 (1 + \theta^2 + \mathcal{O}(\theta^4) - 1) = \frac{1}{2} L_2 \theta^2 \\ &\approx \frac{1}{2} f (NA)^2. \end{aligned}$$

This must be larger than the longitudinal coherence length $l_l = \lambda(\Delta E/E)^{-1}$ and hence

$$\frac{\Delta E}{E} \leq \frac{\lambda}{\Delta s} = 2 \frac{\lambda}{f(NA)^2}, \quad (4.58)$$

which is but a constant factor similar with (4.57).

Now we insert (4.57) into (4.54) and substitute NA for $D_{eff}/(2f)$ to attain

$$\begin{aligned} F_{c,max} &= \frac{\chi^2}{(2\sqrt{2}\ln 2)^4} \mathcal{B} \lambda^2 \frac{\Delta E}{E} \\ &= \frac{\chi^2}{4\pi\alpha\sqrt{2}\ln 2} \mathcal{B} \frac{\lambda^3}{f(NA)^2} \\ &= \frac{\chi^2}{\pi\alpha\sqrt{2}\ln 2} \mathcal{B} \lambda^3 \frac{f}{D_{eff}^2}. \end{aligned} \quad (4.59)$$

When analysing this expression one has to keep in mind, that the effective aperture is constrained by the lateral coherence length $l_{t,i}$ of the incident beam and, therefore, the focal distance is the only parameter, which is free to change the admissible energy bandwidth and hence the coherent flux in the focus. To increase the coherent flux, the focal distance has to be made larger (keeping the effective aperture constant). Since a short focal distance is required for a large demagnification of the source, the flux is effectively limited by the required focus size, due to chromatic aberration of the lens. Considering realistic parameters for the nanofocusing lenses used in the hard x-ray scanning microscope ($\lambda \approx 1 \text{ \AA}$, $D_{eff} \approx 20 \text{ }\mu\text{m}$, $f \approx 10 \text{ mm}$), the required energy bandwidth is in the range of $10^{-3} - 10^{-2}$. Nearly all experiments with the hard x-ray scanning microscope make use of a liquid nitrogen cooled Si-111 double crystal monochromator with an energy band of about 10^{-4} , and for this reason, the nanofocusing lenses do not limit the coherent flux by chromatic aberration.

4.14 Two-Stage Focusing

At the ESRF beamline ID 13 the nanofocusing lenses of the hard x-ray scanning microscope are located in a distance of 47 m (experimental hutch EH2) or in a distance of 98 m (EH3) behind the undulator source. The effective full width at half maximum source size is $S_h = 150 \text{ }\mu\text{m}$ in horizontal and $S_v = 50 \text{ }\mu\text{m}$ in vertical direction. If the microscope is installed in EH3 and operated at a photon energy of $E = 15.25 \text{ keV}$ ($\lambda = 0.813 \text{ \AA}$), the lateral coherence length in the incident aperture plane of the nanofocusing lens is $l_{t,h} = 53 \text{ }\mu\text{m}$ in horizontal and $l_{t,v} = 160 \text{ }\mu\text{m}$ in vertical direction (confer equation (4.51)). The effective aperture D_{eff} of the NFLs is in the range between $10 \text{ }\mu\text{m}$ and $20 \text{ }\mu\text{m}$, depending on the curvature R and the number N of single lenses which make up the lens. In the extreme case of $D_{eff} = 10 \text{ }\mu\text{m}$ of the vertical lens, the vertical lateral coherence length exceeds the effective aperture by a factor of 16, i. e., the focal spot is highly diffraction limited and there is much potential to increase the coherent flux in the focus by either enlarging the effective aperture or by reducing the

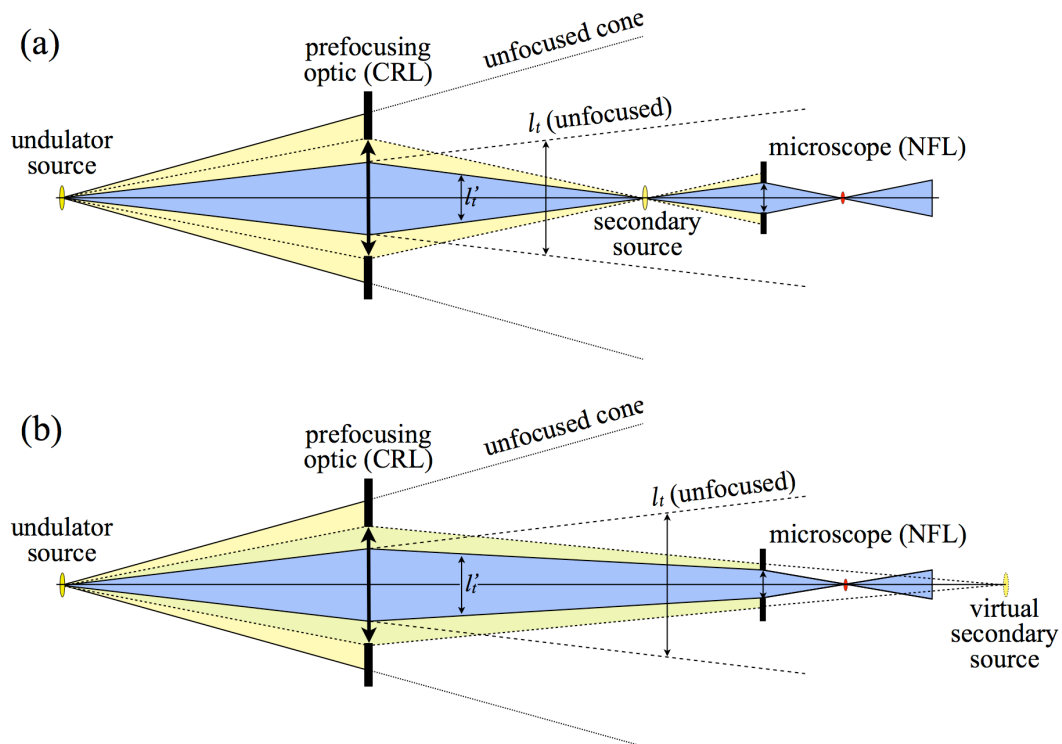


Figure 4.9: Two-stage focusing scheme. The lateral coherence length l_t is adapted to the effective aperture of the nanofocusing length, thereby increasing the coherent flux in the focal spot. (a) With a short focal distance of the prefocusing lens the intermediate secondary source is located between the prefocusing and the nanofocusing lens. (b) If the focal distance of the prefocusing lens is large, a virtual secondary source behind the nanofocusing lens is generated.

lateral coherence length. On the other hand, if the microscope is operated in EH2, the lateral coherence length in the input aperture of the nanofocusing lens is $l_{t,h} = 15 \mu\text{m}$ in horizontal and $l_{t,v} = 45 \mu\text{m}$ in vertical direction. Hence, at least in horizontal direction, the lateral coherence length might not be large enough in order to ensure sufficient lateral coherence for coherent diffraction experiments like CXDI or ptychography.

In order to be able to selectively adjust the lateral coherence length and thus to specifically achieve a diffraction limited focus making use of the full available coherent flux, a two-stage focusing scheme, employing compound parabolic refractive x-ray lenses as a prefocusing device is applied in the hard x-ray scanning microscope and is illustrated in Figure 4.9. The principle concept of the two-stage focusing scheme is explained in the following paragraphs.

4.14.1 The Prefocusing Parameter η

The prefocusing lens is installed at a fixed position between the undulator source and the nanofocusing lens and generates a secondary source, from which the nanofocusing lens induces a demagnified image. As the case may be, the secondary source could be either a

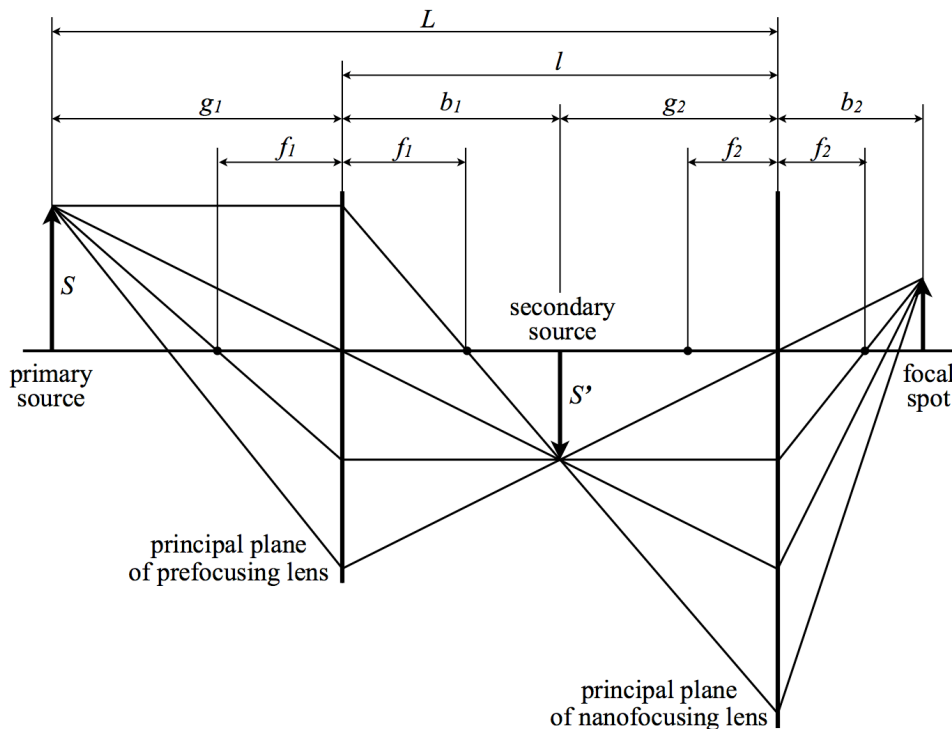


Figure 4.10: Imaging geometry for two-stage focusing. The prefocusing lens generates an image S' of the primary (undulator) source S . The nanofocusing lens creates the focal spot by generating an image of the secondary source. In the drawing, the secondary source is depicted between the prefocusing and the nanofocusing lens. The case of a virtual secondary source (behind the NFL) can be treated analog to the one with a real secondary source.

real source or a virtual source. The two situations are illustrated in Figure 4.9. Depending on the size of the secondary source and on its distance from the nanofocusing lens, a certain lateral coherence length l'_t will arise in the plane of the lens aperture, which might be smaller or larger than the coherence length l_t without the prefocusing lens. We now define the *prefocusing parameter* η as the ratio of the lateral coherence lengths with and without prefocusing

$$\eta = \frac{l'_t}{l_t}. \quad (4.60)$$

In section 4.6 the focus parameter Γ was introduced, and in section 4.12 it was shown, that in a diffraction limited focus with $\Gamma \geq 1$ the lateral coherence length exceeds the lateral focus dimensions. From equation (4.52) we know that diffraction limited focusing is achieved, as soon as the lateral coherence length l_t in the aperture plane of the nanofocusing lens becomes larger than $l_{t,c} := \sqrt{2 \ln 2} D_{eff}$. This suggests to define the critical prefocusing parameter

$$\eta_c = \frac{l_{t,c}}{l_t} = \frac{\sqrt{2 \ln 2} D_{eff}}{l_t}. \quad (4.61)$$

As long as the prefocusing parameter is larger than η_c , the focal spot will be diffraction limited, and vice versa. In most cases, the required prefocusing parameter will be close to the critical parameter η_c , because this maximizes the coherent flux in the focus, as will be shown in the next section. Before doing so, we will calculate the prefocusing parameter η , which is obtained by a certain focal distance f_1 of the prefocusing lens.

4.14.2 Required Refractive Power

Without prefocusing, the lateral coherence length in the aperture plane of the nanofocusing lens is given as

$$l_t \stackrel{(4.51)}{=} \chi \frac{\lambda L}{S}, \quad (4.62)$$

in which λ , L , and S denote the wavelength of the x rays, the distance of the NFL from the source, and the source size, respectively. If the prefocusing lens is inserted between the undulator source and the nanofocusing lens, the situation is described by Figure 4.10. A secondary source of size S' is induced a distance g_2 away from the NFL, entailing a new coherence length

$$l'_t = \chi \frac{\lambda g_2}{S'}, \quad (4.63)$$

and the prefocusing parameter becomes

$$\eta = \frac{l'_t}{l_t} = \frac{g_2}{L} \frac{S}{S'}. \quad (4.64)$$

The intensity distribution of the secondary source is the convolution of the intensity distribution of the geometric image of the primary source (undulator) with the intensity distribution of the Airy disk due to diffraction in the aperture of the prefocusing CRL. With the approximation of Gaussian intensity distributions (full width at half maximum sizes b_g and d_t), one obtains

$$S' = \sqrt{b_g^2 + d_t^2}. \quad (4.65)$$

If we consider the extreme case of x rays with a photon energy of 10 keV and a compound parabolic refractive lens, which consists of 100 single beryllium lenses with a radius of curvature of 200 μm , the effective aperture of the CRL would be about 400 μm . The prefocusing lens is typically installed at a distance of several tens of meters behind the source (41 m at the ESRF beamline ID 13), and the source size is about 50 μm . This yields a lateral coherence length of about 50 μm in the plane of the entry aperture of the prefocusing CRL. Therefore, the diffraction limit d_t in the secondary source is about one order of magnitude smaller than the geometric image size b_g . In a realistic situation the energy would not be lower than 15 keV, and the number of single beryllium lenses in the prefocusing CRL would be well below 100, yielding an even larger effective aperture (and a smaller lateral coherence

length). For this reason, to very good approximation, the Airy disk size can be neglected, and the size of the secondary source becomes

$$S' = b_g = S \frac{b_1}{g_1} = S \frac{f_1}{g_1 - f_1}, \quad (4.66)$$

wherein $b_1 = f_1/(g_1 - f_1)$ indicates the distance of the secondary source from the CRL. The distance g_2 of the secondary source from the nanofocusing lens is

$$g_2 = L - g_1 - b_1 = L - g_1 - \frac{g_1 f_1}{g_1 - f_1}. \quad (4.67)$$

We insert (4.66) and (4.67) in equation (4.64) and get

$$\eta = \left(1 - \frac{g_1}{L}\right) \frac{g_1}{f_1} - 1 \quad \text{or} \quad (4.68)$$

$$f_1 = \frac{g_1(L - g_1)}{L(\eta + 1)}. \quad (4.69)$$

The relation between the prefocusing parameter and the focal distance of the prefocusing lens is illustrated in Figure 4.11. The solid red curve shows the absolute value of η as a function of refractive power $1/f_1$, whereas the dotted curve represents the region with negative η . Within the shaded region, the absolute value of η becomes smaller than the critical value η_c , indicating that a diffraction limited focus is only achieved outside that region. We distinguish three situations A, B, and C, depending on the location of the secondary source with respect to the prefocusing and the nanofocusing lenses. Following the course of the curves in Figure 4.11 from the right to the left (from large refractive power towards weak refractive power), situations A, B, and C occur in this order.

Situation A: secondary source between CRL and NFL

If the refractive power of the prefocusing lens is strong enough ($f_1 \leq g_1 - g_1^2/L$), the secondary source is located between the prefocusing and the nanofocusing lens, as is illustrated in Figure 4.9(a). The secondary source is mirrored with respect to the optical axis, and the prefocusing parameter is positive. With a short focal distance of the prefocusing lens, arbitrarily large η values can be achieved, yielding an arbitrarily large lateral coherence length in the lens aperture. With decreasing refractive power, η becomes smaller, and there is a certain focal distance, for which $\eta = 1$, i. e., the prefocusing lens does not change the lateral coherence length as compared with the situation without prefocusing. If the refractive power is decreased further, the secondary source gets closer to the nanofocusing lens, and the lateral coherence length approaches zero as soon as the secondary source crosses the aperture plane of the NFL.⁴ This is the boundary to situation B.

⁴Of course, the lateral coherence length will never become smaller than the Airy disk of the prefocusing lens.

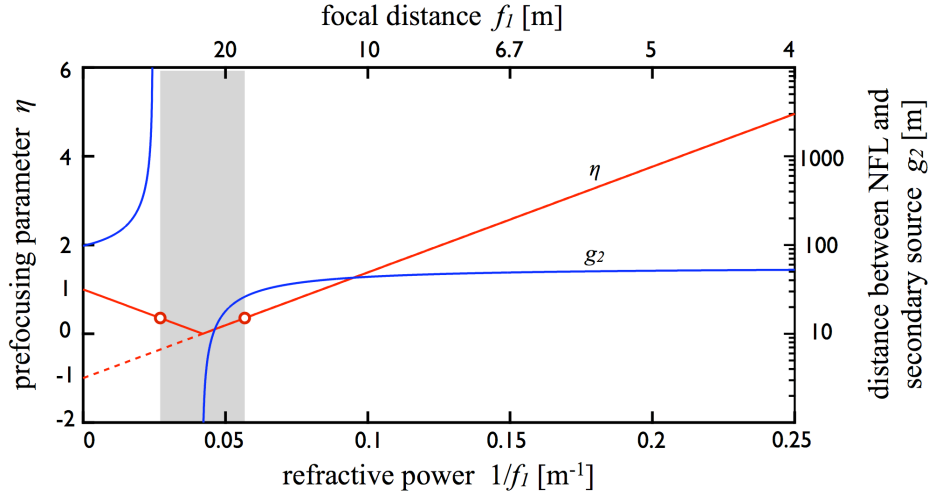


Figure 4.11: Prefocus parameter η (red curve) and secondary source distance g_2 (blue curve) as a function of refractive power. Within the shaded region, the absolute value of η becomes smaller than the critical value η_c , indicating that a diffraction limited focus is only achieved outside that region.

Situation B: secondary source behind NFL

If the refractive power of the prefocusing lens becomes weaker ($g_1 - g_1^2/L \leq f_1 \leq g_1$), the secondary source goes across the nanofocusing lens aperture and is then located behind the NFL. This situation is depicted in Figure 4.9(b). The absolute value of the negative prefocusing parameter becomes larger with decreasing refractive power. With increasing focal distance, the distance of the secondary source from the nanofocusing lens gets larger and larger. For $f_1 \rightarrow g_1$, the secondary source diverges to infinity, while the absolute value of the prefocusing parameter converges against g_1/L . It is interesting to note, that, even though g_2 diverges to infinity, the function $\eta(1/f)$ is still continuously differentiable in $f_1 = g_1$, since the size S' of the secondary source diverges to infinity in the same manner as g_2 . The case $f_1 = g_1$ is especially interesting, because it directly transfers the lateral coherence length in the aperture plane of the prefocusing lens into the aperture plane of the nanofocusing lens, virtually shortening the source-to-lens distance by the gap $L - g_1$ between the prefocusing and the nanofocusing lens.

Situation C: secondary source before primary source

If the refractive power of the prefocusing lens decreases further ($g_1 \leq f_1$), the secondary source appears before the primary source, coming from infinity and converging to the location of the undulator source. While f_1 gets larger ($1/f_1 \rightarrow 0$), the absolute value of η converges against 1, which conforms the case without the prefocusing lens.

4.14.3 Flux Considerations

In the previous section the prefocusing parameter was introduced and a relation with the focal distance was established. Knowing the initial ($l_{t,init}$) and the required ($l_{t,req}$) lateral coherence length in the aperture plane of the nanofocusing lens, the required prefocusing parameter η_{req} , and hence the required focal distance f_{req} of the prefocusing lens, can be calculated by inserting

$$\eta_{req} = \frac{l_{t,req}}{l_{t,init}} \quad (4.70)$$

into equation (4.69). The intention, why one would like to adapt the lateral coherence length in the aperture plane of the nanofocusing lens to its effective aperture, is to maximize the coherent photon flux in the focal spot, i. e., to increase the photon flux while still preserving sufficient lateral coherence. Thus, it is of great interest to estimate the gain of photon flux achieved with a certain prefocusing setup. In this section the photon flux F'_2 in the focal spot in dependence of the focal distance of the prefocusing lens is computed and compared with the photon flux F_2 in the focal spot without the prefocusing lens. For this purpose, we define the *photon flux gain*

$$gain = \frac{F'_2}{F_2}, \quad (4.71)$$

which is achieved by a certain prefocusing setup.

Flux with prefocusing lens

In order to evaluate the photon flux F'_2 in the focal spot of the nanofocusing lens, we will have to estimate the photon flux, which is emitted by the undulator source, propagated to the prefocusing lens, transmitted through the prefocusing lens, propagated to the nanofocusing lens, transmitted through the nanofocusing lens, and finally propagated to the focal spot. We start with the photon flux F'_0 , which arrives at the aperture plane of the prefocusing lens, which is located at distance g_1 behind the source

$$F'_0 = \mathcal{B} \frac{\Delta E}{E} \frac{S_h S_v}{(2\sqrt{2 \ln 2})^2} \frac{D_{eff,1,h} D_{eff,1,v}}{(2\sqrt{2 \ln 2})^2 g_1^2}. \quad (4.72)$$

\mathcal{B} is the brilliance of the source, and S_h, S_v denote its full width of half maximum sizes in horizontal and vertical direction. The term $D_{eff,1,h} D_{eff,1,v} / ((2\sqrt{2 \ln 2})^2 g_1^2)$ accounts for the solid angle spanned by the source and the effective aperture of the prefocusing lens. In order to estimate the transmitted flux F'_1 through the prefocusing lens, the averaged flux density I'_1 in the incident aperture plane of the lens and the cross section $\sigma_{p,1}$ of the prefocusing lens are needed

$$I'_1 = \frac{F'_0}{D_{eff,1,h} D_{eff,1,v}} = \mathcal{B} \frac{\Delta E}{E} \frac{S_h S_v}{(2\sqrt{2 \ln 2})^4} \frac{1}{g_1^2},$$

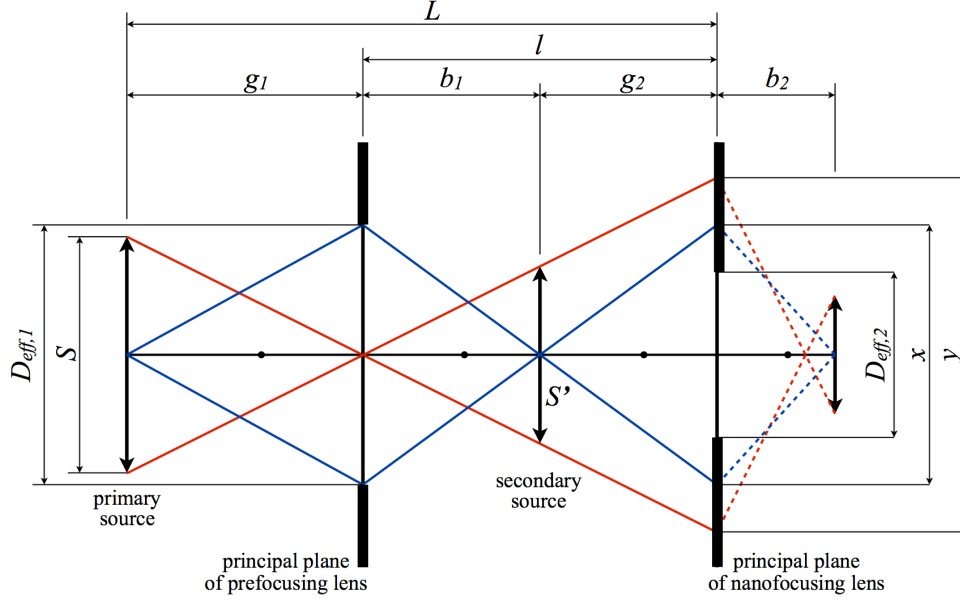


Figure 4.12: Beam size in the NFL aperture plane with prefocusing lens.

and hence

$$F'_1 = \sigma_{p,1} I'_1 = \mathcal{B} \frac{\Delta E}{E} \frac{S_h S_v}{(2\sqrt{2 \ln 2})^4} \frac{\sigma_{p,1}}{g_1^2}. \quad (4.73)$$

This photon flux propagates to the nanofocusing lens, where only a fraction of the photons is collected by the effective lens aperture. For evaluating the transmitted photon flux F'_2 , we need to know the mean flux density I'_2 , which is found in the incident aperture plane of the NFL

$$I'_2 = \frac{F'_1}{B_h B_v}. \quad (4.74)$$

In a next step, the horizontal and the vertical beam sizes $B_{h,v}$ in the incident aperture plane of the nanofocusing lens have to be calculated. The situation is illustrated in Figure 4.12. Each point of the extended primary source generates an intensity pattern X in the aperture plane of the NFL, the shape of which depends on the transmission function of the prefocusing lens. In case of a refractive lens, we can assume a Gaussian transmission function, and hence the intensity pattern X is a Gauss function with a full width at half maximum size of x (confer Figure 4.12). We apply the theorem on intersecting lines and obtain

$$x_{h,v} = \frac{g_2}{b_1} D_{eff,h,v}. \quad (4.75)$$

For an extended source, the intensity pattern X has to be convolved with the intensity distribution Y of the source, imaged into the aperture plane of the NFL. If a Gaussian source is assumed, the intensity pattern Y is also a Gauss function with full width at half

maximum size y (confer Figure 4.12). Applying again the intersect theorem, one gets

$$y_{h,v} = \frac{l}{g_1} S_{h,v}. \quad (4.76)$$

The convolution of X and Y gives the intensity of the beam in the incident aperture plane of the NFL, which is a Gauss function, and thus it is

$$\begin{aligned} B_{h,v} &= \sqrt{x_{h,v}^2 + y_{h,v}^2} \\ &= \sqrt{\left(\frac{g_2}{b_1}\right)^2 D_{eff,h,v}^2 + \left(\frac{l}{g_1}\right)^2 S_{h,v}^2} \\ &= \frac{L}{g_1} \sqrt{\left(\left(1 - \frac{g_1}{L}\right) \frac{g_1}{f_1} - 1\right)^2 D_{eff,h,v}^2 + \left(1 - \frac{g_1}{L}\right)^2 S_{h,v}^2} \\ (4.68) \quad &= \frac{L}{g_1} \sqrt{\eta^2 D_{eff,h,v}^2 + \left(1 - \frac{g_1}{L}\right)^2 S_{h,v}^2}. \end{aligned} \quad (4.77)$$

This expression, together with equations (4.73) and (4.74), gives the flux density in the aperture plane of the nanofocusing lens, just before the x-ray beam enters the lens. The demanded photon flux in the focal spot can now be calculated as the fraction of photons, which is transmitted through the NFL

$$F'_2 = I'_2 \sigma_{p,2} = \frac{F'_1}{B_h B_v} \sigma_{p,2} \quad (4.78)$$

and with (4.73)

$$F'_2 = \mathcal{B} \frac{\Delta E}{E} \frac{S_h S_v}{\left(2\sqrt{2 \ln 2}\right)^4} \frac{\sigma_{p,1}}{g_1^2} \frac{\sigma_{p,2}}{B_h B_v}. \quad (4.79)$$

Flux without prefocusing lens

Without prefocusing, the photon flux F_2 in the focal spot, generated by a nanofocusing lens, is given by the mean flux density I_2 of the incident beam, multiplied by the cross section $\sigma_{p,2}$ of the nanofocusing lens

$$F_2 = I_2 \sigma_{p,2}. \quad (4.80)$$

The mean flux density in the aperture plane of the nanofocusing lens can be computed from the photon flux emitted by the source and collected by the nanofocusing lens, divided by the cross section area of the lens

$$I_2 = \frac{F_0}{D_{eff,2,h} D_{eff,2,v}}. \quad (4.81)$$

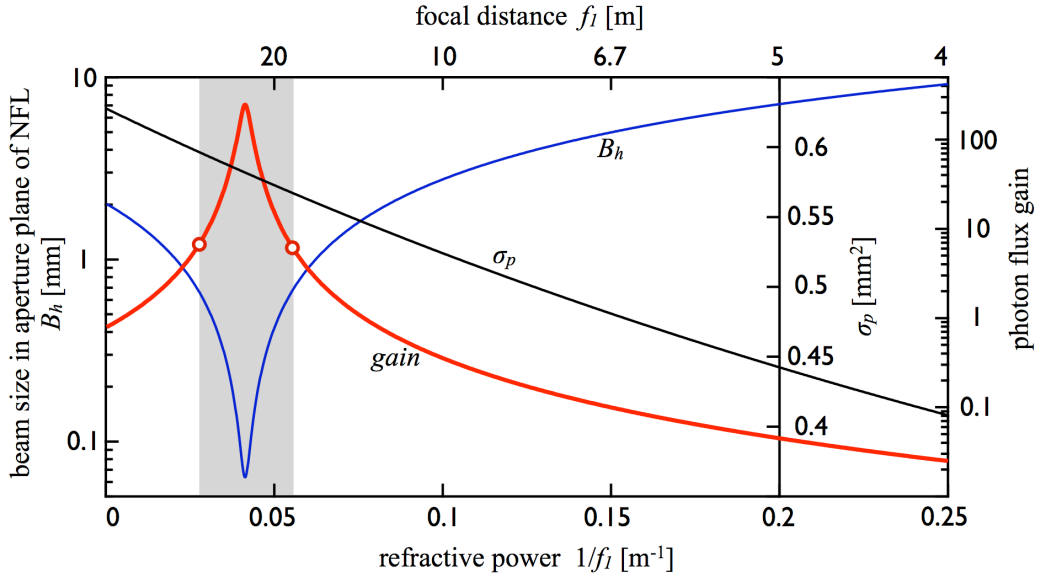


Figure 4.13: Beam size, cross section, and flux gain as functions of refractive power using prefocusing lenses. The flux gain is dominated by the size of the beam in the aperture plane of the NFL. The maximal gain is achieved, if the prefocusing parameter is 0, i. e., if the lateral coherence length in the aperture plane of the NFL reaches its minimum. Within the shaded region the focal spot is not diffraction limited ($\Gamma < 1$) and, therefore, the maximal coherent flux is gained at both edges of the shaded region (indicated by the two red circles).

The photon flux, which arrives at the aperture plane of the nanofocusing lens, depends on the brilliance \mathcal{B} of the source, the energy bandwidth $\Delta E/E$, and the distance L of the NFL from the source,

$$F_0 = \mathcal{B} \frac{\Delta E}{E} \frac{S_h S_v}{(2\sqrt{2 \ln 2})^2} \frac{D_{eff,2,h} D_{eff,2,v}}{(2\sqrt{2 \ln 2})^2 L^2}. \quad (4.82)$$

In the end, the photon flux in the focal spot without prefocusing lens follows with

$$F_2 = \mathcal{B} \frac{\Delta E}{E} \frac{S_h S_v}{(2\sqrt{2 \ln 2})^4} \frac{\sigma_{p,2}}{L^2}. \quad (4.83)$$

Flux gain with prefocusing

If we insert (4.79) and (4.83) in equation (4.71), we obtain an expression for the photon flux gain achieved by prefocusing with a certain focal distance f_1 or prefocusing parameter η , respectively

$$gain = \frac{F'_2}{F_2} = \frac{L^2}{g_1^2} \frac{\sigma_{p,1}}{B_h B_v}, \quad (4.84)$$

and together with (4.77)

$$gain = \sigma_{p,1} \left\{ \left[\eta^2 D_{eff,1,h}^2 + \left(1 - \frac{g_1}{L}\right)^2 S_h^2 \right] \left[\eta^2 D_{eff,1,v}^2 + \left(1 - \frac{g_1}{L}\right)^2 S_v^2 \right] \right\}^{-\frac{1}{2}}. \quad (4.85)$$

When evaluating this expression, one has to take into account the fact that the cross section $\sigma_{p,1}$ of the prefocusing lens depends on the focal distance and is thus a function of the prefocusing parameter η . The red curve in Figure 4.13 shows the flux gain as a function of the refractive power of the prefocusing lens. The curve has its maximum in the region around $\eta \approx 0$, where the beam size in the aperture plane of the NFL and the lateral coherence length are minimal. Within the shaded region, the prefocusing parameter η is smaller than the critical parameter η_c , indicating that Γ is smaller than 1, and hence the focal spot is not diffraction limited, and the lateral coherence length in the focus is smaller than the lateral focus size. For this reason, the maximal coherent flux is achieved at the edge of the shaded region, which is marked by the two red circles in Figure 4.13. Prefocusing beyond the critical prefocusing parameter increases the total flux in the focus, but the focus size starts to exceed the lateral coherence length in the focus, and the lateral coherence is not sufficient for many experiments.

Example from a realistic situation

The parameters used to calculate the curves in Figure 4.11 and 4.13 are taken from a realistic experimental situation of the hard x-ray scanning microscope at the ESRF beamline ID 13 (confer table 4.1). In vertical direction, the transverse coherence length in the aperture plane of the NFL is a factor 3 larger than the effective aperture of the nanofocusing length, whereas, in the the vertical direction, the factor is 8. In the current prototype version of the hard x-ray scanning microscope, prefocusing is only possible without astigmatism, i. e., the focal length of the prefocusing lens is the same in horizontal and vertical direction. For this reason, the transverse coherence length can be matched to the effective aperture in only one of the two directions. Since we need a diffraction limited focus, none of the two directions is allowed to have a smaller transverse coherence length in the aperture plane of the NFL than the effective aperture. Therefore, prefocusing has to be chosen such, that there is aperture matching for one of the two directions, whereas, in the other direction, the transverse coherence length would be larger than the effective aperture. In our situation, this means, that we have to match the horizontal direction, and leave the vertical coherence length larger than the effective aperture. Then, the critical prefocusing parameter becomes $|\eta_c| = D_{eff,2,h}/l_{t,h} = 16 \mu\text{m}/53 \mu\text{m} \approx 0.3$. Considering equation (4.69), this critical prefocusing parameter is either obtained for $f_{1,A} = 18.3 \text{ m}$ (situation A) or for $f_{1,B} = 34.1 \text{ m}$ (situation B), which correspond to the two situations depicted in Figure 4.9. With compound parabolic refractive x-ray lenses the two situations A and B can be achieved by choosing the proper number of single lenses with adequate radius of curvature. Assuming a photon energy of 15 keV, situation B can be established with a CRL, which consists of two single parabolic beryllium lenses with radius of curvature $R = 200 \mu\text{m}$. By this, The coherent photon flux in

E [keV]	$S_h \times S_v$ [μm^2]	g_1 [m]	L [m]	$D_{\text{eff},2,h} \times D_{\text{eff},2,v}$ [μm^2]	$l_{t,h} \times l_{t,v}$ [μm^2]
15.25	150×50	41	98	16×20	53×159

Table 4.1: Parameters used to calculate the curves in Figures 4.11 and 4.13.

the focus is increased by a factor of about 8.5. The gain could even be larger, if it was possible to match the coherence length in both directions simultaneously by astigmatic lenses. This issue is addressed in the following section.

4.14.4 Astigmatic Prefocusing

Usually, the vertical and the horizontal sizes of an undulator source are quite different, giving rise to different lateral coherence lengths at a certain distance from the source. At the ESRF beamline ID 13, for example, the horizontal source size is a factor 3 larger than the vertical one and, therefore, the horizontal transverse coherence length is smaller than the vertical one by the same factor. This means, that the full available coherent flux can only be exploited, if the prefocusing parameter can be adjusted independently in the horizontal and the vertical direction. This can be achieved by astigmatic prefocusing, applying lenses with focal distances $f_{1,h} \neq f_{1,v}$, either by using cylindrically symmetric lenses in crossed geometry or by combining rotationally symmetric lenses with cylindrically symmetric lenses. For this end, cylindrically symmetric compound parabolic refractive x-ray lenses have been developed by Prof. Lengeler at the University of Aachen, and they will be part of the prefocusing device of the nanoprobe at the PETRA III beamline P06. In addition, our research group in Dresden has developed special microstructured parabolic refractive x-ray lenses with large apertures, which are capable of being used for astigmatic prefocusing in the hard x-ray scanning microscope.

Chapter 5

Nanoprobe Setup

In this chapter the design of the prototype version of the hard x-ray scanning microscope is presented. The instrument was developed and built in the course of this thesis, and was installed at the microfocus beamline ID 13 at the third generation synchrotron radiation facility ESRF in Grenoble.

A schematic drawing of the optical components of the beamline ID 13 together with the nanoprobe setup is shown in Figure 5.1. A low- β undulator source emits highly brilliant x rays, which pass through a channel cut silicon 111 monochromator before they arrive at a prefocusing optical device. The monochromator is located inside the optics hutch a few meters away from the undulator. Depending on the needs of the experiment, a prefocusing device can be moved into the beam, generating a real or a virtual secondary source, thereby adapting the transverse coherence length in the aperture plane of the nanofocusing lens to its effective aperture and thus increasing the coherent photon flux in the focal spot. The theoretical concept of two-stage focusing is established in chapter 4. Prefocusing is realized with axially symmetric compound parabolic refractive x-ray lenses. At beamline ID 13, the nanoprobe instrument can be installed either in the experiments hutch EH2 or in the experiments hutch EH3. In case of EH2, the distance of the instrument from the undulator source is about 47 m, whereas in EH3 the distance is nearly 100 m. While the monochromator and the prefocusing lenses are integral parts of the beamline, the scanning microscope itself was designed and built by our research group in Dresden and has to be carried from Dresden to Grenoble each time before an experiment can be carried out.

The current prototype version (NP-2005) of the hard x-ray scanning microscope is the latest of a series of previous versions, which have been designed and built since 2002. Based on the experiences with that prototype, the beamline ID 13 has built its own nanoprobe instrument (NP-2009), for which we provide the optical interface for the nanofocusing lenses and the piezo-scanner.

The hard x-ray scanning microscope consists of a lot of optical and mechanical components such as entrance slits, focusing x-ray optics, a pinhole, shieldings, stages for aligning the optics, stages for aligning and scanning the sample, several detectors and a visible light microscope for sample alignment. In Figure 5.2 the arrangement of the main components of the nanoprobe setup is schematically drawn. Before the incident beam arrives at the verti-

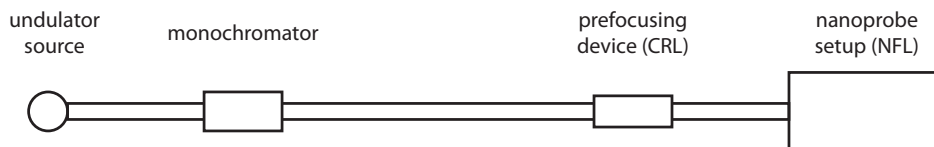


Figure 5.1: Layout of the ID 13 beamline ID 13 at the ESRF in Grenoble with the installed nanoprobe setup. The monochromator and the prefocusing device are integral parts of the beamline, whereas the prototype nanoprobe setup is provided by our research group. The monochromator resides in the optics hutch located just behind the undulator source. The (optional) prefocusing device is realized with compound parabolic refractive x-ray lenses (CRLs) fabricated at the RWTH Aachen by Prof. B. Lengeler. The hard x-ray scanning microscope was installed in a separate experiments hutch 45 m away from the undulator source. Recently, the beamline ID 13 was extended to a length of 100 m. Since then, the nanoprobe can be operated in a distance of about 100 m behind the source.

cally and the horizontally focusing lenses, it is constrained to a size matching the aperture of the nanofocusing lenses by a pair of horizontal and vertical entry slits. After passing the NFLs, the beam propagates to the sample, which is placed within the focal plane. A stainless steel shielding and a platinum pinhole clean the converging beam from unfocused scattered photons. Around the sample environment diverse detectors are placed to measure the interaction of the focused x-rays with the sample.

A major intention of the hard x-ray scanning microscope is to generate a sub-100 nm x-ray focus with sufficient flux and to use this focus to scan samples and retrieve structural and elemental information about the samples with a resolution in the range of the focus size. This is only possible if the sample can be placed relative to the focus with a sufficient accuracy. Therefore, in order to make use of the high focusing potentials of the NFLs, great mechanical demands are made on the components of the instrument. The stages must fulfill high mechanical specifications such as precision, repeatability, resolution, etc. In order to increase mechanical stability of the overall system, the focusing optic with its alignment stages and the sample stages are integrated within one single stiff frame, which we call the “scanner unit”. Figure 5.3 shows a three-dimensional schematic drawing of the scanner unit of the NP-2005. On the top of the roof there are stages to move the platinum pinhole. Underneath the roof a small hexapod is hanging head down. This hexapod table is used to align the vertical lenses. The horizontal lenses are mounted on the frame of the hexapod. In the foreground of the drawing the sample stages can be seen. In the following sections the design of the nanoprobe instrument NP-2005 is described in more detail. A photograph of the whole nanoprobe setup is shown in Figure 5.4.

5.1 X-Ray Optics

The x-ray optics of the hard x-ray scanning microscope are part of the scanner unit. As can be seen in Figure 5.2, the optical components are a pair of entry slits, a pair of horizontally and vertically focusing lenses, a shielding, and a pinhole. These elements are discussed in the following subsections.

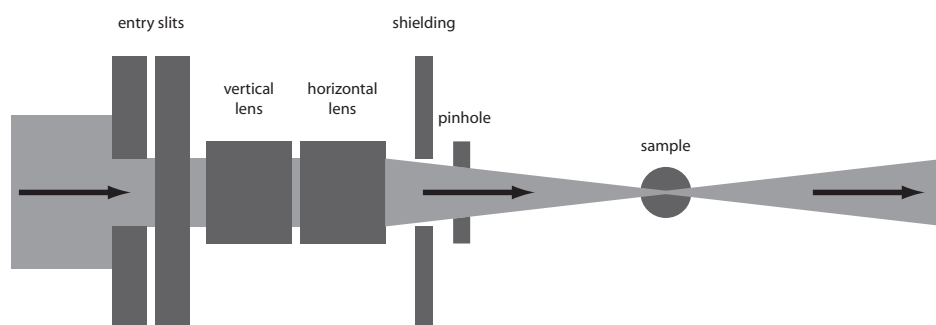


Figure 5.2: Nanobeam setup for the hard x-ray scanning microscope. The incident beam is restricted to a size slightly larger than the geometric aperture of the nanofocusing lenses by a pair of entry slits. Then the x-rays pass the vertically and the horizontally focusing lenses and are focused onto the sample. Background from elastic and inelastic scattering is reduced with means of a small pinhole and additional shielding placed between the exit of the lenses and the sample.

5.1.1 Nanofocusing Lenses

The nanofocusing lenses are the heart of the hard x-ray scanning microscope. They are the responsible component for generating the nano sized intense x-ray focus. Since a single NFL does only focus in one dimension, creating a line focus that is small in one direction but is unfocused in the other direction, a vertically focusing lens and a horizontally focusing lens must be operated in crossed geometry to generate a circular focus (see Figure 4.2 in chapter 4). The lenses must be aligned relative to the direction of the incident beam and relative to each other. Each lens, considered as a mechanical rigid body, has got 6 degrees of freedom (3 translations and 3 rotations), resulting in 12 degrees of freedom for the lens alignment. Implementing motorized stages for 12 degrees of freedom is not so easy, as there are stringent boundary conditions for mechanical precision, travel range and most notably for the amount of space occupied by the stages. Mechanical stability is important in order to guarantee a focus, which is stable for a very long time of hours, days and even weeks. The travel range must be large enough to be able to move all the lenses residing on a single lens wafer into the beam. The lenses, their holders and all the lens stages must be very compact and small leaving sufficient space for the tomographic sample stages and for all kinds of detectors. Fortunately, not all of the 12 degrees of freedom have to be implemented as motorized stages, because some of them are redundant. A movement along the optical axis, for example, is only necessary for one of the two lenses, while the other lens can be fixed to the setup. This is because a movement along the optical axis is only needed for matching the vertical and the horizontal focal planes and for this means one of the two lenses can be moved relative to the other one. Also a rotation around the optical axis has to be implemented for only one of the two lenses. Although the vertical and the horizontal lens must be aligned orthogonal to

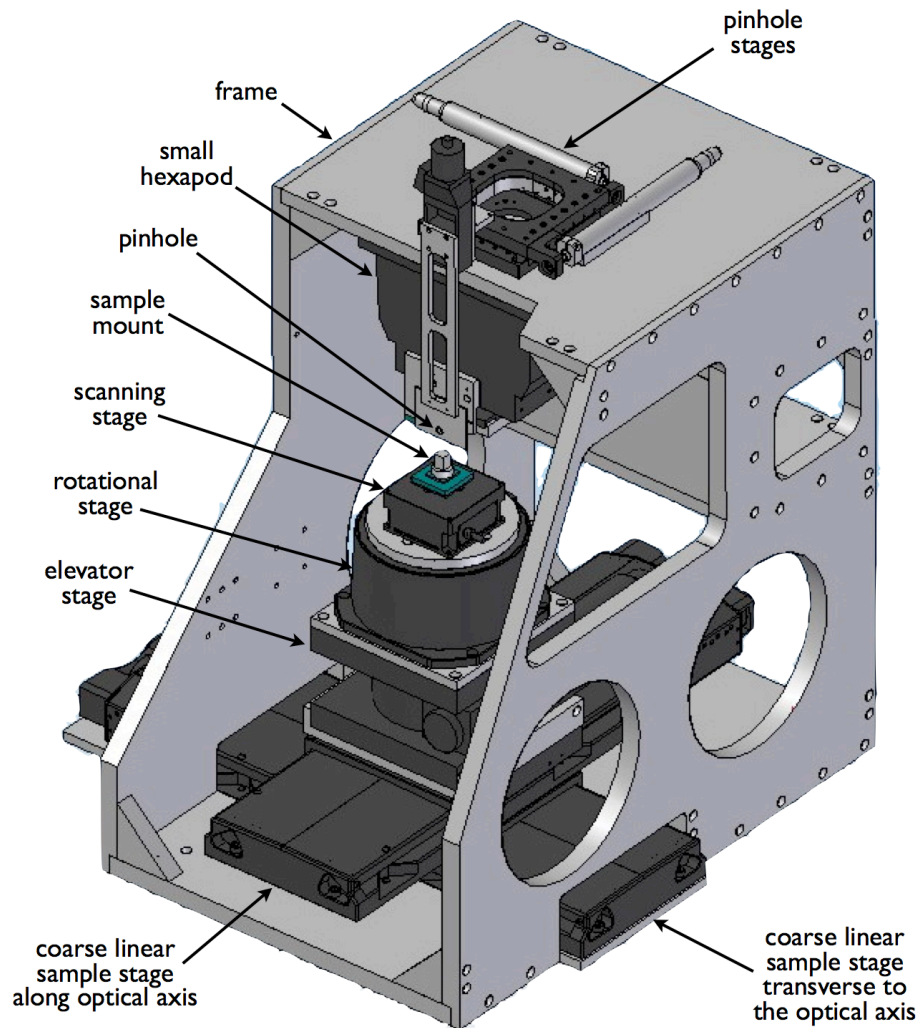


Figure 5.3: Schematic drawing of the scanner unit that I constructed during this thesis. A stiff frame contains the x-ray optics and the sample stages. At the ESRF beamline ID 13 this frame is mounted on the top of a large hexapod table, which is used to align the horizontal lens. The vertical lens is aligned with the small hexapod that is fixed head down at the roof of the frame. The aperture defining entry slits are hidden behind a metallic plate connecting the left and the right side walls of the frame. Not shown is the shielding between the NFLs and the pinhole.

each other with high precision,¹ a tilt of the lenses around the optical axis with respect to the undulator is not very critical. Thus, only a relative tilt is needed and the tilt around the optical axis can be omitted for one of the two lenses. In contrast to the translation along the optical axis, translations transverse to the optical axes have to be provided for both lenses. For just crossing the two lenses, only one of the two lenses needs to be moved in transverse

¹In order to avoid critical aberrations of the focus the deviation of the angle from 90° must be smaller than about $10 \text{ mrad} \approx 0.5^\circ$.

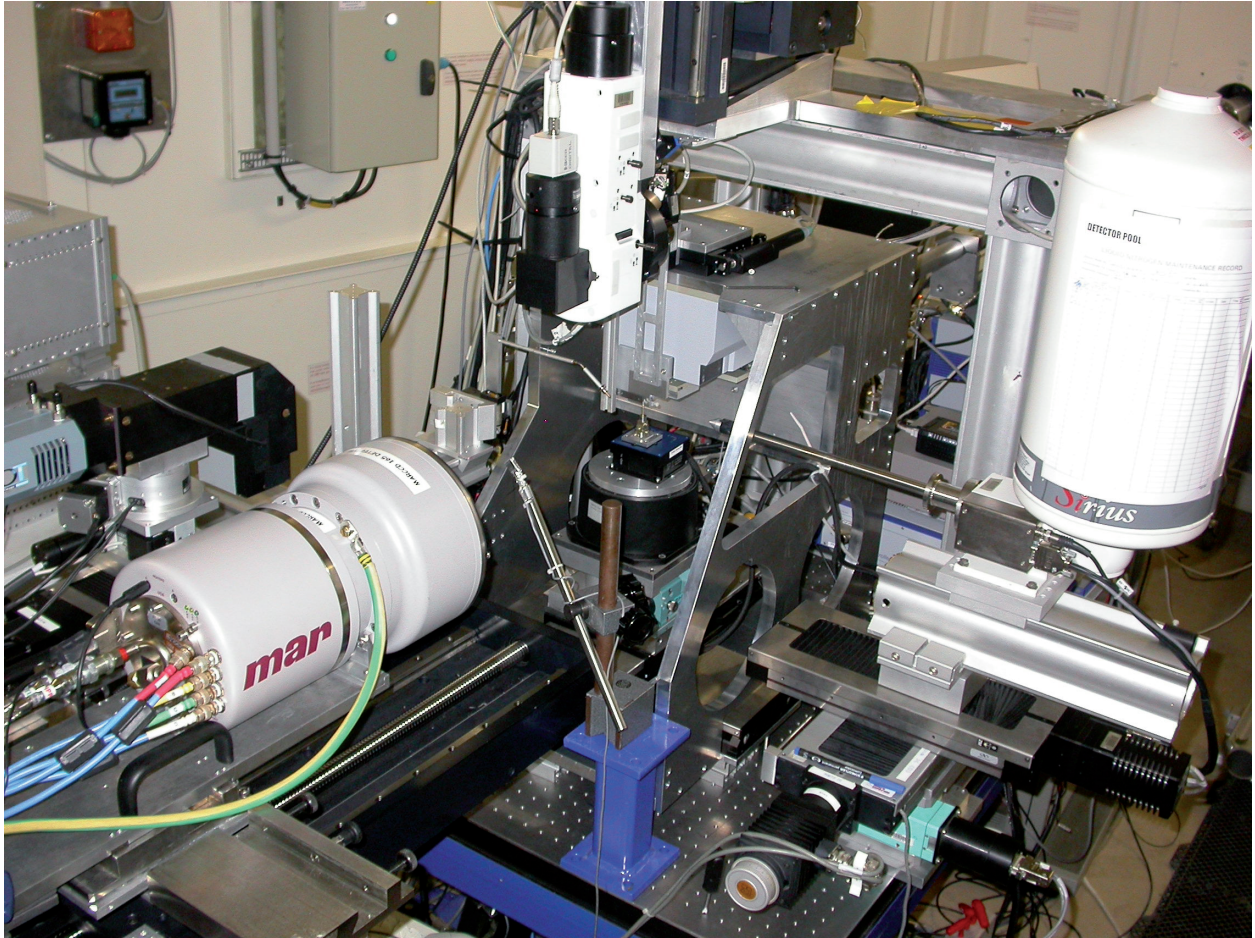


Figure 5.4: Photograph of the nanoprobe setup at ESRF beamline ID 13. The scanner unit in the center of the image is surrounded by a large number of detectors like a diffraction camera (MAR CCD), a high resolution x-ray camera (on the left of the MAR CCD), an energy dispersive Si(Li) detector (on the right side with a large box for liquid nitrogen), a PIN diode, and a visible light microscope.

direction, but the crossed lenses must still be moved into the beam and to an area of the beam, which is sufficiently homogenous and free of structures caused by inhomogeneities of the monochromator. Therefore, 2 degrees of freedom must be implemented as linear stages for each of the 2 transverse directions. It is the same with the tilts around the transverse axes. The optical axis of the vertical lens and the optical axis of the horizontal lens must both be parallel to the direction of the incident beam. To orient a linear axis parallel to a given axis, tilts around 2 axes are needed. Finally 10 degrees of freedom remain to be implemented, as there are 1 linear axis along the optical axis, 1 tilt around the optical axis, 4 linear axes transverse to the optical axis and 4 tilts around axes transverse to the optical axis.

In the current version of the nanoprobe we forego the implementation of a tilt around the optical axis. This is because we hold that it should be possible to pre-align the lenses so that

the deviation from 90° of the crossing angle between the vertical and the horizontal lens is small enough to avoid disturbing distortions of the wave field. Recent experiences showed that this assumption is not true. The precision of the pre-aligned lenses was not sufficient, thus we reintegrated the missing tilt around the optical axis for one of the two lenses.

Whether to integrate 10 motorized axes or only 9 axes, implementing such a number of motorized axes in the setup and still leave enough space for the tomographic sample unit for all the detectors around the sample and for all kinds of shielding, slits and pinholes necessary for a clean beam is a great challenge. Compact and mechanically precise motorized stages have very small travel ranges and stages with sufficiently large travel ranges are quite large and space consuming. In order to alleviate this situation, only one of the two lenses (the vertical one) is provided with motorized stages and can be aligned directly. The other lens (the horizontal one) has to be aligned moving the whole table on which the setup is mounted. At the ESRF beamline ID 13 the nanoprobe setup is mounted on a big hexapod table providing the necessary degrees of freedom. The horizontally focusing lens is firmly fixed to the frame of the nanoprobe and can be moved and tilted with the big hexapod table. After this lens has been moved into the beam and its orientation has been aligned, the vertical lens can be aligned as well, moving this second lens independently from the first one. Instead of building up a tower of single axes, a Stewart platform provides the necessary degrees of freedom for the vertical lens. The small precise hexapod (F-206.S0 from *Physik Instrumente GmbH*) is mounted head down from the roof of the frame leaving space in downstream direction and foremost space under the lenses for the sample stages and the mass of detectors (see Figure 5.3).

5.1.2 Entry Slits

The transverse beam size in the incident aperture plane of the nanofocusing lenses is several millimeters, whereas the geometric aperture of the lenses has a size of only $40\ \mu\text{m}$. For this reason, a double slit with tungsten blades is placed just before the incident aperture plane of the nanofocusing lenses, which is used to limit the beam to a size corresponding the geometric aperture of the NFLs. Without this aperture defining double slit the regions of the beam not passing through the lens aperture would generate disturbing scattering.

One issue to consider if designing slits for hard x rays is to avoid external total reflexes from the blade surface. Due to the relatively large attenuation length, the blades need a relatively large thickness even for materials with high atomic numbers like tantalum or tungsten. To avoid external total reflection, the blades are tilted by an angle of about 2° (see Figure 5.5).

5.1.3 Pinhole

Behind the exit of the second lens a small pinhole is installed to absorb all photons not coming from the exit aperture of the two crossed lenses. The pinhole is made of platinum and has a diameter of $16\ \mu\text{m}$ and a thickness of $250\ \mu\text{m}$ along the optical axis. The diameter

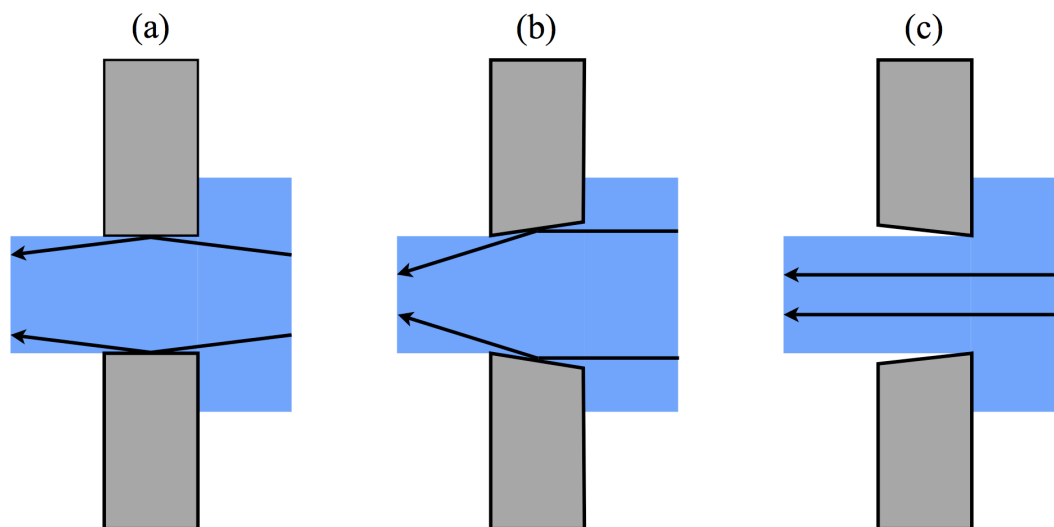


Figure 5.5: Blade geometry for avoiding external total reflection. (a) External total reflection on the blade surfaces has to be avoided. (b) If tilted in the wrong direction, total reflection gets stronger. (c) This geometry avoids external total reflection.

of the pinhole is chosen such that the size of the converging beam at the position of the pinhole is slightly smaller than the pinhole diameter, thus only photons are absorbed, which originate from scattering at the wafer substrate of the nanofocusing lenses. With other words, the pinhole does not function as a beam constraining aperture. Instead it cleans the beam of those photons, which have do not contribute to the focal spot.

5.1.4 Additional Shielding

In order to have a clean beam free of elastically and inelastically scattered photons, additional shieldings are inevitable. With test experiments it could be shown, that entry slits and the pinhole alone are far from generating a nice clean beam. Diffraction patterns recorded with a diffraction camera 2 m behind the sample were superposed by transmission images caused by photons scattered on the lens holder and on the substrate of the lens wafer. Installing tantalum and lead shieldings between the pinhole and the sample, these background photons vanish. The shielding is very effective. It even allows to remove the collimator of the energy dispersive fluorescence detector without introducing additional background. Omitting the shielding, the fluorescence spectrum without a collimator is dominated by background due to elastic and inelastic scattering. In the current nanoprobe version a stainless steel shielding is located between the nanofocusing lenses and the pinhole.

5.1.5 Vacuum and Helium Tubes

If x rays propagate in air, one important issue is absorption and air scattering. This is a problem especially for low x-ray energies. Synchrotron beamlines deal with this problem

with long evacuated tubes inside which the x-ray beam propagates from the source to the experiment. At soft x-ray beamlines, the whole experimental setup must reside in such vacuum tubes, as the penetration depth of soft x rays in air is in the range of few millimeters or less at normal air pressure. For hard x rays, absorption and air scattering are much weaker. Thus, vacuum tubes (or tubes filled with helium) are only necessary for long propagation distances of several meters. Short distances may be left in air, making experiments less difficult, because optical components or the sample can be changed or removed much easier if they are not kept inside vacuum chambers. Beyond that, not all components of the setup need to be capable for vacuum, which, for instance, alleviates the demands on motorized moving stages. In case of the hard x-ray scanning microscope, the x rays are guided through vacuum tubes on their complete path from the undulator source to the entry slits of the microscope. The monochromator and the prefocusing lenses reside in vacuum chambers. In opposition to the distance between the undulator source and the entry slits (about 45 m), the propagation path between the entry slits of the scanning microscope and the sample position — given by the position of the focal spot — is very short (less than 0.30 m). This distance includes both lenses (the horizontal and the vertical), the pinhole, and the shielding. For this reason, the x-ray beam propagates in air from the entry slits to the sample position. Air scattering is still negligible at this rather short distance as long as the energy is high enough (larger than 10 keV). The propagation path from the sample to the detectors is also free from vacuum tubes. The only critical situation occurs if far field diffraction images have to be recorded at a distance larger than about 1 m from the sample. Performing such experiments requires a vacuum tube or a tube filled with helium between sample and diffraction camera in order to avoid air scattering. Recently, a very flexible helium filled tube has been built, which can be mounted between the sample and the diffraction camera.

5.2 Sample Stages

In the previous section the optical components of the hard x-ray scanning microscope were discussed. Now I would like to come to the sample part of the nanoprobe setup. The mechanical demands on the stages for sample alignment and sample scanning are very challenging. It must be possible to move the sample relative to the focus along 3 linear axes, namely along the optical axis and transverse to the optical axis in horizontal and in vertical direction. In addition, there must be the possibility to rotate the sample around a vertical axis with a range of at least 360° . This is important for orienting crystalline samples in diffraction experiments and over and above for tomography experiments.

5.2.1 High Resolution Scanner

The spatial resolution of scanning experiments depends not only on the focus size, but also on the precision and the mechanical resolution of the scanning stages. In order to gain a sufficiently high sampling, the spatial resolution of the scanner should exceed the focus size. The present nanofocusing lenses used in the scanning microscope promise theoretical focus

sizes down to about 30 nm. Thus, a scanning step size of a few nanometers would give an appropriate sampling and, therefore, the scanner should be capable of a mechanical resolution in that range. In addition to mechanical resolution, also position accuracy and bidirectional repeatability of the scanning stage must be as good as possible. When scanning along a certain direction, it must be guaranteed, that positional deviations along the other directions are insignificant. If moved away from a certain position and returned, the deviation from the previous position must be negligible in the range of nanometers. There are commercially available scanners specified for such high performances, but those scanners have always very small travel ranges. Precise scanners with large travel ranges are very difficult to build and are therefore very expensive. The travel range of the sample scanner in the nanoprobe must be large enough to get the region of interest of the sample into the focus and to cover a sufficiently large scanning region. The piezo-electric scanner used in the nanoprobe (NanoCube P-615 from *Physik Instrumente GmbH*) features a travel range of $300 \times 300 \mu\text{m}^2$ horizontally and $250 \mu\text{m}$ vertically. Its resolution is 0.5 nm, and the repeatability is specified as 4 nm in closed-loop mode.

5.2.2 High Precision Rotational Stage

In order to make the nanoprobe capable of tomography, there must be the possibility to rotate the sample around a fixed vertical axis. Therefore, the scanner stands on top of a high precision rotational stage with air bearing (UPR-160 F AIR from *Micos GmbH*). Besides a sufficient angular resolution, very small wobbling, and a low eccentricity, this rotational stage stands out with an extreme low deviation in vertical direction while performing rotations. This feature is important particularly with regard to tomography, because raising and lowering the sample for different rotation angles introduces artifacts in the reconstructed tomograms.

5.2.3 Coarse Linear Stages

The rotational stage sits on a lifting stage, which is mounted on two crossed linear stages. These three stages are not as precise as the scanner and, therefore, they are not appropriate for fine scanning. But their travel range is quite large and helps to position the sample if its distance from the focus is larger than the travel range of the scanner. These linear stages are also useful for coarse scans. Furthermore, the horizontal linear stages are used to move the axis of rotation of the rotational stage relative to the focus. This is not possible with the scanner, because it sits on the platform of the rotational stage, so it moves the sample relative to the center of rotation, but it does not move the center of rotation relative to the focus.

5.2.4 Goniometer Head

The sample itself is mounted on the top of a small goniometer head, which is fixed on the scanner. The goniometer head provides the possibility to manually align the tilt of the

sample and to move it in horizontal direction. Together with a telescopic microscope, which is fastened on the frame of the setup, the sample can be brought to the travel range of the scanner. During the course of the development it turned out that the goniometer head is not very stable. It was then substituted by a magnetic kinematic mount without a manual tilt and without a translation. The loss of flexibility is required by a much better stability.

5.3 Detectors

Besides the scanner unit with its optical components and the sample stages, a number of different detectors is required. Detectors are needed for the lens alignment, for measuring the photon flux in the focus, for recording the fluorescence spectrum in element mapping experiments, for performing knife-edge scans, for recording diffraction patterns and for many more issues. There does not exist a universal detector, which is able to cope with all those kinds of tasks. A high resolution x-ray camera, for example, can record intensity distributions with a quite good spatial resolution, but it does not work energy dispersively. Energy resolving detectors, on the other hand, are well-suited for recording fluorescence spectra, but they are not position sensitive. Diffraction cameras cover a large solid angle and come with high quantum efficiencies but, due to their large pixel size, the spatial resolution is not so satisfying, and so on. For this reason, a lot of different detectors are employed with the hard x-ray scanning microscope. In this section, the detectors, which are used in many experiments with the hard x-ray scanning microscope, are presented and described.

5.3.1 High Resolution X-Ray Camera

The high resolution two-dimensional x-ray camera is used for a lot of experiments, as for example tomography with absorption or phase contrast. Moreover, the high resolution x-ray camera is essential for monitoring the alignment of the nanofocusing lenses, as treated in chapter 6.1.

A schematic sketch and a photograph of the high resolution x-ray detector are shown in Figure 5.6. The detector consists of a mono-crystalline scintillator, a visible light microscope, and a CCD camera. While the optically active layer of the scintillator (*sensitive layer*) converts the incident x rays into visible light photons, the visible light microscope generates a magnified image of the sensitive layer of the scintillator on the chip of the CCD camera [SBW⁺02, GTE02, Pat03]. The spatial resolution of this kind of detector is determined by the thickness of the sensitive layer of the scintillator, by the numerical aperture of the objective, and by the pixel size of the charge-coupled device (CCD). A high spatial resolution requires an objective with a large numerical aperture and thus with a very small depth of focus. The light sensitive layer of the scintillator must be at least as small as the depth of focus but, on the other hand, absorption of the incident x rays depends on the thickness of the scintillator, and if the sensitive layer of the scintillator becomes too thin, the detector becomes ineffective. Because of this, a compromise between high spatial resolution and high quantum efficiency has to be found. The pixel size of the CCD must be small enough to

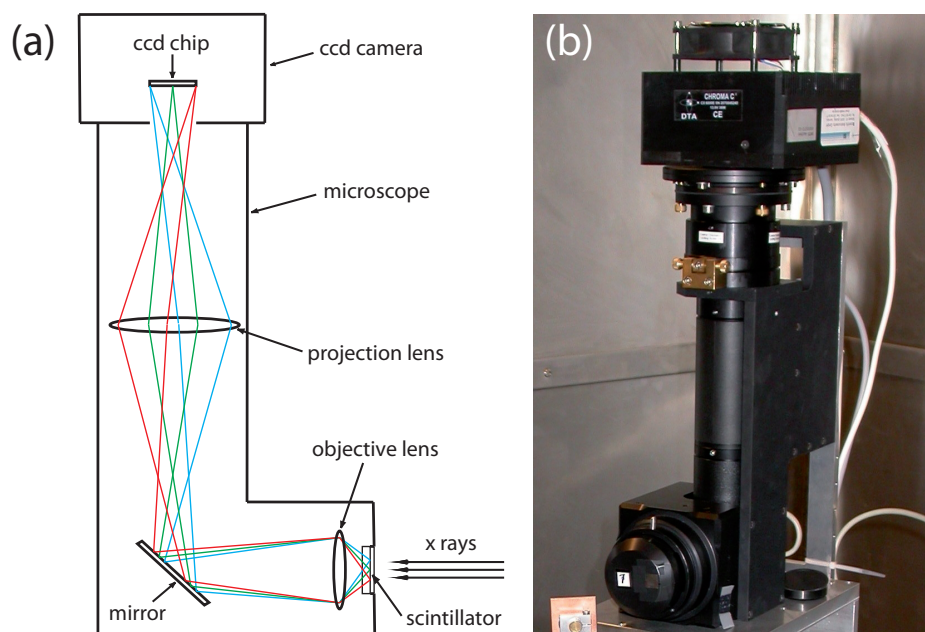


Figure 5.6: High resolution x-ray camera. This area detector is used for the alignment of the nanofocusing lenses, for highly resolved farfield measurements, and for absorption tomography. (a) Schematic drawing of the high resolution x-ray camera. A single crystal scintillator converts the incident x rays into visible light. The sensitive layer of the scintillator is magnified onto a charge-coupled device (CCD). (b) Photograph of one of the high resolution x-ray cameras that are used in the hard x-ray scanning microscope. (drawing and photograph from [Pat03].)

allow a sufficient sampling of the magnified image, but the full-well capacity decreases if the pixels become too small, and then the effective dynamic range is affected. In the end, the scintillator thickness, the objective and the pixel size must be well balanced and have to be adapted to the specific needs of the experiment. For this reason, the high resolution x-ray detector of the scanning microscope is provided with a set of different scintillators and with several objectives, which can be changed easily with an objective revolver.

The scintillators used in the high resolution x-ray camera are mono-crystalline LAG² wafers doped with europium and were fabricated by CEA Lety in Grenoble/Lyon. The thickness of the substrate is 170 μm , and the europium-doped active layer has a thickness of several micrometers (5 μm , 10 μm , 20 μm , and 50 μm). The europium converts the incident x-ray photons into visible light with a wavelength between 580 nm and 700 nm. Most front illuminated CCD chips have their maximum of sensitivity between 600 nm and 750 nm. Therefore, europium is an appropriate dopant element for the high resolution x-ray camera. Moreover, LAG:Eu has a quite low afterglow, which is important for fast exposures [KPH⁺99].

In order to guarantee aberration-free images, high quality objectives from Olympus are used to magnify the sensitive layer of the scintillator onto the CCD chip. The four objectives

²Lutetium aluminium garnet $\text{Al}_5\text{Lu}_3\text{O}_{12}$ is a ceramic material.

have magnifications of $2\times$, $5\times$, $10\times$ and $20\times$. In combination with the $2\times$ projection lens, total magnifications between $4\times$ and $40\times$ are possible. To protect the CCD chip from high energetic x-ray photons, the optical path is deflected by a tilted mirror. The microscopic optic has been developed and manufactured by *OptiquePeter* in cooperation with the detector group of the ESRF.

The technical demands on the CCD camera are very challenging. On the one hand, the pixel size must be as small as possible in order to achieve sufficient sampling of the image provided by the visible light microscope. On the other hand, a high dynamic range is required and, therefore, the full-well capacity must be as high as possible, in contradiction to a small pixel size. We decided in favor of a camera with a very small pixel size of $9\ \mu\text{m}$. For situations without the need for highest resolution, the pixels can be hardware-binned, increasing the full-well capacity and decreasing readout time. Because the high resolution x-ray detector is often used for long-time exposures, dark current shot noise becomes relevant and must be suppressed by cooling the CCD chip. For the nanoprobe project, two different scientific low noise CCD cameras were bought, a Chroma C3 with a Kodak KAF-9000 chip from DTA and a pco.4000 with a KAI-11002 chip from PCO, both with a pixel size of $9\ \mu\text{m}$. The resolutions are 3072×2048 pixels for the DTA and 4008×2672 for the PCO camera. Both cameras are provided with an ADC unit that delivers a digital dynamic range of 14 bit. The major advantage of the pco.4000 against the DTA is the very high frame rate of up to 5 frames per second at highest resolution, allowing life-view of images, which is especially useful for the alignment of the nanofocusing lenses.

The LAG:Eu scintillator emits visible light photons with a wavelength of about $700\ \text{nm}$, and the numerical aperture of the $20\times$ objective is 0.7. Thus the theoretical resolution of the microscope can be estimated to about $\lambda/(2NA) = 700\ \text{nm}/1.4 \approx 500\ \text{nm}$. The $9\ \mu\text{m}$ pixels of the CCD chip sample the scintillator plane with an effective pixel size of $9\ \mu\text{m}/40 = 225\ \text{nm}$, which is quite adequate for an expected resolution of $500\ \text{nm}$. Systematically performed detector tests showed that the actually attained resolution is about $800\ \text{nm}$ [Pat03].

The usage of a visible light microscope in connection with a thin sensitive scintillator layer for high spatial resolution is dearly bought with a low detective quantum efficiency (DQE). Detective quantum efficiency of a detector is defined as the square signal-to-noise ratio (SNR) at the output (digital CCD image) relative to the square SNR at the input (incident x-ray flux density distribution). DQE is a measure of how much the SNR is decreased by the system and is 1 if the SNR is preserved and 0 if there is no information left in the output. The DQE of an optically coupled scintillator is typically quite low. Dependent on the x-ray energy, DQE values between 0.02 (30 keV) and 0.05 (10 keV) are achieved, i. e., the square SNR of the resultant image is a factor 20–50 lower than the square SNR of the incident x-ray flux density.

In case of observing the lens alignment, the camera is placed several millimeters behind the lenses to yield a sharp near-field transmission image of the lenses. The high resolution x-ray camera can also be used to record the far field image of the nanofocusing lenses or the far field speckle patterns of coherently illuminated samples in coherent x-ray diffraction imaging experiments (CXDI). For this reason the camera is mounted on a long translation

stage, capable of moving the camera from the near-field to the far-field region of the focused beam.

5.3.2 Diffraction Cameras

Besides a high resolution x-ray camera, a diffraction camera with large pixels and high detective quantum efficiency is also needed for many experiments. Diffraction experiments with the nanoprobe described in this thesis have been carried out with a MAR CCD 165 and a FReLoN 4M16, both featuring low dark current, high detector quantum efficiency, and a large sensitive area of about 165 mm and 100 mm for the MAR CCD and the FReLoN, respectively. In addition, a noiseless photon counting area detector (MAXIPIX) is employed [PCR⁺07]. Like the high resolution x-ray camera, the diffraction cameras can be moved from near-field to far-field geometry. In experiments hutch EH2 at beamline ID 13 of the ESRF, the detector table can also be moved across the floor on air pads, allowing the measurement of large diffraction angles by moving the table in accordance to the direction of interest (for example in the direction of an expected Bragg reflection).

MAR 165 CCD camera

The key elements of the MAR CCD detector are a poly-crystalline scintillator screen, a 4096×4096 high grade CCD chip and a taper optic that couples the scintillator to the CCD. The problem with x-ray diffraction cameras is the need for large sensitive areas, while the commercially available CCD chips are limited in their lateral size. The MAR CCD detector solves this problem with a demagnifying taper optic, that guides the visible light photons from the large scintillator plane onto the rather small CCD chip. The pixel size of the CCD is $15 \mu\text{m}$, but the minimal hardware-binning is 2×2 . The demagnification factor of the taper optic is specified with $2.7 : 1$, and thus the effective pixel size in the scintillator plane is $80 \mu\text{m}$ and the diameter of the sensitive area results in 165 mm. The scintillator is made of high density gadolinium oxysulfide doped with Terbium ($\text{Gd}_2\text{O}_2\text{S}$). The taper optic is a bundle of many single fibers guiding the visible light photons from the scintillator to the CCD by total reflection. The arrangement of the fibers at the scintillator side of the fiber optic slightly deviates from the arrangement at the CCD side. This introduces image distortions, which are corrected automatically by the camera software.³ The CCD chip is cooled down to a temperature of -80°C , reducing the dark current to a very low level. This allows the camera to be operated for very long exposure times up to several hours without disturbing dark current shot noise. Thanks to very low read-out noise of only 9 electrons rms⁴ and an extremely high detective quantum efficiency of up to 0.80, it is possible to detect single x-ray photons. The rather large pixel size of $30 \mu\text{m}$ results in a quite large full-well capacity of

³ The manufacturer of the MAR CCD camera specifies the distortions fiber by fiber, resulting in a distortion map, which is used by the software for image correction.

⁴ The conversion factor of the MAR CCD detector is about 8 electrons per single 15 keV x-ray photon. Therefore, the 9 electrons relate to only one single x-ray photon!

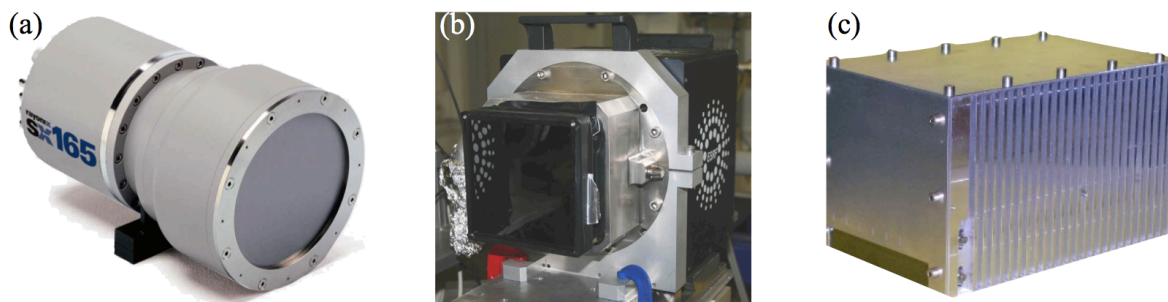


Figure 5.7: Diffraction cameras that were used in nanoprobe experiments. (a) Photograph of a MAR CCD 165. (b) The (**F**ast **R**eadout **L**ow **N**oise) FReLoN 4M is an in-house development of the ESRF. (c) The MAXIPIX is a noiseless photon counting area detector based on the Medipix2 CMOS pixel read-out chip with $55\ \mu\text{m}$ pixel size. Like the FReLoN 4M, the MAXIPIX is an in-house development of the ESRF. (Photo courtesy of Rayonix LLC and Marresearch GmbH.)

400 000 electrons per 2×2 binned pixel. Together with the low readout noise of 9 electrons rms, an effective dynamic range of 15 bit is achieved.

FReLoN 4M16 camera

As an alternative to the MAR CCD detector, a FReLoN 4M16 x-ray camera was applied to carry out diffraction experiments. Like the MAR detector, the FReLoN diffraction camera consists of a scintillating phosphor screen, which is connected to a charge-coupled device via a demagnifying taper optic. The FReLoN (**F**ast **R**eadout **L**ow **N**oise) is a CCD camera developed by the ESRF detector group and is famous for its high readout speed in face of quite low readout noise. It is a very popular detector used at many beamlines at the ESRF. The FReLoN is available as a FReLoN 4M based on a Kodak chip KAF-4320 or as a FReLoN 2k, which is based on an Atmel chip 7899. Both versions come with 2048×2048 pixels, but while the FReLoN 4M can only be operated in full frame mode, the FReLoN 2k can also be run in frame transfer mode increasing readout speed by a factor 2. The 2k version with its very high frame rates is well-suited for time-resolved experiments [LMP⁺07]. In case of experiments that need fast readout but for which low noise is much more important, the FReLoN 4M is the better choice. The readout noise of the FReLoN 4M is only 15 electrons rms and the effective dynamic range is 16 bit while the readout time is still only half a second for an unbinned 2048×2048 image. With $24\ \mu\text{m}$ CCD pixel size and a demagnification factor of about 2, the effective pixel size on the scintillator screen is given by $50\ \mu\text{m}$.

MAXIPIX camera

In addition to the MAR CCD 165 and the FReLoN 4M, a MAXIPIX camera was used as a diffraction camera [PCR⁺07]. The MAXIPIX is a noiseless fast readout photon-counting pixel detector with a pixel size of $55 \times 55\ \mu\text{m}^2$ and a readout dead time of $300\ \mu\text{s}$. It is based on the Medipix2 chip [LCD⁺02]. In opposition to a CCD, each pixel of the MAXIPIX is an

individual stand-alone detector with complete readout electronics. No fluorescence screen is needed to convert the x rays into visible light, since the x rays are directly absorbed within the individual pixels. Like the FReLoN camera, the MAXIPIX was developed by the detector group of the ESRF and is not commercially available.

5.3.3 Energy Dispersive Detectors

A detector for energy resolved x-ray detection is inevitable for the scanning microscope, because fluorescence emission measurements are used not only for fluorescence element mapping and fluorescence tomography, but also for fluorescence knife-edge measurements and, most notably, as a means for finding the region of interest on the sample for all kinds of experiments. There are many kinds of energy dispersive detectors differing in energy resolution, accuracy, noise, maximal count rate, and so on. They are all based on the same physical principle of measuring the amount of charge created by the incident x-ray photon, which is expected to be proportional to the photon energy. The charge is measured as a time integral over the intensity of current, which serves as a criterion to sort the event into a multi-channel analyzer. The main kinds of energy resolving x-ray detectors are proportional counters, Silicon(Lithium) detectors (Si(Li) detectors) and silicon drift detectors. Proportional counters are gaseous ionization detectors that make use of the ionizing properties of x rays. The atoms of a gas are ionized by the x rays and the electrons are separated from the gas ions by an electric field generated by the voltage between two electrodes. The voltage is chosen such that the drifting electrons gain enough kinetic energy to ionize further atoms. This Townsend avalanche process leads to a large amplification of the signal. In contrast to the Geiger-Müller counter, the signal is still proportional to the amount of ions created by the incident x-ray photon and, therefore, it is proportional to the photon energy. Proportional counters are the low cost end of energy dispersive detectors. They lack high detection performance, and hence they are not suited for fluorescence spectroscopy and other experiments to be carried out with the nanoprobe. Solid state detectors like Si(Li) detectors and silicon drift detectors are an order of magnitude more expensive than proportional counters, but they show advanced energy resolution, a better sensitivity, low dead times and very low non-linearity over a large energy range. For this reason, a Si(Li) detector and a silicon drift detector have been employed for the hard x-ray scanning microscope.

Sirius Si(Li) detector

Until the beginning of the year 2008, a nitrogen cooled Si(Li) fluorescence detector from e2v scientific instruments⁵ was used to record the fluorescence spectrum of the samples mounted in the nanoprobe. The main component of a Si(Li) detector is a wafer with two thin positively and negatively doped layers surrounding a thick silicon layer doped with lithium. Like in a PIN-diode, the x-ray photons are absorbed in the intrinsic silicon layer and create an amount of electron-hole-pairs. In contrast to the ordinary PIN-diode, a pulsed

⁵Formerly Gresham.

high voltage is applied on the electrodes in reverse direction in order to guarantee that all electron-hole pairs arrive at the electrodes without recombination. The time integral over the measured electric current is directly proportional to the energy of the x-ray photon, and a fast electronic device is able to feed a multi-channel analyzer with events of different energies. In order to prevent leakage current due to an excess of electron acceptors in silicon, the silicon layer is doped with lithium necessary for compensation of the surplus electron acceptors. Since the high voltage inclines the lithium atoms to diffuse to the cathode and to destroy the detector, Si(Li) detectors must be cooled with liquid nitrogen. The energy resolution of Si(Li) detectors is very good. The Mn K_α line emitted from an Fe⁵⁵ source⁶ appears as a peak with a full width at half maximum of 130 – 150 eV, which is much better than proportional counters are capable of. The maximum count rate of Si(Li) detectors is about 20–30 keps (kilo counts per second) and is limited by the relatively high capacitance of the diode. The Sirius Si(Li) detector has a sensitive area of 80 mm² and can be used outside vacuum. This is not self-evident, because the probe must be kept in ultrahigh vacuum. To be still able to use the Si(Li) detector on air, a thin entry window must be used that is transparent even for low energy x rays but which is stable enough to stand the normal pressure of 10⁵ Pa. The Sirius detector is provided with a several micrometers thick window of beryllium that limits the detection of elements with low atomic numbers. Nowadays, beryllium windows are substituted by ultra thin windows made of structured poly-ethylene, allowing detection of fluorescence light emitted from elements with very low atomic numbers like oxygen, nitrogen, or even carbon.

Vortex-EMTM silicon drift detector

Besides the Sirius Si(Li) detector, a Vortex-EMTM silicon drift detector (Vortex-EM from SII NanoTechnology USA Inc.) have been applied for the scanning microscope. Silicon drift detectors have some advantages over ordinary Si(Li) detectors. The x-ray absorbing layer of the drift detector is made of high-purity silicon instead of lithium doped silicon. As no lithium atoms can diffuse, liquid nitrogen cooling is not required. Cooling is only needed to prevent thermal background current, but for this means, a single stage Peltier element is sufficient. Another advantage of the silicon drift detector is the very high count rate capability without losing energy resolution. The problem with Si(Li) detectors is the relation between the anode capacitance and the size of the absorbing (sensitive) area. A sufficiently large sensitive area goes along with a large capacitance resulting in a low count rate capability. The silicon drift diode avoids this problem separating the absorbing (sensitive) area from the anode area. The electric field is no longer directed transverse the detector surface but parallel to it, driving the generated electrons from the absorption area to the anode. By this way, the size of the sensitive area is decoupled from the anode capacity, and large sensitive areas with small anode capacities can be produced with very high count rate capabilities. The energy resolution is comparable with that of Si(Li) detectors, but the

⁶ Fe⁵⁵ decays to Mn⁵⁵ by electron capture, leaving a vacant electron state in the K shell of the manganese atom. This state is filled by an electron from an energetic higher shell emitting a fluorescence photon.

maximum count rate of silicon drift detectors is more than one order of magnitude higher, reaching values of 500–1000 kcps. Further more, drift detectors do not show peak shifts at high count rates, which is a typical problem with Si(Li) detectors⁷.

5.3.4 Photodiodes

In the previous paragraphs, detectors were discussed, which are used in the hard x-ray scanning microscope for space-resolved and energy-resolved measurements of x-ray intensities. Now, I would like to introduce the photodiodes that are applied for measuring the photon flux of the synchrotron beam. Knowing the photon flux is essential for a lot of applications like alignment of pinholes, performing absorption knife-edge scans, or retrieving normalization signals in fluorescence experiments. Beyond that, it is very interesting to know the photon flux in the focal spot in order to estimate the necessary exposure time for certain scanning experiments with this focus. To measure the photon flux, the hard x-ray scanning microscope comes with a positive-intrinsic-negative diode (PIN-diode) and with an avalanche photodiode (APD), both of which are special types of photodiodes. Whereas the PIN-diode is a rather simple device and its application is quite straight forward, the APD is a high-tech counting detector with minimal dark current and high dynamic range.

PIN-diode

The PIN-diode (abbreviation for *positive-intrinsic-negative diode*) is a semiconductor detector made of a thin positively and a thin negatively doped layer, which are contacted by electrodes. Incident x rays are absorbed by the semiconductor and generate pairs of negatively charged electrons and positively charged holes. If this happens within the depletion region, the barrier voltage causes the charges to flow to the electrodes, and an electric current occurs that is proportional to the incoming photon flux. The current is very weak and has to be measured with a pico-amperemeter. Knowing the x-ray energy and the thickness of the absorbing layer, the absolute photon flux can be calculated from the current. Absorption of hard x rays in silicon is rather weak⁸. In order to increase the induced electric current, and thus to increase the signal-to-noise ratio, the depletion region has to be increased by inserting an intrinsic layer of weakly positively or weakly negatively doped silicon between the p and the n layers. This intrinsic layer can be made very thick (in the order of several hundreds of micrometers up to some millimeters), increasing the efficiency of the photodiode dramatically. The PIN-diode that is employed in our hard x-ray scanning microscope has a sensitive area of $10 \times 10 \text{ mm}^2$, and its current is measured with a Keithley 6485 pico-amperemeter.

⁷ Si(Li) detectors incline to have asymmetric peaks with long tails at the low energy side of the spectrum. This effect increases with higher count rates, shifting the center of the peak against low energies.

⁸The attenuation length of silicon is about $130 \mu\text{m}$ for 10 keV x rays.

Avalanche photodiode

Like the PIN-diode, the avalanche photodiode is a semiconductor detector and makes use of the electron-hole-pairs generated by incident x rays. An intrinsic absorption layer is surrounded by a positively and a negatively doped layer each contacted with electrodes. A reverse high voltage is applied to the electrodes inducing a depleted zone. The electron-hole-pairs generated by the incident x rays are separated and travel to opposite electrodes. The pulses can be registered and counted giving the flux of the incident radiation. Until this point, the detector does not differ from an ordinary PIN-diode. In the case of an avalanche photodiode, the reverse voltages is chosen high enough to set off an avalanche.⁹ This avalanche multiplies the charge arriving at the electrodes, and thus a gain is achieved. The gain depends on the bias voltage, on the geometry of the diode and on the semiconductor material. Typical gains for silicon diodes are values between 100 and 400, while the gain of germanium diodes is an order of magnitude lower. The high gain minimizes the influence of dark current shot noise, allowing the detection of single x-ray photons and thus to measure very weak x-ray fluxes. The APD¹⁰ that is used in the nanoprobe setup has got a sensitive area of $5 \times 5 \text{ mm}^2$ and a dynamic range of 10^8 .

5.4 Control Software

In the previous sections of this chapter I introduced and described the mechanical components of the hard x-ray scanning microscope. Now, I would like to come to the question of how to control all these components. The nanoprobe setup and all its mechanical components are located inside the experiments hutch, which is interlocked as soon as the hutch is exposed by the synchrotron beam. No human operator has access to the hutch during the experiment. For this reason, there must be the possibility to operate the scanning microscope remotely via an appropriate control software. Synchrotron radiation facilities around the world have developed different solutions to that problem. The whole control system with its user interface is part of the infrastructure of the beamline. The user coming to a beamline to perform an experiment usually familiarizes himself with the control software provided by the beamline. This is possible, because most of the hardware that has to be managed by the controlling system is part of the equipment of the synchrotron. In most cases the user brings along only the sample and the sample environment, all the other components are permanently integrated in the beamline setup. This is not true for the hard x-ray scanning microscope, the components of which do not belong to the beamline equipment. Instead of integrating the nanoprobe hardware into the beamline control system directly, a computer software was developed during this thesis, which allows to operate all the components of the nanoprobe independently from the beamline infrastructure. There are two main advantages of following this way. First, instead of being forced to integrate each single hardware com-

⁹ It has to be taken care that the voltage is kept below the breakdown voltage in order to be still in the proportional range.

¹⁰Bought from Oxford Danfysik.

ponent into the beamline control system, which requires a lot of hardware interfaces to be established between the nanoprobe and the beamline control system, we come to the beamline with a self-contained setup, which only needs one interface between our own control software and that of the beamline. Second, we are able to operate the complete nanoprobe setup independently from a special beamline or synchrotron. In principle, we could go to any beamline of any synchrotron in the world, and the only thing to do would be to establish a software interface between our control software and that of the beamline.

The software for controlling all components of the hard x-ray scanning microscope is called *accontrol* (ā-'sē-kən-'trōl). The advantage of a self-developed control software is the great flexibility, which one would not have with a commercial product. *Accontrol* provides a commandline user interface that can be used for entering commands interactively by a human operator. Typical commands would be asking for the positions of mechanical axes, moving a certain axis to a desired position, exposing a single detector or a set of detectors, performing scans in one or more dimensions, opening or closing shutters, and so on. Besides applying a large amount of built-in commands, the user can also create and use his own user-defined functions, combining built-in commands and other user-defined functions with means of control structures like loops, conditional clauses, etc. For this, a special interpreter language was developed during this work, following closely the syntax of the C++ programming language, which makes it very easy for the user to cope with the syntax.

Accontrol supports a large variety of hardware, which can be accessed via different communication interfaces like parallel port, usb port, rs232 port, PCI card or ethernet. Hardware that is hosted by a device server (such as TACO or TANGO [GPTV08]) or by other control systems like *spec*¹¹ or *online*¹² can be accessed via ethernet with special communication protocols. Rather than confronting the user with all those hardware communication details, the hardware is presented to the user in a most transparent way. For all motorized axes like stepper motors, hexapods, piezo stages, etc., *accontrol* provides a standardized user interface, therewith the user needs not to know the technical details of the hardware. Similar user interfaces exist for all kinds of detectors, loggers, shutters, etc.

Accontrol does not only operate in interactive mode, but can be also run in server mode and even in both modes at the same time. Server mode means that the program is listening for requests from remote clients and executes their commands. This way, all nanoprobe hardware can be accessed by other client software, for instance by *spec* or *online*.

Another feature of *accontrol* is the possibility to define sets of virtual motors. Virtual motors are axes with coordinates depending on a subset of real motors or other virtual motors. By this means various coordinate systems can be introduced. For example, the two linear stages mounted on top of a rotational stage change their direction with varying angles of the rotational stage, i. e., the system of coordinates is fixed to the rotating sample. If the sample has to be moved in a certain direction that is fixed in the laboratory (for example

¹¹ *spec* is a UNIX-based software package for instrument control and data acquisition widely used for x-ray diffraction at synchrotrons around the world and in university, national and industrial laboratories (<http://www.certif.com/spec.html>).

¹² *online* is a software to control instruments, perform data acquisition, and monitor measurements. It has been developed at HASYLAB, Hamburg (http://hasylab.desy.de/e2155/e9391/e3252/index_html).

along or transversal to the optical axis), both linear stages have to be moved dependent on the angle of rotation. To make this more comfortable, a set of two virtual axes can be associated with the two real linear stages, the coordinates of which are calculated via linear transformation of the coordinates of the real axes. Virtual axes are also very helpful for moving the two blades of an optical slit. Instead of dealing with blade positions directly, virtual axes can be defined, which are associated to the gap (distance between the blades) and the offset (central position between the blades) of the slit.¹³

¹³ The control software *accontrol* is available as C++ source code and can be retrieved from our cvs repository on request: patommel@nanoprobe.de.

Chapter 6

Experiments

In chapter 5, the design of the hard x-ray scanning microscope was described and the functionality of its components was explained. The nanoprobe is a prototype and still under development, but many successful experiments were carried out with this prototype version, and promising results were obtained so far. In order to demonstrate the performance of the instrument, I will present a selection of experiments. Each experiment makes use of a specific x-ray analytical method such as fluorescence element mapping, fluorescence tomography, nano diffraction, or coherent diffraction imaging. Before presenting these experiments, I would like to demonstrate the lens alignment process. Lens alignment is an important and crucial procedure and has to be carried out carefully in order to ensure a small and bright focal spot.

6.1 Lens Alignment

The strategy for aligning the nanofocusing lenses is to record transmission images of the lenses with a high resolution x-ray camera, and to continue tilting and moving the lenses until the transmission images indicate an adequate alignment (Figure 6.1). For this means, a large field of view of many millimeters is needed, thus the entry slits have to be widely opened, and the pinhole must be removed. Without the nanofocusing lenses the x-ray camera shows a more or less homogeneously bright image of the x-ray beam. Deviations from a homogeneous intensity distribution are caused by the monochromator or other optical components upstream and by inhomogeneities in the sensitive layer of the scintillator screen of the camera. Moving the silicon wafer with the micro-structured lenses into the field of view, parts of the image black out, because the silicon creates absorption contrast. The detector surface is several centimeters away from the nanofocusing lenses. This is close enough for sharp projection images but still too far away to avoid diffraction fringes.

At the beginning of the lens alignment procedure the lenses look as shown in Figure 6.1(a). The directions of the optical axes of the horizontal and the vertical nanofocusing lenses deviate from the direction of the incoming x-ray beam. This misalignment becomes manifest in a strong blurring of the projection of the bar code and of the lenses. The bar code

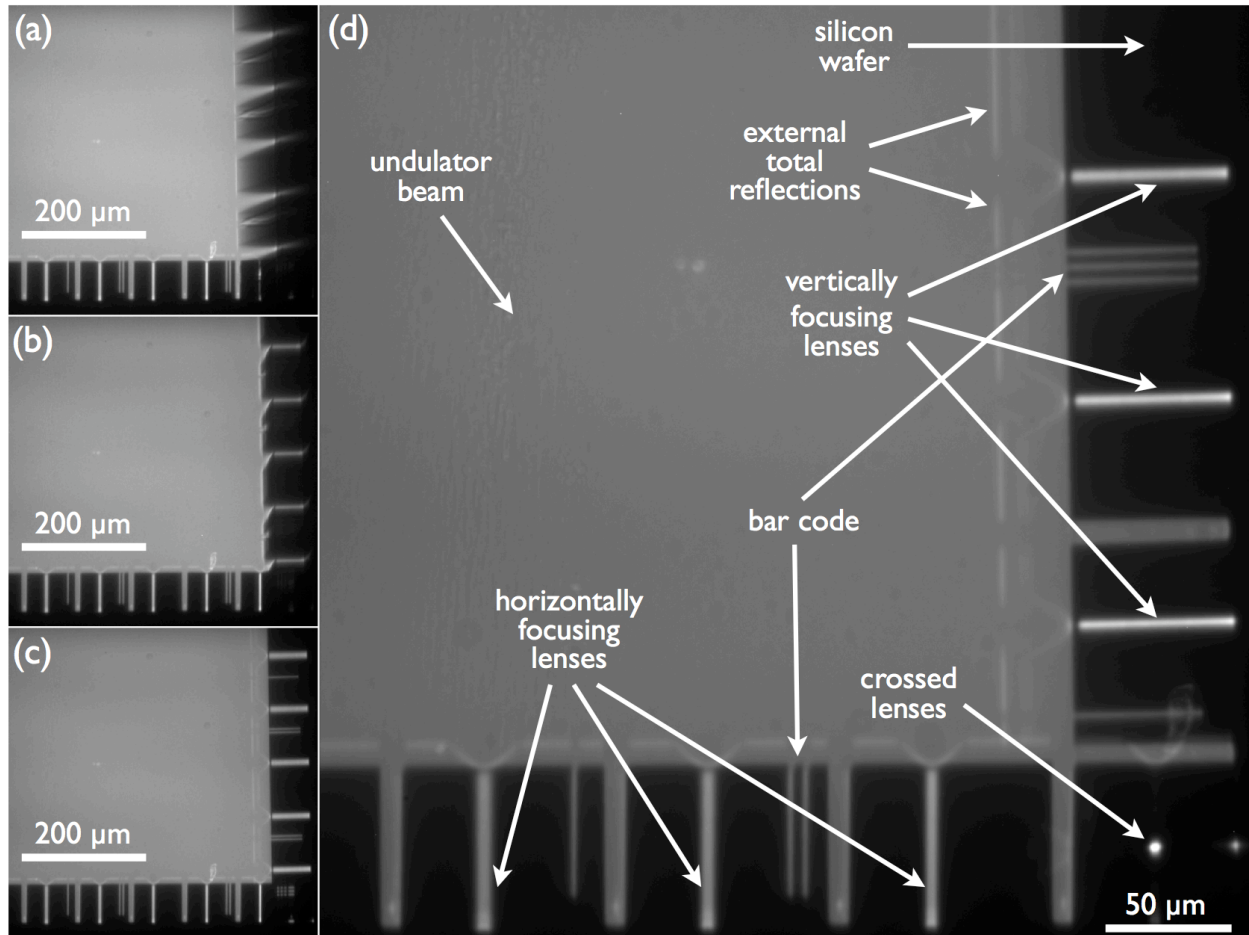


Figure 6.1: Projection images of nanofocusing lenses recorded with a high resolution x-ray camera during lens alignment. The large bright area is the synchrotron beam passing aside the lenses. The dark areas on the right and the bottom are projections of the silicon wafers containing the nanofocusing lenses. (a) The horizontally focusing lenses (bottom side) are well aligned, while the vertically focusing lenses (right side) are very much misaligned. (b) The vertical lenses have been tilted in pitch and yaw. Their projection images are getting better. (c) Both lenses, the horizontal and the vertical, are well aligned. (d) A horizontal and a vertical lens have been crossed displaying a small bright circular area at the right bottom edge of the image.

is required for identifying the different lenses that are present on a certain block of lenses. There are several features in the projection image, which can be used to find the correct tilt angles of the lenses. The wafer surface, for example, can generate a total reflection as long as it is not aligned in parallel with the beam direction. Tilting the wafer in the correct direction, the reflection angle becomes smaller and the distance between the interception of the reflected beam with the detector surface and the projected wafer surface decreases. Another criterion is the total reflection which is created by the side walls of the bar code. While the total reflection from the wafer surface helps aligning the angle around an axis parallel to the wafer surface, the reflection from the side walls of the bar code can be used to align the tilt around the axis that is orthogonal to the wafer surface. There are many

more criteria useful for aligning the lenses such as symmetry, shape of diffraction patterns and intensity inside the area of the lenses.

As discussed in chapter 5 the prototype nanoprobe setup allows direct alignment only for the vertical lenses. The horizontal lenses must be aligned moving the large hexapod carrying the scanner unit. Of course, by moving the complete scanner unit, not only the horizontal lenses, but also the vertical lenses are moved. Hence, the horizontal lenses must be aligned first, and after that, the alignment of the vertical lenses can be carried out. If the lenses are well aligned [Figure 6.1(c)], the lenses with the adequate curvature and proper number of single lenses can be chosen and crossed in order to form a point focus. The target lenses can be identified via the bar code which is arranged between the lenses. Figure 6.1(d) shows the final alignment with two crossed lenses located at the right bottom corner of the projection image. Now, the gap of the entry slits has to be closed as much as possible avoiding cutting into the geometric lens aperture,¹ and the pinhole must be moved to the position of the converging beam behind the crossed lenses. At that time, lens alignment is still not completed. The vertical and the horizontal lenses may generate foci at different positions along the optical axis. By varying the distance between the two lenses, it is possible to bring the horizontal and the vertical focal planes to a common position. For this means, the positions of the horizontal and the vertical focus have to be retrieved. This is done via knife-edge measurements as described in the next section 6.2. Knowing the distance between the two focal planes, the distance between the two lens wafers can be changed by that value. Depending on the precision of the stages, moving one of the two lens wafers along the optical axis may compromise the lens alignment. Therefore, the movement is monitored with the high resolution x-ray camera (of course, the pinhole must be removed and the gap of the entry slits must be wide opened again for a sufficiently large field of view). Up to now, we never observed the need for a realignment of the lenses after bringing the horizontal and the vertical focal planes together.

6.2 Focus Characterization

Once the nanofocusing lenses are aligned, the generated focus must be characterized concerning vertical and horizontal focus size, the caustic around the focus position, and photon flux in the focus.

In an experiment with the hard x-ray scanning microscope the specimen must be brought into the focus. For this means it is inevitable to know the focal position. Beyond that, the positions of the focal planes of the horizontal and the vertical lenses must be retrieved during the lens alignment procedure, in order to make the focal planes coincide. There are several methods to find the focal positions, such as absorption knife-edge scans, fluorescence knife-edge scans, fluorescence contrast scans, or ptychography.

¹In order to obtain a Gaussian transmission through the nanofocusing lens, the effective aperture of the lens must be dominated by absorption of the x rays in the lens material. This is not ensured, if the incident beam is constrained too much by the entry slits.

Apart from knowing the position of the focus, it is necessary to determine the horizontal and the vertical focus size. This can be done applying absorption knife-edge scans, fluorescence knife-edge scans, total reflection knife-edge scans [MYM⁺08] or, most notably, x-ray ptychography [SBF⁺10c].

6.2.1 Knife-Edge Scans

In a knife-edge scan a sharp edge with profile $d(p)$ is moved through the focus in transversal direction to the optical axis (horizontal or vertical), while the signal S (transmitted intensity or fluorescence intensity) is measured as a function of the knife-edge position p . The function $S(p)$ is given by the intensity distribution $I(x)$ of the x-ray beam convolved with the knife-edge function $K(p)$. In case of an absorption knife edge, the knife-edge function is given by the transmission function $K(p) = T(p) = \exp[-\mu d(p)]$, and in case of a fluorescence knife edge, it is directly given by the thickness $d(p)$ of the knife edge. The intensity distribution $I(p)$ can be computed by deconvolution of the signal function $S(p)$ with respect to the knife-edge function $K(p)$. If the knife-edge function is an ideal step function, the convolution $S(p) = I(p) * K(p)$ simplifies as a simple integral $S(p) = \int dp I(p)$, and the intensity distribution can be obtained by differentiating $S(p)$ with respect to the knife-edge position p . In case of an absorption knife edge the thickness of the knife edge must be of the order of the attenuation length, otherwise the contrast between the regions before and behind the edge becomes too low (compared to noise). For hard x rays, the attenuation length amounts to several micrometers even for elements with large atomic numbers. The beam size to be determined is about two order of magnitudes smaller, hence, a step function is not an appropriate approximation of such an absorption knife edge, and the signal has to be deconvolved with the knife-edge function. In opposition to an absorption knife edge, the contrast of a fluorescence knife edge is even large, if the thickness of the knife edge is only several tens of nanometers. The fluorescence knife edge utilized in the hard x-ray scanning microscope is a 30 nm thin gold film deposited on a Si₃N₄-membrane with a thickness of 200 nm. The very sharp edge of the fluorescence knife edge assures that the measured fluorescence signal is actually given by the integral of the intensity distribution, rather than by a convolution with the knife-edge function.

Figure 6.2 shows the result of a fluorescence knife-edge scan performed with the nano-probe setup in 2004 [SKP⁺05b]. In order to obtain sufficient sampling of the signal, the scan was performed with a step size of 10 nm. The continuous line through the measured data points is the least square fit of a double Gauss error function, assuming a Gaussian intensity distribution of the x-ray beam, superposed by background with Gaussian distribution. The dotted line in Figure 6.2 indicates the first derivative of the the double Gauss error function. The large thin peak represents the focal spot, whereas the low broad peak is caused by background and aberrations. The full width at half maximum sizes of the horizontal and the vertical foci are 47 nm and 55 nm, respectively, at a photon energy of 21 keV. With a storage ring current of about 200 mA a photon flux of 1.7×10^8 ph/s was achieved.

In order to obtain sufficient contrast, an absorption knife edge must be thicker than a

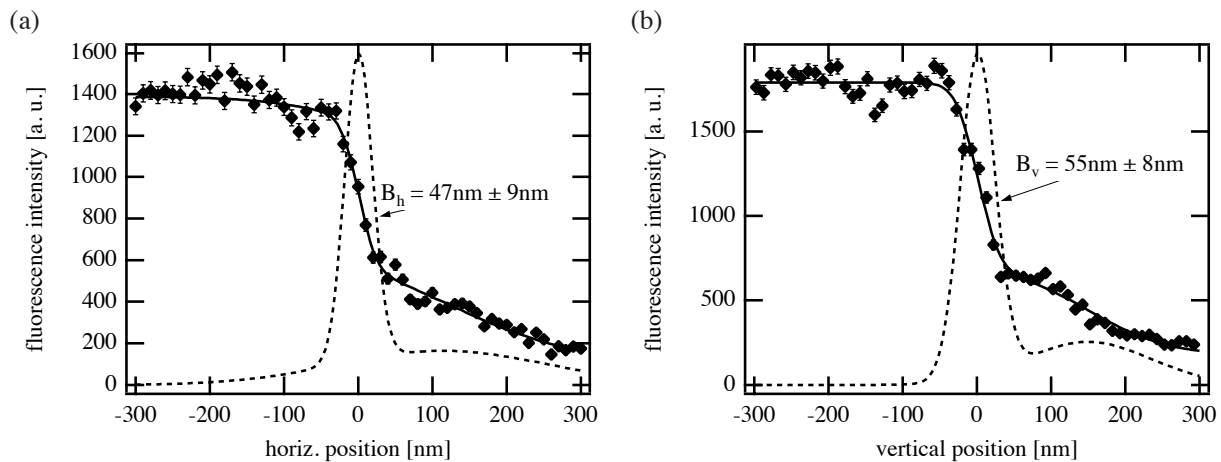


Figure 6.2: Results of a fluorescence knife-edge scan. (a) Horizontal, and (b) Vertical direction. The long tails to the right side of the edge are caused by aberrations of the nanofocusing lenses. (Reprinted with permission from [SKP⁺05b]. Copyright 2005, American Institute of Physics.)

fluorescence knife edge. Depending on the spatial resolution of the knife-edge scan, the measured transmission data must eventually be deconvolved rather than simply differentiated to obtain the intensity distribution of the beam. The spot sizes provided by the nanofocusing lenses in the hard x-ray scanning microscope are well below 100 nm, whereas the required thickness of absorption knife edges is at least one order of magnitude larger. Accordingly, deconvolution is essential in order to obtain the actual size of the x-ray beam. But the transmission signal contains noise, and the transmission function of the knife edge depends on the orientation of the knife edge, and thus evaluation of the data is quite difficult. If one is not interested in the absolute size of the beam, but wants to know the position of the minimal beam size along the optical axis, deconvolution is not required. Since absorption knife-edge scans need only short exposure times per scanning position, such scans are qualified for caustic measurements and quickly finding the position of the focal plane. In the hard x-ray scanning microscope we used a cylindric gold wire with 50 μm diameter for performing fast absorption knife-edge scans.

In addition to absorption and fluorescence knife-edge scans, there are other knife-edge techniques, exploiting other contrast mechanisms. One interesting technique is based on total reflection [STTT05, MYM⁺08] and is called *total reflection knife edge* or *dark-field knife edge*. The primary beam hits the surface of the knife edge with an angle smaller than the critical angle, giving rise to total reflection. The unreflected portion of the beam is blocked by a beamstop, and the intensity of the reflected beam is measured with a high resolution x-ray camera. Similar to fluorescence knife-edge scans, dark-field knife-edge scans provide signals which need not to be deconvolved even in case of measuring a very small nanobeam.

The relevance of knife-edge scans recedes, since we successfully introduced x-ray ptychography as a beam characterizing tool [SBF⁺10c], which allows to retrieve the complex

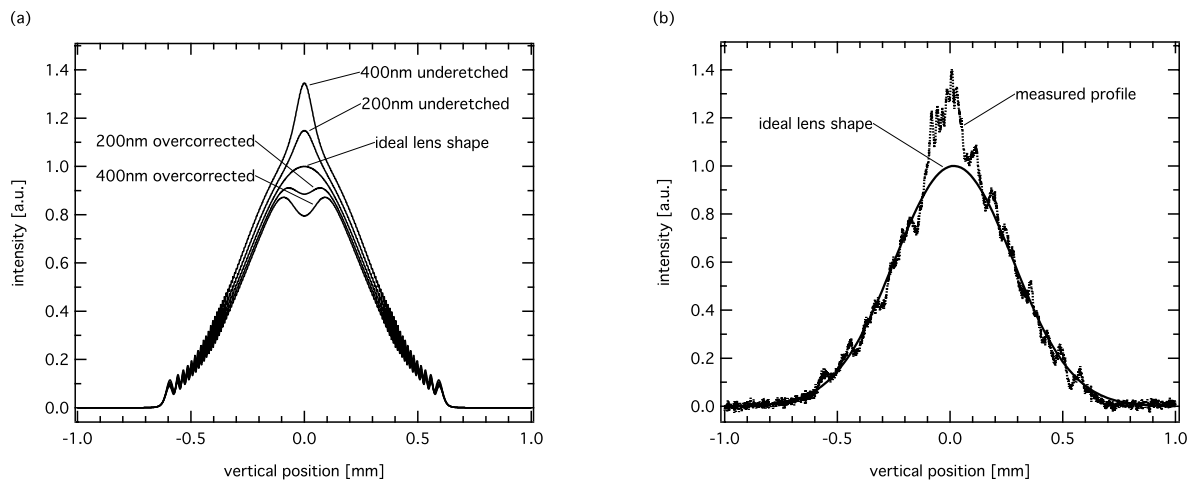


Figure 6.3: Vertical line profiles of the far-field image of the focus (distance of 1m between focus and detector). (a) Simulated data for different lens shape errors. The steep curves are the result of underetched lenses, whereas the broadened curves are caused by lenses of which the correction for underetching is too large. (b) Measured data. The curve shows a steep peak at the center indicating that the lens is not corrected enough for underetching.

wavefield of the region around the focus by evaluation of diffraction images from a scattering sample located in the focal plane.

6.2.2 Far-Field Measurements

In addition to knife-edge techniques, we employed far-field measurements to retrieve information about the x-ray nanobeam. In this method, a high resolution x-ray camera is used to record the far-field image of the nanofocusing lenses. According to Quiney et al. [QPC⁺06] the far-field image of a focus can be used to characterize the complex wave field around the focus. With a detailed model of the focusing optical system we are able to simulate the wavefields including shape errors and roughness of the lenses. Each distinct feature of the recorded far-field image can be associated with a characteristic property of the setup like slits, pinholes, lens shape, lens roughness, etc. Figure 6.3(a) shows the profile of the simulated far-field image of nanofocusing lenses with perfect smoothness of the lens surface (neglected roughness) but with different lens shape errors. The most significant aberrations result from the so-called underetching effect.² The nanofocusing lenses are corrected for this kind of shape error, but the correction parameters have to be determined by experiment. The profiles shown in 6.3(a) belong to simulations of lenses with different degrees of underetching. In Figure 6.3(b) the measured profile is plotted in comparison with the simulated profile of an ideal lens. Obviously, the lens is not enough corrected for the underetching effect. This

² One important step of the lens fabrication process is transferring the lens structures from a SiO₂ mask into the silicon wafer. Underetching is the effect of etching regions underneath the mask which actually should be protected by the mask from being etched [BFP⁺09, Boy10].

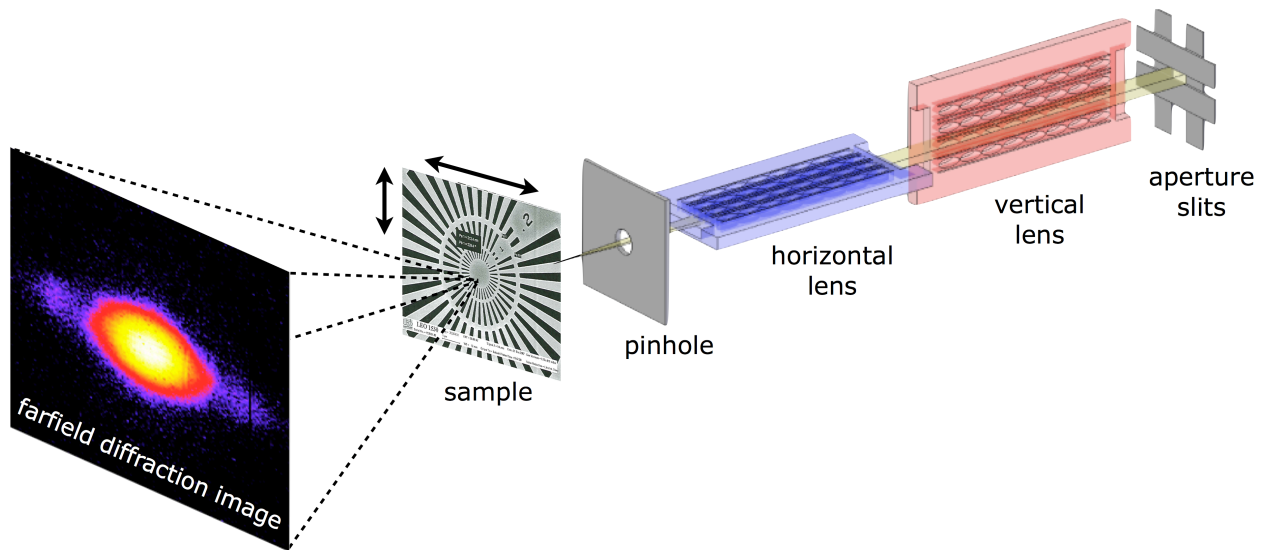


Figure 6.4: Experimental setup for x-ray ptychography. The sample is scanned and illuminated by a focused x-ray beam with sufficiently large transverse coherence length. The scattered photons generate a diffraction pattern that is recorded by a diffraction camera.

knowledge was used to modulate the parameters for the process of lens fabrication, resulting in new nanofocusing lenses with even less aberrations [BFP⁺09, Boy10].

6.2.3 X-Ray Ptychography

An advanced technique to characterize a nanobeam is the combination of scanning microscopy with coherent x-ray diffraction imaging. This method is called *ptychography* and was developed, in order to retrieve the complex transmission function of an object with high spatial resolution without the need for large numerical apertures of imaging optics [RF04, RHC⁺07, TDM⁺08]. As a byproduct, ptychography also yields the complex wavefield of the illuminating beam. We applied x-ray ptychography with the hard x-ray scanning microscope, in order to characterize the nanobeam generated by the nanofocusing lenses [SBF⁺10c].

In x-ray ptychography, an object is scanned by a coherent x-ray beam along the horizontal and the vertical direction with sufficient overlap of neighboring illuminated areas [BDK⁺08]. At each position, the far-field intensity diffraction pattern is recorded with a diffraction camera (Figure 6.4). From the diffraction patterns and the knowledge of the scan positions the complex wavefield of the illuminating x-ray beam and the transmission function of the object can be reconstructed by phase-retrieval algorithms [RF04, RHC⁺07, MR09]. No prior information about the object or the illumination is needed, if the scanned object contains scattering structures of a sufficiently large diversity in length scale, and if sufficiently large contrast is yielded in the diffraction patterns [GSF09]. The transverse coherence length of the illuminating beam must be larger than the beam size. The nanobeam of the hard x-

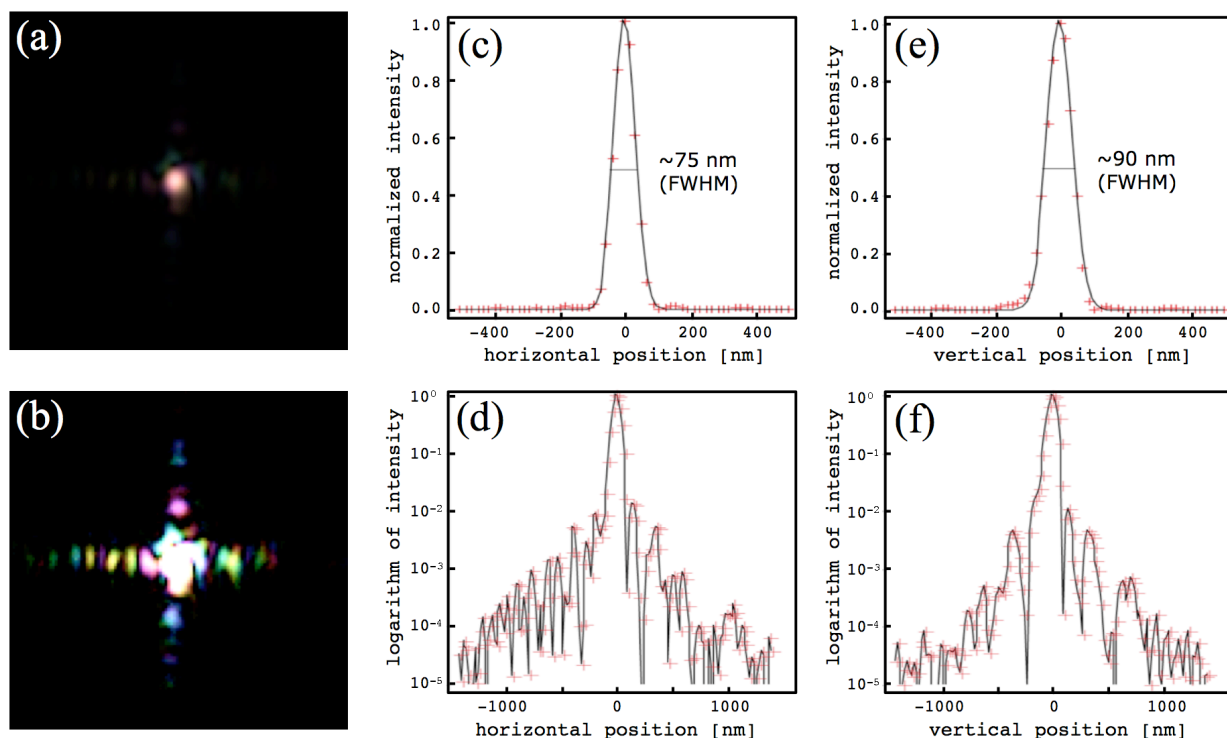


Figure 6.5: Reconstructed complex wavefield in the focal plane. (a) and (b) depict a section through the beam caustic near the focal plane. The phase of the complex wavefield is encoded by hue and the amplitude by brightness. To two images show the same wavefield but with different scaling. (c)-(f) show reconstructed intensity profiles along the horizontal and the vertical beam directions, respectively. Note that the intensity of the side maxima is at least two orders of magnitude lower than the maximum of the central peak. (Reprinted with permission from [SBF⁺10c]. Copyright 2010, American Institute of Physics.)

ray scanning microscope is usually diffraction limited and thus ensures sufficient transverse coherence. For nanobeam characterization, a strong scatterer can be chosen as an object. This allows short exposure times, and, thereby, a large number of diffraction patterns at different scanning positions can be obtained within a manageable period of time. This is important, because a large number of diffraction patterns at differing scanning positions guarantees an accurate reconstruction of the complex wavefield of the illuminating beam despite unavoidable inaccuracy of the scan point positions. The retrieved complex wavefield is that immediately behind the scattering object. By applying Fresnel-Kirchhoff propagation on this wavefield in forward and backward direction (confer chapter 2.1.4), the complete caustic of the nanobeam can be computed.

Figure 6.5 presents the result of such a ptychography scan carried out with the hard x-ray scanning microscope for nanobeam characterization. We used a resolution test chart³ made of tantalum with smallest lines and spaces of 50 nm. With its thickness of 500 nm, the test pattern is a strong scatterer, thus an exposure time of 0.1 s per scan point was sufficient to

³model ATN/XRESO-50HC by NTT-AT

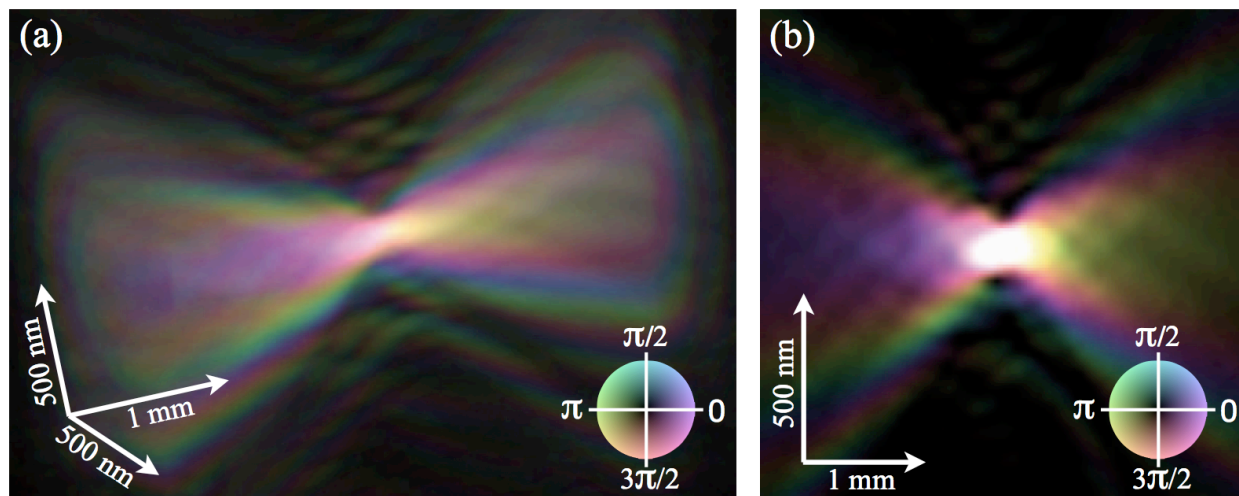


Figure 6.6: Reconstructed complex caustic of the nanofocused x-ray beam. Phases and amplitudes are codes as colors and brightness, respectively. Note the differently scaled axes along and transverse the beam direction. (a) Three-dimensional view of the complex wavefield around the focal plane. (b) Horizontal slice of the complex wavefield in direction of the optical axis. (Reprinted with permission from [SBF⁺10c]. Copyright 2010, American Institute of Physics.)

record the diffraction patterns. By this, no less than 15 000 diffraction images at different scanning positions were acquired with the single photon counting MAXIPIX camera (see chapter 5.3.2). The x-ray energy was 15.25 keV and the distance of the detector from the sample was marginally smaller than 2 m. The reconstructed wavefield in the focal plane is shown in Figure 6.5(a) and 6.5(b). The phase and the amplitude of the complex wavefield are encoded by color and brightness, respectively. The complex caustic of the x-ray beam is shown in Figure 6.6.

6.3 Fluorescence Spectroscopy

One of the greatest benefits of hard x rays as a testing probe is its ability to excite electrons of inner atomic shells. The vacant electron state left behind after such an excitation will be filled again by an electron from a higher energetic state of the same atom. The excessive energy can be transferred to another bound electron of the same atom, which will be raised to an unbound state. This *Auger process* competes with a different process, where the excessive energy is not used to emit another electron, but to emit a photon with an energy, which is the energy difference between the initial and the final state. A Measurement of the photon energy of such a *fluorescence* photon enables one to specify the atomic number of the atom in which the process occurs.

In classical x-ray fluorescence spectroscopy a relatively large region of a specimen is illuminated with unfocused x rays, and the emitted fluorescence photons are recorded with an energy dispersive detector. If this detector is sufficiently shielded from the incident

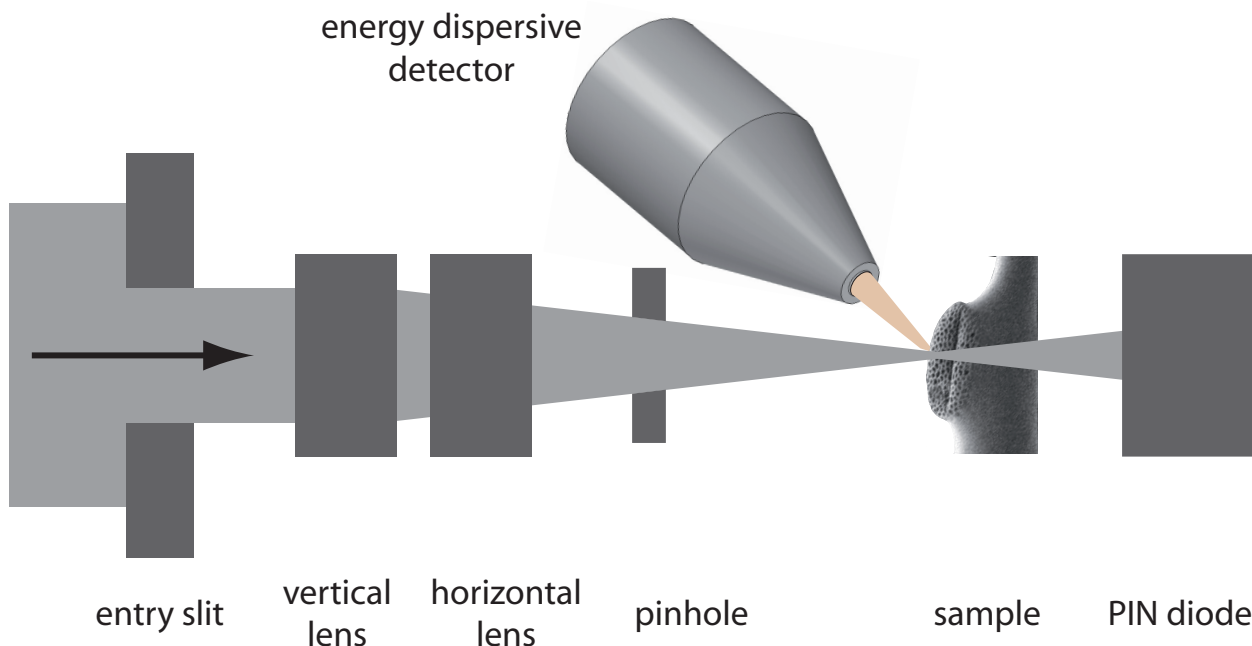


Figure 6.7: Schematic drawing of a scanning fluorescence experiment. The incident synchrotron x-ray beam passes the aperture defining entry slits and then enters the vertically and the horizontally focusing lenses. The sample is scanned through the focal spot, while the transmission signal and the fluorescence spectrum are recorded with a photo diode and an energy dispersive detector, respectively.

x-ray beam, the measured spectrum shows peaks at energies which correspond to diverse fluorescence emission lines. These lines are characteristic for specific elements and can be used to qualitatively prove the existence of specific elements in the sample. From the heights of the fluorescence peaks, the concentration of elements in the sample can be derived. For this means, one needs to know the probability that an incident x-ray photon excites the electron of a specific state in a specific atom, the probability to fill the vacant state with an electron from a specific higher state in the considered atom emitting a fluorescence photon, and the probability that this fluorescence photon is detected by the energy dispersive detector. Quantitative analysis of such a spectrum is made difficult by background originating from elastic and inelastic scattering of x-ray photons within the sample and in the air surrounding the sample. But if x-ray fluorescence spectroscopy is performed with synchrotron radiation, the background level is very low. In contrast to that, the fluorescence spectra that are retrieved by fluorescence spectroscopy on x-ray tubes and also the spectra from fluorescence spectroscopy induced by electrons are superposed with a much higher background level.

A classical fluorescence experiment allows one to verify the existence of chemical elements in a sample, and even to measure their averaged concentration. But this method delivers no information about the spatial distribution of the elements within the sample. With a focused x-ray beam, local information about the concentration of the elements in a sample can be retrieved laterally to the incident x-ray beam. Since the incident x-ray beam is

focused to a small spot size, the recorded fluorescence spectrum does not come from the whole sample, but originates from a small region defined by the intersection of the small beam with the sample. In the case of samples which are thin compared to the depth of focus of the nanobeam, this region is approximately a cylinder. The focus size equates the diameter, and the sample thickness in direction of the optical axis defines the height of the cylinder. Thus, the spectrum is the integral over a small cylinder, and the concentrations of chemical elements can be retrieved as an average over this cylinder. In a fluorescence x-ray element mapping experiment, the sample is scanned with the focused x-ray beam in horizontal and vertical direction, while the fluorescence spectrum is recorded at each scan point. As a result one obtains the two-dimensional distribution of the element concentrations averaged over the thickness of the sample in the direction of the incoming x-ray beam. A schematic drawing of the setup of a scanning fluorescence experiment is shown in Figure 6.7.

The real three-dimensional element distribution can be retrieved applying tomographic methods. The sample is rotated around an axis transverse to the primary x-ray beam, and for each rotation angle a lateral scan orthogonal to the axis of rotation is performed, recording the fluorescence spectrum at each scan point. From this set of spectra, sinograms for each element of interest can be extracted. Applying tomographic reconstruction algorithms on these sinograms leads to the real element distribution of a single slice through the sample. In order to get information about the third dimension in the direction of the rotational axis, a number of slices at different positions along the axis of rotation has to be recorded. The lateral resolution depends (among others) on the size of the focused x-ray beam and on the step size of the tomographic scan.

Fluorescence x-ray tomography encounters the difficulty of self-attenuation. To be detected by the energy dispersive detector, the fluorescence photon must escape from the inner part of the sample. Especially low energetic fluorescence photons are attenuated within the specimen. Thus concentrations of elements with low atomic numbers are underestimated significantly, mainly for large samples. In addition, distortions arise, because attenuation is larger for fluorescence photons emitted from those regions of the sample that are on the opposite side of the energy dispersive detector, as their path through the sample is larger than for photons emitted from regions near the detector. Algorithms have been developed that successfully cope with self-attenuation [YAT⁺97b, YAT⁺97a, Sch01].

In the following sections, results from fluorescence x-ray element mapping and fluorescence x-ray tomography experiments are presented, which were performed with the hard x-ray scanning microscope installed at the ESRF beamline ID 13.

6.3.1 Fluorescence Element Mapping

Mapping the elements in a sample via x-ray induced fluorescence can be applied to any kinds of samples. As part of this work, fluorescence element mapping was performed on gold test structures evaporated on thin silicon membranes, on diverse biological samples, on cosmic dust particles (from the NASA stardust mission), and many more. Biological samples are especially appropriate for x-ray induced fluorescence, because of their relatively

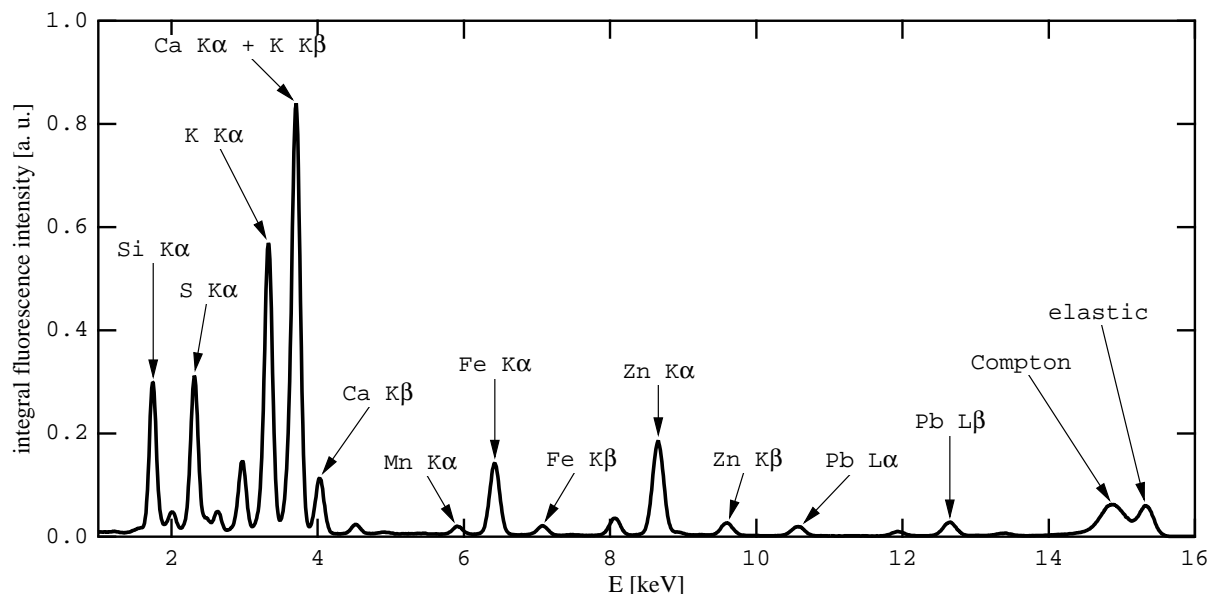


Figure 6.8: Fluorescence spectrum of the pollen of *Arabidopsis thaliana* integrated over all scan points.

weak self-attenuation of the fluorescence light.

As an example I describe a fluorescence element mapping experiment with a single pollen of the plant *Arabidopsis thaliana* [cf. Figure 6.9(a)]. The flowering plant *Arabidopsis thaliana* is a popular object of investigation in plant biology and genetics, because its genome is one of the smallest among plant genomes and, therefore, it was the first one to be sequenced. Plant physiologists are able to deactivate specific genes and to study its consequences. In the fluorescence experiment presented here, the element distribution of the pollen of *Arabidopsis thaliana* was measured. Plant physiologists make use of these kinds of results to study nutritive substance transport mechanisms.

The freeze-dried pollen was glued on a glass capillary [cf. Figure 6.9(b)]. The sample was scanned horizontally and vertically with the focused x-ray beam provided by the nanoprobe. Even though the horizontal and vertical full width at half maximum size of the x-ray beam was about 100 nm, a quite large step size of 300 nm was chosen for a coarse scan. The photon energy of the incident beam was 15.25 keV, and the photon flux was determined to be about 3×10^8 ph/s. The exposure time for a single scan point was 1.5 s, but the periodic time between two neighboring scan points was twice as high, since the scanner needs time to move the sample from the current to the next scan point. A nitrogen-cooled energy dispersive Si(Li) fluorescence detector was used to record the fluorescence spectrum. A PIN-diode measured the absorption signal, which was used to normalize the spectrum. This was possible, because absorption is very weak. Normalizing the data is essential, because the ESRF does not operate in top-up mode, giving rise to a continuous flux decay during the experiment and to sudden flux increase after storage ring refills (see section 3.3).

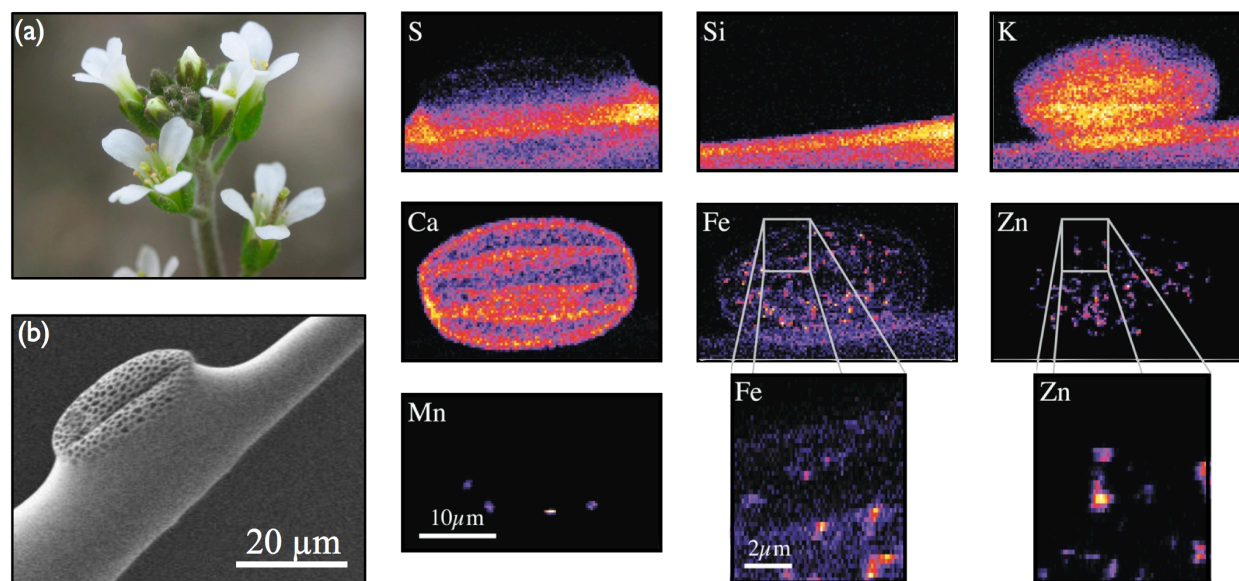


Figure 6.9: Fluorescence element mapping of the pollen of *Arabidopsis thaliana*. (a) Photograph of an *Arabidopsis thaliana* plant. (b) SEM image of the pollen of *Arabidopsis thaliana*. The pollen is glued on the outside surface of a thin glass capillary. (right) The right part depicts the measured element distribution retrieved from the fluorescence signal. Resolved features range down to the size of only one or two pixels, which corresponds to a spatial resolution of about 100 nm.

The resulting data of such a fluorescence scan is a set of fluorescence spectra, each corresponding to a certain scan point. Figure 6.8 shows the fluorescence spectrum of the pollen integrated over all scan points. Note the low background level that allows the detection of many elements even if they are present with only very low concentrations. The relative concentration of a specific element at a scan point is related to the heights of the peaks for that element. Unfortunately, the peaks for the different elements are not independent of each other, since there is the chance of overlapping of neighboring peaks. Therefore, a linear combination of base vectors (normalized spectra of all relevant elements in the sample) has to be determined. Each base vector consists of multiple Gauss peaks for diverse emission lines, such as K_{α} , K_{β} , L_{α} , etc. The coefficients of the linear combination are proportional to the element concentrations at the concerning scan point.

Another important instance is the presence of background in the fluorescence spectrum. Elastic and inelastic scattering makes the energy dispersive detector record not only fluorescence photons, but also the photons from the scattering processes. Modeling the background is very challenging, but also essential for quantitative analysis.

The part to the right of Figure 6.9 shows the measured distributions of the elements silicon, sulfur, potassium, calcium, iron, zinc, and manganese, retrieved from linear combinations of base vectors. In order to correctly understand these element maps, one must keep in mind that the concentrations are projections along the direction of the incident x-ray beam. As the pollen was significantly extended in all three dimensions, spatial information gets lost along that direction. For instance, in the calcium map, there are horizontal stripes

of high calcium concentration. It is not known if these stripes are in the interior of the pollen or if they are located near the surface. This information cannot be retrieved from this single projection. It is the same with the iron map, and with all the other element distributions. The iron map, for example, shows small distinct areas of high iron concentrations, but there is still no information about their distribution along the beam direction. The iron might be situated inside or it might be located on the periphery of the pollen. This missing information must be obtained with tomographic methods as discussed in the next section.

Nevertheless the projection maps show some interesting information about the sample. Silicon, for example, is distributed only inside the glass capillary, but not in the pollen. Sulfur, on the contrary, is located in the area between the capillary and the pollen, from which one concludes that it is a component of the glue. The other elements (potassium, calcium, iron, zinc, and manganese) are ingredients of the pollen itself. But while potassium shows a rather homogenous distribution, calcium is more structured, and iron, zinc, and manganese are concentrated in small dot-like areas. Some of these spots have the size of only one pixel, indicating a spatial resolution in the range of the step size of the scan or even better.

In order to retrieve a better sampling compared to the focus size, a fine scan with 80 nm step size and 2 s exposure time was performed. The results are shown as zoomed areas in the lower part of Figure 6.9. The little areas of high element concentration of iron and zinc are still only one or a few pixels large, proving that features of about 100 nm are easily resolved with the hard x-ray scanning microscope.

6.3.2 Fluorescence Tomography

Fluorescence element mapping experiments as described in the previous section are useful for specimens, which are thin along the beam direction, or for samples with a homogenous element distribution along the optical axis, because one obtains only projections along the optical axis. If one is interested in the real three-dimensional distribution of the element concentration, tomography has to be applied. In a tomography experiment the sample is rotated around an axis orthogonal to the incident beam, while projections of a specific property (attenuation, fluorescence, etc.) are recorded for each rotation angle. The set of projections is mathematically given by the radon transform of the three-dimensional distribution of the property of interest. Hence, the three-dimensional distribution can be calculated applying the inverse radon transform to the set of projections [KS88].

The same pollen of the plant *Arabidopsis thaliana* as presented in the previous section was used in a tomographic scan, which was performed right after the element mapping experiment. For this, the sample was rotated with an angular step size of 4 degrees over full 360 degrees. At each angle the sample was scanned with a lateral step size of 300 nm over a range of 22 μm and an exposure time of 2 s per scan point. Within 6 hours, 91×74 spectra were recorded.

Multiple Gauss functions were fitted to the spectra, in order to retrieve the coefficients of linear combinations of base vectors for the different elements as a function of the rotation

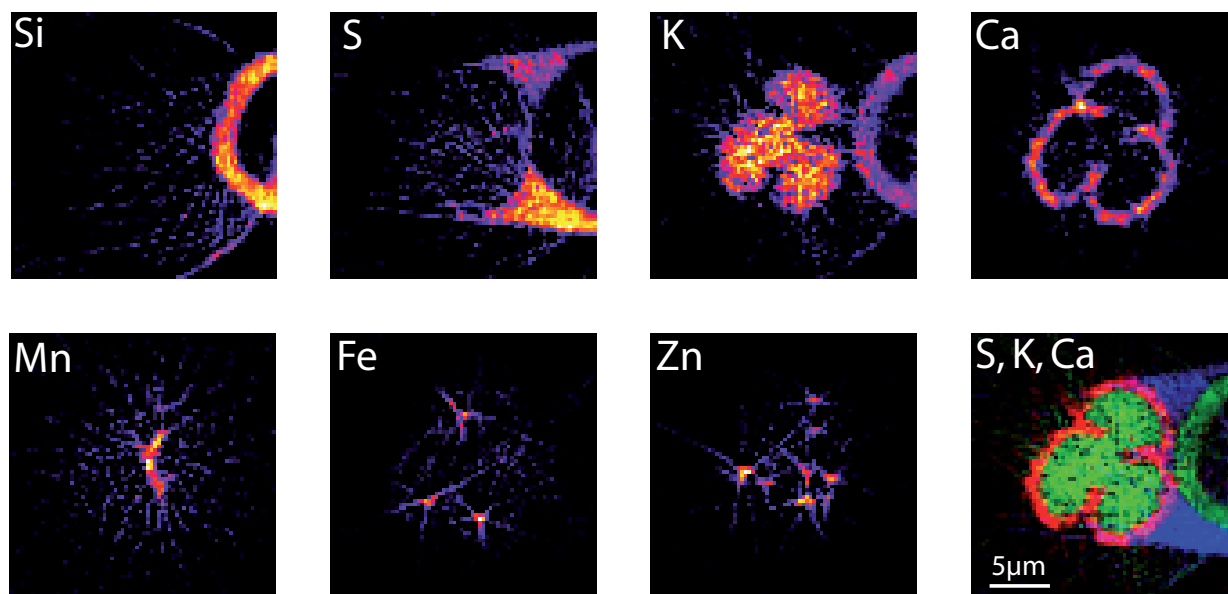


Figure 6.10: Reconstructed element distribution of the pollen of *Arabidopsis thaliana* retrieved from the tomogram of the fluorescence signal. The specimen is the same as seen in Figure 6.9.

angle and the transverse scanning position, thereby extracting sinograms for each element. By performing the filtered back-projection algorithm on those sinograms, the reconstructed spatially resolved element concentrations are obtained [KS88].

In case of strong attenuation of the fluorescence light within the sample, self-attenuation artifacts may arise. In that case, a self-consistent iterative reconstruction algorithm has to be applied [YAT⁺97b, YAT⁺97a, Sch01].

The reconstructed distributions of the elements are shown in Figure 6.10. In contrast to the two-dimensional mapping it can be clearly seen that the calcium is located in the shell of the pollen, whereas the potassium is concentrated inside the pollen. The high concentrations of iron and zinc are found in the inner of the pollen rather than on its periphery. This clearly demonstrates the necessity of applying tomographic methods for inhomogenous three-dimensional objects.

6.4 Diffraction Experiments

Besides fluorescence, other x-ray analytical contrast mechanism can be exploited with the hard x-ray scanning microscope. The following sections describe experiments using diffraction and coherent diffraction methods. The diffraction patterns are recorded with diffraction camera, while in parallel, the fluorescence signal is measured with an energy dispersive detector. By this, element maps can be associated with the diffraction patterns, which are recorded during a scan.

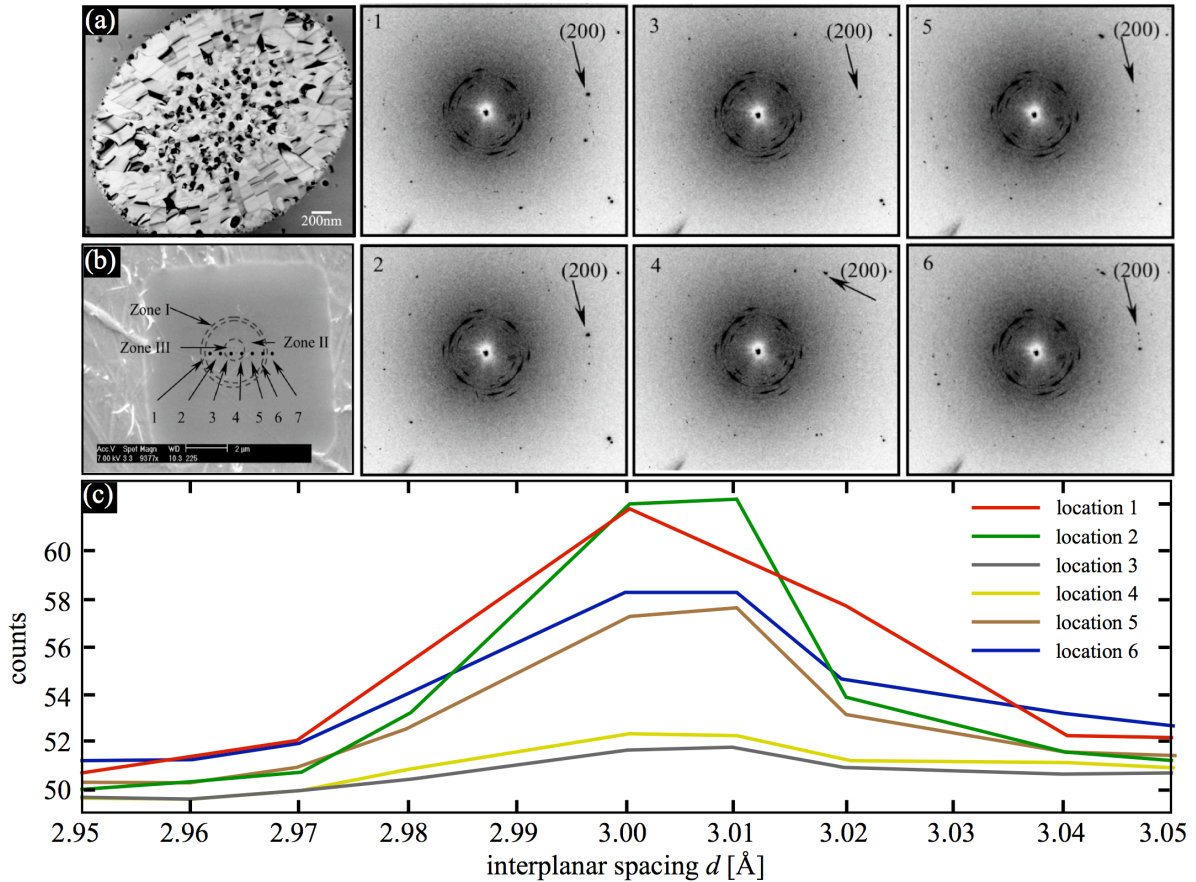


Figure 6.11: Nano diffraction of phase change media. (a) TEM image of a crystalline bit of $\text{Ge}_2\text{Sb}_2\text{Te}_5$ within amorphous environment. (b) Scanning positions along a line through the crystalline region. The diffraction images are shown on the top right (1–6). (c) Integrated count rate of the (200) Bragg reflection caused by the different scan positions through the crystalline bit as a function of the inter-planar spacing that belongs to the specific scattering angle. (Published in [Kur05].)

6.4.1 Microdiffraction on Phase Change Media

One of the first nano-diffraction experiments with an early version of the hard x-ray scanning microscope was carried out in the year 2005. Phase change media were scanned with the nanoprobe, and the diffraction images at each scan point were recorded. The results are published in a PhD thesis about the development of nanofocusing lenses [Kur05].

Phase change media are utilized for data storage devices that make use of the differing visible light reflectivity for different crystalline phases of an alloy. Data bits are written by changing the crystalline phase by laser induced heating and cooling. Set and unset bits are distinguished, i. e., the stored information is read, by the differing visible light reflectivity for different crystalline phases. The hard x-ray scanning microscope was used to perform a diffraction experiment on $\text{Ge}_2\text{Sb}_2\text{Te}_5$, an alloy commonly discussed as a material for phase change storage disks [IIT⁺93, Kim99, WFZW99, FWN⁺00, Njo01, WS07]. The aim of the

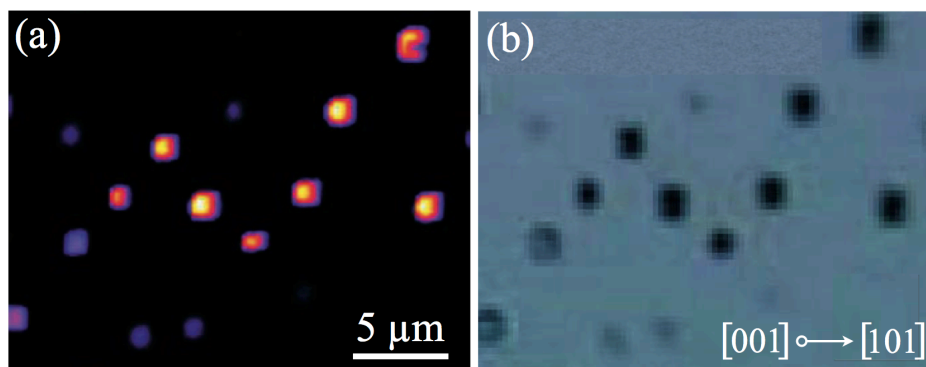


Figure 6.12: Fluorescence mapping of Stranski-Krastanow islands. (a) Map of the Ge $K\alpha$ fluorescence signal of SiGe/Si(001) islands, which were scanned with the focused x-ray beam provided by the nanoprobe. The beam had a size of 200 nm in vertical and horizontal direction, and the photon energy was 15.25 keV. An optical micrograph of the same region is shown in (b). Each single island of the fluorescence scan can be identified in this visible light micrograph. (Reprinted with permission from [HDS⁺08]. Copyright 2008, American Institute of Physics.)

experiment was to investigate the crystalline phase at different positions on and around a single written data bit. The diameter and the thickness of a single data bit are 2.5 μm and 80 nm, respectively. Figure 6.11(a) shows a transmission electron microscopic image of such a data bit. A nanobeam with a full width at half maximum size of $180 \times 100 \text{ nm}^2$ was used to radiate the data bit at different positions. At each position, the diffraction pattern was recorded by a MAR CCD 165 diffraction camera with an exposure time of 90 s. Figure 6.11b illustrates the scanned positions and the corresponding diffraction patterns. The illuminated volume had a size of only $180 \text{ nm} \times 100 \text{ nm} \times 80 \text{ nm}$ ($0.0014 \mu\text{m}^3$), i. e., only 10^7 atoms were irradiated. For this reason, even diffraction patterns of polycrystalline samples will show single Bragg reflections rather than showing diffraction rings. The intensity within a single Bragg reflection is a measure for the crystal size. In Figure 6.11(c), the scattered count rate of the (200) Bragg reflections is plotted for the different scanning positions as a function of the inter-planar spacing that belongs to the specific scattering angle. The result suggests that the average size of the crystals varies with the distance from the center of the data bit. This is in good agreement with the results from other experiments [DW51], and it demonstrates the feasibility of hard x-ray diffraction with nanosized x-ray beams to study the crystalline structure of inhomogeneous samples with a spatial resolution of about 100 nm.

6.4.2 Microdiffraction on Stranski-Krastanow Islands

In a further experiment that was carried out during this work Stranski-Krastanow islands were scanned with the hard x-ray scanning microscope, while diffraction patterns and the fluorescence signal were recorded. Stranski-Krastanow islands are well investigated and, therefore, they are an adequate model system for testing the method of scanning nano-diffraction. The results are published in [HDS⁺08] and they prove the feasibility of nano-

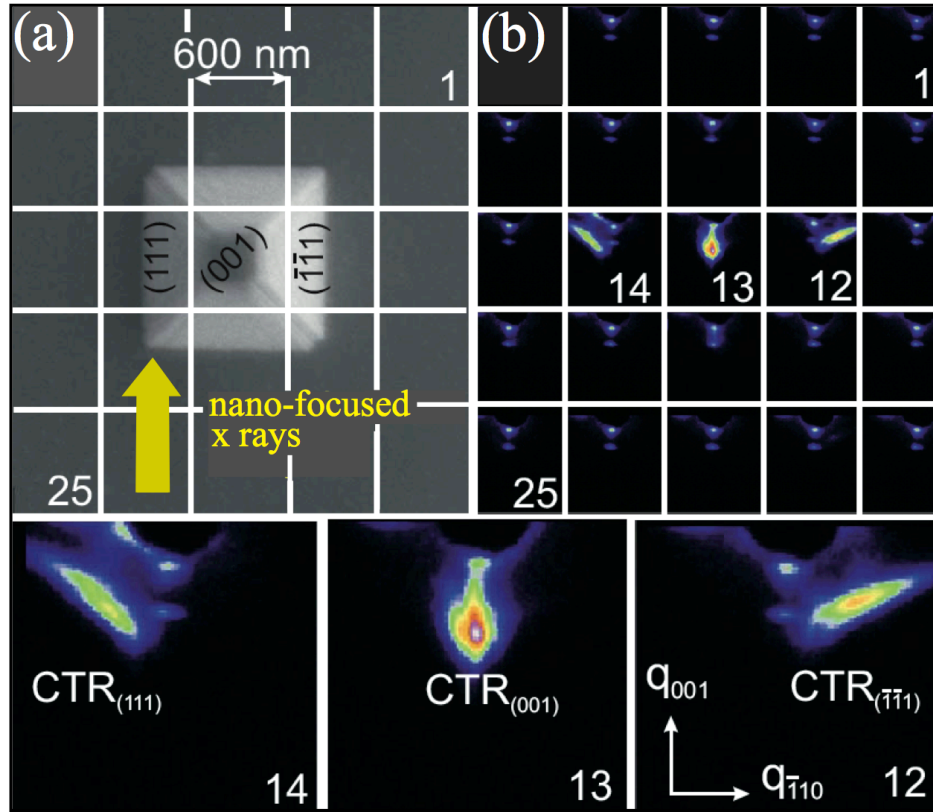


Figure 6.13: (a) Scanning electron micrograph of a typical SiGe/Si(001) island. (b) An area of $3 \times 3 \mu\text{m}^2$ was symmetrically divided into 25 points, where the shape and strain were locally probed with a 200 nm (FWHM) nanobeam provided by the hard x-ray scanning microscope. Frames 1-25 of the scanning x-ray diffraction micrograph give the diffusely scattered x-ray intensity near the symmetric Si(004) reflection, which itself was suppressed by an absorber. When the incident x-ray beam subsequently illuminates different $\{111\}$ island facets, the corresponding facet rods are excited and thus contribute to the scattering pattern shown in the frames 12-14. (Reprinted with permission from [HDS⁺08]. Copyright 2008, American Institute of Physics.)

diffraction with the instrument.

Stranski-Krastanow islands are small pyramids of SiGe/Si(001) [SK37]. A single island is a truncated pyramid with a square base. The top surface is parallel to the (001) plane, and the four sloped surfaces are parallel to the (111), ($\bar{1}11$), ($\bar{1}\bar{1}1$), and ($1\bar{1}1$) plane, respectively. In the experiment, a single island was scanned with the focused x-ray beam provided by the hard x-ray scanning microscope, while the fluorescence spectra and the diffraction patterns were recorded with an energy dispersive detector and a diffraction camera (FReLoN 4k, $50 \mu\text{m}$ pixel size), respectively. The focus size was 200 nm in horizontal and vertical direction with a photon flux of 10^9 ph/s. In Figure 6.12(a) the Ge $K\alpha$ fluorescence signal reveals the distribution of SiGe/Si(001) islands on the silicon substrate. This map can be linked to the optical micrograph of the corresponding region as shown in Figure 6.12(b). From the map a single island was selected for further investigation [see Figure 6.13(a)]. Around that island a grid of 5 by 5 scan points spanned an area of $3 \times 3 \mu\text{m}^2$. The diffraction patterns in Figure

6.13(b) are arranged according to the grid in Figure 6.13(a). Depending on the illuminated part of the scanned region, different facet rods contribute to the scattering patterns. The results of this experiment are in good agreement with theoretical predictions (simulations) and with experimental data retrieved from diffraction experiments with large beams on ensembles of Stranski-Krastanow islands [HDS⁺08]. One year later, a similar experiment was performed with the hard x-ray scanning microscope utilizing nanofocusing lenses and, in addition, KB-mirrors, which confirms the results described in this paragraph [DHS⁺10].

6.4.3 Coherent X-Ray Diffraction Imaging of Gold Particles

The hard x-ray scanning microscope is also capable of coherent x-ray diffraction imaging (CXDI). Coherent x-ray diffraction imaging is a lensless imaging method, which measures the projected electron density of a specimen with the potential of reaching spatial resolution in the range of the probe's wavelength, which is beyond 1 Å in case of hard x rays. The reconstructed electron density is a projection along the beam direction, and the three-dimensional distribution can be retrieved by combining CXDI with tomographic techniques.

In a CXDI experiment the specimen is coherently illuminated with x rays, while the far field diffraction pattern is recorded. If one was able to measure the complex far field amplitudes, the complex wavefield right behind the sample (and thus the complex transmission function) could be computed via back propagation. Propagation from the sample to the far field can be described by a Fourier transform, hence the wavefield immediately behind the sample can be calculated by the inverse Fourier transform of the complex far field. But with the detectors that are available today it is not possible to directly measure the phase of the complex field amplitudes. Instead, the intensity is measured, which is proportional to the square of the amplitude. Despite missing phase information, CXDI allows to reconstruct the transmission function (and thereby the electron density distribution) of the sample by means of diverse iterative reconstruction algorithms. Practically, the spatial resolution is limited by the relatively low coherent flux density even at third generation synchrotron radiation facilities. For small objects the coherent dose can be increased by focusing the available coherent flux on the sample [SS10]. This was done as part of this work in an experiment described in this section. The results are published in [SBF⁺08, SBF⁺10a] and prove a spatial resolution of about 5 nm.

Figure 6.14(a) shows a transmission electron micrograph of nano gold particles on a Si₃N₄ membrane, which was used as a test object for the coherent x-ray diffraction imaging experiment. The average diameter of the gold particles is about 100 nm. The isolated particle marked by the arrow in 6.14(a) was coherently illuminated by the focused x-ray beam. The focus had a size of 100 nm vertically and horizontally and the photon flux exceeded 10⁸ ph/s. A diffraction camera recorded diffraction patterns of the sample at a distance of 1.25 m. The intensity of the unscattered primary beam is several orders of magnitude larger than the intensity of the scattering signal. The dynamic range of presently available diffraction cameras is not large enough to detect intensity variations of that magnitude. Therefore, a beam stop behind the sample absorbs the unscattered photons of the primary beam. Since

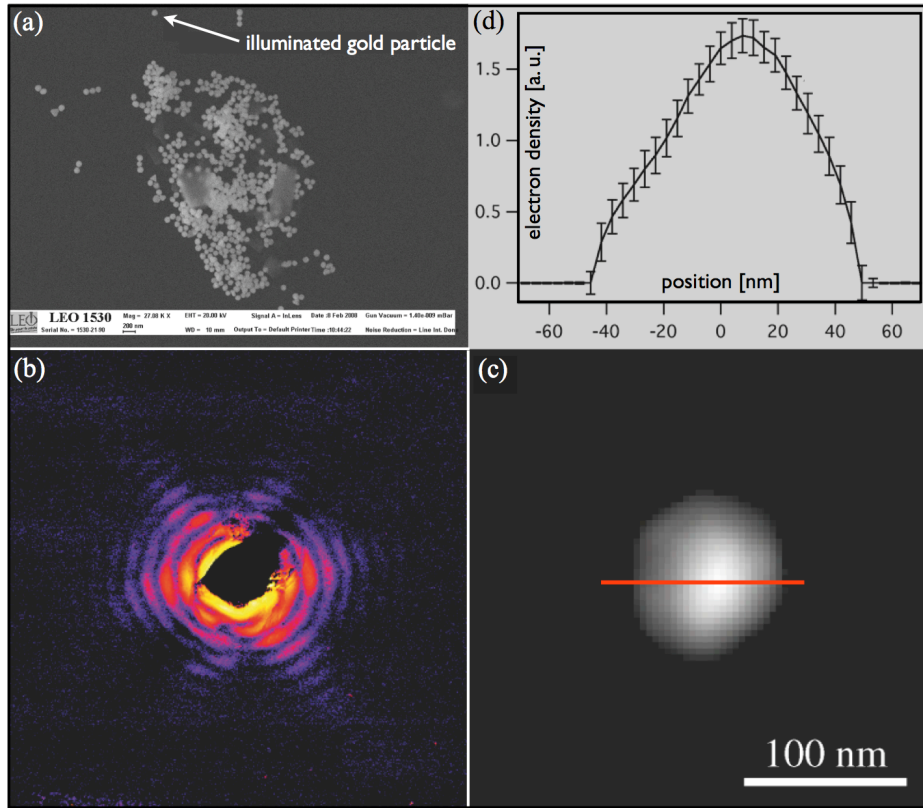


Figure 6.14: Coherent x-ray diffraction on gold particles. (a) SEM image of nano gold particles on a Si_3N_4 membrane. The arrow marks the particle illuminated by the focused x-ray beam. (b) Composed diffraction pattern of the coherently illuminated single gold particle marked in (a). The dark area in the center is caused by the beam stop that blocks the primary beam. (c) Reconstructed (projected) electron density of the gold particle. A combination of the hybrid input-output algorithm with the shrink-wrap algorithm was used, implemented by A. Schropp [Sch08]. (d) Line profile through the region marked with a red line in (c). The lateral resolution is about 5 nm. (Published in [SBF⁺08]. Copyright 2005 by the American Physical Society.)

the beam stop was a bit larger than necessary, it was moved around the central position in order to retrieve the inner parts of the diffraction pattern in several steps.

The composed diffraction pattern is shown in Figure 6.14(b). The high visibility of the fringes is due to a high degree of transverse coherence in the focus. The amplitude full width at half maximum beam size was $150 \times 150 \text{ nm}^2$ horizontally and vertically (a factor $\sqrt{2}$ larger than the intensity beam size), whereas the transverse coherence length was $180 \times 360 \text{ nm}^2$ along the horizontal and the vertical axes. Thus, in both transverse directions, the coherence length exceeded the dimensions of the beam as well as the dimensions of the gold particle with its diameter of about 90 nm. For this reason, many diffraction fringes are observable, and the CXDI method is applicable to measure the projected electron density of the gold particle.

Applying a combination of the hybrid input-output method [Fie82] and the shrink-wrap

algorithm [MHC⁺03] allows to reconstruct the projected electron density of the sample. The algorithms were improved and implemented by A. Schropp based on the results of his PhD thesis about capabilities and limitations of CXDI [Sch08]. Figure 6.14(c) shows an image of the reconstructed projected electron density of the isolated gold particle that is marked with an arrow in Figure 6.14(a). A line profile through the center of the reconstructed particle is plotted in Figure 6.14(d). The spatial resolution is about 5 nm and the total exposure time to obtain this result was 10 minutes. Without focusing the coherent photon flux onto the sample, a total exposure time of more than two months would be necessary in order to obtain the same result, i. e., the gain by focusing was about 10^4 .

This CXDI experiment was a pioneering experiment in several aspects. It was for the first time that coherent x-ray diffraction imaging was successfully applied to x rays with a wavelength below 1 Å without using a Bragg reflection of a crystalline sample. In addition, a spatial resolution of below 10 nm in direct space was obtained, which had never been achieved before. This was only possible, because the available coherent photon flux of the undulator source was focused on the specimen by the nanofocusing lenses.

6.4.4 X-Ray Ptychography of a Nano-Structured Microchip

In section 6.2.3 it was demonstrated that x-ray ptychography can be used for nanobeam characterization by retrieving the complex wavefield of the x-ray beam. In addition to that, ptychography allows also to retrieve the complex transmission function (also known as *object function*) of the illuminated specimen. In fact, reconstructing phase and amplitude of the object function is the primary intention of x-ray ptychography, whereas the reconstructed illumination is rather a supplemental information provided by the method. Both kinds of information, the object function as well as the illumination, are retrieved simultaneously with the same experiment utilizing the same diffraction patterns.

With the hard x-ray scanning microscope we applied x-ray ptychography in order to retrieve the complex transmission function of a nano-structured microchip. The front-end processed passivated microchip⁴ was manufactured in 80 nm technology containing smallest structures with a size of 80 nm. The chip was composed of aluminum, tungsten, silicon, silicon oxide and silane nitride and was in a condition as it comes from the production line after waver dicing. The micro-electronical elements of interest were buried and not accessible by other microscopic techniques like scanning electron microscopy (SEM), transmission electron microscopy (TEM), or soft x-ray microscopy without destructive sample preparation.

The microchip was exposed and scanned by a nanobeam with a full width at half maximum size of about $80 \times 80 \text{ nm}^2$ generated by the hard x-ray scanning microscope at a photon energy of 15.25 keV. With a photon flux of about 10^7 ph s^{-1} an exposure time of 0.1 s per scan position was sufficient to get adequate diffraction patterns. The scan was performed on a grid of 81×81 scan points with a step size of 50 nm that ensured appropriate overlapping of neighboring scan points. The 6561 diffraction patterns were recorded by the MAXIPIX diffraction camera (chapter 5.3.2) at a distance of 1.9 m behind the sample. The

⁴512 Megabit DDR2 RAM by Qimonda

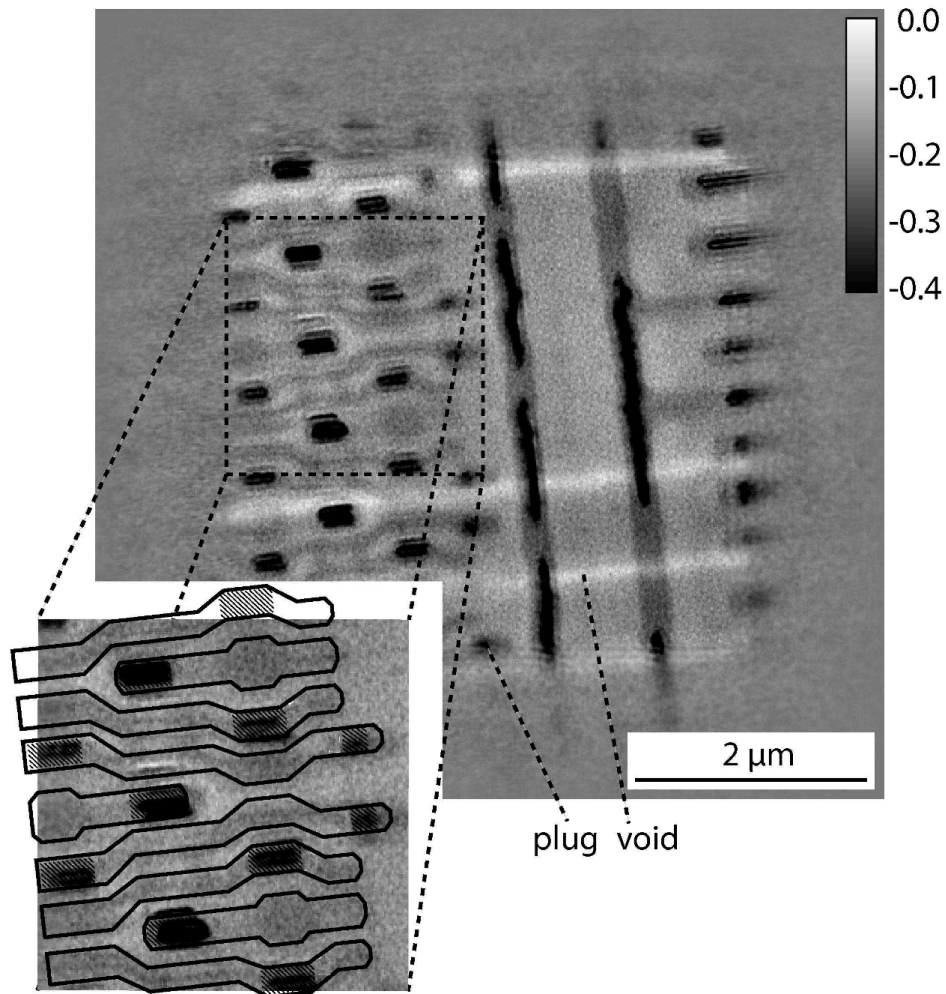


Figure 6.15: Reconstructed front-end processed passivated microchip. The map shows the phase shift that is induced by refraction of the x rays within the object. The measured phase shift ranges from 0 rad (voids) to -0.7 rad (tungsten plugs). In order to enhance the visibility of small and thin structures, the color code of the map ranges only from 0 rad (white) to -0.4 rad (black), whereupon phase shifts larger than 0.4 rad are represented by black. This phase map allows the identification of the electronic layout, which is redrawn in the magnified inset. (Reprinted with permission from [SBG⁺11]. Copyright 2010 by John Wiley and Sons.)

space between sample and detector was furnished with a helium tube in order to reduce background scattering from air.

The data were processed with a phase retrieval algorithm [RF04, RHC⁺07, MR09] yielding the complex object function and the complex illumination. Figure 6.15 depicts the phase contribution of the reconstructed object function of the microchip. The phase shift is induced by refraction of the x rays within the object. The measured phase shift in the microchip ranges between 0 rad (voids without material) and -0.7 rad (tungsten plugs). From the phase map, the electronic layout can be redrawn as shown in the inset of Figure 6.15. The spatial resolution of the object function is slightly better than 40 nm. The reconstructed

illumination function yields a beam size of $81 \times 84 \text{ nm}^2$ in horizontal and vertical direction, respectively, confirming the expected size of $80 \times 80 \text{ nm}^2$. The results of this experiment are submitted for publication.

In future ptychography experiments, the resolution can be improved by increasing the coherent dose on the sample by more efficient focusing and by increasing the acquisition time. A precondition for that is a setup with better mechanical stability, since inaccurate sample positioning introduces artifacts. The higher the spatial resolution the more important becomes a stable setup.

Chapter 7

Conclusion and Outlook

In many fields of science, medicine and technology, there is a large demand to retrieve the spatial distribution of certain structural, chemical and physical properties hidden inside specimens. Thanks to their large attenuation length in matter, hard x rays are an appropriate probe for revealing the inner structure of an object. In combining x-ray analytical methods with scanning techniques, certain properties of an object can be obtained with two-dimensional or three-dimensional spatial resolution. Since the spatial resolution is restricted by the size of the microbeam which is used to scan the sample, great efforts were undertaken to generate smallest x-ray beams with high photon flux.

The Instrument

During this thesis the prototype of a hard x-ray scanning microscope was designed and built, which provides a small and intense focal spot with a transverse full width at half maximum size of 50–100 nm. This focus can be used to illuminate and scan samples, exploiting diverse contrast mechanism like absorption, fluorescence, small-angle scattering and coherent diffraction. Among linear scanning, rotation of the specimen around a vertical axis is possible, permitting the application of tomographic techniques. The prototype was installed and successfully tested at the ESRF beamline ID 13. A selection of experiments performed with the scanning microscope is reported in this thesis.

User Experiments

The aim of a number of experiments was to characterize the instrument with respect to beam size, photon flux, coherence properties, mechanical stability, and repeatability. Even though planned as a prototype, the performance and reliability of the instrument attracted the interest of many scientists. Most notably biologists, astrophysicists and scientists from material research investigated their specimens with the microanalytical capabilities of the scanning microscope.

Nanofocusing Lenses

The key element of the hard x-ray scanning microscope are microstructured refractive nanofocusing silicon lenses, which are developed and fabricated by our study group in Dresden. They create a demagnified image of the x-ray source, thus generating a small and high intense x-ray spot. We could demonstrate a smallest focus with a full width at half maximum size of about 50 nm in horizontal and vertical direction with a photon flux of 1.7×10^8 ph/s at an x-ray energy of 21 keV [SKP⁺05a]. The nanofocusing lenses are most effective at x-ray energies in the range between 10–30 keV, but they are also suitable for higher energies.

Nanobeam Characterization

The transverse coherence of the focal spot provided by the scanning microscope has been shown to be sufficient for ptychography. Ptychographic reconstruction not only reveals the complex transmission function of the sample, but also — as a side product — the complex wavefield of the illuminating beam. By propagating this field along the optical axis, the caustic of the focus can be reconstructed [SBF⁺10d]. We employ this ptychographic method for nanobeam characterization. In addition, we use a detailed mathematical model of the nanofocusing lenses to simulate the expected wavefield and to compare it with the wavefield retrieved from the reconstructed ptychographic data set. This way we obtain information about the shape of the nanofocusing lens. The knowledge gained by this method was incorporated in the design for a next generation of nanofocusing silicon lenses, which led to significant improvements manifesting in reduced aberrations.

Prefocusing

Compound parabolic refractive lenses made of beryllium are employed in order to prefocus the coherent flux into the aperture of the nanofocusing lens. This way the lateral coherence properties of the focus can be adapted to the needs of the experiment. We demonstrated that the flux in the focus could be increased by a factor of 10, if the prefocusing was activated, while the focus size was enlarged by a factor of only 1.5.

As an improvement for the future, astigmatic prefocusing with cylindrically symmetric lenses will be installed. For this, two different types of refractive lenses will be utilized. On the one hand, there are cylindrically symmetric compound parabolic refractive x-ray lenses made of beryllium, which are under development by B. Lengeler at the University of Aachen (RWTH). On the other hand, microstructured refractive silicon lenses are also suitable and will be optionally used for astigmatic prefocusing.

Diamond Lenses

Besides nanofocusing silicon lenses, we are also engaged in developing nanofocusing lenses made of diamond. The hard x-ray scanning microscope was provided with the prototype of such a diamond lens. First results are quite promising, but there is obviously the necessity

for improvements. Optimized diamond lenses will provide focal spots that are much smaller and have a larger flux than those generated by silicon lenses.

Potential Improvements

Based on the experiences we made with the current prototype version, a new setup was designed and will be installed at PETRA III beamline P06 [SBF⁺10b]. Some improvements concern thermal drifts and mechanical stability. In addition, the design of the detector unit will be improved, allowing more flexibility and efficiency.

Thermal Drifts

Thermal drifts can be reduced to a minimum with air conditioning systems regulating the air temperature inside the experimental hutch. The PETRA III beamline P06 will be equipped with an air conditioner keeping the air temperature constant with a variation of less than 0.1 K. In order to prevent mechanical disturbances by the air stream produced by the air conditioner, the air flow must be laminar. In order to take the load of the air conditioner and thus, reduce the air flow involved, thermal sources like control units have to be removed from the experimental hutch.

Laser Interferometry

Even though air conditioning systems and avoidance of thermal sources in the experimental hutch considerably improves the situation, thermal drifts may still remain, which might be critical for experiments with sub 100 nm resolution. In order to cope with these remaining thermal drifts, advanced concepts for monitoring such drifts by means of laser interferometry are under development. The feasibility of interferometric monitoring in the context of microanalysis has been demonstrated at the Hard X-ray Nanoprobe Beamline at the Advanced Photon Source (APS) [MSS⁺04, SMLV04, MWH⁺06]. The present design of the PETRA III nanoprobe includes laser interferometer axes, which are intended to measure the relative distance between the sample and the nanofocusing lenses in horizontal and vertical direction. The knowledge of the drifts can be used in a feedback system which compensates the drifts during the experiment. Alternatively, if not considered online, the information about the drifts might be accounted for afterwards, when evaluating the experimental data.

Mechanical Stability

Analyzing the sources for mechanical instabilities is a very complicated matter and we invested much effort to investigate this problem. Oscillations of the nanoprobe components were monitored by means of acceleration sensors, and two main sources for instability have been identified.

Environmental Vibration

The first kind of instability is introduced by the vibrating ground floor, which stimulates forced oscillation of the nanoprobe setup. Even if the ground floor effectively vibrates with rather low frequencies, the weak mechanical coupling between the nanoprobe setup and the ground leads to a shift of the excitation power spectrum to higher frequencies. But these high frequencies of all are a problem, because they make the focusing lens and the sample vibrate with uncorrelated phases, and hence the sample and the focal spot are vibrating relatively to each other. Low frequencies, however, correspond to wavelengths large enough to make the nanofocusing lens and the sample oscillate with a common phase, and hence their relative position remains unaffected. Based on this insight, the scanner unit of the PETRA III microscope will be mounted on a massive block of granite, which guarantees a hard mechanical connection to the ground, and hence, the vibration power spectrum of the floor, which is dominated by low frequencies, will be transferred one-to-one to the scanner unit.

Motorized Stages

The second source for mechanical instability has been identified in relaxing drifts after mechanical disturbances, which arise whenever the sample is mounted, or whenever a motorized stage is moved. While disturbances generated by mounting a sample can hardly be avoided, stage-induced disturbances can be minimized by utilizing appropriate stages which are optimized for high stability. In particular, the vertical coarse sample stage shaped up as the main contribution to mechanical drifts. After a vertical movement, the vertical stage shows drifts of several hundreds of nanometers. Therefore, the coarse vertical stage used for the PETRA III microscope has been chosen with regard to highest mechanical stability. But also some of the other stages have been replaced. The most important substitution concerns the scanner stage. While the scanner stage of the prototype has quite a large scanning range of about $250\ \mu\text{m}$, the new scanner for the PETRA III setup is limited to $100 \times 100\ \mu\text{m}^2$ horizontally and to only $30\ \mu\text{m}$ vertically, thereby improving resolution, precision, repeatability, and stability drastically.

Final Remark

The prototype of a hard x-ray scanning microscopy using refractive nanofocusing lenses is evidence of the feasibility of combining x-ray analytical methods with two-dimensional mapping and scanning tomography yielding structural, chemical and physical information from inside of an object with a spatial resolution of well below $100\ \text{nm}$, and even beyond $50\ \text{nm}$ in the case of applying x-ray ptychography. Based on the insights obtained from the prototype, an advanced nanoprobe setup is under development and will be installed at PETRA III in the middle of 2010. A large user community is looking forward to benefit from this highly performing instrument.

Bibliography

- [ABK⁺89] V. V. Aristov, Y. A. Basov, G. N. Kulipanov, V. F. Pindyurin, A. A. Snigirev, and A. S. Sokolov. Focusing properties of a Bragg-Fresnel lens in the white spectrum of synchrotron radiation. *Nucl. Instrum. Meth. A*, 274:390–393, 1989.
- [ANM01] Jens Als-Nielsen and Des McMorrow. *Elements of Modern X-ray Physics*. Wiley, 2001.
- [AOH⁺00] Erik H. Anderson, Deirdre L. Olynick, Bruce Harteneck, Eugene Veklerov, Gregory Denbeaux, Weilun Chao, Angelic Lucero, Lewis Johnson, and David Attwood. Nanofabrication and diffractive optics for high-resolution x-ray applications. *Papers from the 44th international conference on electron, ion, and photon beam technology and nanofabrication*, 18(6):2970–2975, 2000.
- [BC03] B. B. Baker and E. T. Copson. *The Mathematical Theory of Huygens’ Principle*. Ams Chelsea Publishing, 3rd edition, 2003.
- [BDK⁺08] Oliver Bunk, Martin Dierolf, Søren Kynde, Ian Johnson, Othmar Marti, and Franz Pfeiffer. Influence of the overlap parameter on the convergence of the ptychographical iterative engine. *Ultramicroscopy*, 108(5):481–487, 2008.
- [BFP⁺09] Pit Boye, Jan M. Feldkamp, Jens Patommel, Andreas Schwab, Sandra Stephan, Robert Hoppe, Christian G. Schroer, Manfred Burghammer, Christian Riekkel, Andre van der Hart, and Matthias KÜchler. Nanofocusing refractive x-ray lenses: Fabrication and modeling. In *9th International Conference on X-ray Microscopy*, volume 186 of *Journal of Physics: Conference Series*, page 012063, 2009.
- [BH15] U. Bonse and M. Hart. An x-ray interferometer. *Applied Physics Letters*, 6(8):155–156, 04 1965/04/15/.
- [BHS⁺07] M. J. Berger, J. H. Hubbell, S. M. Seltzer, J. Chang, J. S. Coursey, R. Sukumar, and D. S. Zucker. Xcom: Photon cross sections database. Technical report, National Institute of Standards and Technology (NIST), September 2007.
- [BHT94] D. Bilderback, S. A. Hoffman, and D. Thiel. Nanometer spatial resolution achieved in hard x-ray imaging and Laue diffraction experiments. *Science*, 263:201–203, 1994.

- [BKv03] C. Bergemann, H. Keymeulen, and J. F. van der Veen. Focusing X-ray beams to nanometer dimensions. *Phys. Rev. Lett.*, 91(20):204801, 2003.
- [Bor06] M. Born. *Optik - Ein Lehrbuch der elektromagnetischen Lichttheorie*. Springer, Berlin, 1933 (4th edition 2006).
- [Boy10] Pit Boye. *Nanofocusing Refractive X-Ray Lenses*. PhD thesis, Technical University of Dresden (TU Dresden), 2010. urn:nbn:de:bsz:14-qucosa-27137, <http://nbn-resolving.de/urn:nbn:de:bsz:14-qucosa-27137>.
- [BW99] Max Born and Emil Wolf. *Principles of Optics*. Cambridge University Press, Cambridge, 1999.
- [CDL⁺95] P. Chevallier, P. Dhez, F. Legrand, M. Idir, G. Soullie, A. Mirone, A. Erko, A. Snigirev, I. Snigireva, A. Suvorov, A. Freund, P. Engström, J. Als Nielsen, and A. Grübel. First test of the scanning x-ray microprobe with Bragg-Fresnel multilayer lens at ESRF beam line. *Nucl. Instrum. Methods A*, 354:584–587, 1995.
- [Cla04] James A. Clarke. *The Science and Technology of Undulators and Wigglers*. Oxford University Press, Oxford, 2004. <http://www.oup.com/>.
- [COD⁺07] C.T. Chantler, K. Olsen, R.A. Dragoset, J. Chang, A.R. Kishore, S.A. Kotochigova, and D.S Zucker. X-ray form factor, attenuation and scattering tables (version 2.1). Technical report, National Institute of Standards and Technology (NIST), September 2007.
- [CT65] James W. Cooley and John W. Tukey. An algorithm for the machine calculation of complex fourier series. *Mathematics of Computation*, 19(90):297–301, 1965.
- [CTJ⁺97] D. Chapman, W. Thomlinson, R. E. Johnston, D. Washburn, E. Pisano, N. Gmur, Z. Zhong, R. Menk, F. Arfelli, and D. Sayers. Diffraction enhanced x-ray imaging. *Physics in Medicine and Biology*, 42(11):2015–2025, 1997.
- [DGG⁺17] T. J. Davis, T. E. Gureyev, D. Gao, A. W. Stevenson, and S. W. Wilkins. X-ray image contrast from a simple phase object. *Physical Review Letters*, 74(16), 04 1995/04/17/.
- [DGG⁺nt] T. J. Davis, D. Gao, T. E. Gureyev, A. W. Stevenson, and S. W. Wilkins. Phase-contrast imaging of weakly absorbing materials using hard x-rays. *Nature*, 373(6515):595–598, 02 1995/02/16/print.
- [DHS⁺10] M. Dubslaff, M. Hanke, S. Schoeder, M. Burghammer, T. Boeck, and J. Patommel. X-ray nanodiffraction at individual SiGe/Si(001) dot molecules and its numerical description based on kinematical scattering theory. *Appl. Phys. Lett.*, 96(13), March 2010.

- [DKM⁺95] C. David, B. Kaulich, R. Medenwaldt, M. Hettwer, N. Fay, M. Diehl, J. Thieme, and G. Schmahl. Low-distortion electron-beam lithography for fabrication of high-resolution germanium and tantalum zone plates. *The 38th International symposium on electron, ion, and photon beams*, 13(6):2762–2766, 1995.
- [DRG⁺99] E. Di Fabrizio, F. Romanato, M. Gentili, S. Cabrini, B. Kaulich, J. Susini, and R. Barrett. High-efficiency multilevel zone plates for keV X-rays. *Nature*, 401:895–898, 1999.
- [DW51] Henning Dieker and Matthias Wuttig. Influence of deposition parameters on the properties of sputtered Ge₂Sb₂Te₅ films. *Thin Solid Films*, 478(1-2):248–251, 5 2005/5/1.
- [EGLP47] F. R. Elder, A. M. Gurewitsch, R. V. Langmuir, and H. C. Pollock. Radiation from electrons in a synchrotron. *Phys. Rev.*, 71(11):829–830, Jun 1947.
- [Els03] Veit Elser. Phase retrieval by iterated projections. *J. Opt. Soc. Am. A*, 20(1):40–55, 2003.
- [Fie82] James R. Fienup. Phase retrieval algorithms: a comparison. *Appl. Opt.*, 21(15):2758, 1982.
- [FM10] Jens Falta and Thomas Möller. *Forschung mit Synchrotronstrahlung*. Vieweg+Teubner, 2010.
- [FR04] H. M. L. Faulkner and J. M. Rodenburg. Movable aperture lensless transmission microscopy: A novel phase retrieval algorithm. *Phys. Rev. Lett.*, 93:023903, 2004.
- [FSD⁺98] Y. P. Feng, S. K. Sinha, H. W. Deckman, J. B. Hastings, and D. S. Siddons. X-ray flux enhancement in thin-film waveguides using resonant beam couplers. *Phys. Rev. Lett.*, 71(4):537–540, 1998.
- [FSF⁺95] Y. P. Feng, S. K. Sinha, E. E. Fullerton, G. Grübel, D. Abernathy, D. P. Siddons, and J. B. Hastings. X-ray Fraunhofer diffraction patterns from a thin-film waveguide. *Appl. Phys. Lett.*, 67(24):3647–3649, 1995.
- [FWN⁺00] I. Friedrich, V. Weidenhof, W. Njoroge, P. Franz, and M. Wuttig. Structural transformations of Ge₂Sb₂Te₅ films studied by electrical resistance measurements. *Journal of Applied Physics*, 87:4130, May 2000.
- [GPTV08] A. Götz, J. L. Pons, E. Taurel, and P. Vervier. The TANGO control system. *ICFA Beam Dynamics Newsletter*, 47:66–80, Dec 2008. <http://icfa-usa.jlab.org/archive/newsletter.shtml>.
- [GSF09] Manuel Guizar-Sicairos and James R. Fienup. Measurement of coherent x-ray focused beams by phase retrieval with transverse translation diversity. *Opt. Express*, 17(4):2670–2685, 2009.

- [GTE02] Sol M. Gruner, Mark W. Tate, and Eric F. Eikenberry. Charge-coupled device area x-ray detectors. *Review of Scientific Instruments*, 73(8):2815–2842, January 2002.
- [HDS⁺08] M. Hanke, M. Dubsclaff, M. Schmidbauer, T. Boeck, S. Schöder, M. Burghammer, C. Riekkel, J. Patommel, and C. G. Schroer. Scanning x-ray diffraction with 200 nm spatial resolution. *Appl. Phys. Lett.*, 92(19):193109, Jan 2008.
- [HFS⁺97] Ya. Hartman, A. K. Freund, I. Snigireva, A. Souvorov, and A. Snigirev. Two-dimensional X-ray microfocusing using a curved crystal Bragg-Fresnel lens. *Nucl. Instrum. Meth. A*, 385:371–375, 1997.
- [HIS⁺01] Shinjiro Hayakawa, Natsuki Ikuta, Motohiro Suzuki, Masao Wakatsuki, and Takeshi Hirokawa. Generation of an x-ray microbeam for spectromicroscopy at SPring-8 BL39XU. *J. Synchrotron Rad.*, 8:328–330, 2001.
- [Hof04] A. Hofmann. *The Physics of Synchrotron Radiation*. SAO/NASA Astrophysics Data System, July 2004.
- [HRC⁺01] Olivier Hignette, Gérard Rostaing, Peter Cloetens, Amparo Rommeveaux, Wolfgang Ludwig, and Andreas Freund. Submicron focusing of hard X-rays with reflecting surfaces at the ESRF. In Ian McNulty, editor, *X-Ray Micro- and Nano-Focusing: Applications and Techniques II*, volume 4499 of *Proceedings of the SPIE*, pages 105–116, Bellingham, 2001. SPIE.
- [HS07] J. H. Hubbell and S. M Seltzer. Tables of x-ray mass attenuation coefficients and mass energy-absorption coefficients. Technical report, National Institute of Standards and Technology (NIST), September 2007.
- [HS08] Ingolf H. Hertel and Claus-Peter Schulz. *Atom-, Molekul- Und Optische Physik*. Springer, 2008.
- [HTB94] S. A. Hoffman, D. J. Thiel, and D. H. Bilderback. Developments in tapered monocapillary and polycapillary glass X-ray concentrators. *Nucl. Instrum. Methods A*, 347:384–389, 1994.
- [HWF98] G. Hölzer, O. Wehrhan, and E. Förster. Characterization of flat and bent crystals for x-ray spectroscopy and imaging. *Cryst. Res. Technol.*, 33(4):555–567, 1998.
- [IB95] V N Ingal and E A Beliaevskaya. X-ray plane-wave topography observation of the phase contrast from a non-crystalline object. *Journal of Physics D: Applied Physics*, 28(11):2314–2317, 1995.
- [IIT⁺93] Makoto Ichinose, Takashi Ishida, Yuji Takagi, Motoshi Ito, Shunji Ohara, Isao Satoh, Yukinori Okazaki, and Ryoichi Imanaka. A high-density phase-change optical disk system possessing read/write compatibility with 90 mm magneto-optical disks. *Jap. J. Appl. Phys.*, 32:5320–5323, August 1993.

- [Jac98] J. D. Jackson. *Classical Electrodynamics*. Wiley, New York, third edition edition, 1998.
- [JCD⁺01] W. Jark, A. Cedola, S. Di Fonzo, M. Fiordelisi, S. Lagomarsino, N. V. Kovalenko, and V. A. Chernov. High gain beam compression in new-generation thin-film x-ray waveguides. *Appl. Phys. Lett.*, 78(9):1192–1194, 2001.
- [KB48] P. Kirkpatrick and A. Baez. Formation of optical images by x-rays. *J. Opt. Soc. Am.*, 38(9):766–774, 1948.
- [Kim87] Kwang-Je Kim. Brightness and coherence of synchrotron radiation and high-gain free electron lasers. *Nuclear Instruments and Methods in Physics Research Section A: Accelerators, Spectrometers, Detectors and Associated Equipment*, 261(1-2):44 – 53, 1987.
- [Kim99] Jin-Hong Kim. Correlation between microstructure and optical properties of ge2sb2te5 thin films. *Journal of Applied Physics*, 86:6770, Dec 1999.
- [KPH⁺99] Andreas Koch, Françoise Peyrin, Philippe Heurtier, Bernard Ferrand, Bernard Chambaz, Wolfgang Ludwig, and Maurice Couchaud. X-ray camera for computed microtomography of biological samples with micrometer resolution using lu3al5o12 and y3al5o12 scintillators. In *Proceedings of SPIE*, volume 3659, pages 170–179. SPIE, the International Society for Optical Engineering, Society of Photo-Optical Instrumentation Engineers, Bellingham, WA, ETATS-UNIS (1981) (Revue), January 1999.
- [KS88] Avinash C. Kak and Malcolm Slaney. *Principles of Computerized Tomographic Imaging*. IEEE Press, New York, 1988.
- [KSA⁺02] N. Kamijo, Y. Suzuki, M. Awaji, A. Takeuchi, H. Takano, T. Ninomiya, S. Tamura, and M. Yasumoto. Hard X-ray microbeam experiments with a sputtered-sliced Fresnel zone plate and its applications. *J. Synchrotron Rad.*, 9:182–186, 2002.
- [KSJ⁺01] L. Kipp, M. Skibowski, R. L. Johnson, R. Berndt, R. Adelung, S. Harm, and R. Seemann. Sharper images by focusing soft X-rays with photon sieves. *Nature*, 414:184–188, 2001.
- [Kur05] Olga Kurapova. *Development of Nanofocusing Refractive X-Ray Lenses*. PhD thesis, Aachen University (RWTH), 2005. <http://nbn-resolving.de/urn:nbn:de:hbz:82-opus-13411>.
- [KYW⁺08] Hyon Chol Kang, Hanfei Yan, Robert P Winarski, Martin V Holt, Joerg Maser, Chian Liu, Ray Conley, Stefan Vogt, Albert T Macrander, and G. Brian Stephenson. Focusing of hard x-rays to 16 nanometers with a multilayer laue lens. *Appl. Phys. Lett.*, 92(22):221114, Jan 2008.

- [Lar97] J. J. Larmor. On a dynamical theory of the electric and luminiferous medium. *Philosophical Transactions of the Royal Society*, 190:205–300, 1897.
- [LCC⁺97] S. Lagomarsino, A. Cedola, P. Cloetens, S. Di Fonzo, W. Jark, G. Soullié, and C. Riekel. Phase contrast hard x-ray microscopy with submicron resolution. *Appl. Phys. Lett.*, 71(18):2557–2559, 1997.
- [LCD⁺02] X. Llopart, M. Campbell, R. Dinapoli, D. San Segundo, and E. Pernigotti. Medipix2: A 64 k pixel readout chip with 55 um square elements working in single photon counting mode. *Nuclear Science, IEEE Transactions on*, 49(5):2279 – 2283, oct 2002.
- [LCQ⁺07] C. Liu, R. Conley, J. Qian, C. M. Kewish, A. T. Macrander, J. Maser, H. C. Kang, H. Yan, and G. B. Stephenson. Bonded Multilayer Laue Lens for focusing hard X-rays. *Nuclear Instruments and Methods in Physics Research A*, 582:123–125, November 2007.
- [Len03] B. Lengeler. “Unterschieden” und “unterscheidbar” sind entschieden zu unterscheiden. *Aus einem Disput mit Til Florian Günzler über Kohärenz in der Quantenmechanik*, 2003.
- [Lié98] Alfred Liénard. Champ électrique et magnétique produit par une charge électrique. *L’Éclairage Électrique*, 16, 1898.
- [Lio37] J. Liouville. Second mémoire sur le développement des fonctions ou parties de fonctions en séries dont les divers termes sont assujettis à satisfaire à une même équation différentielle du second ordre, contenant un paramètre variable. *J. math. pures et appl.*, 2:16–35, 1837.
- [LMP⁺07] Jean-Claude Labiche, Olivier Mathon, Sakura Pascarelli, Mark A. Newton, Gemma Guilera Ferre, Caroline Curfs, Gavin Vaughan, Alejandro Homs, and David Fernandez Carreiras. Invited article: The fast readout low noise camera as a versatile x-ray detector for time resolved dispersive extended x-ray absorption fine structure and diffraction studies of dynamic problems in materials science, chemistry, and catalysis. *Review of Scientific Instruments*, 78(9):091301, 2007.
- [LSFO99] F. Laerme, A. Schilp, K. Funk, and M. Offenbergl. Bosch deep silicon etching: improving uniformity and etch rate for advanced mems applications. In *Micro Electro Mechanical Systems, 1999. MEMS ’99. Twelfth IEEE International Conference on*, pages 211–216. IEEE, Jan 1999.
- [LSH⁺98] U. Lienert, C. Schulze, V. Honkimäki, Th. Tschentscher, S. Garbe, O. Hignette, A. Horsewell, M. Lingham, H. F. Poulsen, N. B. Thomsen, and E. Ziegler. Focusing optics for high-energy x-ray diffraction. *J. Synchrotron Rad.*, 5:226–231, 1998.

- [LST⁺99] Bruno Lengeler, Christian Schroer, Johannes Tümmeler, Boris Benner, Matthias Richwin, Anatoly Snigirev, Irina Snigireva, and Michael Drakopoulos. Imaging by parabolic refractive lenses in the hard x-ray range. *J. Synchrotron Rad.*, 6:1153–1167, 1999.
- [LYL⁺92] B. Lai, W. Yun, D. Legnini, Y. Xiao, J. Chrzas, P. Viccaro, V. White, S. Bajikar, D. Denton, F. Cerrina, E. Di Fabrizio, M. Gentili, L. Grella, and M. Baciocchi. Hard x-ray phase zone plate fabricated by lithographic techniques. *Appl. Phys. Lett.*, 61(16):1877–1879, 1992.
- [MBP97] A. G. Michette, C. J. Buckley, and S. J. Pfauntsch. Phase modulating zone plates for x-rays of energy 1-8 keV. *Optics Communications*, 141(3-4):118 – 122, 1997.
- [MCKS99] Jianwei Miao, Pambos Charalambous, Janos Kirz, and David Sayre. Extending the methodology of X-ray crystallography to allow imaging of micrometre-sized non-crystalline specimens. *Nature*, 400:342–344, 1999.
- [MHC⁺03] S. Marchesini, H. He, H. N. Chapman, S. P. Hau-Riege, A. Noy, M. R. Howells, U. Weierstall, and J. C. H. Spence. X-ray image reconstruction from a diffraction pattern alone. *Physical Review B*, 68(14):140101(R), Jan 2003.
- [MHK⁺05] D. M. Mills, J. R. Helliwell, Å. Kwick, T. Ohta, I. A. Robinson, and A. Authier. Brightness, spectral brightness or brilliance – Report of the Working Group on Synchrotron Radiation Nomenclature. *Journal of Synchrotron Radiation*, 12(3):385, May 2005.
- [Mom05] Atsushi Momose. Recent advances in x-ray phase imaging. *Japanese Journal of Applied Physics*, 44(9A):6355–6367, 2005.
- [Mot51] H. Motz. Applications of the Radiation from Fast Electron Beams. *Journal of Applied Physics*, 22:527–535, May 1951.
- [MPPZ99] Ch. Morawe, P. Pecci, J. Ch. Peffen, and E. Ziegler. Design and performance of graded multilayers as focusing elements for x-ray optics. *Rev. Sci. Instrum.*, 70(8):3227–3232, 1999.
- [MR09] Andrew M Maiden and John M Rodenburg. An improved ptychographical phase retrieval algorithm for diffractive imaging. *Ultramicroscopy*, 109(10):1256–1262, Jan 2009.
- [MSS⁺04] J. Maser, G. B. Stephenson, D. Shu, B. Lai, S. Vogt, A. Khounsary, Y. Li, C. Benson, and G. Schneider. Conceptual design for a beamline for a hard x-ray nanoprobe with 30 nm spatial resolution. In Tony Warwick, Joachim Stohr, Howard A. Padmore, and John Arthur, editors, *Eighth International Conference*

- on *Synchrotron Radiation Instrumentation*, volume 705, pages 470–473. AIP, 2004.
- [MTW53] H. Motz, W. Thon, and R. N. Whitehurst. Experiments on radiation by fast electron beams. *Journal of Applied Physics*, 24(7):826–833, Jul 1953.
- [MUF+99] T. Missalla, I. Uschmann, E. Förster, G. Jenke, and D. von der Linde. Monochromatic focusing of subpicosecond x-ray pulses in the keV range. *Rev. Sci. Instrum.*, 70(2):1288–1299, 1999.
- [MWH+06] J. Maser, R. Winarski, M. Holt, D. Shu, C. Benson C, B. Tieman, C. Preissner, A. Smolyanitskiy, B. Lai, S. Vogt, G. Wiemerslage, and G. Stephenson. The hard x-ray nanoprobe beamline at the advanced photon source. In *Proceedings of the 8th Int. Conf. on X-ray Microscopy*, 7, pages 26–29. Institute of Pure and Applied Physics, 2006.
- [MYM+08] Hidekazu Mimura, Hirokatsu Yumoto, Satoshi Matsuyama, Soichiro Handa, Takashi Kimura, Yasuhisa Sano, Makina Yabashi, Yoshinori Nishino, Kenji Tamasaku, Tetsuya Ishikawa, and Kazuto Yamauchi. Direct determination of the wave field of an x-ray nanobeam. *Phys. Rev. A*, 77(1):015812, Jan 2008.
- [MYT+06] Atsushi Momose, Wataru Yashiro, Yoshihiro Takeda, Yoshio Suzuki, and Tadashi Hattori. Phase tomography by x-ray talbot interferometry for biological imaging. *Japanese Journal of Applied Physics*, 45(6A):5254–5262, 2006.
- [Njo01] Walter Kamande Njoroge. *Phase Change Optical Recording : Preparation and X-ray Characterization of GeSbTe and AgInSbTe films*. PhD thesis, RWTH Aachen, 2001. <http://nbn-resolving.de/urn:nbn:de:hbz:82-opus-2723>.
- [Pat03] Jens Patommel. *Entwicklung einer hochauflösenden Kamera für die Mikroskopie mit harter Röntgenstrahlung*. SLUB Dresden (Qucosa: Quality Content of Saxony), November 2003. Engl.: Development of a high resolution x-ray camera for magnified tomography with hard x rays. Diploma thesis, RWTH Aachen 2003, <http://nbn-resolving.de/urn:nbn:de:bsz:14-qucosa-64429>.
- [PCH81] E. F. Plechaty, D. E. Cullen, and R. J. Howerton. Tables and graphs of photon-interaction cross sections from 0.1 keV to 100 MeV derived from the LLL evaluated-nuclear-data library. Technical report, SAO/NASA Astrophysics Data System, November 1981.
- [PCR+07] Cyril Ponchut, Joël Clément, Jean-Marie Rigal, Emmanuel Papillon, John Vallega, Daniel LaMarra, and Bettina Mikulec. Photon-counting x-ray imaging at kilohertz frame rates. *Nuclear Instruments and Methods in Physics Research Section A: Accelerators, Spectrometers, Detectors and Associated Equipment*, 576(1):109–112, 2007.

- [PV98] V. V. Protopopov and K. A. Valiev. Theory of an ideal compound x-ray lens. *Optics Communications*, 151(4-6):297 – 312, 1998.
- [PWBDnt] Franz Pfeiffer, Timm Weitkamp, Oliver Bunk, and Christian David. Phase retrieval and differential phase-contrast imaging with low-brilliance x-ray sources. *Nat Phys*, 2(4):258–261, 04 2006/04//print.
- [QPC⁺06] H. M. Quiney, A. G. Peele, Z. Cai, D. Patterson, and K. A. Nugent. Diffractive imaging of highly focused X-ray fields. *Nature Physics*, 2:101–104, 2006.
- [RF04] J. M. Rodenburg and H. M. L. Faulkner. A phase retrieval algorithm for shifting illumination. *Appl. Phys. Lett.*, 85(20):4795–4797, 2004.
- [RHC⁺07] J. M. Rodenburg, A. C. Hurst, A. G. Cullis, B. R. Dobsen, F. Pfeiffer, O. Bunk, C. David, K. Jefimovs, and I. Johnson. Hard-x-ray lensless imaging of extended objects. *Phys. Rev. Lett.*, 98:034801, 2007.
- [Rön95] Wilhelm Conrad Röntgen. Ueber eine neue Art von Strahlen. *Sitzungsberichte der physikal.-medizin. Gesellschaft*, 132, 1895.
- [Rön98] Wilhelm Conrad Röntgen. Ueber eine neue Art von Strahlen. *Annalen der Physik*, 300:12–17, 1898. Provided by the SAO/NASA Astrophysics Data System.
- [SBF⁺08] Christian G. Schroer, Pit Boye, Jan Feldkamp, Jens Patommel, Andreas Schropp, Andreas Schwab, Sandra Stephan, Manfred Burghammer, Sebastian Schöder, and Christian Riekell. Coherent x-ray diffraction imaging with nanofocused illumination. *Phys. Rev. Lett.*, 101(9):090801, 2008.
- [SBF⁺10a] C. G. Schroer, P. Boye, J. M. Feldkamp, J. Patommel, A. Schropp, D. Samberg, S. Stephan, M. Burghammer, S. Schöder, C. Riekell, B. Lengeler, G. Falkenberg, G. Wellenreuther, M. Kuhlmann, R. Frahm, D. Lützenkirchen-Hecht, and W. H. Schroeder. Hard X-ray microscopy with elemental, chemical, and structural contrast. *Acta Physica Polonica A*, 117(2):357–368, 2010.
- [SBF⁺10b] Christian G. Schroer, Pit Boye, Jan M. Feldkamp, Jens Patommel, Dirk Samberg, Andreas Schropp, Andreas Schwab, Sandra Stephan, Gerald Falkenberg, Gerd Wellenreuther, and Nadja Reimers. Hard X-ray nanoprobe at beamline P06 at PETRA III. *Nucl. Instrum. Meth. A*, 616(2-3):93–97, 2010.
- [SBF⁺10c] Andreas Schropp, Pit Boye, Jan M. Feldkamp, Robert Hoppe, Jens Patommel, Dirk Samberg, Sandra Stephan, Klaus Giewekemeyer, Robin N. Wilke, Tim Salditt, Johannes Gulden, Adrian P. Mancuso, Ivan A. Vartanyants, Edgar Weckert, Sebastian Schöder, Manfred Burghammer, and Christian G. Schroer. Hard x-ray nanobeam characterization by coherent diffraction microscopy. *Appl. Phys. Lett.*, 96(9):091102, 2010.

- [SBF⁺10d] Andreas Schropp, Pit Boye, Jan M. Feldkamp, Robert Hoppe, Jens Patommel, Dirk Samberg, Sandra Stephan, Klaus Giewekemeyer, Robin N. Wilke, Tim Salditt, Johannes Gulden, Adrian P. Mancuso, Ivan A. Vartanyants, Edgar Weckert, Sebastian Schöder, Manfred Burghammer, and Christian G. Schroer. Hard x-ray nanobeam characterization by coherent diffraction microscopy. *Appl. Phys. Lett.*, 96(9):091102, 2010.
- [SBG⁺11] A. Schropp, P. Boye, A. Goldschmidt, S. Hönig, R. Hoppe, J. Patommel, C. Rakete, D. Samberg, S. Stephan, S. Schöder, M. Burghammer, and C. G. Schroer. Non-destructive and quantitative imaging of a nano-structured microchip by ptychographic hard x-ray scanning microscopy. *Journal of Microscopy*, 241(1):9–12, 2011.
- [SBW⁺02] Marco Stampanoni, Gunther Borchert, Peter Wyss, Rafael Abela, Bruce Patterson, Steven Hunt, Detlef Vermeulen, and Peter Rügsegger. High resolution X-ray detector for synchrotron-based microtomography. *Nucl. Instrum. Meth. A*, 491(1–2):291–301, Sep 2002.
- [Sch45] Julian Schwinger. *On Radiation by Electrons in a Betatron*. LBNL-39088/CBP Note-179, 1945.
- [Sch46] Julian Schwinger. Electron radiation in high energy accelerators. *Phys. Rev.*, 70:798, 1946.
- [Sch49] Julian Schwinger. On the classical radiation of accelerated electrons. *Phys. Rev.*, 75(12):1912–1925, Jun 1949.
- [Sch01] Christian G. Schroer. Reconstructing x-ray fluorescence microtomograms. *Appl. Phys. Lett.*, 79(12):1912–1914, 2001.
- [Sch08] A. Schropp. *Experimental Coherent X-Ray Diffractive Imaging: Capabilities and Limitations of the Technique*. PhD thesis, University of Hamburg, 2008. http://www.physnet.uni-hamburg.de/services/fachinfo/___Kurzfassungen/Andreas___Schropp.htm.
- [SG95] M. Schuster and H. Göbel. Parallel-beam coupling into channel-cut monochromators using curved graded multilayers. *J. Phys. D: Appl. Phys.*, 28:A270–A275, 1995.
- [SGB⁺99] M. Schuster, H. Göbel, L. Brügemann, D. Bahr, F. Burgäzy, C. Michaelsen, M. Störmer, P. Ricardo, R. Dietsch, T. Holz, and H. Mai. Laterally graded multilayer optics for x-ray analysis. In C. A. MacDonald, editor, *EUV, X-Ray, and Neutron Optics and Sources*, volume 3767 of *Proceedings of the SPIE*, pages 183–198, 1999.

- [SJT97] S. J. Spector, C. J. Jacobsen, and D. M. Tennant. Process optimization for production of sub-20 nm soft x-ray zone plates. *Papers from the 41st international conference on electron, ion, and photon beam technology and nanofabrication*, 15(6):2872–2876, 1997.
- [SK37] I. N. Stranski and L. Krastanow. Zur Theorie der orientierten Ausscheidung von Ionenkristallen aufeinander. *Monatshefte für Chemie / Chemical Monthly*, 71(1):351–364, 1937.
- [SKH⁺03] Christian G. Schroer, Marion Kuhlmann, U. Thomas Hunger, Til Florian Günzler, Olga Kurapova, Sebastian Feste, Fatima Frehse, Bruno Lengeler, Michael Drakopoulos, Andrea Somogyi, Alexandre S. Simionovici, Anatoly Snigirev, Irina Snigireva, Christoph Schug, and Walter H. Schröder. Nanofocusing parabolic refractive x-ray lenses. *Appl. Phys. Lett.*, 82(9):1485–1487, 2003. Editor’s Choice in *Science* **299** (5613), 1628 (2003).
- [SKP⁺05a] C. G. Schroer, O. Kurapova, J. Patommel, P. Boye, J. Feldkamp, B. Lengeler, M. Burghammer, C. Riekkel, L. Vincze, A. van der Hart, and M. Küchler. Hard x-ray nanoprobe based on refractive x-ray lenses. *Appl. Phys. Lett.*, 87(12):124103, 2005.
- [SKP⁺05b] C. G. Schroer, O. Kurapova, J. Patommel, P. Boye, J. Feldkamp, B. Lengeler, M. Burghammer, C. Riekkel, L. Vincze, A. van der Hart, and M. Küchler. Hard x-ray nanoprobe based on refractive x-ray lenses. *Appl. Phys. Lett.*, 87(12):124103, 2005.
- [SKSL96] A. Snigirev, V. Kohn, I. Snigireva, and B. Lengeler. A compound refractive lens for focusing high energy x-rays. *Nature (London)*, 384:49, 1996.
- [SL05] C. G. Schroer and B. Lengeler. Focusing hard x rays to nanometer dimensions by adiabatically focusing lenses. *Phys. Rev. Lett.*, 94:054802, 2005.
- [SLH⁺98] C. Schulze, U. Lienert, M. Hanfland, M. Lorenzen, and F. Zontone. Microfocusing of hard x-rays with cylindrically bent crystal monochromators. *J. Synchrotron Rad.*, 5:77–81, 1998.
- [SMLV04] D. Shu, J. Maser, B. Lai, and S. Vogt. Design for an x-ray nanoprobe prototype with a sub-10-nm positioning requirement. In Tony Warwick, Joachim Stohr, Howard A. Padmore, and John Arthur, editors, *Conference Proceedings: Eighth International Conference on Synchrotron Radiation Instrumentation*, volume 705, pages 1287–1290. AIP, 2004.
- [SS74] Eberhard Spiller and Armin Segmüller. Propagation of x rays in waveguides. *Applied Physics Letters*, 24(2):60–61, 1974.

- [SS10] Andreas Schropp and Christian G. Schroer. Dose requirements for resolving a given feature in an object by coherent x-ray diffraction imaging. *New Journal of Physics*, 12:035016, 2010.
- [SSA95] G. Schneider, T. Schliebe, and H. Aschoff. Cross-linked polymers for nanofabrication of high-resolution zone plates in nickel and germanium. *The 38th International symposium on electron, ion, and photon beams*, 13(6):2809–2812, 1995.
- [SSK⁺95] A. Snigirev, I. Snigireva, V. Kohn, S. Kuznetsov, and I. Schelokov. On the possibilities of x-ray phase contrast microimaging by coherent high-energy synchrotron radiation. *Review of Scientific Instruments*, 66(12):5486–5492, 1995.
- [STTT05] Yoshio Suzuki, Akihisa Takeuchi, Hidekazu Takano, and Hisataka Takenaka. Performance test of fresnel zone plate with 50 nm outermost zone width in hard x-ray region. *Japanese Journal of Applied Physics*, 44(4A):1994–1998, 2005.
- [SU92] Y. Suzuki and F. Uchida. Hard x-ray microprobe with total-reflection mirrors. *Rev. Sci. Instrum.*, 63(1):578–581, January 1992.
- [Suz04] Yoshio Suzuki. Resolution limit of refractive lens and fresnel lens in x-ray region. *Japanese Journal of Applied Physics*, 43(10):7311–7314, 2004.
- [Tal07] Richard Talman. *Accelerator X-Ray Sources*. WILEY-VCH Verlag GmbH & Co. KGaA, 1 edition, 2007.
- [TDM⁺08] Pierre Thibault, Martin Dierolf, Andreas Menzel, Oliver Bunk, Christian David, and Franz Pfeiffer. High-resolution scanning x-ray diffraction microscopy. *Science*, 321(5887):379–382, 2008.
- [TDR07] TDR. The European X-Ray Free-Electron Laser (XFEL) - Technical Design Report. Technical report, Deutsches Elektronen-Synchrotron (DESY), 2007. ISBN 978-3-935702-17-1, http://www.xfel.eu/documents/technical_documents/.
- [TYK⁺02] S. Tamura, M. Yasumoto, N. Kamijo, Y. Suzuki, M. Awaji, A. Takeuchi, H. Takano, and K. Handa. Development of a multilayer Fresnel zone plate for high-energy synchrotron radiation X-rays by DC sputtering deposition. *J. Synchrotron Rad.*, 9:154–159, 2002.
- [UBF86] J. Underwood, T. Barbee Jr., and C. Frieber. X-ray microscope with multilayer mirror. *Appl. Opt.*, 25(11):1730–1732, June 1986.
- [Und86] J. Underwood. High-energy x-ray microscopy with multilayer reflectors (invited). *Rev. Sci. Instrum.*, 57(8):2119–2123, 1986.
- [UTWG88] J. Underwood, A. Thompson, Y. Wu, and R. Giauque. X-ray microprobe using multilayer mirrors. *Nucl. Instrum. Methods A*, 266:296–302, 1988.

- [WFZW99] V. Weidenhof, I. Friedrich, S. Ziegler, and M. Wuttig. Atomic force microscopy study of laser induced phase transitions in Ge₂Sb₂Te₅. *Journal of Applied Physics*, 86:5879, Nov 1999.
- [WGG⁺96] S. W. Wilkins, T. E. Gureyev, D. Gao, A. Pogany, and A. W. Stevenson. Phase-contrast imaging using polychromatic hard x-rays. *Nature*, 384(6607):335–338, Nov 1996.
- [Wie07] H. Wiedemann. *Particle Accelerator Physics*. Springer-Verlag Berlin, 3rd edition, 2007.
- [Wil92] Klaus Wille. *Physik der Teilchenbeschleuniger und Synchrotronstrahlungsquellen*. B. G. Teubner Stuttgart, 1st edition, 1992.
- [Wil00] Klaus Wille. *The Physics of Particle Accelerators - An Introduction*. Oxford University Press, 1st edition, 2000.
- [Wol87] Hermann Wollnik. *Optics of charged particles*. Academic Press, Orlando, 1987.
- [WS07] M. Wuttig and C. Steimer. Phase change materials: From material science to novel storage devices. *Applied Physics A*, 87:411, Jun 2007.
- [YAT⁺97a] T. Yuasa, M. Akiba, T. Takeda, M. Kazama, A. Hoshino, Y. Watanabe, K. Hyodo, F.A. Dilmanian, T. Akatsuka, and Y. Itai. Reconstruction method for fluorescent x-ray computed tomography by least-squares method using singular value decomposition. *Nuclear Science, IEEE Transactions on*, 44(1):54–62, Feb 1997.
- [YAT⁺97b] Tetsuya Yuasa, Masahiro Akiba, Tohoru Takeda, Masahiro Kazama, Atsunori Hoshino, Yuuki Watanabe, Kazuyuki Hyodo, F. Avraham Dilmanian, Takao Akatsuka, and Yuji Itai. Incoherent-scatter computed tomography with monochromatic synchrotron x ray: Feasibility of multi-ct imaging system for simultaneous measurement of fluorescent and incoherent scatter x rays. *IEEE Trans. Nucl. Sci.*, 44(5):1760–1769, 1997.
- [YLC⁺99] W. Yun, B. Lai, Z. Cai, J. Maser, D. Legnini, E. Gluskin, Z. Chen, A. A. Krasnoperova, Y. Vladimirovsky, R. Cerrina, E. Di Fabrizio, and M. Gentili. Nanometer focusing of hard x rays by phase zone plates. *Rev. Sci. Instrum.*, 70(5):2238–2241, 1999.
- [ZBP⁺00] M. J. Zwanenburg, J. H. H. Bongaerts, J. F. Peters, D. Riese, and J. F. van der Veen. Focusing of coherent X-rays in a tapered planar waveguide. *Physica B*, 283:285–288, 2000.

List of Figures

2.1	Integral Theorem of Helmholtz and Kirchhoff: region of integration	7
2.2	Illustrating the derivation of Fresnel-Kirchhoff's Diffraction Formula	9
2.3	Illustrating the Diffraction formula: diffracting plane and observation plane .	11
2.4	Contributions to the mass attenuation coefficient	15
2.5	Refraction of visible light and x rays at an interface	18
3.1	Radiation field of an accelerated electron	25
3.2	Peak brilliance of dipole magnets, wigglers and undulators	26
3.3	Layout of a 3rd generation synchrotron radiation facility	27
3.4	Drawing of a dipole magnet, wiggler and undulator	32
3.5	Angular distribution of synchrotron light	33
3.6	Geometry for an observer of dipole magnet radiation	34
4.1	Compound parabolic refractive x-ray lenses (CRLs)	41
4.2	Schematic drawing of nanofocusing lenses (NFLs)	43
4.3	Nanofocusing lenses made of silicon	44
4.4	Drawing of an adiabatically focusing x-ray lens	45
4.5	Principal and focal plane of a focusing optic	46
4.6	Path of a single ray as it passes through a compound parabolic refractive lens	47
4.7	Chromaticity of a compound parabolic refractive x-ray lens (CRL or NFL) .	56
4.8	Path difference in a focusing lens	63
4.9	Two-stage focusing scheme	65
4.10	Imaging geometry for two-stage focusing	66
4.11	Prefocus parameter as a function of refractive power	69
4.12	Beam size in the NFL aperture plane with prefocusing lens	71
4.13	Beam size, cross section, and flux gain with prefocusing lenses	73
5.1	Layout of the ESRF beamline ID 13	78
5.2	Nanobeam setup for the hard x-ray scanning microscope	79
5.3	Schematic drawing of the scanner unit	80
5.4	Photograph of the nanoprobe setup at ESRF beamline ID 13	81
5.5	Blade geometry for avoiding external total reflection	83
5.6	High resolution x-ray camera	87

5.7	Diffraction cameras as used in nanoprobe experiments	90
6.1	Alignment of nanofocusing lenses	98
6.2	Fluorescence knife edge scan	101
6.3	Line profiles of the far-field image of the focus	102
6.4	Experimental setup for x-ray ptychography	103
6.5	Reconstructed complex wavefield in the focal plane	104
6.6	Reconstructed complex caustic of the nanofocused x-ray beam	105
6.7	Layout of a fluorescence element mapping experiment	106
6.8	Fluorescence spectrum of the pollen of <i>Arabidopsis thaliana</i>	108
6.9	Element distribution of the pollen of <i>Arabidopsis thaliana</i>	109
6.10	Reconstructed element distribution of the pollen of <i>Arabidopsis thaliana</i>	111
6.11	Nano diffraction of phase change media	112
6.12	Fluorescence mapping of Stranski-Krastanow islands	113
6.13	Diffraction images from individual Stranski-Krastanow islands	114
6.14	Coherent x-ray diffraction on gold particles	116
6.15	Ptychography: phase of the reconstructed object function of a microchip	118

List of Publications

- [1] Andreas Schropp, Pit Boye, Andy Goldschmidt, Susi Hönig, Robert Hoppe, Jens Patommel, Christoph Rakete, Dirk Samberg, Sandra Stephan, Sebastian Schöder, Manfred Burghammer, and Christian G. Schroer. Non-destructive and quantitative imaging of a nano-structured microchip by ptychographic hard x-ray scanning microscopy. *Journal of Microscopy*, 241(1):9–12, 2011.
- [2] Andreas Schropp, Pit Boye, Jan M. Feldkamp, Robert Hoppe, Jens Patommel, Dirk Samberg, Sandra Stephan, Klaus Giewekemeyer, Robin N. Wilke, Tim Salditt, Johannes Gulden, Adrian P. Mancuso, Ivan A. Vartanyants, Edgar Weckert, Sebastian Schöder, Manfred Burghammer, and Christian G. Schroer. Hard x-ray nanobeam characterization by coherent diffraction microscopy. *Appl. Phys. Lett.*, 96(9):091102, 2010.
- [3] M. Dubslaff, M. Hanke, S. Schoeder, M. Burghammer, T. Boeck, and J. Patommel. X-ray nanodiffraction at individual SiGe/Si(001) dot molecules and its numerical description based on kinematical scattering theory. *Appl. Phys. Lett.*, 96(13), March 2010.
- [4] Christian G. Schroer, Pit Boye, Jan M. Feldkamp, Jens Patommel, Dirk Samberg, Andreas Schropp, Andreas Schwab, Sandra Stephan, Gerald Falkenberg, Gerd Wellenreuther, and Nadja Reimers. Hard X-ray nanoprobe at beamline P06 at PETRA III. *Nucl. Instrum. Meth. A*, 616(2-3):93–97, 2010.
- [5] C. G. Schroer, P. Boye, J. M. Feldkamp, J. Patommel, A. Schropp, D. Samberg, S. Stephan, M. Burghammer, S. Schöder, C. Riekkel, B. Lengeler, G. Falkenberg, G. Wellenreuther, M. Kuhlmann, R. Frahm, D. Lützenkirchen-Hecht, and W. H. Schroeder. Hard X-ray microscopy with elemental, chemical, and structural contrast. *Acta Physica Polonica A*, 117(2):357–368, 2010.
- [6] Pit Boye, Jan M. Feldkamp, Jens Patommel, Andreas Schwab, Sandra Stephan, Robert Hoppe, Christian G. Schroer, Manfred Burghammer, Christian Riekkel, Andre van der Hart, and Matthias Küchler. Nanofocusing refractive x-ray lenses: Fabrication and modeling. In *9th International Conference on X-ray Microscopy*, volume 186 of *Journal of Physics: Conference Series*, page 012063, 2009.
- [7] Marion Kuhlmann, Jan M. Feldkamp, Jens Patommel, Stephan V. Roth, Andreas Timmann, Rainer Gehrke, Peter Müller-Buschbaum, and Christian G. Schroer. Grazing

- incidence small-angle x-ray scattering microtomography on a self-ordered dried drop of nanoparticles. *Langmuir Lett.*, 25(13):7241–7243, 2009.
- [8] Christian G. Schroer, Pit Boye, Jan M. Feldkamp, Jens Patommel, Andreas Schropp, Andreas Schwab, Sandra Stephan, Manfred Burghammer, Sebastian Schöder, Christian Riekkel, and Walter H. Schröder. Hard x-ray scanning microscopy with fluorescence and diffraction contrast. In *9th International Conference on X-ray Microscopy*, volume 186 of *Journal of Physics: Conference Series*, page 012016, 2009.
- [9] M. Hanke, M. Dubslaff, M. Schmidbauer, T. Boeck, S. Schöder, M. Burghammer, C. Riekkel, J. Patommel, and C. G. Schroer. Scanning x-ray diffraction with 200 nm spatial resolution. *ESRF Spotlight on Science*, 64, August 2008.
- [10] M. Hanke, M. Dubslaff, M. Schmidbauer, T. Boeck, S. Schöder, M. Burghammer, C. Riekkel, J. Patommel, and C. G. Schroer. Scanning x-ray diffraction with 200 nm spatial resolution. *Appl. Phys. Lett.*, 92(19):193109, Jan 2008.
- [11] C. G. Schroer, P. Boye, J. M. Feldkamp, J. Patommel, A. Schropp, A. Schwab, S. Stephan, M. Burghammer, S. Schöder, and C. Riekkel. Gold nanoparticle imaged with 5 nm spatial resolution. *ESRF Spotlight on Science*, 68, October 2008.
- [12] Christian G. Schroer, Pit Boye, Jan Feldkamp, Jens Patommel, Andreas Schropp, Andreas Schwab, Sandra Stephan, Manfred Burghammer, Sebastian Schöder, and Christian Riekkel. Coherent x-ray diffraction imaging with nanofocused illumination. *Phys. Rev. Lett.*, 101(9):090801, 2008.
- [13] Christian G. Schroer, Pit Boye, Jan M. Feldkamp, Jens Patommel, Andreas Schropp, Andreas Schwab, Sandra Stephan, Manfred Burghammer, Sebastian Schöder, and Christian Riekkel. Coherent x-ray diffraction imaging with nanofocused illumination. *Virtual Journal of Nanoscale Science & Technology*, 18(10), 2008.
- [14] J. M. Feldkamp, C. G. Schroer, J. Patommel, B. Lengeler, T. F. Günzler, M. Schweitzer, C. Stenzel, M. Dieckmann, and W. H. Schröder. Compact x-ray microtomography system for element mapping and absorption imaging. *Rev. Sci. Instrum.*, 78(7):073702, 2007.
- [15] J.-D. Grunwaldt, S. Hannemann, B. Kimmerle, A. Baiker, P. Boye, J. Patommel, and C. G. Schroer. Spatial changes of the catalyst structure inside a fixed-bed microreactor during the partial oxidation of methane. In *HASYLAB Jahresbericht*, page 797, Hamburg, 2007. DESY.
- [16] M. Krings, A. Mahnken, C. Schroer, J. Patommel, W. Kalender, and B. Glasmacher. CT, μ -CT und μ -Tomographie (Synchrotron) der in vitro Kalzifizierung. In *Bildverarbeitung für die Medizin 2006*, Informatik aktuell, pages 444–448. Springer, 2006.

- [17] Christian G. Schroer, Olga Kurapova, Jens Patommel, Pit Boye, Jan Feldkamp, Bruno Lengeler, Manfred Burghammer, Christian Riekkel, Laszlo Vincze, Andre van der Hart, and Matthias Kuchler. Hard x-ray nanoprobe based on refractive x-ray lenses. In Jae-Young Choi and Seungyu Rah, editors, *Synchrotron Radiation Instrumentation: Ninth International Conference on Synchrotron Radiation Instrumentation*, volume 879 of *AIP Conference Proceedings*, pages 1295–1298, 2006.
- [18] Christian G. Schroer, Olga Kurapova, Jens Patommel, Pit Boye, Jan Feldkamp, Bruno Lengeler, Manfred Burghammer, Christian Riekkel, Laszlo Vincze, Andre van der Hart, and Matthias Kuchler. Hard x-ray nanoprobe based on refractive x-ray lenses. *ESRF Highlights 2005*, pages 55–57, 2006.
- [19] Christian G. Schroer, Marion Kuhlmann, Til Florian Günzler, Boris Benner, Olga Kurapova, Jens Patommel, Bruno Lengeler, Stephan V. Roth, Rainer Gehrke, Anatoly Snigirev, Irina Snigireva, Norbert Striebeck, Armando Almendarez-Camarillo, and Felix Beckmann. Full-field and scanning microtomography based on parabolic refractive x-ray lenses. In U. Bonse, editor, *Developments in X-Ray Tomography V*, volume 6318 of *Proceedings of the SPIE*, page 63181H, Bellingham, WA, 2006. SPIE, SPIE.
- [20] C. G. Schroer, O. Kurapova, J. Patommel, P. Boye, J. Feldkamp, B. Lengeler, M. Burghammer, C. Riekkel, L. Vincze, A. van der Hart, and M. Kuchler. Hard x-ray nanoprobe based on refractive x-ray lenses. *Appl. Phys. Lett.*, 87(12):124103, 2005. Highlighted in *Nature Materials*, nanozone news.
- [21] C. G. Schroer, O. Kurapova, J. Patommel, P. Boye, J. Feldkamp, B. Lengeler, M. Burghammer, C. Riekkel, L. Vincze, A. van der Hart, and M. Kuchler. Hard x-ray nanoprobe with refractive x-ray lenses. In Yasushi Kagoshima, editor, *Proceedings of the 8th International Conference on X-ray Microscopy*, volume 7 of *IPAP Conference Series*, pages 94–96, Tokyo, 2006. IPAP.
- [22] Christian G. Schroer, Olga Kurapova, Jens Patommel, Pit Boye, Jan Feldkamp, Bruno Lengeler, Manfred Burghammer, Christian Riekkel, and Laszlo Vincze. Hard x-ray nanoprobe based on refractive x-ray lenses. *Acta Cryst. A*, 61:C64–C65, 2005.
- [23] Christian G. Schroer, Olga Kurapova, Jens Patommel, Pit Boye, Jan Feldkamp, Bruno Lengeler, Manfred Burghammer, Christian Riekkel, Laszlo Vincze, Andre van der Hart, and Matthias Kuchler. Hard x-ray nanoprobe based on refractive x-ray lenses. *Virtual Journal of Nanoscale Science & Technology*, 12(13), 2005.
- [24] Christian G. Schroer, Boris Benner, Til Florian Günzler, Marion Kuhlmann, Jens Patommel, Bruno Lengeler, Andrea Somogyi, Timm Weitkamp, Christoph Rau, Anatoly Snigirev, and Irina Snigireva. Nanotomography using parabolic refractive x-ray lenses. In U. Bonse, editor, *Developments in X-Ray Tomography IV*, volume 5535 of *Proceedings of the SPIE*, pages 701–708, Bellingham, 2004. SPIE.

- [25] S. V. Roth, H. Walter, P. Müller-Buschbaum, G. Bauer, T. Titz, N. Hermsdorf, M. Stamm, A. Snigirev, I. Snigireva, B. Lengeler, C. Schroer, M. Kuhlmann, J. Patommel, M. Burghammer, and C. Riekel. Investigating a silver cluster layer in confined geometry using the advanced scattering method microbeam GISAXS. In *Proceedings of Euromat 2003*, 2004.

Danksagung

Seit dem Beginn meiner Doktorarbeit vor reichlich sechs Jahren an der RWTH Aachen bis zur Abgabe dieses Dokuments im Sommer 2010 haben mich viele Menschen sowohl beruflich als auch privat begleitet und in unmittelbarer oder mittelbarer Weise zum Gelingen dieser Arbeit beigetragen. Nun ist es an der Zeit, mich bei all jenen zu bedanken.

An erster Stelle — und mit größtem Nachdruck — danke ich meinem Doktorvater Prof. Dr. Christian Schroer für das Vertrauen, das er mir entgegenbrachte, als er mich mit dem vielseitigen und spannenden Projekt „Rastersondenmikroskopie mit harter Röntgenstrahlung“ betraute. Neben der ausgezeichneten Betreuung unter exzellenten Rahmenbedingungen für ein erfolgreiches wissenschaftliches Arbeiten, ist es vor allem seine stets enthusiastische Art, andere Menschen für neue Ideen zu begeistern, die ich sehr zu schätzen weiß. An der außergewöhnlich guten Atmosphäre in der Arbeitsgruppe hat Christian durch seine humorvolle Art und sein lockeres Auftreten maßgeblichen Anteil.

Des weiteren bedanke ich mich bei Prof. Dr. Uwe Klemradt für die Bereitschaft, meine Doktorarbeit zu begutachten. Außerdem erinnere ich mich noch dankbar daran, wie Herr Klemradt noch während meiner Aachener Zeit ganz unbürokratisch seine Beamline E2 am HASYLAB zur Verfügung stellte, als ich ganz dringend unsere hochauflösende Röntgenkamera charakterisieren musste.

Auch wenn seit meiner Aachener Schaffensperiode bereits ein paar Jährchen ins Land gezogen sind, denke ich noch gern an die Kolleginnen und Kollegen unserer damaligen Aachener Arbeitsgruppe zurück. Für die schöne Zeit mit den Dispersiven Propagatoren danke ich Boris Benner, Christian Schroer, Florian Günzler, Mario Schweizer, Marion Kuhlmann, Olga Kurapova, Pit Boye, Regina Weinkauff, Sixta Vurgun, Sebastian Feste und Prof. Dr. Bruno Lengeler. Bereits damals in Aachen nannten wir uns `xray-lens.de`, und noch heute in Dresden treten wir unter diesem Namen auf.

Besonders hervorheben möchte ich an dieser Stelle die Bedeutung Herrn Lengelers für das erfolgreiche Zustandekommen dieser Arbeit. Unsere Bekanntschaft und Zusammenarbeit währt nun bereits über 8 Jahre. Es begann mit einer Anstellung als wissenschaftliche Hilfskraft in Herrn Lengelers Arbeitsgruppe, anschließend durfte ich bei ihm meine Diplomarbeit zum Thema „Hochauflösende Kamera für die Mikroskopie mit harter Röntgenstrahlung“ anfertigen. Bis zu seiner Emeritierung im Sommer 2004 war ich danach bei Herrn Lengeler Doktorand (betreut von Christian Schroer). Während der darauf folgenden 2 verbleibenden Jahre

in Aachen stand Herr Lengeler mit Rat und Tat beiseite. Als einer der Erfinder der refraktiven parabolischen Röntgenlinsen war er wie kein anderer ein Experte auf dem Gebiet der Röntgenmikroskopie. Auch in den vergangenen 4 Jahre in Dresden blieb der Kontakt stets erhalten. In Aachen trieb Herr Lengeler die Entwicklung hochwertiger Berylliumlinsen voran, während in Dresden die Rastersondenmikroskopie mit nanofokussierenden Linsen weiterentwickelt wurde. Zu erwähnen auch die zahlreichen erhellenden Diskussionen über Kohärenz in der Quantenmechanik und über Felder und Potentiale. Vielen Dank Herr Lengeler!

Während meiner ersten beiden Doktorandenjahre war Christian noch kein Professor, Herr Lengeler aber bereits emeritiert. Während dieser Übergangszeit war ich wissenschaftlicher Mitarbeiter in der Arbeitsgruppe von Professor Markus Morgenstern, der Lengelers Nachfolge angetreten hatte. Obwohl fachfremd (Herr Morgenstern beschäftigt sich mit Rastertunnelmikroskopie bei tiefen Temperaturen) wurde ich sehr herzlich von ihm und seinem jungen Team aufgenommen. Herrn Morgenstern und seiner damaligen Arbeitsgruppe danke ich für eine wunderbare Zeit.

An Aachen denkend muss ich aber vor allem auch den Mitarbeitern der Werkstatt des II. Physikalischen Instituts danken, insbesondere Peter Kordt, Wolfgang Retezki und Frank Neubauer. Die ersten Prototypversionen des Rastersondenmikroskops wären ohne das kompetente Team der Aachener Werkstatt nicht zustande gekommen. Immer wieder musste die Werkstatt meine Sonderwünsche erfüllen, galt es, ein dringend benötigtes Bauteil womöglich noch gestern zu fertigen — für die Werkstatt kein Problem. Neben der außergewöhnlich hohen Flexibilität bei der Realisierung meiner nicht immer ganz DIN-gemäßen Konstruktionszeichnungen wusste ich die hohe Qualität der gefertigten Werkstücke sehr zu schätzen. Also noch einmal ein ganz großes Lob und besten Dank an die Mitarbeiter der Aachener Werkstatt.

Im Jahre 2006 folgte Christian einem Ruf als Professor nach Dresden, wo er die Nachfolge von Prof. Dr. Peter Paufler antrat und das noch in Aachen begonnene Projekt „Rastersondenmikroskopie mit harter Röntgenstrahlung“ mitbrachte. So verschlug es mich zusammen mit meinen beiden Aachener Kollegen Jan und Pit nach Dresden, wo wir den Kern einer neuen Arbeitsgruppe bildeten (den Namen `xray-lens.de` behielten wir natürlich bei). Im Zuge der Zeit bekam die Arbeitsgruppe Zuwachs an Doktoranden und Studenten und nahm so manchen Post-Doktoranden und Diplomanden in ihre Reihen auf. Und so freue ich mich sehr, meinen Dresdner Kolleginnen und Kollegen für eine wunderschöne Zeit danken zu dürfen, namentlich Vivienne Meier, Susi Hönig, Sandra Stephan, Robert Hoppe, Pit Boye, Jan Feldkamp, Dirk Samberg, Christoph Rakete, Christian Schroer, Andy Goldschmidt, Andreas Schwab, Andreas Schropp und Alexander Shavkan. Es ist sehr angenehm, mit euch zusammenzuarbeiten. Ein großartiges Team, in dem ich mich immer sehr wohl fühle. Gemeinsam haben wir viel erreicht, die zahlreichen wochenlangen Messzeiten am ESRF oder an anderen Synchrotronstrahlungsquellen haben wir mit Bravour gemeistert; die meisten Ergebnisse dieser Doktorarbeit sind im wesentlichen Früchte dieser Einsätze.

Ich danke Frau Böltzig und Frau Junker für das Erledigen all der Verwaltungsangelegenhei-

ten, für das Organisieren der Projekttage, Institutsgrillfeste, Weihnachtsfeiern, Geburtstagsgratulationen, und so weiter.

Was in Aachen galt, stimmt auch hier in Dresden. Ohne Mechanikwerkstatt läuft einfach gar nichts. Deshalb einen ganz großen Dank an unsere Werkstatt unter der Leitung von Martin Siegel.

Herausstellen möchte ich insbesondere meine beiden langjährigen Weggefährten Jan und Pit. Wir kennen uns bereits aus Aachen, wo die beiden Diplomanden bei Herrn Lengeler waren. Zusammen mit Christian teilten wir eine gemeinsame Vorliebe, nämlich das Indern. Bereits zu Aachener Zeiten, später fortgeführt in Dresden, war es Tradition, mindestens ein bis zwei mal im Monat indisch Essen zu gehen (oder auch vietnamesisch, chinesisches, mexikanisches, aber am liebsten indisch). Und als Kompensation gingen wir im Plauener Grund und Umgebung joggen. War wirklich eine tolle Zeit mit euch!

Das Röntgenmikroskop wurde am Strahlrohr ID 13 der Synchrotronstrahlungsquelle ESRF, Grenoble aufgebaut. Über Jahre hinweg ist unsere Arbeitsgruppe regelmäßig zu Gast an der ID 13 gewesen, um dort wochenlang die Beamline zu besetzen und Experimente mit dem Röntgenmikroskop durchzuführen. Dabei konnten wir auf eine exzellente Betreuung durch die Mitarbeiter der Beamline bauen. Und wir waren weiß Gott keine leichten User, unsere Aufbauten alles andere als minimalinvasiv. Ich danke hiermit Christian Riekkel, Manfred Burghammer, Lionel Lardiere und Sebastian Schoeder für eine fruchtbare Zusammenarbeit.

Christian Riekkel war bis zu seiner Pensionierung 2009 Chef der ID 13 und hat das Projekt „Rastersondenmikroskopie mit harter Röntgenstrahlung“ durch langjährige Kollaboration und großzügig gewährte Messzeiten gefördert und somit zu dessen Erfolg beigetragen.

Manfred und Sebastian sind unsere Ansprechpartner an der Strahllinie ID 13 (Local Contact). Weit über die üblichen Aufgaben eines Beamline Scientists und Local Contacts hinaus setzten sie sich mit unermüdlichem Eifer für das Gelingen der Experimente ein. Hätte sich jemand die Mühe gemacht, die Überstunden aufzuschreiben — die beiden hätten für den Rest des Jahres frei nehmen können. Inzwischen ist Manfred Beamline-Chef der ID 13, was ihn aber nicht davon abhält, nach wie vor aktiv an den Experimenten teilzunehmen. Ein Glücksfall ist zudem die Tatsache, dass Manfred und Sebastian auswärtige Restaurants genauso gern mögen wie die Mitglieder unserer Arbeitsgruppe, so dass wir hinreichend oft der ESRF-Kantine zu entgehen vermochten. Manfred verdanke ich auch das Kennenlernen zahlreicher Perlen der Filmgeschichte, die er mir zu jeder Messzeit als DVD mitbrachte. Danke auch für unermesslich viele Kaffee-Einladungen und für all die hochinteressanten, tiefsinnigen, humorvollen Diskussionen und Dispute, die nicht immer auf physikalische Themen beschränkt blieben.

Lionel ist Mechaniker an der ID 13 und somit einfach unverzichtbar. Gerade wenn man einen Prototypen mit seinen vielfältigen mechanischen und elektronischen Komponenten entwickelt, ist man heilfroh, einen Mechaniker zur Hand zu haben, der auch ganz schnell mal Notlösungen improvisieren kann. Einen riesen großen Dank an Lionel.

In puncto Kontrollsoftware und IT habe ich sowohl Manuel Perez (ESRF BLISS-Gruppe) als auch Jens Meyer (ESRF TANGO-Gruppe) zu danken. Manuel braucht man ein hochkomplexes Problem mit nur wenigen Worten zu erläutern und schon liefert er eine saubere funktionierende Lösung. Mit seiner effizienten Arbeitsweise war er grundlegend an der erfolgreichen Kommunikation zwischen SPEC (zur Steuerung der Beamline-Komponenten) und unserem *accontrol* (zur Steuerung der Komponenten des Röntgenmikroskops) beteiligt. Jens Meyer danke ich für seine Bereitschaft, mir bei diversen Fragen bezüglich TANGO-Deviceservern zu helfen. Insbesondere beim Portieren der TANGO-Bibliotheken für Mac OS X war er sehr hilfsbereit.

Wenn ich über Experimente am ESRF rede, muss ich auch die zahlreichen Wissenschaftler erwähnen, die mit uns an der ID 13 zusammenarbeiteten. Hier jetzt jeden Einzelnen aufzuführen ist unmöglich, nennen möchte ich aber vor allem Walter Schröder, Laszlo Vincze, Michael Hanke, Martin Dubsloff, Martin Schmidbauer, Klaus Giewekemeyer, Robin Wilke, Tim Salditt, Johannes Gulden, Adrian Mancuso, Ivan Vartaniants, Stephan Roth, Ralf Röhlsberger, Christoph Steimer und Katharina Hartmann.

Das Projekt „Rastersondenmikroskopie mit harter Röntgenstrahlung“ findet finanzielle Unterstützung vom Bundesministerium für Bildung und Forschung (BMBF), das unter anderem auch meine Doktorandenstelle finanziert.

Andreas Schropp danke ich für seine Korrekturen und wertvollen Kommentare bezüglich des vorliegenden Dokuments. Er hat mich auch immer wieder daran erinnert, an der Arbeit weiterzuschreiben, sonst hätte ich mich wohl auch weiterhin zu gern durch andere interessante Dinge ablenken lassen.

Ich danke meiner Familie für jegliche Unterstützung und allen Menschen, die mir in welcher Form auch immer Beistand geleistet haben.

Curriculum Vitae

- Name : Jens Patommel
- Date of Birth: 7th of June 1977
- Place of Birth: Wilhelm-Pieck-Stadt Guben, GDR
-
- 08/1984 – 08/1990: Polytechnische Karl-Marx-Oberschule
in Guben, GDR
- 09/1990 – 08/1991: Secondary school “Realschule an der Josefskirche”
in Viersen, Germany
- 09/1991 – 06/1997: Grammar school “Erasmus-von-Rotterdam Gymnasium”
in Viersen, Germany
- 09/1997 – 09/1998: Community service in a day-care center
in Viersen, Germany
- 10/1998 – 12/2003: Studies of physics
at Rheinisch-Westfälische Technische
Hochschule Aachen, Germany
- 01/2003 – 12/2003: Diploma thesis
at II. Institute of Physics B, RWTH Aachen, Germany
*“Entwicklung einer hochauflösenden Kamera für
die Mikroskopie mit harter Röntgenstrahlung”*
(*“Development of a high resolution x-ray camera
for magnified tomography with hard x rays”*)
- 01/2004 – 03/2006: PhD studies of physics
at II. Institute of Physics B, RWTH Aachen, Germany
- 04/2006 – 06/2010: PhD studies of physics
at Institute of Structural Physics,
Technische Universität Dresden, Germany

Erklärung

Hiermit versichere ich, dass ich die vorliegende Arbeit ohne unzulässige Hilfe Dritter und ohne Benutzung anderer als der angegebenen Hilfsmittel angefertigt habe; die aus fremden Quellen direkt oder indirekt übernommenen Gedanken sind als solche kenntlich gemacht. Die Arbeit wurde bisher weder im Inland noch im Ausland in gleicher oder ähnlicher Form einer anderen Prüfungsbehörde vorgelegt.

Ich erkenne die Promotionsordnung der Fakultät Mathematik und Naturwissenschaften der Technischen Universität Dresden vom 17.07.2008 in vollem Umfang an.

Die Dissertation wurde unter der wissenschaftlichen Betreuung von Prof. Dr. C. G. Schroer am Institut für Strukturphysik angefertigt.

(Jens Patommel)
Dresden, 30. Juni 2010